Study of shape coexistence in nuclei with A≈100 using stable and radioactive ion beams

Desislava Kalaydjieva

université PARIS-SACLAY

Study of shape coexistence in nuclei with $A \approx 100$ using stable and radioactive ion beams

Etude de la coexistence de formes dans les noyaux $A \approx 100$ à l'aide de faisceaux d'ions stables et radioactifs

Thèse de doctorat de l'université Paris-Saclay

École doctorale n°576 Particules, Hadrons, Énergie et Noyau : Instrumentation, Image, Cosmos et Simulation (PHENIICS)
Spécialité de doctorat: Physique Nucléaire
Graduate School : Physique
Référent : Faculté des Sciences d'Orsay

Thèse préparée dans le **Département de Physique Nucléaire** (Université Paris-Saclay, CEA), sous la direction de **Magda ZIELIŃSKA**, Ingénieure-chercheuse, et la co-direction de **Wolfram KORTEN**, Directeur de Recherche

Thèse soutenue à Paris-Saclay, le 20 octobre 2023, par

Desislava KALAYDJIEVA

Composition du jury

Membres du jury avec voix délibérative

David JOSS Professeur, University of Liverpool, Royaume-Uni	Président
Claes FAHLANDER Professeur émérite, University of Lund, Suède	Rapporteur & Examinateur
Agnieszka KORGUL Professeur, University of Warsaw, Pologne	Rapportrice & Examinatrice
Amel KORICHI Directrice de Recherche, IJCLab, Université Paris-Saclay	Examinatrice
Jan JOLIE Professeur, University of Cologne, Allemagne	Examinateur

THESE DE DOCTORAT
NNT : 2023UPASP134

université PARIS-SACLAY

ÉCOLE DOCTORALE
Particules, hadrons, énergie et noyau : instrumentation, imagerie, cosmos et simulation (PHENIICS)

Titre: Etude de la coexistence de formes dans les noyaux $A \approx 100$ à l'aide de faisceaux d'ions stables et radioactifs
Mots clés: excitation coulombienne, spectroscopie gamma, formes de noyaux

Résumé: Le sujet de la thèse porte sur les manifestations du phénomène de coexistence de formes dans les noyaux atomiques de nombre de masse $A \approx 100$, en particulier les noyaux de ^{106}Cd et de ^{100}Zr.

Le ^{106}Cd a été étudié via l'excitation coulombienne au-delà l'énergie "sûre" en utilisant le dispositif expérimental AGATA + VAMOS au GANIL, France. Les sections efficaces d'excitation extraites de cette mesure ont été analysées à l'aide des codes en voies couplées GOSIA et FRESCO. Les probabilités de transition obtenues ont été comparées aux résultats d'études précédentes d'excitation coulombienne "sûre" et de mesures de durée de vie, démontrant que les informations sur la structure nucléaire peuvent être obtenues à partir de données d'excitation coulombienne au-delà l'énergie "sûre". La coexistence de formes dans le ^{106}Cd est discutée dans le cadre des calculs au-delà du champ moyen. Les probabilités de transition E3 vers plusieurs états de parité négative ont été mesurées pour la première fois.

Une étude du ^{100}Zr par désintégration bêta a été réalisée avec le spectromètre GRIFFIN à TRIUMF, Canada. Dans ce travail de thèse, le schéma de niveau de ce noyau a été étendu. Les rapports d'embranchement et de mélange ont été extraits pour plusieurs transitions. En utilisant les corrélations angulaires γ-γ, plusieurs nouveaux états 0^+ excités ont été identifiés, ainsi que des candidats pour les états 2^+ construits sur eux. Les résultats sont discutés dans le cadre de récents calculs de type modèle en couches utilisant la technique Monte Carlo, qui prédisent la coexistence de formes multiples.

Title: Study of shape coexistence in nuclei with $A \approx 100$ using stable and radioactive ion beams
Keywords: Coulomb excitation, gamma-ray spectroscopy, nuclear shapes

Abstract: The thesis focuses on the manifestations of the shape-coexistence phenomenon in atomic nuclei with mass number $A \approx 100$, specifically ^{106}Cd and ^{100}Zr.

The ^{106}Cd nucleus was studied via unsafe Coulomb excitation using the AGATA+VAMOS setup at GANIL, France. The measured excitation cross sections were analysed with help of coupled-channel codes GOSIA and FRESCO. The deduced transition probabilities were compared to results of previous safe Coulomb-excitation studies and lifetime measurements, demonstrating that nuclear structure information can be reliably obtained from unsafe Coulomb-excitation data. Shape coexistence in ^{106}Cd is discussed in the context of Beyond-Mean-Field calculations. Information on E3 transition strengths to several negative-parity states in ^{106}Cd is reported for the first time.

A β-decay study of ^{100}Zr was performed with the GRIFFIN spectrometer at TRIUMF, Canada. In the present work, the level scheme of this nucleus has been extended. Branching and mixing ratios were extracted for multiple transitions. Using γ-γ angular correlations, several new low-energy excited 0^+ states were identified, as well as candidates for the 2^+ states built on them. The results are discussed in the framework of recent Monte-Carlo Shell-Model calculations, which predict multiple shape coexistence.

На жените, които ме отгледаха с любов и отдаденост:
майка ми Снежина и бабите ми Мария, Горанка и Стефана.

Acknowledgements

Firstly, I would like to express my gratitude to my supervisors Magda Zielińska and Wolfram Korten. Thank you for accepting me as your student and for your unwavering support on my way to becoming a Doctor. I have gained an incredible amount of knowledge and skills from you for which I am truly grateful beyond words.

The guidance of a great teacher is key in studying a complex and demanding subject. That is why I am happy to have had the opportunity to learn about Coulomb excitation from Magda. With a lot of patience, she introduced me to the method and to GOSIA in a clever and understandable way, down to the most intricate details, and always found time to answer my ceaseless questions. I appreciate Magda for being highly supportive of my ideas, helping me to further develop them, and letting me explore and learn through them at my own pace. Her day-to-day guidance shaped my analysis and indeed, this work, and especially the quality of this manuscript owe a lot to her dedication and her thoughtful corrections, ideas, and improvements. Furthermore, I am grateful to Magda for introducing me to a wonderful collaboration of experimentalists, involving me in many fruitful projects, and making sure to present me with numerous opportunities to grow as a scientist. Despite my insecurities, she always encouraged me to share my work, aided me in presenting it in the best possible way, and kindly eased my worries with much-needed reassurance. Thank you, Magda, for believing in me, especially when I didn't quite believe in myself. You truly helped me fight my fears of flying (both figuratively and literally). Thank you for sharing with me your experience and knowledge and for the time and effort you devoted to my scientific and personal growth.

I would also like to thank Wolfram, with whom I had many fruitful and inspirational discussions on various topics. Wolfram was always open to my questions and pointed me toward the appropriate literature and resources to continue learning. Thank you for involving me in your projects to broaden my view with different experimental techniques outside of my thesis work, as well as for your valuable advice and support on scientific, administrative, and personal matters.

Jokingly I was often telling Marco Siciliano and Marco Rocchini that I had been graced with the "Marco-s' blessing". However, I could have never been more serious by saying this since it is completely true. It was a blessing to have both of you around during my PhD journey, despite being separated by thousands of kilometers most of the time.

I kindly thank Marco Siciliano for trusting me with the analysis of his dataset on unsafe Coulomb excitation of ^{106}Cd and for always giving me a helping hand when needed. Marco was very kind and honest to me and always found time to meet and answer my various questions, even if sometimes he had to sacrifice his free time.

Thank you, Marco, for sharing your ideas and passion for nuclear physics with me and for being there for me, especially in the moments when I was feeling down.

Although I met Marco Rocchini later in my PhD, I am no less grateful to him. With the same kindness and patience, he always found time to help me with my projects. Considering the tight schedule of my studies, Marco was able to quickly introduce me to the data analysis of GRIFFIN data and guide me to obtain the needed results. While I had no previous experience with GRSISort, I was very lucky to also have the help of Vinzenz Bildstein. It was indeed a pleasure to work with both of you during my stay at the University of Guelph. I would like to also thank the welcoming nuclear physics group there full of promising students, whom I am happy to have met.

Furthermore, I cannot miss the opportunity to also thank Prof. Paul Garrett for sharing his experience and infectious passion for knowledge with me. I am grateful to him for trusting me with his outstanding data set from the GRIFFIN spectrometer and for his thoughtful guidance and patience. I learned a lot from Paul, who despite his busy schedule, always found time for my questions on nuclear structure and data analysis. Indeed, I owe a lot to the discussions with Paul for understanding the structure of both ^{106}Cd and ^{100}Zr, and for the interpretation of the results I obtained.

While working on unsafe Coulomb-excitation data I had the pleasure to meet and work with Nicholas Keeley and Valérie Lapoux. I appreciate the detailed advice of Nick and thank him for teaching me how to properly work with FRESCO. I am grateful to Valérie for finding time to answer my questions about the scattering processes and to improve my understanding by providing me with all the needed literature.

I would also like to express my gratitude to the welcoming LENA and LEARN groups at CEA. I am happy to have been part of your great team at IRFU. I would like to especially thank Frank Gunsing, who was truly caring and never missed an opportunity to make my stay at CEA better with his thoughtfulness, Barbara Sulignano for her kindness, and Stephane Platchkov who always found time to help me ease my worries and engage in fascinating discussions about physics and its history.

During my Ph.D. I had the privilege to participate in several experiments and meet wonderful researchers from all around the world. I truly enjoyed the time we spent together and thank the welcoming teams at HIL, TRIUMF, LNL Legnaro, ISOLDE, and ALTO. I would like to especially thank Kasia Wrzosek-Lipska, Kasia Hadyńska-Klęk, Paweł Napiorkowski, Michalina Komorowska, Naomi Marchini, and Adriana Nannini. Dear Michalina, thank you for the enjoyable conversations that made the night shifts pass so quickly.

I would like to thank Prof. Claes Fahlander, Prof. Agnieszka Korgul, Prof. David Joss, Dr. Amel Korichi, and Prof. Jan Jolie for accepting to be part of my jury and for the time they dedicated to reading my thesis work. I am grateful

for your thoughtful questions and comments. I would like to especially thank my referees, Prof. Fahlander and Prof. Korgul, for the effort they put into preparing their reports. I am truly grateful to Prof. Fahlander for the kind words he shared with me after my defense. I will always remember them and promise myself and him to work on becoming more confident and proud of my work.

My journey in the world of Nuclear Physics would have never been the same without many thoughtful and helping people I have met on my way as the list above is not anyhow exhaustive.

I am lucky to have been born into a loving and supportive family, which did not stop me from pursuing my dreams regardless of the difficulties. I am deeply thankful for the care and love I always felt despite the distance. In particular, I want to thank my Mother, Snezhina, for her kind love and for all the sacrifices she made so I can have a better life. I dearly love you. My sweet cousins, Yana and Maria, I am sure a great future awaits you. I often feel sorry for the fun moments we have missed in these years and hope we can catch up soon. My beloved grandmothers, Maria, Goranka, and Stefana, you will always be in my heart and I deeply miss you.

My dear friends back home, Hrisi, Boris, Kalin (x2), Kaloyan, Marina, and Nedko, thank you for always cheering me up and encouraging me to follow my dreams.

Nothing I have achieved would have been possible without the unconditional support from (now Dr.) Konstantin Stoychev. You were truly my rock and I am blessed to have shared all the happy and sad moments with you during our studies. I will forever cherish the memories we made together and I am looking forward to our new adventures. Thank you for always being there for me, I will always be there for you.

Table of contents

Résumé

Une des questions phares dans le domaine de la structure nucléaire concerne l'émergence de collectivité, qui se traduit par l'apparition de formes nucléaires déformées, et son lien avec la structure microscopique du noyau. La forme du noyau, c'est-à-dire l'écart de sa distribution de masse et de charge par rapport à la sphéricité, est une des propriétés nucléaires fondamentales. Elle est gouvernée par des effets macroscopiques (goutte liquide) et microscopiques (structure en couches du noyau). Leur compétition est à l'origine des changements rapides de forme des noyaux en fonction du nombre de nucléons.

Comme la forme d'un état nucléaire dépend des particularités de sa fonction d'onde, il est également possible d'observer des états aux formes radicalement différentes au sein du même noyau et même dans une très petite gamme d'énergie d'excitation, ce que l'on appelle la coexistence de formes. On pensait initialement que la coexistence de formes était un phénomène rare, mais son occurrence a été établie a travers la carte de noyaux. Les preuves expérimentales décisives de ce phénomène sont difficiles à obtenir, car elles nécessitent une connaissance exhaustive d'un grand nombre de propriétés nucléaires liées à la déformation nucléaire. Cependant, ces études sont essentiels pour tester les interactions nucléaires et les modèles de structure du noyau.

Ce travail de thèse est focalisé sur les manifestations du phénomène de coexistence de formes dans les noyaux atomiques de nombre de masse $A \approx 100$, en particulier les noyaux de ^{106}Cd et de ^{100}Zr. Les résultats expérimentaux ont été obtenus par spectroscopie gamma de haute résolution en utilisant deux des systèmes de détection à la pointe de la technologie : AGATA au GANIL et GRIFFIN à TRIUMF. Ces résultats sont discutés dans le cadre de récents calculs théoriques de type Au delà du Champ Moyen (BMF) ou Modèle en Couches utilisant la technique Monte Carlo (MCSM), qui prédisent la coexistence de formes multiples dans ces noyaux.

Excitation coulombienne du ^{106}Cd au-delà de l'énergie "sûre" étudié avec le multi-détecteur AGATA

Les isotopes stables du cadmium étaient considérés comme de parfaits exemples de noyaux avec des états fondamentaux sphériques et les états excités qui résultent des vibrations autour de leur forme d'équilibre sphérique. Cependant, suite aux études expérimentales récentes, avec l'aide des calculs au-delà du champ moyen, une interprétation différente des schémas de niveaux des $^{110-112}$Cd a été proposée, à savoir en termes de la coexistence de formes multiples [10]. Dans le cadre de ce projet de thèse, ces études ont été étendues au ^{106}Cd en utilisant les données de diffusion inélastique. Ces données ont été issues d'une expérience de mesure

des temps de vie en utilisant la technique Doppler (Recoil-Distance Doppler Shift, RDDS [54]) qui a été effectuée au GANIL en 2015 et qui était focalisée sur les propriétés des noyaux d'étain et de cadmium [49, 50]. Le noyaux d'intérêt ont été produits utilisant des réactions de Transfert de Multi-Nucléons (MNT) entre le faisceau du ^{106}Cd à l'énergie de 770 MeV, et la cible du ^{92}Mo. Les rayonnements γ émis par les produits de réaction ont été mesurés par huit détecteurs triples du spectromètre AGATA [52] en coïncidence avec les produits de réaction qui ont été identifiés en termes du nombre de masse A et du numéro atomique Z dans le dispositif VAMOS++ [51].

Dans la même expérience, plusieurs états excités dans le noyau du ^{106}Cd ont été peuplés grâce à l'excitation coulombienne, c'est-à-dire le processus de diffusion quasi-élastique de deux noyaux, ou le champ électromagnétique qui agit entre eux est à l'origine de leur excitation. Ce processus a eu lieu à une énergie de faisceau qui se trouvait entre 8 et 40% (en fonction de l'angle de diffusion) au dessus de l'énergie "sûre", donnée par le critère empirique de Cline [40]. Ce critère, qui donne la distance minimale d'approche entre le projectile et la cible (ce qui correspond à une faible énergie incidente et un angle de déviation relativement faible), est habituellement utilisé pour assurer que l'interaction nucléaire de courte portée peut être négligée. Dans ce cas, il est possible d'extraire le jeu d'éléments de matrice de l'opérateur électromagnétique à partir des sections efficaces de population des états excités. Ils sont liés aux probabilités de transition réduites et aux moments quadripolaires, et donc aux moments statiques et dynamiques de la distribution de charge (c'est-à-dire à la forme) des noyaux étudiés. Si le critère de Cline n'est pas rempli, comme dans le cas de l'expérience décrite ici, l'interaction nucléaire peut influencer les sections efficaces d'excitation mesurées expérimentalement, rendant l'extraction des propriétés nucléaires impossible sans recours aux modèles. Par conséquent, un des objectifs de ce travail de thèse était l'évaluation des effets de l'interaction nucléaire sur les sections efficaces en fonction de l'angle de diffusion et du spin-parité de l'état excité.

Dans un premier temps, les section efficaces de peuplement de certains niveaux excités dans le ^{106}Cd ont été simulés grâce au code de réaction FRESCO [36]. Cela a permis de prendre en compte les effets induits par la présence de l'interaction nucléaire en utilisant le modèle du potentiel optique. Ces calculs ont montré que les données obtenues aux angles de diffusion les plus petits, même si le critère de Cline n'était pas rempli, étaient très peu affectées par l'interaction nucléaire. Aux angles de diffusion plus élevés, un écart systématique par rapport au processus d'excitation coulombienne a été prédit, lié à l'interférence entre l'interaction nucléaire et l'interaction coulombienne.

L'étape suivante a consisté à simuler les intensités gamma issus des désintégrations de 20 états dans le ^{106}Cd sur la base des données spectroscopiques existantes (les temps de vie, les rapports d'embranchement et de mélange) en supposant que l'excitation était due à l'interaction purement coulombienne. Cette tache a été

réalisée à l'aide du code en voies couplées GOSIA [68], qui est un outil standard pour analyser les données d'excitation coulombienne à l'énergie "sûre". À partir d'une comparaison entre les intensités simulées et mesurées en fonction de l'angle de diffusion, il a été possible d'évaluer dans quelle mesure l'interaction nucléaire a affecté les données. Notamment, les distributions obtenues pour les états qui ont été fortement peuplés dans l'expérience, comme par exemple le 4_1^+ et le 2_2^+, étaient similaires à ceux calculées pour le processus d'excitation purement coulombien.

Enfin, l'ajustement des éléments de matrice par minimisation du χ^2 a été réalisé avec GOSIA pour extraire l'information concernant la structure du ^{106}Cd à partir des intensités gamma mesurées. 43 éléments de matrice ont été obtenus, y compris un certain nombre de nouveaux résultats. En comparant les éléments de matrice ainsi extraits et ceux issus de mesures précédentes nous avons démontré qu'il est possible d'obtenir les probabilités de transition fiables à partir des données d'excitation coulombienne au-delà de l'énergie "sûre", notamment pour les états fortement peuplés. En outre, les signes relatifs de certains éléments de matrice ont été déterminés pour la première fois.

Ces résultats apportent de nouvelles informations sur la structure du ^{106}Cd. Une comparaison avec les résultats des calculs BMF [50] favorise l'interprétation en termes de coexistence de formes, même si certains conclusions sont limitées par le désaccord entre les rapports d'embranchement présents dans la littérature. Pour la première fois, la probabilité de transition réduite B(E2) pour la voie de désintégration dominante de la tête de bande "oblate" (0_3^+) a été déterminée, et elle est en excellent accord avec les calculs BMF. En revanche, la collectivité dans la bande bâtie sur l'état 0_3^+ est plus faible que ne le suggèrent les prédictions théoriques, et aussi plus faible que dans les bandes correspondantes dans les ^{110,112}Cd.

En appliquant le formalisme de Quadrupole Sum Rules [5, 6] aux éléments de matrice E2 déduits des intensités gamma mesurées, les invariants rotationnels $\langle Q^2 \rangle$ ont été déterminés pour plusieurs états dans la bande fondamentale du ^{106}Cd. Ils sont liés a leur déformation globale β. Leur tendance en fonction du spin est en bon accord avec celle prédite par les calculs BMF, mais en désaccord avec le modèle vibrationnel [71]. En outre, le schéma de niveaux de basse énergie dans le ^{106}Cd a été réorganisé sur la base des probabilités de transition B(E2) extraites de notre analyse. Notamment, une bande "gamma" a été proposée, ce qui suggère une certaine triaxialité de l'état fondamental. Les énergies des états qui forment cette bande sont en accord avec la systématique des niveaux excités dans les $^{106-112}$Cd.

Les sections efficaces d'excitation coulombienne sont aussi sensibles aux éléments de matrice E3 qui sont liés à la collectivité octupolaire (le noyau adopte une forme de poire). L'élément de matrice $\langle 3_1^- || E3 || 0_1^+ \rangle$ déduit de notre analyse est en bon accord avec celui déterminé de l'expérience récente [75] qui utilisait l'excitation coulombienne à l'énergie "sûre". Pour la première fois, les limites supérieures des éléments de matrice E3 liés au peuplement des états $5_{1,2}^-$ and 1_1^- ont été déterminés, fournissant un aperçu de la collectivité octupolaire du ^{106}Cd.

De plus, nous avons démontré que le peuplement des états 5_2^- et 1_1^- peut être expliqué par la présence de transitions E2 collectives entre ces états et le 3_1^-, ce qui est en accord avec le scénario du couplage quadripolaire-octupolaire. Pour vérifier cette hypothèse, une expérience de décroissance β de précision a été proposée à TRIUMF avec le spectromètre gamma GRIFFIN [127] (S2313, porte-paroles : P. Garrett, D. Kalaydjieva, M. Zielińska). Le but de cette mesure est de chercher les voies de désintégration faibles des états 5_2^- et 1_1^-, et de résoudre les diverses énigmes concernant la structure du ^{106}Cd, mises en évidence dans ce travail de thèse. Cette proposition d'expérience a été acceptée avec la priorité élevée et l'expérience devrait être planifiée au cours des trois prochaines années.

Coexistence de formes multiples dans le ^{100}Zr étudiée via décroissance β avec le spectromètre GRIFFIN

Les noyaux riches en neutrons de nombre de masse A≈ 100 présentent une des rares transitions abruptes de forme de l'état fondamental qui apparaît brusquement à $N = 60$ [4]. Ce comportement unique est mis en évidence par les mesures de masse et de rayons de charge, ainsi que par une baisse soudaine de l'énergie d'excitation du premier état 2^+ dans les noyaux pairs-pairs et une augmentation de la probabilité de transition réduite $B(E2; 2_1^+ \rightarrow 0_1^+)$. L'observation dans les noyaux autour de $N = 60$ d'états 0^+ à basse énergie d'excitation suggère un scénario de coexistence de formes.

Récemment, Togashi et al. ont reproduit dans le cadre du modèle en couches utilisant la technique Monte Carlo (MCSM) [134] la systématique en énergie des premiers états excités dans les isotopes de zirconium autour de $N = 60$ et les probabilités de transition correspondantes. Par ailleurs, une explication de la rapidité de la transition de forme observée à $N = 60$ a été proposée en invoquant le phénomène d'«évolution de couches de type II» [182] et l'inversion de configurations du ^{98}Zr et ^{100}Zr avec un mélange faible. Précisément, l'état 0_2^+ observé à environ 1 MeV dans le ^{98}Zr, qui a une forme $prolate$, devient l'état fondamental du ^{100}Zr, tandis que l'état fondamental sphérique du ^{98}Zr correspond à un état 0_4^+ dans le ^{100}Zr qui n'a pas été identifié encore, mais il est prédit à l'énergie d'excitation d'environ 1.5 MeV. En outre, l'état 0_2^+ d'une forme $oblate$ a été prédit de coexister dans le ^{100}Zr avec l'état 0_3^+ $prolate$.

Afin d'étudier la coexistence de formes multiples suggérée dans le ^{100}Zr, une expérience de décroissance β du ^{100}Y vers ^{100}Zr a été effectuée à l'aide du spectromètre GRIFFIN [127] au laboratoire TRIUMF-ISAC fin 2021. Un mélange d'ions radioactifs ^{100}Sr et ^{100}Rb – les noyaux père et grand-père du ^{100}Y – a été implanté dans une bande magnétique située au centre du dispositif expérimental, composé de 15 détecteurs Clover de gros volume du système GRIFFIN, sept scintillateurs $LaBr_3$ pour déterminer les temps de vie des états excités, et le multi-détecteur Si(Li) PACES [144] pour mesurer le spectre d'électrons de conversion.

La plupart des données ont été accumulées selon le cycle suivant : une phase de mesure du bruit de fond (0.25s) suivi par une phase de collection (3.5s, ce qui est équivalent à 5 durées de vie de ^{100}Y), ensuite une phase de décroissance (1s), et finalement une phase de mouvement de la bande d'implantation (1s).

Le pré-traitement des données a été effectué en utilisant l'environnement d'analyse GRSISort [164]. Ensuite, chaque cristal HPGe a été étalonné en énergie à l'aide de sources radioactives, suivi par un ajustement fin sur la base des données sous faisceau. La procédure add-back et des corrections de diaphonie ont été appliquées, ce qui a contribué à améliorer la résolution en énergie et le rapport pic sur total. Enfin, l'étalonnage en efficacité a été effectué, ce qui était indispensable pour déterminer les intensités γ relatives. Le nombre total de coïncidences γ-γ, après la suppression Compton, la procédure add-back et la suppression de coïncidences fortuites, était $\approx 4 \times 10^9$.

L'un des principaux objectifs de cette expérience était de développer le schéma de niveaux du ^{100}Zr grâce aux coïncidences γ-γ. Dans ce projet de thèse, le travail s'est concentré sur les états au-dessous de 2.2 MeV. A l'aide de l'ensemble de logiciels RadWare [170], plus de 60 transitions gamma ont été placés dans le schéma proposé, parmi lesquelles 30 ont été observés pour la première fois. A partir des spectres conditionnées sur des transitions peuplant les niveaux d'intérêt, plusieurs rapports d'embranchement ont été déterminés avec une précision nettement améliorée. Par ailleurs, six nouveaux états ont été identifiés, notamment le 2^+ à 2208 keV, proposée dans notre article [172], et deux états de spin 0. Parmi les résultats notables on peut aussi mentionner la première observation d'une transition collective entre l'état 2_3^+, précédemment interprété comme la tête de bande γ [146], et le 0_3^+. Par conséquent, le 2_3^+ a été proposé de faire partie d'une bande rotationnelle (correspondant probablement à une forme $prolate$) bâtie sur le 0_3^+.

Grâce à l'analyse de corrélations angulaires γ-γ, les rapports de mélange $E2/M1$ ont été déterminés pour plusieurs transitions. Les spins de six états ont été attribués pour la première fois, y compris trois états de spin 0. La technique de mélange des évènements [133] a été appliquée aux matrices de coïncidence γ-γ à l'aide de GRSISort. Pour chaque cascade étudiée, une condition a été appliquée sur l'une des transitions, et l'autre transition de la cascade a été ajustée dans les spectres projetés pour chacun des 49 angles uniques entre les différents cristaux de Ge de GRIFFIN. L'évolution de cette intensité en fonction de l'angle entre les deux rayons γ dans la cascade a été analysée afin de déterminer le spin de l'état initial et le rapport de mélange de la transition, si applicable. De plus, les simulations Geant4 ont été réalisées pour prendre en compte des effets induits sur les corrélations angulaires par la taille des détecteurs germanium.

Les résultats obtenus pour les structures bâties sur les états $0_{1,2}^+$ ont été comparés avec les prédictions du MCSM et du modèle de mélange à deux niveaux. Le paramètre d'élongation β de l'état fondamental et celui de l'état 0_2^+ ont été calculés en appliquant le formalisme de Quadrupole Sum Rules aux éléments de

matrice E2 déduits à partir des temps de vie des états 2_1^+, 2_2^+ et 0_2^+ et les rapports de mélange et d'embranchement déterminés dans ce travail de thèse. Cette analyse a démontrée de fortes similitudes entre les structures des ^{100}Zr et ^{98}Sr à basse énergie d'excitation, et les arguments importants en faveur de coexistence de formes dans le ^{100}Zr. Cependant, nous avons démontré que contrairement au ^{98}Sr le modèle de mélange à deux niveaux n'est pas capable de décrire de manière cohérente les probabilités de transition dans le ^{100}Zr et le scénario de mélange impliquant les états à basse énergie est plus compliqué. Enfin, l'état 2^+ à 2208 keV a été proposé comme le membre de spin 2 d'une bande bâtie sur le 0_4^+. L'espacement de niveaux dans cette structure proposée suggère que sa collectivité est inférieure à celle des autres bandes bâties sur les états 0^+ dans le ^{100}Zr, mais plus grande que celle de l'état fondamental du ^{98}Zr, qui peut être déduite de l'énergie d'excitation de l'état 2^+ quasi-sphérique correspondant. Dans le futur proche, une extraction plus rigoureuse de rapports d'embranchement est prévue avec notamment les corrections des pertes par sommation. Le schéma de niveaux du ^{100}Zr sera aussi étendu aux énergies d'excitation plus élevées.

Preamble

This manuscript is divided into two main parts.

The first part presents results of the analysis of "unsafe" Coulomb excitation of ^{106}Cd. I gave presentations on this project at two large collaboration meetings (GOSIA Workshop, HIL Warsaw, March 27-20, 2023; AGATA Collaboration Meeting, Legnaro, June 10, 2022). The final publication is at an advanced stage of preparation and is intended to be submitted to European Physics Journal A in autumn 2023. I am a co-spokesperson of an experiment aiming to study the structure of ^{106}Cd via β decay, motivated by the results obtained within this thesis, which has been approved by the TRIUMF NP-EEC in July 2023.

The second part presents preliminary results of a β-decay study investigating low-spin states in ^{100}Zr. The analysis of this data set is in progress, and I presented selected results at two international conferences (ISTROS '23, Casta-Papiernicka, Slovakia, May 14-19, 2023; Zakopane Conference on Nuclear Physics, Zakopane, Poland, August 28 – September 4, 2022) and in conference proceedings (D. Kalaydjieva *et al.*, Acta Phys. Pol. B Proc. Suppl. 16, 4-A15 (2023)).

1 - Nuclear deformation and collectivity

The nucleus is a quantum system consisting of a large number of fermions, called nucleons - protons and neutrons - connected via the strong nuclear force. The forces acting between the interacting nucleons depends on all their coordinates, which makes the description of the many-body system a challenging task. Therefore, usually a mean-field approximation is applied, in which the protons and neutrons move in a mean field generated by all of the nucleons. This simplification is at the origin of the shell model, which proposes that the nucleons occupy particular orbitals following the principle of Pauli, similar to the atomic shells. When major shells are completely filled (closed), the system is observed to be more strongly bound, as reflected in the measured nuclear masses and two-neutron separation energies [1].

1.1 Description of the nuclear surface

Describing the nucleus through the time-dependent coordinates of each nucleon forming it is an overwhelming task even for simple nuclei built from a few nucleons. Instead, a set of coordinates that defines the nuclear surface can be used. This way the nucleus is treated as a whole in an analogy to a liquid drop [1].

The electrons in an atom experience a Coulomb potential ($\propto 1/r$) generated by the "point-like" nucleus, which is reflected in the spherical shape of the atomic system. In contrast, the complex nucleon-nucleon interaction can give rise to various nuclear shapes. While nuclei that have a closed neutron or proton shell are typically spherical in their ground states, an onset of deformation is observed when moving away from shell closures. The nuclear surface can be expanded in a series of spherical harmonics by:

$$R(\theta,\phi) = R_0\left(1+\sum_{\lambda\mu}\alpha^*_{\lambda\mu}Y_{\lambda\mu}(\theta,\phi)\right), \tag{1.1}$$

where R_0 is the radius of the nuclear surface in a spherical configuration, $Y_{\lambda\mu}$ are the spherical harmonics of degree λ and order μ, and $\alpha_{\lambda\mu}$ are expansion parameters describing the deformation of the nuclear surface. The leading contribution to the departure from a spherical shape originates from the terms with $\lambda = 2$ corresponding to the quadrupole deformation, followed by $\lambda = 3$ (octupole shapes).

A more natural description of the expansion parameters $\alpha_{\lambda\mu}$ can be provided in the principal axis frame of the nucleus. In particular, the $\alpha_{2\mu}$ coefficients describing the quadrupole deformation can be expressed via deformation parameters β_2 and γ:

$$a_{20} = \beta_2\cos\gamma, \quad a_{2\pm1} = 0, \quad a_{22} = \frac{1}{\sqrt{2}}\beta_2\sin\gamma. \tag{1.2}$$

The β_2 parameter corresponds to the quadrupole deformation along the symmetry axis, while γ describes the degree of axial symmetry [1]. Depending on the values of β_2 and γ, the nuclear shapes are classified as prolate (corresponding to an ellipsoid with two equal short axes) oblate (an ellipsoid with two equal long axes) and triaxial (all three axes of the ellipsoid have different lengths), as shown in Fig. 1.1.

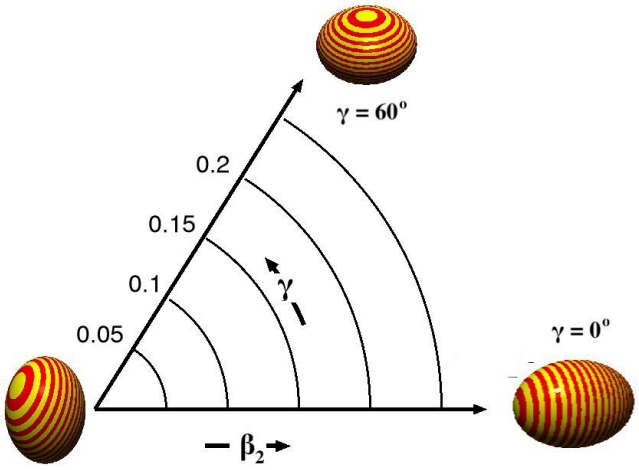

Figure 1.1 – Different quadrupole shapes of the nucleus as a function of the deformation parameters β_2 and γ [1].

1.2 Excited nuclear states and γ-ray decay

The ground state of a nucleus is its state with the minimal energy. Any other state with a higher energy is an excited state and appears due to the reorganization of one or more nucleons forming the nucleus. Each excited state is described by its excitation energy (with respect to that of the ground state), angular momentum, parity and lifetime. The lifetime of an excited nuclear state is the mean time in which the nucleus remains in that state before naturally reducing its energy by decaying to a lower-energy state. The decay has a statistical character following a certain transition probability. The mean lifetime τ of a nuclear state is inversely proportional to the decay constant λ, which determines how many decays on average will be observed in a given time window.

The decay can proceed via emission of a γ ray with energy given by the difference of the excitation energies of the initial and final states. Due to the conservation of the total angular momentum, the following selection rule for the γ decay has to be satisfied:

$$|I_i - I_f| \leq L \leq I_i + I_f, \tag{1.3}$$

where L is the angular momentum carried by the γ ray (corresponding to the multipole order 2^L, e.g. $L = 1$ corresponds to a dipole transition) and $I_{i,f}$ are

the spins of the initial and final nuclear state. Therefore, transitions between two nuclear states with spin 0 can only occur via internal conversion (in which the excess energy is transferred to an atomic electron) as the γ ray is a boson and has a spin of 1. Furthermore, to conserve parity, i.e. $\pi_i = \pi_f \pi_\gamma$, the following rules are valid for the two possible types of electromagnetic transitions (magnetic and electric):

$$\pi(EL) = (-1)^L, \tag{1.4}$$

$$\pi(ML) = (-1)^{L+1}. \tag{1.5}$$

For two transitions with the same L, an electric one is more probable. If more than one transition type is allowed by the selection rules, those with the lowest multipolarity usually dominate, although electric transitions with $L+1$ multipolarity often compete with magnetic ones of multipolarity L, giving rise to a mixed transition, e.g. $M1 + E2$.

1.3 Observables related to collectivity

Nuclear states resulting from a promotion of one nucleon (or a few) to a higher-energy orbital are classified as "single-particle" nuclear excitations, and are commonly observed e.g. in even-odd nuclei that have an unpaired valence nucleon. On the contrary, if a large number of nucleons are involved in the excitation, it has a"collective" character. For deformed nuclei, the rotational symmetry is broken and collective rotational excitations can occur, resulting in rotational bands built on each intrinsic shape of the nucleus. For an axially symmetric deformed nucleus, only rotations perpendicular to the symmetry axis are allowed. Rotational bands are characterized by the moment of inertia $\mathcal{J}$ and the excitation energies of band members with spin I are given by:

$$E(I) = \frac{\hbar^2}{2\mathcal{J}}[I(I+1) - K(K+1)], \tag{1.6}$$

where K is the projection of the angular momentum on the symmetry axis. The energies of the rotational states and the spacing between them increase smoothly as a function of the angular momentum.

The rigid-rotor model is one of the algebraically solvable limits of the standard collective model developed by Bohr and Mottelson [2]. Its other limit predicts the appearance of surface vibrations, understood as oscillations of the nucleus about its spherical shape forming a spectrum of equally spaced states. Finally, the third limit is the γ-soft model [3], in which the nucleus has a rigid β deformation, but exhibits oscillations in γ, which for even-even nuclei leads to an appearance of a $K = 2$ band at low excitation energy. The single-particle excitations, for which a pair of nucleons has to be broken (which typically requires an energy of $1-2$ MeV), appear higher in excitation energy. Therefore, the excited states of even-even nuclei that are lowest in energy are usually of a collective character.

A measure of the deformation of the nucleus in a specific state is given by the intrinsic quadrupole moment Q_0. However, experimentally only the spectroscopic quadrupole moment can be accessed in the laboratory frame, given by:

$$eQ_s = \sqrt{\frac{16\pi}{5}} \frac{1}{\sqrt{2I+1}} (I, I, 2, 0|I, I) \langle I||\mathcal{M}(E2)||I\rangle, \tag{1.7}$$

where $(I, I, 2, 0|I, I)$ is a Clebsch–Gordan coefficient and $\langle I||\mathcal{M}(E2)||I\rangle$ is the reduced diagonal matrix element of the electric quadrupole operator [4]. Within the assumption that the nucleus is an axially symmetric rotor, the matrix elements of the electric quadrupole operator (both transitional and diagonal ones) can be related to the intrinsic quadrupole moment via:

$$\langle KI_f\|\mathcal{M}(E2)\|KI_i\rangle = \sqrt{(2I_i+1)}(I_i, K, 2, 0|I_f, K)\sqrt{\frac{5}{16\pi}}eQ_0, \tag{1.8}$$

By combining Formulas 1.7 and 1.8, the following relation between the quadrupole moments in the laboratory and intrinsic frame, under the assumption of the axial rigid rotor model, can be obtained:

$$Q_s = \frac{3K^2 - I(I+1)}{(I+1)(2I+3)} Q_0. \tag{1.9}$$

By definition if the sign of Q_0 is positive/negative, the state is prolate/oblate. However, if $I = 0$ or $1/2$, even if the intrinsic quadrupole moment is nonzero, the spectroscopic quadrupole moment is zero as $K = I$. Thus no information can be obtained about the shapes of the ground states of even-even nuclei (spin 0^+) or spin-$1/2$ states in odd-A nuclei by measuring Q_s.

Assuming constant charge density and axial symmetry of the nucleus, Formula 1.1 can be approximated by

$$R(\theta, \phi) \approx R_0\Big(1 + \beta_2 Y_{20}(\theta, \phi)\Big) \tag{1.10}$$

and the following expression relating the intrinsic quadrupole moment Q_0 to the deformation parameter β_2 can be obtained [4]:

$$Q_0 \approx \frac{3}{\sqrt{5\pi}} Z R_0^2 \, \beta_2 \Big(1 + 0.36 \, \beta_2\Big). \tag{1.11}$$

The latter formula is commonly used to estimate the deformation within the approximation of an axially symmetric rotor from Q_0 deduced using Formula 1.8 from experimentally measured $E2$ matrix elements, obtained from e.g. Coulomb-excitation studies or calculated from directly measured lifetimes.

While the quadrupole moments depend on the coordinate system, zero-coupled products of the electric quadrupole operator are rotationally invariant due to the nature of the electromagnetic multipole operators being spherical tensors. Those

invariants are identical in both laboratory and intrinsic coordinate systems and can be evaluated using the Kumar-Cline sum rules [5,6]. In the principal-axis frame, the electric quadrupole operator can be expressed through the Q and δ parameters, which are analogous to the β_2 and γ deformation parameters:

$$\begin{aligned} \mathcal{M}'(E2,\mu=0) &= \quad Q\cos\delta, \\ \mathcal{M}'(E2,\mu=\pm1) &= \quad 0, \\ \mathcal{M}'(E2,\mu=\pm2) &= \quad \frac{1}{\sqrt{2}}Q\sin\delta. \end{aligned} \tag{1.12}$$

The lowest-order invariant can be calculated using experimentally obtained reduced matrix elements of the electromagnetic quadrupole operator via:

$$\frac{(-1)^{2I_i}}{\sqrt{2I_i+1}}\sum_j \langle I_i\|\mathcal{M}(E2)\|I_j\rangle\langle I_j\|\mathcal{M}(E2)\|I_i\rangle \begin{Bmatrix} 2 & 2 & 0 \\ I_i & I_i & I_j \end{Bmatrix} = \frac{1}{\sqrt{5}}\langle Q^2\rangle, \tag{1.13}$$

where the expression in curly brackets is a $6j$ symbol, I_i is the spin of the investigated state and the sum runs over all states I_j connected to the state of question via a direct $E2$ transition. Formula 1.13 can be simplified to:

$$\langle Q^2\rangle = [1/(2I_i+1)]\sum_j |\langle I_j||\mathcal{M}(E2)||I_i\rangle|^2. \tag{1.14}$$

One should note that not all matrix elements contribute equally to the sum in Formula 1.14. For example the coupling to the 2_1^+ state is known to strongly dominate the sum for the ground state in even-even nuclei [4].

By coupling three quadrupole operators to angular momentum zero one obtains a higher-order invariant $\langle Q^3\cos 3\delta\rangle$ given by:

$$\frac{(-1)^{2I_i}}{2I_i+1}\sum_{jk}\langle I_i\|\mathcal{M}(E2)\|I_j\rangle\langle I_j\|\mathcal{M}(E2)\|I_k\rangle\langle I_k\|\mathcal{M}(E2)\|I_i\rangle \begin{Bmatrix} 2 & 2 & 2 \\ I_k & I_i & I_j \end{Bmatrix} = \\ = \sqrt{\frac{2}{35}}\langle Q^3\cos 3\delta\rangle. \tag{1.15}$$

This invariant can be used to deduce whether, for a given $Q>0$, the nucleus has a prolate ($\langle Q^3\cos 3\delta\rangle \approx 1$), oblate ($\langle Q^3\cos 3\delta\rangle \approx -1$), or maximally triaxial shape ($\langle Q^3\cos 3\delta\rangle \approx 0$). It should be noted that in order to determine the $\langle Q^3\cos 3\delta\rangle$ invariant, the relative signs of the involved matrix elements need to be known as well.

The obtained $\langle Q^2\rangle$ quadrupole invariant can be related to the β_2 deformation parameter via:

$$\langle Q^2\rangle = \left(\frac{3ZeR_0^2}{4\pi}\right)^2\langle\beta_2^2\rangle, \tag{1.16}$$

where $R_0 = 1.2A^{1/3}$ and Z is the atomic mass of the investigated nucleus.

1.4 Shape coexistence

The shape of a nuclear state depends on the particularities of its microscopic wave function. Therefore, it is possible to observe distinct intrinsic nuclear shapes occurring within the same nucleus and in a narrow range of excitation energies. This phenomenon, known as "shape coexistence", was believed to be rarely manifested in nature and has been first suggested to involve the $0^+_{1,2}$ states in ^{16}O by Morinaga et al. [7] in 1956. In the years to follow, it has been shown that it is a much more common effect, as manifestations of shape coexistence were established throughout the nuclear chart [4], as shown in Figure 1.2. Recently, experimental observations consistent with multiple shape coexistence have been reported for several nuclei, for example ^{186}Pb [8, 9], ^{110,112}Cd [10, 11], ^{66}Ni [12].

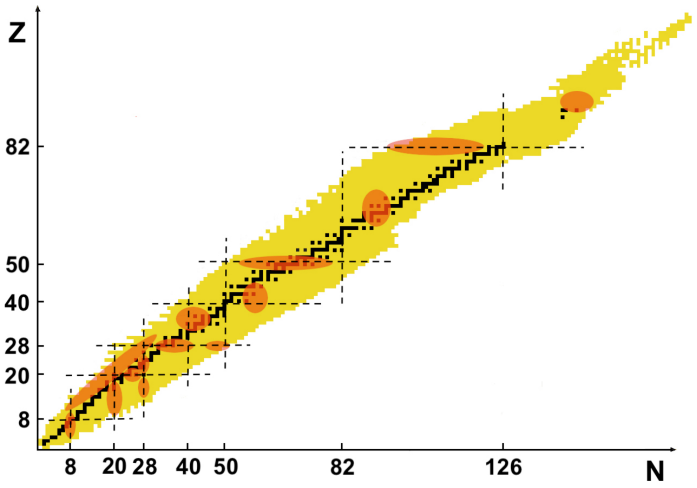

Figure 1.2 – Regions of the nuclear chart where shape coexistence has been experimentally confirmed. Figure adapted from Ref. [13].

The main driving mechanism behind shape coexistence in the vicinity of closed shells or sub-shells is the gain in correlation energy from both pairing and quadrupole–quadrupole interactions when pairs of nucleons are promoted across shell gaps. Thus, mostly due to the change in the proton–neutron quadrupole interaction energy, the excitation energies of shape-coexisting states related to proton excitations often have a parabolic-like behaviour as a function of the neutron number in a particular isotopic chain. Therefore, the energy systematics of intruder 0^+ states, appearing at low excitation energy, can be a hint of shape coexistence. Enhanced $E0$ transitions between 0^+ states also indicate different mean-square charge radii of the two configurations and mixing of their wave functions.

Shape coexistence offers one of the most demanding tests of modern nuclear theories. However, to firmly establish it experimentally requires an exhaustive knowledge of a large number of nuclear properties related to the nuclear deformation, discussed in Section 1.3.

Part I

Unsafe Coulomb excitation of ^{106}Cd

2 - Introduction

Coulomb excitation is a process, occurring during a collision between a beam and a target nucleus, in which excited states of one or both nuclei are populated via the mutually-generated time-dependent electromagnetic field. This experimental technique has been used for many years to probe nuclear properties such as transition probabilities and spectroscopic quadrupole moments [14–16]. First experiments date back to early 1950s (e.g. [17, 18]), when only light-ion beams were available, limiting excitation to only few low-lying excited states that could be populated via a single-step process (Section 3.3). Multi-step Coulomb excitation (Section 3.3.1) was extensively used during the 1960s and 70s when heavy-ion accelerators became common. The current renaissance of this technique is mostly related to the advent of exotic beam facilities, broadening its applicability to short-lived radioactive nuclei [14, 15].

One can distinguish between "safe" and "unsafe" Coulomb-excitation processes. The former is governed purely by the electromagnetic interaction, while the latter - by both Coulomb and nuclear potentials. The two processes can formally be distinguished by applying Cline's criterion for low-energy Coulomb excitation [5]:

$$b_{min} = 1.25\left(A_P^{1/3} + A_T^{1/3}\right) + 5\,\mathrm{fm}\ , \tag{2.1}$$

where A_P and A_T are the mass numbers of the projectile and the target, respectively. This is an empirical rule, stating that if the separation distance between the surfaces of the colliding nuclei is larger than 5 fm, the excited nuclear states are populated predominantly via the electromagnetic interaction acting between the reaction partners and the effects due to the nuclear interaction are below 0.5%. This criterion was deduced by systematically analysing inelastic scattering and transfer-reaction data collected at beam energies of few MeV/A for nuclei with $A \approx 30$ and heavier [5].

On the other hand, the distance of closest approach as a function of the scattering angle θ_{CM} and the beam energy E_{lab} is given by:

$$b(\theta_{CM}) = \frac{\alpha hc}{4\pi}\frac{Z_P Z_T}{E_{lab}}\frac{A_P + A_T}{A_T}\left(1 + \frac{1}{\sin(\theta_{CM}/2)}\right)\ , \tag{2.2}$$

where Z_P and Z_T are the atomic numbers of the projectile and the target, respectively, α is the fine-structure constant, h is the Planck constant and c is the speed of light. Using Formulas 2.1 and 2.2, one can calculate the "safe" bombarding energy for a given scattering angle and vice versa - the largest "safe" scattering angle for a given beam energy. It should be mentioned that while Cline's criterion can be used as a guideline for performing and analysing Coulomb-excitation experiments, discrepancies were observed for certain systems, e.g. when light projectiles

are used [19–24]. In such cases a separation of 5 fm is not sufficient and 6.5 fm is often used instead.

Under safe conditions, the excitation process can be analytically described to a high precision using the semi-classical approach discussed in Section 3.2. In this way, intrinsic properties of the nucleus, related to the matrix elements (MEs) of the electromagnetic operator, can be extracted. However, once the nuclear interaction starts to play an important role in the excitation process, it becomes quite complicated to extract electromagnetic MEs in a reliable way, as one needs to account for the changes in the excitation cross section induced by the nuclear interaction, for which no general analytical expression exists. On the other hand, unsafe Coulomb excitation can be an efficient method to populate off-yrast excited states that are not easily accessible using other reaction mechanisms, such as e.g. fusion-evaporation. Notably, multiple "unsafe" Coulomb-excitation studies addressed the properties of high-spin states in the actinide region [25–29]. The beam energies used in these experiments were 5 to 15% larger than the "safe" energy. This resulted, in particular, in an enhanced population of negative-parity bands. Similar enhancement of the population of 3^- states was observed also in a recent Coulomb-excitation study of ^{102}Ru with ^{12}C and ^{16}O beams [30]. Moreover, unsafe Coulomb excitation was used to populate the states of interest in a number of lifetime measurements, e.g. [31–33]. More recent studies with radioactive ion beams (RIBs) also benefited from the unsafe Coulomb-excitation process, which led to an increase of the excitation cross sections partly compensating low intensities of the RIBs [34, 35].

Unsafe Coulomb-excitation data are often collected as a by-product of studies using deep-inelastic reactions, but they are rarely analysed due to the complexity of the procedure to account for the effects of the Coulomb-nuclear interference on the excitation cross sections. In principle, such data can be accurately described using coupled-channel reaction codes, such as FRESCO [36] or PTOLEMY [37, 38], as will be discussed in Section 5.6. However, an adequate optical potential has to be used to describe the effective interaction between the collision partners, including the nuclear force. The task becomes especially difficult if no elastic scattering data, needed to adjust the potential parameters, are available. Consequently, there are not many studies that carefully analyze the effects of Coulomb-nuclear interference at slightly "unsafe" energies with the aid of detailed coupled-channel calculations, especially for target-projectile combinations of nuclei with masses around 100.

It is hard to generalize the effects of the nuclear interaction on the inelastic scattering data, as they differ from one state to another and depend on the beam energy. An empirical rule, proposed in Ref. [39], states that "the initial Coulomb-nuclear interference will be constructive (destructive) if the excitation function for pure Coulomb excitation is approaching or at minimum (maximum)". Examples of constructive interference were already discussed (for the off-yrast states), while a decrease with respect to the pure Coulomb-excitation cross section, resulting from

the destructive Coulomb-nuclear interference, was reported for the states in the ground-state bands of ^{162}Dy [40] and ^{232}Th [41].

Summarizing, the Coulomb-nuclear interference is a rather complex phenomenon, which may result in an increase or a decrease of the excitation cross section depending on the kinematic conditions (scattering angle or beam energy range). At small scattering angles, the nuclear interaction leads to an oscillatory behaviour of the excitation cross section as a function of the scattering angle around the values resulting from the pure Coulomb-excitation process while at high angles larger discrepancies are expected. Hence, further investigating the effects caused by the unsafe conditions would help to better understand to what extent nuclear-structure parameters can be extracted from such data. This can provide guidance for future studies aiming to benefit from the enhancement of the cross section due to the Coulomb-nuclear interference.

This manuscript presents an exploratory work focusing on the the effects induced by the nuclear interaction on the γ-ray yields observed following the inelastic scattering of a ^{106}Cd ion beam, impinging on a ^{92}Mo target at 770 MeV beam energy (exceeding the "safe" energy by 8% and 40% for the minimum and maximum scattering angles, respectively). This analysis demonstrates the possibility to extract information from such data that is complementary to the direct lifetime measurement that was the main goal of the experiment under study.

3 - "Safe" and "unsafe" Coulomb excitation

The Coulomb-excitation process can be accurately described using the semi-classical approach, presented in Sections 3.1-3.2, if the excitation is exclusively due to the well-known electromagnetic force. At beam energies exceeding the "safe"-energy criterion (Formula 2.2), the nuclear interaction starts to contribute and can significantly affect the excitation cross sections via Coulomb-nuclear interference discussed in Section 3.4.

3.1 Semi-classical treatment of safe Coulomb excitation

From a classical point of view, in the scattering of projectiles on a target, the fraction of the total number of nuclei scattered at a certain solid angle $d\Omega$, i.e. the differential cross section, is described using Rutherford's formula:

$$\frac{d\sigma}{d\Omega} = \frac{a^2}{4}\frac{1}{\sin^4(\theta_{CM}/2)}, \tag{3.1}$$

where θ_{CM} is the scattering angle in the center-of-mass system, and a is half of the distance of the closest approach in a head-on collision, given by $Z_P Z_T e^2/(m_o v^2)$. Z_P and Z_T are the atomic numbers of the projectile and target, respectively, e is the electron charge, m_o is the reduced mass of the projectile and the target and v is the relative velocity at large distances. The parameter a can also be expressed using the mass numbers $A_{P,T}$ and the beam energy expressed in MeV as $a = 0.72(1 + A_P/A_T)Z_P Z_T/E$.

Following the scattering, the target and projectile will move along hyperbolic trajectories governed by the long-range Coulomb term $Z_P Z_T e^2/r$, where r is the distance between the two nuclei. On the other hand, the mutually-generated electromagnetic potential experienced by the nuclei depends on the position on the orbit ($r(t)$). This time-dependent potential can cause excitation in the beam and/or the target nucleus. A full quantum-mechanical treatment can be applied to describe this process, as the theory of the electromagnetic interaction is well known. However, the problem can be simplified by describing the relative motion of the projectile and the target in a classical manner, while treating the excitation process in terms of quantum mechanics. This semi-classical approach was developed by K. Alder and A. Winther [42] and requires that certain criteria are fulfilled in order to provide reliable results. In general, the interaction between the nuclei has to be purely electromagnetic.This is usually true for beam energies below the Coulomb barrier, when the separation distance between the two nuclei is sufficiently large and consequently the nuclear interaction between them can be neglected. It is also required that the wave function of the projectile does not penetrate into the target nucleus, i.e. the de Broglie wavelength of the projectile, $\lambda\!\!\!^{-}$, must be small

compared to the distance of closest approach in a head-on collision b:

$$\eta = \frac{b}{2\lambda\!\!\!^{-}} = \frac{Z_P Z_T e^2}{\hbar v} \gg 1 \,, \tag{3.2}$$

where η is the Sommerfeld parameter. A deviation from the exact calculations of the order of $1/\eta$ can be expected [42]. When the inequality 3.2 is not fulfilled, as it is often the case for light ions, a full quantum-mechanical description of the process is necessary. Additionally, the trajectory of the scattered projectile must not be strongly affected by the transferred energy ΔE. As the energy exchange happens at an unknown moment, it is not possible to accurately account for this effect, thus $\Delta E/E \ll 1$. For the excitation of a state to occur, the perturbation of the electromagnetic potential experienced by the nucleus of interest has to be sudden, i.e. the collision time τ_{coll} (which is of the order of a/v) must be shorter or of the same order of magnitude as the characteristic nuclear time for such a transition ($\hbar/\Delta E$). This is usually quantified by the adiabaticity parameter ξ:

$$\xi \equiv \frac{\tau_{coll}}{\tau_{nucl}} = \frac{a\Delta E}{\hbar v} \leq 1. \tag{3.3}$$

The adiabaticity condition (Formula 3.3) limits the energy that can be transferred in low-energy Coulomb excitation. The beam energies used in typical Coulomb-excitation experiments are of the order of a few MeV/A, which results in an energy-transfer cut-off of about 1 – 2 MeV. This eliminates potential issues related to the energy transfer, but other conditions listed above are not automatically fulfilled.

3.2 Theory of safe Coulomb excitation

The electromagnetic potential $\hat{W}(P, T, \vec{r}(t))$ acting between the projectile (P) and the target (T) nuclei can be decomposed into terms corresponding to the mutual electric multipole-multipole interaction ($\hat{W}_E$), the magnetic multipole-multipole interaction ($\hat{W}_M$) and the interaction between the electric and the magnetic multipole moments caused by the relative motion of the two systems ($\hat{W}_{EM}$). Their explicit forms can be found in Ref. [42]. The dominant term is the monopole-monopole electric Coulomb interaction that describes the hyperbolic trajectories of the collision partners, as discussed in Section 3.1. This term does not depend on the intrinsic degrees of freedom of the colliding nuclei, thus it cannot result in their excitation. On the contrary, the terms describing the interaction between the monopole moment of the projectile (target) and the electric multipole moments of the target (projectile) can give rise to target (projectile) excitation. Interaction between higher-order electric multipoles can cause simultaneous mutual excitations, which are usually negligible (being of the order of $1/\eta^2$) [42]. Within the semi-classical approach, the motion of the center-of-mass of the system can be completely separated from the intrinsic motion, thus the excitation process can

be described by the time-dependent Schrödinger equation:

$$i\hbar\frac{\partial}{\partial t}|\Psi_{int}(\vec{r},t)\rangle = \left(\hat{H}_P + \hat{H}_T + \hat{W}\left(P,T,\vec{r}(t)\right) - \frac{Z_P Z_T e^2}{r(t)}\right)|\Psi_{int}(\vec{r},t)\rangle\ , \tag{3.4}$$

where $\hat{H}_{P,T}$ are the intrinsic Hamiltonians of the projectile/target and $\Psi_{int}(\vec{r},t)$ can be asymptotically expressed as $|\Psi_{int}(-\infty)\rangle = |\Psi_0^P\rangle|\Psi_0^T\rangle$, where $\Psi_0^{P,T}$ are the ground-state wave functions of the projectile/target. Considering that only the interaction between the monopole of one of the nuclei and the multipoles of the other (denoted as $\hat{V}\left(\vec{r}(t)\right)$) is of importance for the excitation process, separate equations can be obtained for the wave functions of the target and of the projectile, each of them of the form:

$$i\hbar\frac{\partial}{\partial t}|\Psi(\vec{r},t)\rangle = \left(\hat{H}_0 + \hat{V}\left(\vec{r}(t)\right)\right)|\Psi(\vec{r},t)\rangle\ , \tag{3.5}$$

where $|\Psi(\vec{r},t)\rangle$ is the wave function of the investigated nucleus and $\hat{H}_0$ is its free Hamiltonian. One can expand $|\Psi(\vec{r},t)\rangle$ into orthogonal eigenstates of $\hat{H}_0$:

$$|\Psi(\vec{r},t)\rangle = \sum_n a_n(t)|n\rangle, \tag{3.6}$$

where $|n\rangle$ solves the equation $\hat{H}_0|n\rangle = E_n|n\rangle$ and $a_n(t)$ are time-dependent coefficients defined as [42]:

$$a_n(t) = \langle n|\Psi(\vec{r},t)\rangle \exp\left(\frac{iE_n t}{\hbar}\right). \tag{3.7}$$

The expansion coefficients are referred to as excitation amplitudes and they are related to the excitation cross section for populating a specific $|n\rangle$ state from the ground state via:

$$\left(\frac{d\sigma}{d\Omega}\right)_n = P_n\left(\frac{d\sigma}{d\Omega}\right)_{Ruth}, \tag{3.8}$$

where P_n are the excitation probabilities, which correspond to $|a_n(t)|^2$ in the asymptotic limit ($t = +\infty$), and $(d\sigma/d\Omega)_{Ruth}$ is the Rutherford cross section, given by Formula 3.1. On the other hand, if Formulas 3.6 and 3.7 are substituted into Formula 3.5, a set of differential equations can be obtained for the excitation amplitudes:

$$i\hbar\frac{d}{dt}a_k(t) = \sum_n \langle k|\hat{V}(\vec{r}(t))|n\rangle \exp\left(i(E_k - E_n)t/\hbar\right) a_n(t). \tag{3.9}$$

The interaction potential $\hat{V}(t)$ can be expanded into a series of multipoles:

$$\hat{V}(\vec{r}(t)) = \sum_{\lambda=1}^{\infty}\sum_{\mu=-\lambda}^{\lambda}\frac{4\pi Ze}{2\lambda+1}(-1)^{\mu}S_{\lambda\mu}^{E,M}(\vec{r},t)\hat{M}(^{E}_{M}\lambda,-\mu)\ , \tag{3.10}$$

where $\hat{M}(^{E}_{M}\lambda,\mu)$ is the electromagnetic operator of multipole order λ with a projection μ, Z is the atomic number of the collision partner, and the $S^{E,M}_{\lambda\mu}(\vec{r},t)$ functions are defined as [42]:

$$S^{E}_{\lambda\mu}(\vec{r},t) = \frac{Y_{\lambda\mu}(\vartheta(t),\varphi(t))}{r(t)^{\lambda+1}}, \tag{3.11}$$

$$S^{M}_{\lambda\mu}(\vec{r},t) = \frac{1}{\lambda c}\frac{\frac{d\vec{r}(t)}{dt}(\vec{r}\times\nabla)}{r(t)^{\lambda+1}}Y_{\lambda\mu}(\vartheta(t),\varphi(t)), \tag{3.12}$$

where $Y_{\lambda\mu}(\vartheta,\varphi)$ are spherical harmonics and $r(t)$, $\vartheta(t)$ and $\varphi(t)$ are the time-dependent spherical coordinates of the position vector $\vec{r}(t)$ of the investigated nucleus.

This makes it possible to relate a_n (Formula 3.9) to the matrix elements of the $\hat{M}(^{E}_{M}\lambda,\mu)$ operator. These matrix elements, $\langle I_k, m_k|\hat{M}(^{E}_{M}\lambda,\mu)|I_n,m_n\rangle$, govern both the excitation and the de-excitation process between two states with spin $I_{k,n}$ and spin projection $m_{k,n}$ and thus carry nuclear structure information. Therefore, on one hand, by solving the coupled-channel system, one can obtain the excitation amplitudes related to the matrix elements (MEs) of the multipole electromagnetic operator, while on the other hand, the excitation cross sections $(d\sigma/d\Omega)_n$, which are related to $|a_k|$ via Formula 3.8, can be measured experimentally. Thus, information on the structure of the investigated nucleus can be obtained in a model independent way using Coulomb excitation.

3.3 First-order and higher-order effects

When the interaction is relatively weak, i.e. the excitation probability of the populated states is much smaller than unity, the problem can be treated within the first-order perturbation theory. Solving the differential equation system (Formula 3.9) yields the following expression for the electric excitation cross section of a state I_f from the initial state I_i [42]:

$$\sigma_{E\lambda} = \left(\frac{Z_2 e}{\hbar v}\right)^2 (a)^{-2\lambda+2}\, B(E\lambda; I_i \to I_f) \int_{\theta_{min}}^{\theta_{max}} \frac{df_{E\lambda}(\xi,\theta_{CM})}{d\Omega} d\Omega, \tag{3.13}$$

where $B(E\lambda; I_i \to I_f)$ is the reduced transition probability, related to the reduced matrix element $\langle I_f||E\lambda||I_i\rangle$ and Z_2 is the atomic number of the collision partner. In an analogous way, a formula for excitation caused by the magnetic field can be obtained, in which v is replaced by c [42]. This results in a suppression of magnetic excitations by a factor of $(v/c)^2$ with respect to the electric excitations, making them negligible in low-energy Coulomb-excitation studies in which (v/c) rarely exceeds 0.1.

The reduced matrix elements $\langle I_f||^{E}_{M}\lambda||I_i\rangle$ can be calculated from the matrix elements of the $\hat{M}(^{E}_{M}\lambda,\mu)$ operator using the Wigner-Eckart theorem [43]. The $f_{^{E}_{M}\lambda}(\xi,\theta)$ are referred to as excitation functions and they depend on the scattering

angle, the adiabacity parameter ξ (Formula 3.3) and the multipolarity ${}^{E}_{M}\lambda$ [42]. The $f_{{}^{E}_{M}\lambda}(\xi)$ functions for several multipolarities (integrated over all possible θ angles) are presented in Fig. 3.1. The largest values are obtained for $E1$ transitions, however, since $B(E1)$ values are orders of magnitude smaller than typical reduced transition probabilities for higher-order multipolarities, the resulting excitation cross sections are negligible. Therefore, the $E2$ and $E3$ transitions are dominant in the Coulomb-excitation process, even though $E1$ or $M1$ transitions may be more important in the subsequent decay.

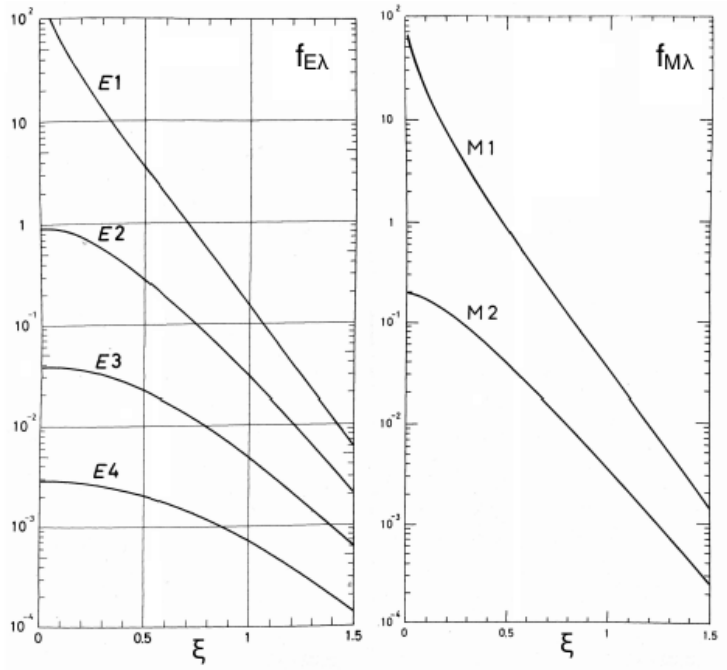

Figure 3.1 – The electric (left) and magnetic (right) excitation functions $f_{{}^{E}_{M}\lambda}(\xi)$ as a function of the adiabaticity parameter ξ. Figure adapted from Ref. [42].

3.3.1 Multi-step excitation

Formula 3.13 can be readily used when direct excitations from the ground state are investigated, however, when the collision time is large and the electromagnetic interaction is strong (e.g. for heavier reaction partners), second-order effects such as multi-step excitation become relevant. In principle, as the excitation process depends on the kinematics, a range of scattering angles can be selected in which the second-order effects are suppressed, e.g. only very forward angles. Similarly, the strength of the electromagnetic field can be reduced by using a light partner. On the other hand, second-order effects play an important role in the population of certain states, e.g. excited 0^+ states, which cannot be populated in a one-step excitation from the ground state (excitation via $E0$ transitions is forbidden). However, the presence of competing excitation paths may result in complications

in the analysis. The excitation amplitudes have contributions from both first and second order effects, $a^{total} = a^{(I)} + a^{(II)}$. For instance, let us consider the second excited 2^+ state, which can be populated either by a one-step $E2$ transition from the ground state or via two-step excitation through an intermediate state, i.e. the 2_1^+ state. The excitation probability $P(0_1^+ \rightarrow 2_2^+)$ will be given by:

$$P(0_1^+ \rightarrow 2_2^+) = |a^{(I)}(0_1^+ \rightarrow 2_2^+) + a^{(II)}(0_1^+ \rightarrow 2_1^+ \rightarrow 2_2^+)|^2. \quad (3.14)$$

Thus, apart from the single-step excitation term, which depends on $\langle 0_1^+||E2||2_2^+\rangle^2$ and the two-step term, proportional to $\langle 0_1^+||E2||2_1^+\rangle^2\langle 2_1^+||E2||2_2^+\rangle^2$, an interference term $\langle 0_1^+||E2||2_1^+\rangle\langle 2_1^+||E2||2_2^+\rangle\langle 0_1^+||E2||2_2^+\rangle$ will appear, which contains non-squared reduced MEs, therefore it depends on their relative signs. The interference term can affect the excitation cross section by increasing it, if its sign is positive (constructive interference) or decreasing it, if it is negative (destructive interference). It should be noted that multi-step excitations and second-order effects in general are more probable at large scattering angles (implying a smaller distance of closest approach) as the nucleus experiences a stronger electromagnetic field during the scattering process.

3.3.2 Reorientation effect

Another second-order phenomenon is the reorientation effect, defined as the change of the Coulomb-excitation cross section caused by the static quadrupole moment Q_s of an excited state. The effect can be understood as a two-step excitation in which the intermediate state and the final state are magnetic substates of the same excited state. It can be related to a time-dependent hyperfine splitting of the nuclear levels during the collision.The magnitude of this splitting depends on Q_s and increases with scattering angle. Depending on whether the sign of the Q_s is positive or negative, the most strongly populated $m = 0$ substate will be lowered/raised in excitation energy, which, because of the strong dependence of the Coulomb-excitation cross section on level energy, will result in its increase/decrease [44]. Thus by observing the introduced changes in the experimental excitation cross sections, the static quadrupole moments of excited nuclear states can be measured, which are directly related to the nuclear shape [4]. As already mentioned, this effect depends on the scattering angle and has a maximum influence on the excitation cross sections at $\theta = 180^\circ$ due to the maximum in the hyperfine splitting at backward scattering.

3.4 Inelastic scattering and Coulomb-nuclear interference

Coulomb excitation is governed by the electromagnetic interaction between the collision partners. In a more general case of inelastic scattering, nuclear forces may play an important role.

A general form of the Hamiltonian of the collision system is given by:

$$\hat{H} = \hat{T}(\mathbf{R}) + \hat{H}_P(\xi_P) + \hat{H}_T(\xi_T) + \hat{V}(\mathbf{R}, \xi_P, \xi_T), \tag{3.15}$$

where $\hat{T}(\mathbf{R})$ is the kinetic energy operator, $\hat{H}_P(\xi_P)$ and $\hat{H}_T(\xi_T)$ are the internal Hamiltonians of the projectile and the target, respectively and $\hat{V}(\mathbf{R}, \xi_P, \xi_T)$ is the projectile-target interaction. The Hamiltonians of the target and the projectile depend on the internal coordinates ξ (which can be e.g. coordinates of each nucleon, or be linked to a collective model description), while $\hat{V}$ depends both on the relative coordinate between the collision partners $\mathbf{R}$ and on the internal coordinates ξ. Therefore, due to $\hat{V}$, it is possible to rearrange the nucleons inside the colliding nuclei and thus induce excitations. In the particular case of Coulomb excitation, $\hat{V}$ is the electromagnetic interaction $\hat{W}\left(P, T, \vec{r}(t)\right)$, as explained in Section 3.2. Note that Formula 3.15 is more general than the Hamiltonian in Formula 3.4, as the latter has no part related to elastic scattering due to the use of the semi-classical approximation.

Solving the time-independent Schrödinger equation for the Hamiltonian defined via Formula 3.15 would yield an infinite number of possible final states. Therefore a limited model space is usually selected, which is restricted to the channels of interest. The full Hamiltonian is replaced by an effective one, which incorporates the "bare" interaction, governing the channels of interest and a polarisation part, which accounts for couplings to the remaining channels. Usually, an effective projectile-target interaction $U(\mathbf{R})$ is adopted, which reflects the properties of the polarization part of the Hamiltonian. Subsequently, within a chosen structure model for the internal Hamiltonians, the model wave function Ψ can be expanded using the eigenfunctions of the internal Hamiltonians ($\Phi_n(\xi)$, being products of the eigenfunctions of the projectile and the target) and a set of coefficients depending on the relative motion of the two nuclei ($\chi_n(\mathbf{R})$). Using this expansion, multiplying the time-independent Schrödinger equation by Φ_n^* (describing a particular n state of the system) and integrating over the internal coordinates ξ, one can obtain the following coupled-channel system of equations for χ_n:

$$[E - \epsilon_n - \hat{T}(\mathbf{R}) - U_{n,n}(\mathbf{R})]\chi_n(\mathbf{R}) = \sum_{n \neq n'} U_{n,n'}(\mathbf{R})\chi_{n'}(\mathbf{R}), \tag{3.16}$$

where E is the total energy of the system, ϵ_n is the eigenenergy of state n and $U_{n,n'}$ is the so-called coupling potential, responsible for exciting the system from state n to state n', given by:

$$U_{n,n'}(\mathbf{R}) = \int d\xi \Phi_n^*(\xi) U(\xi, \mathbf{R}) \Phi_{n'}(\xi). \tag{3.17}$$

A more complete derivation of the above equations and an introduction to the methods used to solve the coupled equations 3.16 for particular reaction channels, including elastic and inelastic scattering, can be found in Ref. [45].

Asymptotically (at very large distances from the collision point), the solution of the time-independent Schrödinger equation has the form:

$$\Psi^{(+)}_{\mathbf{K}_\alpha} \rightarrow \Phi_\alpha(\xi_\alpha)e^{i\mathbf{K}_\alpha.\mathbf{R}_\alpha} + \Phi_\alpha(\xi_\alpha)f_{\alpha,\alpha}(\theta)\frac{e^{iK_\alpha R_\alpha}}{R_\alpha} + \sum_{\alpha' \neq \alpha} \Phi_{\alpha'}(\xi_\alpha)f_{\alpha',\alpha}(\theta)\frac{e^{iK_\alpha R_\alpha}}{R_\alpha}, \tag{3.18}$$

where $\hbar K$ is the linear momentum and $\Phi(\xi)$ is the product of the eigenfunctions of the projectile and the target in either the elastic (α, ground state), or an inelastic channel (α', excited state) The first term in expression 3.18 describes a plane wave propagating in the direction of the beam ($e^{i\mathbf{K}_\alpha.\mathbf{R}_\alpha}$). The second term describes the elastic channel - a spherical outgoing wave $\frac{e^{iK_\alpha R_\alpha}}{R_\alpha}$ propagating isotropically, modulated with a function $f_{\alpha,\alpha}$ depending on the scattering angle. The last term has a similar construction with the summation running over all possible final states α'. The $f_{\alpha,\alpha'}$ functions (including the $\alpha' = \alpha$ case) are referred to as scattering amplitudes, and are related to cross sections via:

$$\left(\frac{d\sigma}{d\Omega}\right)_{\alpha\rightarrow\alpha'} = \frac{K_{\alpha'}}{K_\alpha} \mid f_{\alpha,\alpha'}|^2. \tag{3.19}$$

Hence, they are closely related to excitation amplitudes used in the description of Coulomb excitation (Formula 3.8).

When the nuclear interaction can be neglected, the scattering amplitudes are directly related to the matrix elements of the electromagnetic operator. However, if the nuclear interaction is not negligible, the excitation cross section depends on both f^{COUL} and f^{NUC}:

$$\left(\frac{d\sigma}{d\Omega}\right)_{i\rightarrow f} = \frac{K_f}{K_i} \mid f^{COUL}_{if} + f^{NUC}_{if} \mid^2. \tag{3.20}$$

This leads to the appearance of Coulomb-nuclear interference terms, and thus even for small f^{NUC} the effects from the nuclear interaction on the observed cross sections may be large [45].

The general formalism presented above can be applied to other direct reactions, i.e. those occurring without a compound-nucleus formation, with only a small fraction of the nucleons being involved in the process and a small momentum transfer. Those are for example transfer and break-up reactions [45].

4 - Experimental details and observables

The data analysed in the present work are a byproduct of a lifetime measurement populating nuclei of interest via multinucleon transfer reactions. This experimental project, the setup used for the measurement and the experimental observables investigated in the present study are introduced in Sections 4.1, 4.2 and 4.3, respectively.

4.1 Experiment E664 at GANIL

The original goals of experiment E664, which provided data for the present study, were to investigate the structure of the neutron-deficient ^{106,108}Sn and in particular to probe the robustness of the proton $Z = 50$ shell closure for nuclei with neutron number approaching 50. This was to be achieved by performing, for the first time, direct lifetime measurements of the lowest 2^+ and 4^+ states in ^{106,108}Sn. The reduced transition probabilities $B(E2, 2_1^+ \rightarrow 0_1^+)$ were previously obtained in Coulomb-excitation studies, however, the reported values were subject to large uncertainties.

The experiment took place in 2015 at the experimental hall G1 of the largest accelerator facility in France, GANIL [46]. The stable ^{106}Cd beam was produced in the ECR (Electron Cyclotron Resonance) ion source [47], subsequently pre-accelerated in the Compact Cyclotron unit (C0) up to 1 MeV/u and after final acceleration in the Separated-Sector Cyclotron accelerator (CSS1) up to an energy of 7.3 MeV/u, delivered onto a ^{92}Mo target [48]. At this beam energy, a number of Cd and Sn isotopes were populated via multi-nucleon transfer (MNT) reactions, however, the strongest observed channel was the inelastic scattering of the ^{106}Cd beam on the Mo target.

The main goals of the E664 experiment were accomplished within the PhD thesis work of M. Siciliano [48] and subsequently published [49]. Moreover, the analysis yielded a number of lifetimes in the $^{102-108}$Cd isotopes obtained using the RDDS technique [50]. As discussed in the present manuscript, it was possible to further benefit from this data set, as the detection system, which included a position-sensitive particle detector, allowed to simultaneously collect data suitable for a Coulomb-excitation analysis. The experimental setup will be presented in more detail in the following section.

4.2 Experimental setup

The beam-like nuclei, produced in the ^{106}Cd + ^{92}Mo collisions, were identified using VAMOS++ (VAriable MOde Spectrometer) [51], while the de-excitation γ rays, emitted by the reaction products, were registered using eight AGATA triple clusters [52]. The data were collected in a particle-gamma coincidence mode, with

a prompt coincidence time window of 2μs. The RDDS method [53,54] was used for the lifetime measurement. This required using a plunger device, where the ^{92}Mo target and a ^{nat}Mg degrader foils were mounted [54]. The experimental setup is schematically presented in Fig. 4.1. Further details are provided in the following subsections.

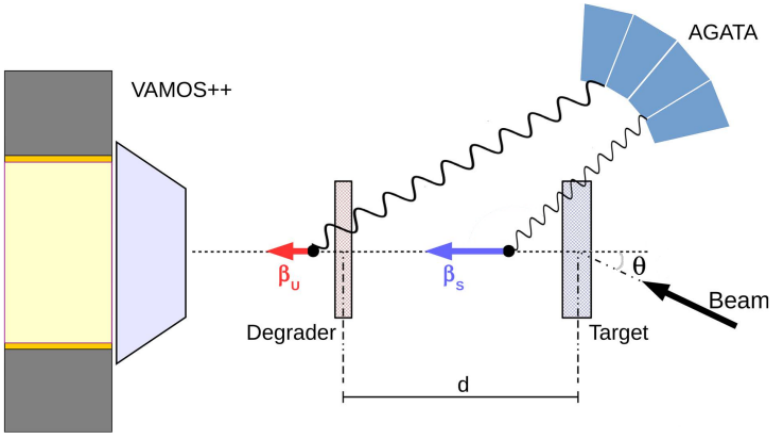

Figure 4.1 – Schematic presentation of the experimental setup. Only the entrance detector of VAMOS++ is included, together with the first focusing magnet. The foils of the target and the degrader are mounted on a plunger device, which is placed inside a vacuum reaction chamber. Eight AGATA triple clusters are used to detect γ rays emitted by the beam-like reaction products moving with velocity β_S between the foils, or with β_U, after slowing down in the degrader.

4.2.1 VAMOS++

To select specific reaction channels, the mass number A and atomic number Z of the reaction products needed to be determined. Furthermore, measuring the velocity of the ions after the degrader was crucial for performing a Doppler correction of γ-ray energies. This was achieved using the large-acceptance ion spectrometer VAMOS++, which allows to identify the registered ions and fully reconstruct their trajectories inside the spectrometer on an event-by-event basis. The VAMOS++ spectrometer is schematically presented in Fig. 4.2 and described below.

- **A dual position-sensitive Multi-Wire Proportional Counter (MWPC)** is placed at the entrance of VAMOS++. This proportional counter provides the initial position of the ion and its scattering angle θ_i (with respect to the beam direction) and ϕ_i (with respect to the horizontal plane).

- **Two large-aperture quadrupole magnets and one magnetic dipole** are used for focusing and bending of the ion trajectory, respectively. The magnetic rigidity $B\rho$ is fixed for a certain nominal trajectory.

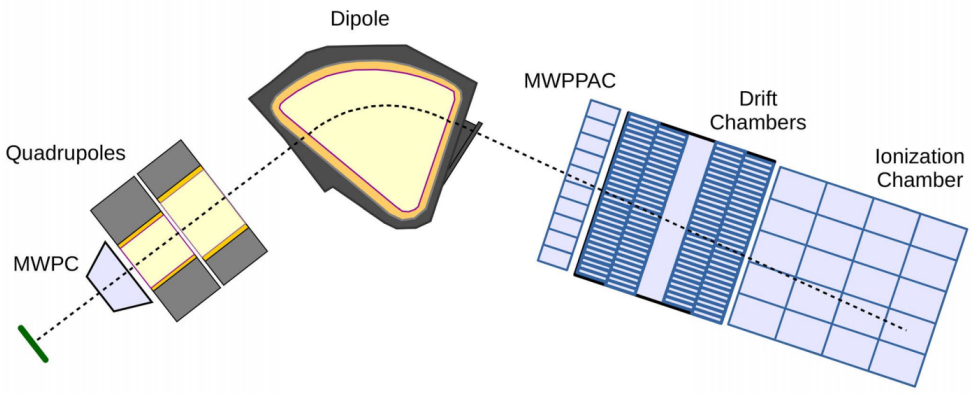

Figure 4.2 – Schematic presentation of the VAMOS++ spectrometer. The dashed line depicts an example ion trajectory inside the spectrometer. The system includes a double Multi-Wire Proportional Counter (MWPC), two quadrupole magnets, a dipole magnet, a Multi-Wire Parallel Plate Avalanche Counter (MWPPAC), two Drift Chambers (DC), and an Ionization Chamber (IC). Figure adapted from Ref. [48].

- **A Multi-Wire Parallel Plate Avalanche Counter (MWPPAC)** is placed at the focal plane of the spectrometer. Together with the entrance MWPC, the signals from the MWPPAC are used to obtain the Time Of Flight (TOF) of the ions.
- **A pair of two-dimensional position-sensitive Drift Chambers (DC)** measures the position of the ion at the focal plane, including θ_f and ϕ_f.
- **A multi-segmented Ionization Chamber (IC)** is placed at the end of VAMOS++, where the ions deposit their total kinetic energy E_{TOT}. Measuring the energy loss of the ions allows the determination of the atomic number Z of the ions, as $\Delta E/\Delta x \propto Z^2$ [55].

A dedicated software is used to reconstruct the trajectories of the ions using both simulations and reconstruction algorithms specific to VAMOS++. From the measured coordinates of the ion at the focal plane, it is possible to reconstruct the path of the ion, determine its initial coordinates (and compare them with those measured by the entrance detector), and obtain the magnetic rigidity for the specific trajectory. Using the information on the path of each ion and its initial and final coordinates, the length of their trajectory D between the MWPC and the MWPPAC can be calculated. Subsequently, from the measured TOF, the velocity of the ion can be calculated, which is needed for the Doppler correction of the γ-ray energy. Using the obtained velocity, TOF, D, and the magnetic rigidity $B\rho$, the mass-over-charge (A/q) ratio can be extracted. Finally, using the measured E_{TOT}, related to the mass of the ion, and the A/q ratio, one can obtain the charge

state q and the mass number A of the ion. More details about the VAMOS++ spectrometer, trajectory reconstruction process and data processing can be found in the PhD thesis of M. Siciliano [48].

4.2.2 AGATA spectrometer

Registration of γ rays with high-resolution and high-efficiency detectors is crucial for nuclear spectroscopy. Typically, such detection systems are based on semiconductors, and in particular the High-Purity Germanium (HPGe). The performance of HPGe γ-ray detectors is often affected by the Compton-scattering process, which leads to deterioration of the peak-to-total ratio, as some of the γ rays leave the detector without depositing their full energy, which results in higher background levels. To reduce these effects, passive and/or active Compton shielding is introduced. However, this usually limits the total solid angle covered by the detectors, and consequently their efficiency. The Advanced Gamma Tracking Array (AGATA) [52] was developed to overcome this limitation. AGATA consists of n-type HPGe crystals, electrically segmented into 36 parts. Each segment is equipped with its own preamplifier, therefore segment signals can be analysed individually. From the pulse-shape analysis of the signals from the segments and from the central electrode, the energy, timing and spatial coordinates of each interaction point within the detector volume are determined, using state-of-the-art front-end electronics, based on advanced digital signal processing techniques. Subsequently, the trajectory of the γ ray inside the AGATA spectrometer is reconstructed through γ-ray tracking algorithms [56]. This information was used to extract the precise angle at which the γ ray was emitted, needed for the Doppler correction procedure [48]. In addition, the use of γ-ray tracking resulted in an increased efficiency by about 30% for the γ rays with energies between 500 and 1200 keV [48]. In the present experiment, eight AGATA triple clusters were placed at approximately 18.5 cm distance from the target, as presented in Fig. 4.3. The data collected with three of these crystals had unsolvable issues and needed to be excluded from the analysis. This limited the total number of detectors to 21. More details on the data processing and the analysis of raw AGATA data can be found in Ref. [48].

4.2.3 Plunger device

The E664 experiment aimed to measure lifetimes in the picosecond range using the RDDS method [53, 54]. For this purpose, a differential plunger device [54], developed by Institute for Nuclear Physics, University of Cologne, was placed inside the reaction chamber. The target and degrader foils were mounted on frames inside the device and the distance between them was controlled by a piezo-electric motor. The target foil was oriented to be perpendicular to the axis of VAMOS++ placed at the grazing angle of the transfer reaction (25° with respect to the beam direction, as shown in Fig. 4.3). The ^{92}Mo target had a thickness of 0.715 mg/cm^2, while the degrader was made of 1.6 mg/cm^2 natural Mg. The reaction products recoiling out of the target decayed via γ-ray emission either while flying between the foils

with a velocity β_s ($= v/c \approx 10\%$) or after the degrader with a velocity β_u ($\approx 9\%$) that was reduced compared to β_s due to energy losses in the degrader foil [50]. Due to the Doppler effect the emitted γ rays are registered at a shifted energy E with respect to the actual transition energy E_0. The magnitude of this shift depends on the velocities $\beta_{s/u}$ and on the angle between the directions of the ion and of the emitted γ ray:

$$E = E_0 \frac{\sqrt{1-\beta^2}}{1-\beta\cos\theta} \approx E_0(1+\beta\cos\theta). \tag{4.1}$$

Thus, in a spectrum obtained with a HPGe detector placed at a certain θ angle with respect to the ion direction, one would observe two differently shifted components of each γ-ray peak, corresponding to the two emitter velocities β_s and β_u, as shown in Fig. 4.4.

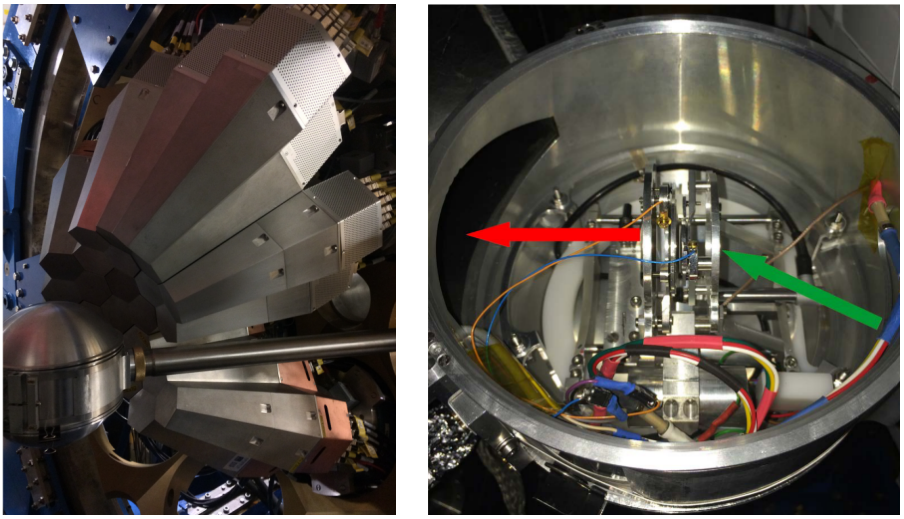

Figure 4.3 – Left - the reaction chamber and eight AGATA triple clusters placed at backward angles. Right - the plunger device placed inside the reaction chamber [48]. The directions of the beam and the reaction products are indicated with green and red arrows, respectively.

Doppler correction of γ-ray energies is possible thanks to the precise measurements of the γ-ray emission angle, achieved with AGATA, and of the velocity of the projectile β_u, provided by VAMOS++. The γ rays emitted after the degrader will be fully Doppler corrected, while those emitted from nuclei with higher velocities (β_s) will still appear at a shifted energy in the obtained spectra. In order to maximize the Doppler effect and thus the separation between the shifted and unshifted components, the AGATA detectors were placed at backward angles as far as possible from 90°, as presented in Fig. 4.3. A shift towards smaller energies was observed under such conditions.

The data were collected at eight different target-degrader distances ranging from 35 to 521 μm. They were analyzed using the Decay Curve and Differential Decay Curve methods (DCM and DDCM, respectively [53,54]), in order to extract level lifetimes from the measured evolution of the intensities of the shifted and unshifted components as a function of the distance between the foils. This analysis was performed by M. Siciliano in his PhD work [48] and the final results were published in Refs. [49,50].

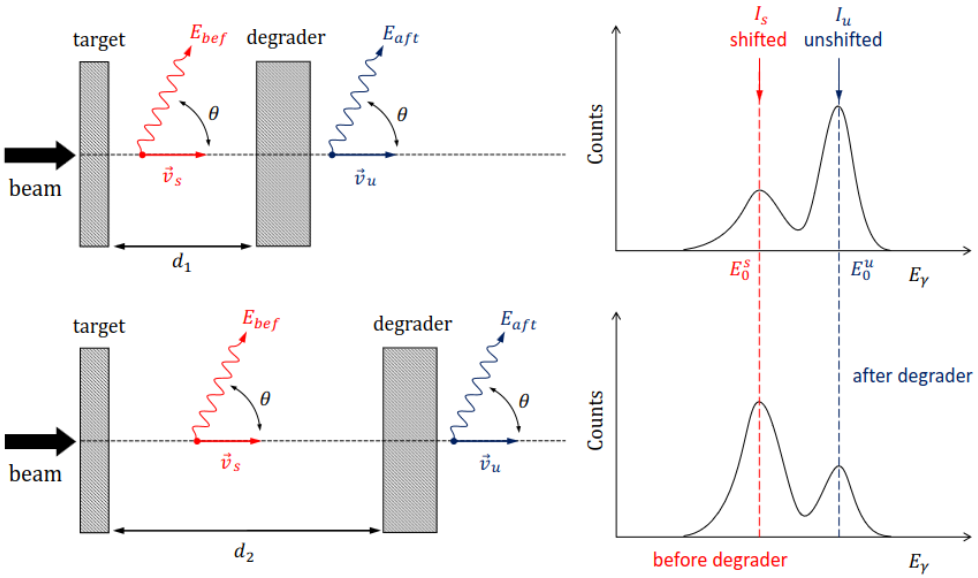

Figure 4.4 – A schematic presentation of the RDDS method. Two different target-degrader distances d_1 and d_2 are considered. The number of γ rays emitted before (red) or after (blue) the degrader depends on the lifetime τ of the state of interest. Using the evolution of the shifted/unshifted peak intensities as a function of the target-degrader distance, one can extract τ. Figure adapted from Ref. [57].

4.2.4 Unsafe Coulomb-excitation data

As discussed in Section 2, in a typical Coulomb-excitation study one should ensure that the excitation process occurs at a "safe" beam energy fulfilling Cline's criterion (Formula 2.1). Under such conditions, it is possible to obtain information on the electromagnetic MEs in a model-independent way. However, this has not been the case of the described experiment, as its original goals required optimizing of the detection system for nuclei of primary interest, which resulted in placing VAMOS++ around the grazing angle of the MNT reactions, i.e. $\theta_{LAB} = 25^\circ$ [48]. Under these conditions, ions scattered at $19.4^\circ \leq \theta_{LAB} \leq 30^\circ$ could reach the focal plane of VAMOS++.

Using Formula 2.2 and the beam energy in the middle of the target $E_{Bmid} = 757$ MeV (calculated with elo [58]), one can deduce the distance of the closest approach of colliding nuclei. For the smallest scattering angle a distance of 4.1 fm

was obtained. If a similar calculation is carried out for the highest scattering angle, $\theta_{LAB} = 30°$, it results in a separation of about 0.15 fm.Thus, considering the Cline's safe-energy criterion, a contribution from the nuclear interaction greater than 0.5% is expected to be present in the experimental excitation cross sections [40] and the collected Coulomb-excitation data are considered "unsafe" in the entire scattering angle range covered by VAMOS++.

4.3 Experimental observables

The experimental observables in a typical Coulomb-excitation experiment are the intensities of the γ rays registered in coincidence with the projectile or target nuclei scattered into a specific angular range. In the present analysis, the γ rays registered in coincidence with ^{106}Cd ions identified in VAMOS++ within a time window of 2 μs were organized in a γ-particle two-dimensional spectrum presented in Fig. 4.5. While in the RDDS method level lifetimes are deduced from the evolution of the shifted and unshifted components of the depopulating transitions as a function of the plunger distance, for a Coulomb-excitation study such a division of the data is irrelevant. Thus, the data collected at all plunger distances were summed together. However, one should note that due to the use of the plunger technique, the observed γ-ray peaks may appear at a shifted energy or have both shifted and unshifted components, depending on the lifetime of the nuclear state.

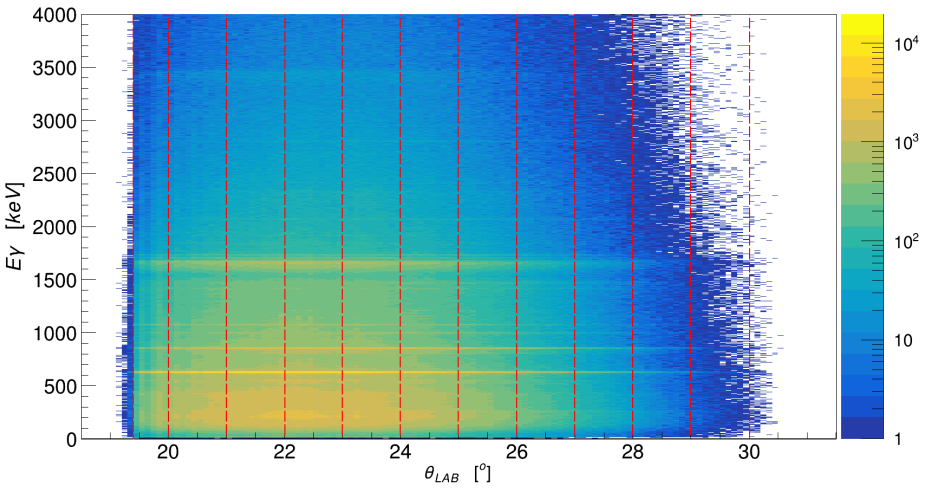

Figure 4.5 – Two-dimensional spectrum, with energy of the γ rays on the Y axis and scattering angle of ^{106}Cd in the laboratory coordinate system (θ_{LAB}) on the X axis, filled with coincidence γ-particle events using a time window of 2 μs [48]. The dashed lines indicate the borders of θ_{LAB} ranges considered in the analysis of the Coulomb-excitation data.

4.3.1 Partial level scheme of ^{106}Cd

A number of excited nuclear states in the beam and the target nuclei were populated in the process of inelastic scattering of ^{106}Cd on ^{92}Mo. Figure 4.6 shows the total γ-ray spectrum up to $E_\gamma \approx 2150$ keV summed over all scattering angles. The observed transitions in ^{106}Cd are labeled with their energies. At energies higher than 2.2 MeV only a peak at $2805(1)$ keV was observed, which is shown in the inset of Fig. 4.6. This peak was interpreted as the shifted component of the transition depopulating a spin-1 state at 2824.6 keV.

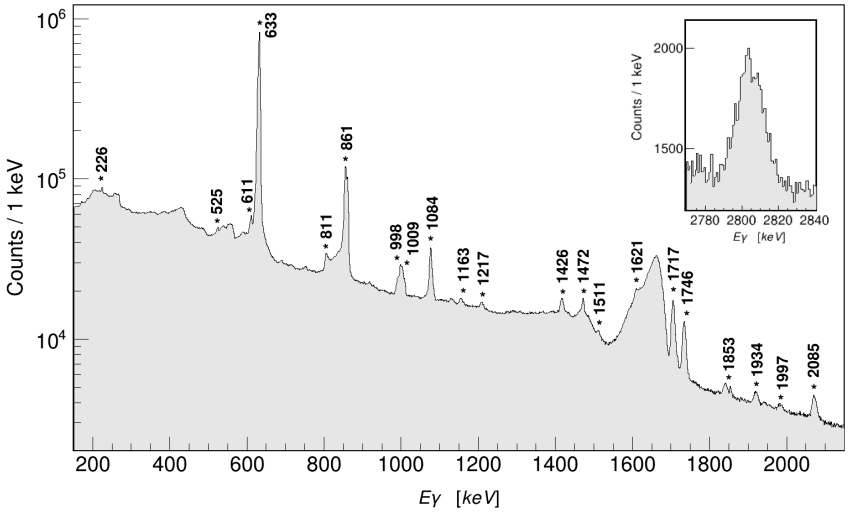

Figure 4.6 – Total γ-ray spectrum up to $E_\gamma \approx 2150$ keV. The γ-ray peaks, resulting from depopulation of excited states in ^{106}Cd, are labeled with their energies corresponding to emission at rest, even though in some cases only the shifted components are present. The inset shows the decay of the spin-1 state at 2824.6 keV.

It is important to stress that the Doppler correction is optimized for the beam nucleus, thus the peaks corresponding to the excited states in ^{92}Mo are very wide and shifted towards higher energy. This effect can be clearly seen in Fig. 4.6 where a broad structure around 1650 keV corresponds to the $2_1^+ \rightarrow 0_1^+$ transition in ^{92}Mo with an unshifted energy of 1509.5 keV.

The observed transitions depopulating excited nuclear states in ^{106}Cd are summarized in the partial level scheme presented in Fig. 4.7. There are a few main differences between Fig. 4.7 and the level scheme reported in Ref. [50], which was deduced from the RDDS study based on the same data set. First, the $(2)^+$ level at 2348 keV was removed from the current level scheme. From the analysis of the total γ-γ matrix it was concluded that the peak at 1715 keV, reported in Ref. [50] as the $(2)^+ \rightarrow 2_1^+$ decay, can be fully attributed to the $2_2^+ \rightarrow 0_1^+$ transition. This is further supported by the 1084 keV/1715 keV branching ratio obtained from the present data $(0.95(6))$, which is consistent within 1σ with the values reported in

the literature for $I_\gamma(2_2^+ \to 2_1^+)/I_\gamma(2_2^+ \to 0_1^+)$ [59, 60]. By summing the data collected at all plunger distances and carefully investigating the total projection for low-intensity peaks, a number of transitions were also added to the level scheme, namely:

- **A 1217-keV transition between a state with spin $2-6$ at 2711 keV and the 4_1^+ state**, due to the observation of a peak at $1210(1)$ keV in the γ-ray spectra. The observed peak was interpreted as the shifted component of a 1217-keV transition, de-exciting the $2-6$ level proposed in Refs. [61, 62]. An alternative interpretation can be found in Ref. [63], where this γ ray was attributed to the decay of a state at 2933.7 keV to the 2_2^+ state. However, the 2933.7-keV level has not been confirmed by later studies and has no counterparts in the heavier Cd nuclei that would exhibit a similar decay pattern;

- **A 1511-keV transition between the 0_3^+ state at 2144.1 keV and the 2_1^+ state**: at short plunger distances a peak at $1511(2)$ keV was observed, which corresponds to the unshifted component of the $0_3^+ \to 2_1^+$ transition. At longer distances a shifted component also appears, which suggests that the 0_3^+ state has a lifetime within the sensitivity range of the RDDS method;

- **A 1621-keV transition between the (2^+,3^+) state at 2254.0 keV and the 2_1^+ state**: two peaks were observed on the background of the Doppler-broadened $2_1^+ \to 0_1^+$ line of ^{92}Mo at ≈ 1609 keV and ≈ 1620 keV. They were interpreted as the shifted and unshifted components, respectively, of the γ-ray peak resulting from the de-excitation of the $(2^+, 3^+)$ state. However, a decay with a similar energy could be observed from the (4^+) state at 2252.2 keV. Due to the proximity in energy, it is not possible to exclude the alternative interpretation, and moreover, the observed intensity can have contributions resulting from the decay of both states;

- **A 1997-keV transition originating from the 2_5^+ state at 2630.1 keV**, due to the observation of a peak at $1984(2)$ keV corresponding to the shifted component of the $2_5^+ \to 2_1^+$ transition;

- **A 2085-keV transition from the $2^+, 3$ state at 2717.9 keV**: in the γ-ray spectra a peak at $2072(1)$ keV was observed. It can be interpreted as the shifted component of a transition depopulating either the $2^+, 3$ state at 2718 keV, or the $1, 2^+, 3$ state at 2720.6 keV, or have contributions resulting from the decay of both states;

- **A 2824-keV γ ray between the state of spin 1 at the same excitation energy, and the ground state**.

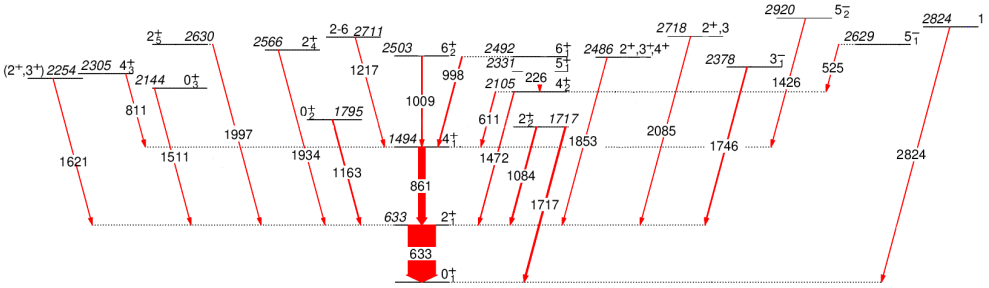

Figure 4.7 – Partial level scheme of ^{106}Cd presenting the γ-ray transitions observed in the present experiment with their energies given in keV.

Additionally, the intensity of the $4_2^+ \rightarrow 4_1^+$ transition was determined, which has not been analysed in Ref. [50] due to its proximity to the intense $2_1^+ \rightarrow 0_1^+$ peak.

4.3.2 Division of the data according to scattering angle

Considering the fact that the current Coulomb-excitation data were collected in an unsafe regime, the observed excitation cross sections are likely to be affected by the nuclear interaction. It is expected that the importance of this effect will increase with the scattering angle, as the separation distance between the nuclear surfaces decreases. The contribution from the nuclear interaction may differ from state to state, depending on the different transition strengths and multipolarities involved in the excitation process. Thus, in order to probe the effects of the nuclear interaction on the excitation cross section with a fine $\Delta\theta_{LAB}$ step, eleven cuts on the scattering angle were applied as shown in Fig. 4.5 with red dashed lines. The first $\Delta\theta_{LAB}$ range is only 0.6° wide ($19.4^\circ < \theta_{LAB} < 20.0^\circ$), while all others scattering angle ranges cover $\Delta\theta_{LAB} = 1^\circ$. Subsequently, the intensities of all γ-ray transitions indicated in the level scheme in Fig. 4.7, were measured for all eleven cuts. Examples of γ-ray spectra corresponding to individual $\Delta\theta_{LAB}$ cuts are presented in Fig. 4.8.

Figure 4.9 shows the hit pattern in the MWPC at the entrance of VAMOS++ under the condition that a ^{106}Cd ion was identified. For the identification to be successful, ^{106}Cd ions have to pass through all focal plane detectors and reach the ionization chamber (see Section 4.2.1).Thus, the number of registered Cd ions strongly depends not only on the reaction cross section but also on the geometry and transmittance of VAMOS++. The $\Delta\theta_{LAB}$ ranges considered in the current analysis, indicated in Fig. 4.9, correspond to sections of the MWPC detector with different ϕ angular coverage. Moreover, certain areas, e.g. around $|\phi| = 20^\circ$, appear to be "shadowed" due to the use of magnets in VAMOS++, which prevent some of the ^{106}Cd ions from reaching the IC. A significantly lower statistics is also observed at angles greater than $\theta_{LAB} = 27^\circ$, which is mostly related to the decrease of the cross section for inelastic scattering with scattering angle.

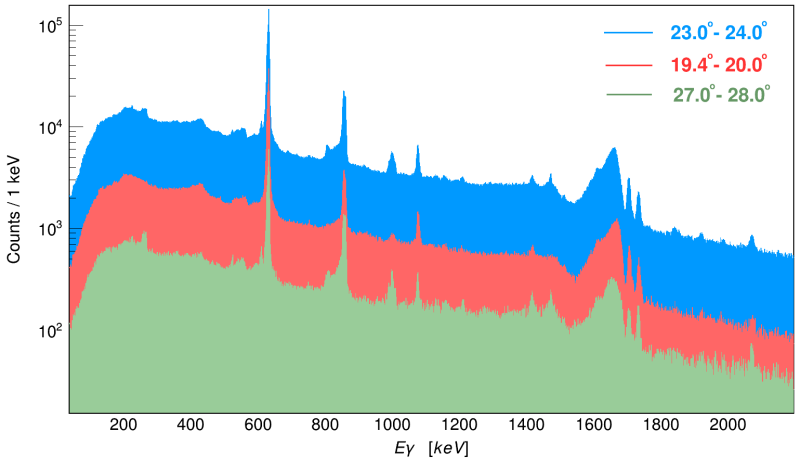

Figure 4.8 – Total γ-ray spectra obtained in coincidence with different $\Delta\theta_{LAB}$ angular ranges indicated in the plot. No normalization is applied.

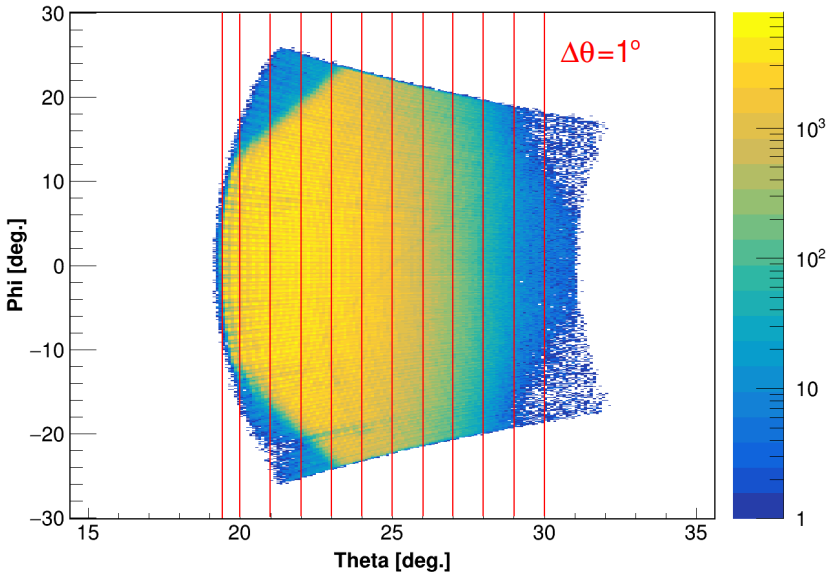

Figure 4.9 – Hit pattern of ^{106}Cd ions identified in VAMOS, presented in spherical coordinates with $\theta_{LAB} = 0°$ corresponding to the beam direction and $\phi = 0°$ to the horizontal plane. The red lines indicate the borders of θ_{LAB} ranges considered in the analysis of the Coulomb-excitation data.

As can be seen in Fig. 4.8, the level of statistics in γ-ray spectra corresponding to individual θ_{LAB} ranges varies rapidly with the scattering angle. Considering the effects discussed above, an efficiency calibration of VAMOS++ would be necessary in order to enable a comparison between the absolute γ-ray intensities measured in coincidence with projectiles scattered at different $\Delta\theta_{LAB}$ ranges. This could be

achieved by comparing the total number of scattered ions (including both elastic and inelastic scattering) in each $\Delta\theta_{LAB}$ range with a calculated one. Unfortunately, the analog electronics of the IC could not support very high counting rates. To reduce loss of data due to pile-up, the rate of validated events was reduced to 4.5 kHz, and only ions identified in VAMOS++ in coincidence with a γ ray registered in AGATA were accepted. Thus, information on elastically scattered ^{106}Cd ions was not collected during the experiment, and consequently it was not possible to perform an efficiency calibration of VAMOS++. A simple way to circumvent this issue is to normalize the γ-ray intensities measured for each $\Delta\theta_{LAB}$ range over the intensity of the $2_1^+ \rightarrow 0_1^+$ transition. Adopting such a procedure will result in a slight increase in the uncertainties of the experimental observables, which are now the relative γ-ray intensities.

4.3.3 Extraction of the γ-ray intensities

As discussed earlier, due to the use of the RDDS technique, the observed γ-ray peaks often consisted of both shifted and unshifted components. Therefore, a sophisticated procedure is needed to properly extract the γ-ray intensities (peak areas) from the particle-gated spectra. Furthermore, in particular cases the estimation of the area can be additionally hindered due to an overlap with peaks at similar energies originating from different transitions. Several types of fits were attempted under the guidance of M. Siciliano using different fitting programs. The adopted fits were performed by M. Siciliano within the ROOT framework [64].

In the case of a well-defined (fully shifted or unshifted) and isolated γ-ray peak, a combination of a Gaussian and a linear function was adopted to reproduce its shape and the underlying background, respectively. An example of the fitting procedure used for the more complicated cases, in which two components of the peak are discerned, is illustrated in Fig. 4.10 for the peak at 633 keV, originating from the $2_1^+ \rightarrow 0_1^+$ transition. First, the particle-gated spectra at the shortest and longest plunger distances, summed over all scattering angles, were fitted with a combination of a linear function and two Gaussian functions. This was used to determine the optimal peak positions and constrain their widths: the unshifted/shifted component of a γ-ray peak dominates at the shortest/longest plunger distance, enhancing sensitivity to its position and width, see Fig. 4.10.

The fit parameters obtained in this way can be used to fit the components of the 633-keV peak at any plunger distance. Of course, small variations of the parameters are allowed. This method was validated in Ref. [65] by measuring the intensities of the two components of the 633-keV peak at all plunger distances. Subsequently, the extracted intensities were used to perform DCM and DDCM analysis, yielding lifetimes $\tau(2_1^+)$ of $10.7(4)$ ps and $10.4(2)$ ps, respectively. These measurements are in perfect agreement with the previously reported values ($10.5(1)$ ps [66]), demonstrating that this analysis strategy is suitable even if the peak components are difficult to separate.

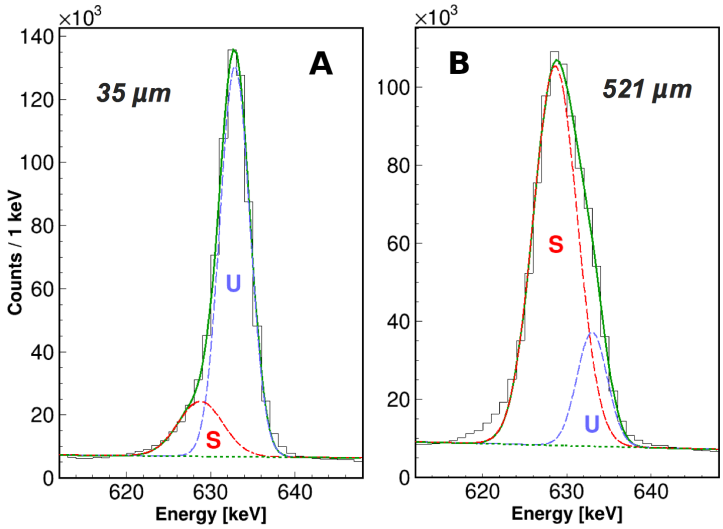

Figure 4.10 – Example fit (solid green line) of the peak originating from the $2_1^+ \rightarrow 0_1^+$ transition with its shifted (S) and unshifted (U) components at the shortest (A) and longest (B) plunger distances. A combination of two Gaussian functions (long-dashed lines) and a linear background (dashed green line) were used.

The spectra obtained by applying cuts on the scattering angle (but summed for all plunger distances) can be fitted using fit parameters obtained in the same manner, while still allowing their small variations. The results of this procedure for the 633-keV peak observed in coincidence with ^{106}Cd nuclei detected in the $\Delta\theta_{LAB}$ range between $21.5°$ and $22.5°$ are presented in Fig. 4.11.

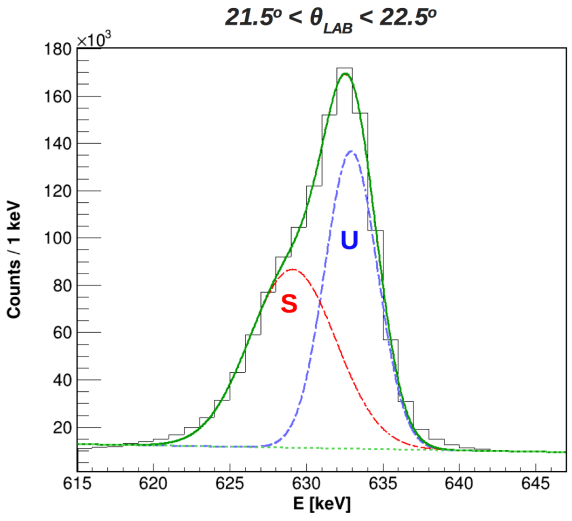

Figure 4.11 – The 633-keV peak in the $21.5° < \theta_{LAB} < 22.5°$ gated spectrum fitted using the routine described in the text. The shifted and unshifted components of the peak are marked accordingly.

The fitting procedure described above was also applied in the complex cases of overlapping peaks with multiple components. For example, the peak at 998 keV, which corresponds to the unshifted component of the $6_1^+ \rightarrow 4_1^+$ transition, may overlap with the shifted component of the peak at 1009 keV from the $6_2^+ \rightarrow 4_1^+$ transition. Furthermore, the shifted component of the 998-keV peak overlaps with the peak at 992 keV, originating from the $2^+, 3^+, 4^+ \rightarrow 4_1^+$ transition. A combination of four Gaussian functions and a linear background function was used to fit this region of the spectrum. The fit parameters were obtained following the strategy described above, namely using the spectra at the shortest (Fig. 4.12 (A)) and the longest (Fig. 4.12 (B)) plunger distance. As the peaks originating from the decay of the 6_1^+ and $2^+, 3^+, 4^+$ states could not be separated, they were treated as a doublet in the following analysis described in Section 6.2.

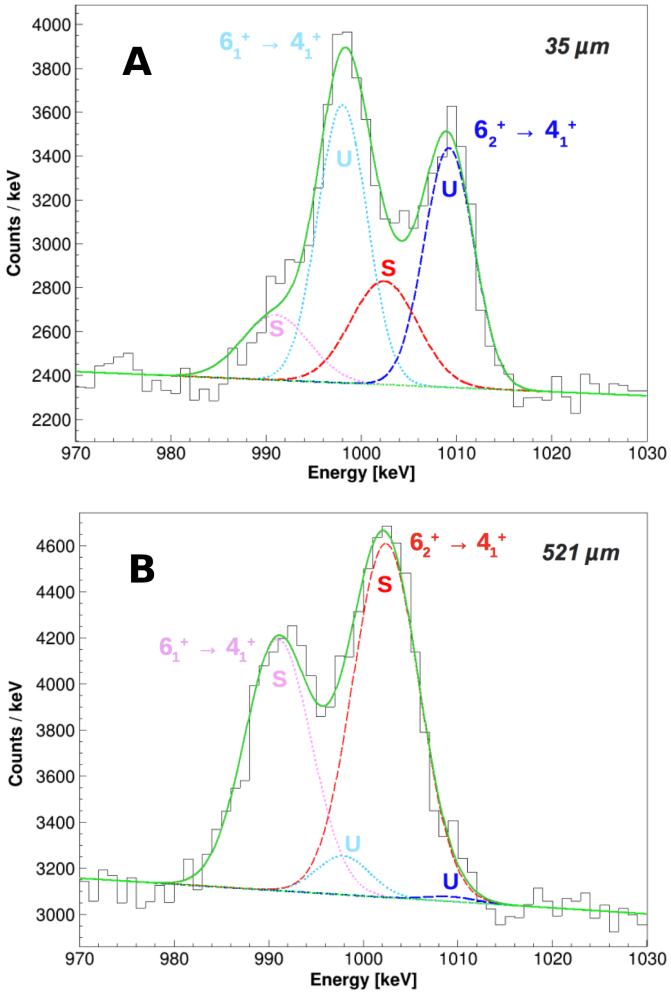

Figure 4.12 – Same as Fig. 4.10 but for the γ-ray peaks originating from the $6_1^+ \rightarrow 4_1^+$ and $6_2^+ \rightarrow 4_1^+$ transitions. Their shifted and unshifted components are marked accordingly.

As a next step, the estimated areas of the shifted and unshifted components of each peak were corrected for the difference in the relative detection efficiency and summed together. The respective uncertainties were calculated using standard error propagation. A 4% systematic error was adopted, arising from the fit of the γ-ray efficiency curve of AGATA. While the efficiency calibration was obtained using γ rays emitted at rest from a ^{152}Eu radioactive source [65], the γ rays of interest were emitted in flight and thus had to be Doppler corrected. Therefore, the used efficiency curve was additionally modified to account for the fact that the efficiency correction should be applied for the energy of the peak before Doppler correction, i.e., for the real energy at which the γ rays were registered. Due to the large angular acceptance of AGATA the non-corrected peaks were Doppler-broadened and the efficiency correction had to be performed for an averaged energy. This resulted in an additional systematic error of $0.8 - 2.7\%$, depending on the transition energy, which is represented with the error band in Fig. 4.13.

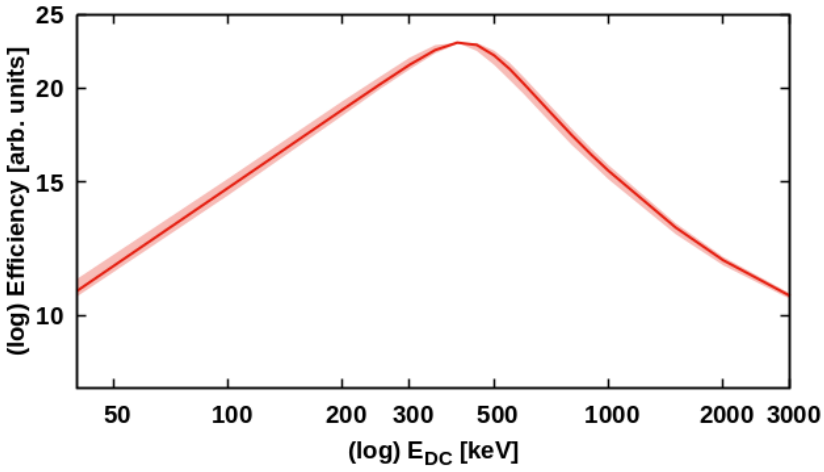

Figure 4.13 – The modified AGATA efficiency as a function of the Doppler corrected γ-ray energy E_{DC}, presented in doubly-logarithmic scale. The error corridor accounts for the broadness of the γ-ray peaks before Doppler correction, while the solid line represents the efficiency for an averaged energy. No other systematic errors are presented.

The results of the described fitting procedure for all individual γ-ray transitions, normalized to the intensity of the $2_1^+ \rightarrow 0_1^+$ transition determined in the same way, are presented in Figs. 6.2 - 6.10 in black.

5 - Analysis strategies

As discussed in Section 4.2.4, the collected Coulomb-excitation data are considered unsafe at all scattering angles covered by the present measurement, which correspond to separation distances ranging from 4 fm to almost touching nuclear surfaces at the highest scattering angle. As mentioned in Section 4.3.2, we can use such unsafe Coulomb-excitation data to probe in more detail how the effects of the nuclear interaction evolve with the scattering angle. Moreover, it is of great interest to investigate how these effects differ from one state to another, as a function of their excitation energy and spin-parity.

Possible approaches to "unsafe" Coulomb-excitation data analysis are presented in Sections 5.1, 5.2 and 5.3. A survey of available spectroscopic data on ^{106}Cd relevant for the present analysis can be found in Section 5.4, while an introduction to coupled-channels codes FRESCO and GOSIA is given in Sections 5.6 and 5.7, respectively. The former section also presents results of a qualitative FRESCO calculation for the system analysed in the present study.

5.1 Nuclear influence on the data

A proper analysis of unsafe Coulomb-excitation data would require the use of coupled-channel codes such as FRESCO [36], PTOLEMY [37], etc., which can account for possible effects of the nuclear interaction on the excitation cross section in a model-dependent way. This is achieved by employing an optical potential model (OPM), as described later in Section 5.6.3. The optical potentials are usually obtained empirically and aim to account for effects originating beyond the channel of interest. For example, in the case of elastic scattering, the OPM is obtained by fitting experimental elastic-scattering data in a way that will effectively describe the cumulative effect of the remaining open reaction channels on the elastic-scattering cross section.

A serious limitation of this approach can be the lack of an appropriate optical potential to describe the nuclear interaction in the specific physics case (combination of collision partners and beam energy). General parametrizations of optical potential models exist, however, their parameters typically require additional adjustments of their parameters using elastic (and inelastic) scattering data for the specific experimental conditions. Unfortunately, such data are scarce. This is also the case of the present experiment - as stressed in Section 4.3.2, no elastic-scattering particle singles data were collected as only ^{106}Cd ions, which were in coincidence with γ rays registered in AGATA, entered the trigger.

Another important note is that the empirical optical potentials are often fitted to elastic-scattering data at high scattering angles and usually reproduce nicely only the main interference peak (the so-called Coulomb rainbow), e.g. Fig. 1 of Ref. [67].

At small scattering angles, the oscillations resulting from the Coulomb-nuclear interference have much smaller amplitudes, while exhibiting a higher frequency. Thus, they are often not described very precisely due to the insufficient number of experimental data points. This presents yet another possible difficulty for analyzing the current unsafe Coulomb-excitation data, which were collected only at small scattering angles (up to $\theta_{LAB} = 30^{\circ}$).

Considering the above, in the present case it is not possible to perform a quantitative analysis of the unsafe Coulomb-excitation data and to account for the nuclear influence on the data in an exact way. However, a qualitative description could be obtained, which is described in Section 5.6.

5.2 Safe Coulomb-excitation approach based on spectroscopic data

Another approach to evaluate the effects resulting from the nuclear influence on the excitation process is to compare the experimentally observed excitation cross sections with calculated ones, assuming a safe Coulomb-excitation process. The coupled-channel code GOSIA [68] can be used for this goal.

In a typical Coulomb-excitation experiment, the experimentally observed cross sections depend solely on a set of matrix elements (MEs) of the electromagnetic operator. This, of course, implies that the nuclear interaction had a negligible contribution to the excitation process. Based on known spectroscopic data, such as lifetimes, spectroscopic quadrupole moments, mixing and branching ratios, a set of transitional and diagonal MEs can be calculated and used to simulate the intensities expected for a safe Coulomb-excitation process. The geometry of the detection system must be taken into account in order to enable a proper comparison between the calculated and measured cross sections.

By performing such a comparison for each observed transition the effects of the nuclear influence on the excitation process can be evaluated both qualitatively and quantitatively. Moreover, those effects may change from one excited state to another, which will provide valuable information on their character. However, a major drawback of this approach is that it strongly depends on the availability of previously obtained spectroscopic data. Lack of such measurements or their insufficient precision will limit its applicability. Such issues are not uncommon even for stable isotopes like ^{106}Cd. However, one advantage of analysing byproduct data from a lifetime measurement is that the RDDS analysis has already provided some of the needed lifetimes. The application of this approach is described in Section 6.1.

5.3 Fitting unsafe Coulomb excitation with GOSIA

As explained in the previous subsection, the expected excitation cross sections can be obtained using a set of MEs, calculated from the known lifetimes and other

spectroscopic data. On the other hand, a new set of MEs can be deduced by fitting the measured intensities with GOSIA. This new set of MEs will be based on the measured excitation cross sections combined with literature branching and mixing ratios, but will no longer depend on the previously measured lifetimes. Thus, with this approach it will be possible to indirectly extract lifetimes from the unsafe Coulomb-excitation data, in an independent way from the RDDS measurement, and subsequently compare them to the literature τ values. Furthermore, this will open a possibility to determine lifetimes that are too short for an RDDS analysis. Moreover, information on the negative-parity states can be obtained, which is not accessible via decay spectroscopy. In particular, from the observed population of such states it may be possible to determine the $E3$ matrix elements, corresponding to weak decay branches which are rarely observed experimentally.

A serious drawback of this approach comes from the impossibility to account for the nuclear interaction using GOSIA. This code is designed to describe safe Coulomb-excitation experiments, where the excitation process is governed solely by the electromagnetic force. In order to partially circumvent this issue, a limited number of experimental points can be included in the fit, namely those obtained at the smallest scattering angles, where the separation distance is largest and the excitation process will be the least affected by the nuclear interaction. Subsequently, the new set of fitted MEs can be used to calculate the intensities at higher scattering angles. If a good agreement is observed between the experimental and calculated γ-ray yields for a particular state, it is likely that the excitation process is affected very little by the nuclear interaction. Disagreements with the "spectroscopic" prediction may then suggest issues with the complementary spectroscopic data. The application of this approach and obtained results are described in Section 6.2.

5.4 Spectroscopic information on ^{106}Cd

To implement any of the approaches proposed in Sections 5.1-5.3, providing spectroscopic information on the nucleus of interest is necessary. This includes the excitation energies of the relevant nuclear states, their spin-parities, known lifetimes, previously measured spectroscopic quadrupole moments, multipolarities of the transitions populating and depopulating each state, as well as the branching and mixing ratios of those transitions. A summary of the adopted spectroscopic data is provided in the following subsections.

5.4.1 Excitation energy and spin-parity

All of the levels populated in the unsafe Coulomb-excitation process must be included in the analysis. They are summarized in the partial level scheme in Fig. 4.7. In addition, the 8_1^+ state at 3044 keV excitation energy was included in the analysis as a "buffer state" [69]. The excitation energies of the states were taken from the ENSDF database [59], with the exception of the state at 2711 keV, taken from

Ref. [62], as explained in Section 4.3.1. These data are listed in Table 5.1.

Table 5.1 – Adopted spectroscopic information on ^{106}Cd including excitation energies (E_x), spin-parities (I^π) and lifetimes (τ). The E_x and I^π values are taken from the ENSDF database [59], with a few marked exceptions which are described in the text. The lifetimes are taken from the references provided in the table. Those marked with daggers are a weighted average of values reported in the listed references. Alternative τ measurements are given in the last column.

E_x [keV]	I^π	τ [ps]		Alternative τ [ps]
632.64(4)	2_1^+	$10.37(15)^\dagger$	[50, 65]	$10.3(2)^\dagger$ [72–75]
1493.78(5)	4_1^+	1.4(2)	[50]	$1.40(5)^\dagger$ [71, 72, 75]
1716.53(8)	2_2^+	$0.50(2)^\dagger$	[50, 60]	$0.48(3)^\dagger$ [71, 72, 75]
1795.25(11)	0_2^+	$1.29(10)^\dagger$	[50, 61]	–
2104.53(6)	4_2^+	4.1(7)	[50]	≤ 2.9 [76], > 1 [61]
2144.06(4)	0_3^+	> 1.58	[61]	11^{+32}_{-6} [71]
2254.0(5)	2^{+*}	$0.57^{+0.27}_{-0.19}$	[61]	–
2304.92(12)	4_3^+	1.1(1)	[50]	< 0.36 [61]
2330.56(6)	5_1^+	870(290)	[59]	–
2378.50(4)	3_1^-	0.20(3)	[61]	< 0.3 [50]
2485.72(14)	4^{+*}	$2.34(17)^\dagger$	[50]	> 0.92 [61]
2491.66(6)	6_1^+	< 2	[50]	> 0.35 [61]
2503.08(7)	6_2^+	$1.22(15)^\dagger$	[50]	$0.26^{+0.44}_{-0.14}$ [61], 0.54(8) [75], 0.73(13) [71]
2566.26(11)	2_4^+	0.10(1)	[61]	< 0.3 [50]
2629.20(7)	5_1^-	8.2(4)	[50]	–
2630.08(5)	2_5^+	0.19(3)	[61]	$0.25^{+0.13}_{-0.09}$ [61]
2710.8(3) [62]	2^{+*}	$0.16^{+0.05}_{-0.04}$	[61]	Shifted‡
2717.86(4)	2^{+*}	$0.38^{+0.11}_{-0.09}$	[61]	Shifted‡
2824.58(5)	$1^{(-)*}$	0.029(1)	[60]	Shifted‡
2920.14(8)	5_2^-	$0.20^{+0.05}_{-0.04}$	[61]	< 0.3 [50]
3044.13(7)	8_1^+	560(250)	[59]	–

* Assumptions were made for the spin-parity.

† The lifetime is a weighted average of the values given in the listed references. Note that Ref. [50] provides for certain states two alternative τ values resulting from DCM and DDCM analyses.

‡ Only a shifted component of the γ-ray peak was observed in the present measurement ($\tau < 0.3$ ps).

Assumptions for the spin-parity of some states had to be made due to the lack of information in the literature. Namely, for the states $(2^+, 3^+)$ at 2254 keV, $(2-6)$ at 2711 keV and $2^+, 3$ at 2718 keV, spin-parity of 2^+ was adopted for simplicity. As explained in Section 4.3.1, the γ rays originating from these states could be assigned to the decay of other closely-lying states, which makes it pointless to attempt a more precise spin assignment. For the $2^+, 3^+, 4^+$ state at 2486-keV excitation energy, a 4^+ spin-parity was assumed. Such spin-parity was proposed in a β^+-decay study of ^{106}In [70] and following inelastic neutron scattering on ^{106}Cd [61]. Moreover, a spin 4^+ was also adopted in another Coulomb-excitation study of ^{106}Cd, published recently [71]. The spin of the state at 2824 keV is firmly assigned to be 1 [59], but there is not enough evidence in the literature to constrain the parity of this state. However, its low population in the β^+/EC decay of the $(2)^+$ state in ^{106}In [60] favours a negative parity, which was adopted in the present analysis. For the remaining states considered in the analysis, the spin-parities given by the evaluated database ENSDF [59] were assumed. The adopted spin-parities are listed in the second column of Table 5.1. Those, for which assumptions were made, as discussed above, are marked with an asterisk.

5.4.2 Branching ratios

In Coulomb excitation, the population process does not necessarily have to follow the observed de-excitation path, i.e. apart from the the observed transitions, all possible excitation/de-excitation paths have to be included. This is clearly illustrated by the fact that for the negative-parity states, which primarily decay via $E1$ transitions, an $E3$ population path has to be considered, as discussed in Section 3.3. In the present analysis, this consideration resulted in the addition of the $E3$ $3^-_1 \rightarrow 0^+_1$, $5^-_{1,2} \rightarrow 2^+_1$ and $1^{(-)} \rightarrow 2^+_1$ transitions to the level scheme, although they were not observed in the de-excitation spectra.

Following a comparison of several literature resources [59, 61, 62], a set of branching ratios was adopted, which is presented in the fourth column of Table 5.2. Most of the branching ratios were taken from the recent PhD thesis of T. Schmidt [62] and were extracted using γ-γ and γ-p coincidence information, obtained via inelastic proton scattering (^{106}Cd$(p, p'\gamma)$). The branching ratio from Ref. [59] was used for the decay of the 8^+_1 state, while for the $I_\gamma(2^+_2 \rightarrow 2^+_1)/I_\gamma(2^+_2 \rightarrow 0^+_1)$ branching ratio, the value reported in Ref. [61] was assumed. The latter choice is based on the good agreement between the result obtained by A. Linnemann [61] $(0.94(14))$ and the branching ratio measured from the current data set $(0.95(6))$.

Considering everything discussed above, the partial level scheme in Fig. 4.7 transforms into a more complex one, presented in Fig. 5.1. As can be seen, 46 transitions are being considered in the analysis, including 4 $E3$ transitions (depicted in blue), while only 22 of them were observed in the experimental data (depicted in red). The arrow widths of the observed transitions correspond to their relative intensities. The transitions, which were not directly observed in the present study, are depicted in black.

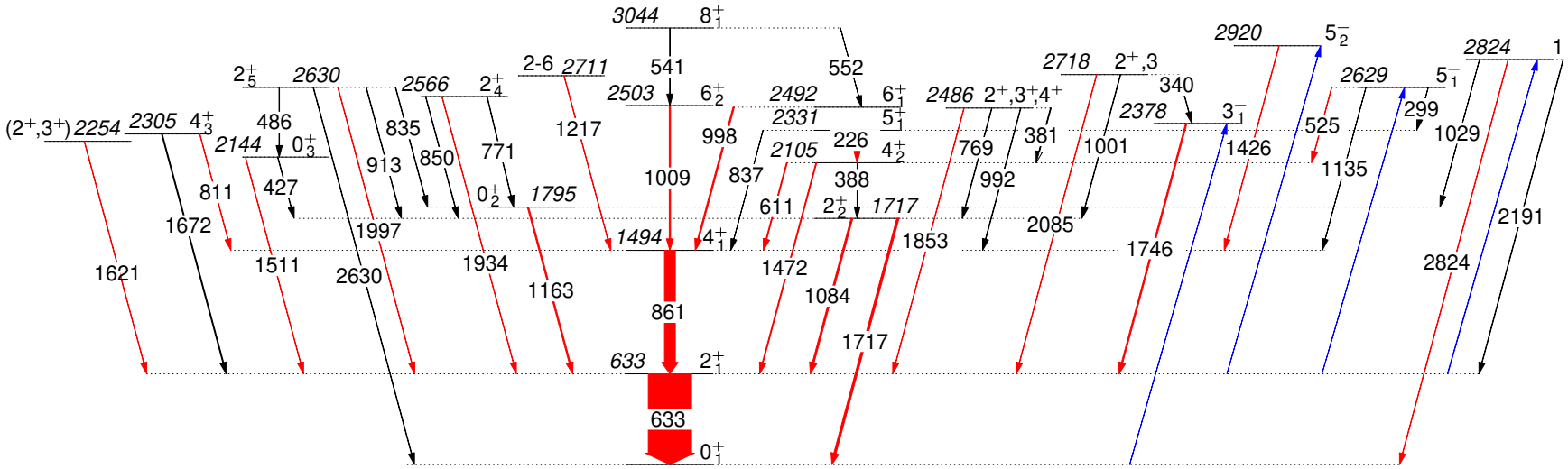

Figure 5.1 – Partial level scheme of ^{106}Cd assumed in the GOSIA analysis. The transitions marked in red were observed in the present experiment, while those in black are included due to literature branching ratios. The $E3$ transitions important for the population of the negative-parity states are marked in blue. The arrow widths correspond to the experimentally observed intensities (in red) or known branching ratios (in black). The arrangement of levels into bands follows the recommendations of Ref. [50].

Table 5.2 – γ-ray transitions in ^{106}Cd with their energy (E_γ), relative γ-ray intensities (I_γ) and transition multipolarities ($\sigma\lambda$). E_γ are taken from the ENSDF database [59], except for the values marked with daggers, which are taken from Ref. [62]. I_γ and $\sigma\lambda$ are adopted from the corresponding references. The multipolarities resulting from assumptions are marked accordingly.

I_i^π	I_f^π	E_γ[keV]	I_γ	$\sigma\lambda$
2_1^+	0_1^+	632.66(4)	100 [59]	$E2$
4_1^+	2_1^+	861.16(4)	100 [59]	$E2$ [59]
2_2^+	0_1^+	1716.40(9)	100(10) [61]	$E2$ [59]
	2_1^+	1084.25(23)	94(10) [61]	$M1$+$E2$ [59]
0_2^+	2_1^+	1162.60(10)	100 [59]	$E2$
4_2^+	4_1^+	610.77(5)	100.0(41) [62]	$M1$+$E2$ [59]
	2_1^+	1471.86(5)	51.2(22) [62]	$E2$ [59]
	2_2^+	387.78(18)	3.12(20) [62]	$E2$ [59]
0_3^+	2_1^+	1511.41(4)	100.0(41) [62]	$E2$
	2_2^+	427.35(9)	37.6(16) [62]	$E2$
$(2^+, 3^+)$	2_1^+	1621.3(3)	100 [61, 62]	$E2^\ddagger$
4_3^+	4_1^+	811.14(10)	100.0(41) [62]	$M1$+$E2$ [59]
	2_1^+	1672.6(3)	10.90(53) [62]	$E2$ [61]
5_1^+	4_2^+	226.4(5)	100.0(42) [62]	$M1$+$E2$ [59]
	4_1^+	836.79(7)	37.9(20) [62]	$M1$+$E2$ [59]
3_1^-	2_1^+	1745.82(3)	100 [59]	$E1$ [59]
$2^+, 3^+, 4^+$	2_1^+	1853.5(3)†	100.0(42) [62]	$E2$ [59]
	4_1^+	992.2(3)†	39.2(19) [62]	$E2^\ddagger$
	2_2^+	769.4(3)†	14.52(78) [62]	$E2$ [61]
	4_2^+	381.4(3)†	4.23(33) [62]	$E2^\ddagger$
6_1^+	4_1^+	997.87(4)	100 [62]	$E2$ [59]
6_2^+	4_1^+	1009.27(6)	100 [59]	$E2$ [59]
2_4^+	2_1^+	1933.6(3)†	100.0(41) [62]	$M1$+$E2$ [59]
	2_2^+	849.3(3)†	0.79(7) [62]	$E2^*$
	0_2^+	771.4(3)†	0.24(7) [62]	$E2$
5_1^-	4_2^+	524.65(5)	100.0(43) [62]	$E1$ [59]
	4_1^+	1135.68(11)	23.8(12) [62]	$E1$ [59]
	5_1^+	298.5(4)	5.91(76) [62]	$[E1]$ [59]
2_5^+	2_1^+	1997.4(3)†	100.0(41) [62]	$M1+E2$ [59]
	2_2^+	913.4(3)†	8.94(45) [62]	$E2^*$
	0_1^+	2629.5(3)†	7.01(33) [62]	$E2$
	0_2^+	835.2(3)†	0.54(8) [59]	$E2$
	0_3^+	485.6(3)†	0.46(8)	$E2$

† E_γ is taken from Ref. [62].
‡ $\sigma\lambda$ was adopted (due to assumptions made for the spin-parity).
* $\sigma\lambda$ was adopted (due to lack of literature data on the mixing ratio).

Table 5.2 – γ-ray transitions in ^{106}Cd - continued

I_i^π	I_f^π	E_γ[keV]	I_γ	$\sigma\lambda$
$2-6$	4_1^+	$1216.9(3)^\dagger$	100 [61, 62]	$E2^\ddagger$
$2^+, 3$	2_1^+	$2084.9(3)^\dagger$	100(40) [62]	$E2^\ddagger$
	2_2^+	$1000.8(3)^\dagger$	17.8(53) [62]	$E2^\ddagger$
	3_1^-	$339.2(3)^\dagger$	5.4(16) [62]	$E1^\ddagger$
$1^{(-)}$	0_1^+	$2823.4(3)^\dagger$	100.0(42) [62]	$E1$ [60, 61]
	0_2^+	$1029.3(3)^\dagger$	5.19(35) [62]	$E1^\ddagger$
	2_1^+	$2191.1(3)^\dagger$	2.87(32) [62]	$E1^\ddagger$
5_2^-	4_1^+	1426.36(6)	100 [59]	$E1^*$
8_1^+	6_1^+	552.53(5)	100(3) [59]	$E2$ [59]
	6_2^+	541.00(6)	63(5) [59]	$E2$ [59]

- **The 4_2^+ state at 2105 keV** decays by three transitions, connecting it to the 2_1^+, 4_1^+ and 2_2^+ states. Discrepancies in the literature are found for the reported branching ratios [59, 62]. For consistency, the values given in Ref. [62] were used. However, the branching ratios deduced from the current data set significantly differ from the literature values, as presented in Fig 5.2. This suggests a presence of contamination in the data. Unfortunately it is not clear which one of the branches is affected. Thus, firm conclusions regarding the population of the 4_2^+ state may not be possible.

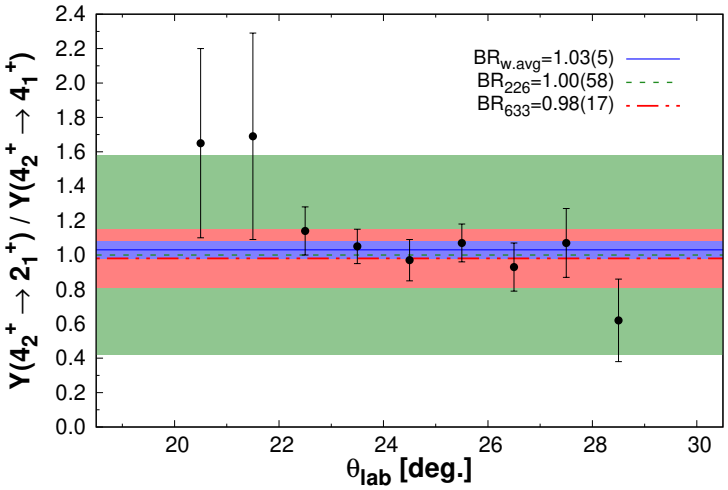

Figure 5.2 – Ratio of the measured $4_2^+ \rightarrow 2_1^+$ and $4_2^+ \rightarrow 4_1^+$ intensities as a function of scattering angle [77]. The weighted average (in blue) of the results obtained using singles γ-ray spectra (in black) is compared with those measured using γ-γ coincidence analysis with gates on the 226-keV (in green) and 633-keV (in red) transitions. The filled areas correspond to 1σ uncertainty. The literature value of $Y(4_2^+ \rightarrow 2_1^+)/Y(4_2^+ \rightarrow 4_1^+)$ is $0.51(2)$ [62].

- **The $(2^+, 3^+)$ state at 2254.0 keV** decays via two transitions - to the 2_1^+ ($E_\gamma \approx 1621$ keV) and to the 2_2^+ state ($E_\gamma \approx 536$ keV) - according to the ENSDF database [59]. However, in the study of T. Schmidt [62], as well as in the work of A. Linnemann [61], the 536-keV γ ray is attributed to the decay of the $(4)^+$ state at 2252.2 keV to the 2_2^+ state. This interpretation is adopted in the current analysis.

- **The $2^+, 3^+, 4^+$ state at 2486 keV** decays via two equally strong branches to the 4_1^+ and to the 2_1^+ state, according to Ref. [59]. However, a much smaller branch to the 4_1^+ state is reported in Ref. [62], in agreement with Ref. [61]. Moreover, two new decay branches are observed - to the 2_2^+ [61, 62] and to the 4_2^+ state [62]. Later, in Section 6.1, it will be shown that using the unsafe Coulomb-excitation data it is possible to distinguish between discrepant literature values in this particular case.

- As reported in Ref. [59], **the 6_1^+ state at 2492 keV** decays to the 4_1^+ and 5_1^+ states. However, the latter branch was not confirmed by the recent studies [61, 62] and thus it is excluded from the analysis.

- **The 2_4^+ state at 2566 keV** decays predominantly via the $2_4^+ \rightarrow 2_1^+$ transition, as reported in the ENSDF database. Additionally, two much weaker branches - $2_4^+ \rightarrow 0_2^+$ and $2_4^+ \rightarrow 2_2^+$ - were observed in Ref. [61] (with I_γ of $0.2(1)$ and $0.4(1)$, respectively) and in Ref. [62] (with I_γ of $0.24(7)$ and $0.79(7)$). The branching ratios from Ref. [62] were adopted in the current study.

- **The 5_1^- state at 2629 keV** decays by three transitions, connecting it to the 4_1^+, 4_2^+ and 5_1^+ states [59, 62]. For consistency the branching ratios reported in Ref. [62] were used in the analysis, however one should note that the intensity of the $5_1^- \rightarrow 5_1^+$ transition reported in Ref. [59] ($3.2(8)$) is about two times lower than that adopted in Table 5.2.

- Only two transitions depopulating **the 2_5^+ level at 2630 keV** are reported in Ref. [59] (to the ground state and to the first excited 2^+ state). In contrast, in Ref. [62], three additional transitions were observed (to the 0_2^+, 2_2^+ and 0_3^+ states). The latter two were also confirmed by Ref. [61].

- According to the ENSDF database, **the state at 2718 keV** decays solely by a transition to the 2_1^+ state. However in Refs. [61, 62] two additional weak branches are observed, namely to the 3_1^- and 2_2^+ states. They were included in the current analysis.

- Finally **the $1^{(-)}$ state at 2825 keV** decays by three transitions - to the ground state and to the first excited 0^+ and 2^+ states - as communicated

in Ref. [62], in contrast to Refs. [59, 61], where only the transition to the 0_1^+ state is reported.

5.4.3 Transition multipolarities and mixing ratios

The importance of a specific γ-ray transition in the population and decay processes depends on many factors, among which is their type (σ) - electric or magnetic - and their multipolarity (λ). Those for ^{106}Cd have been investigated in the past using multiple experimental techniques, in particular γ-ray angular distributions and γ-γ angular correlations [78]. Comparing the work of A. Linnemann [60, 61] and the evaluated data in Ref. [59] a set of multipolarities $\sigma\lambda$ was adopted in the current analysis, which is summarized in the last column of Table 5.2. Most of the adopted multipolarities are taken from the ENSDF database with a few exceptions - for the $4_3^+ \rightarrow 2_1^+$, $(2^+, 3^+, 4^+) \rightarrow 2_2^+$ and $1^{(-)} \rightarrow 0_1^+$ transitions - taken from Refs. [60, 61].

As discussed in the previous subsection, for some states a certain spin-parity had to be adopted due to lack of information in the literature (these states are marked with asterisks in Table 5.1). This implies making assumptions also for the multipolarities of the transitions depopulating those states (which are marked with double daggers in Table 5.2). For simplicity, an $E2$ multipolarity was adopted for the transitions originating from the states at 2254, 2486, 2711 and 2718 keV, with the exception of the $2^+, 3 \rightarrow 3_1^-$ transition, where an $E1$ type was adopted in line with the selection rules. An $E1$ multipolarity was adopted also for the transitions depopulating the $1^{(-)}$ state.

For the $M1 + E2$ transitions, mixing ratios ($\delta(E2/M1)$) are important constraints of the the analysis. The adopted values are summarized in Table 5.3. For consistency, the values from the ENSDF database [59] were used, with a few exceptions. More specifically, a discrepancy was found in the literature for the mixing ratios of the transitions depopulating the 5_1^+ state [59]. Arbitrarily, the $\delta(E2/M1)$ reported in Ref. [79] were adopted in the analysis. They were obtained from a γ-ray angular distribution analysis following the ^{96}Mo(^{13}C,$3n\gamma$)^{106}Cd reaction.

Table 5.3 – Mixing ratios in ^{106}Cd used in the analysis with corresponding references. Alternative solutions are presented in the last column. More details are given in the text.

I_i^π	I_f^π	$\delta(E2/M1)$		Alternative δ	
2_2^+	2_1^+	$-1.44(11)$	[59]	$-1.53(14)$	[61]
2_4^+	2_1^+	$+0.312(33)$	[61]	$+2.5(2)$	[59]
2_5^+	2_1^+	$-0.11(4)$	[59]	$-0.126(50)$	[61]
4_2^+	4_1^+	$-0.314(22)$	[59]	$-0.36^{+0.44}_{-0.62}$	[61]
4_3^+	4_1^+	$-0.17(4)$	[59]	$-0.14(11)$	[61]
5_1^+	4_1^+	$-0.18(5)$	[79]	$-0.24(19)$, $-0.03(5)$ or -5.4^{+21}_{-12}	[59]
5_1^+	4_2^+	$-0.58(12)$	[79]	$-0.27(4)$ or $-0.57(12)$	[59]

As can be seen in Table 5.3, the results obtained in Ref. [61] are in a very good agreement with those reported in Ref. [59], with the only exception being the mixing ratio of the $2_4^+ \rightarrow 2_1^+$ transition. The value reported in Ref. [61] was preferred over the evaluated one. This choice is justified later in Section 6.1. Finally, for some transitions, due to lack of literature data for the multipolarity or mixing ratio, assumptions had to be made (which are marked with asterisks in Table 5.2). More specifically, for the $2_4^+ \rightarrow 2_2^+$ and $2_5^+ \rightarrow 2_2^+$ transitions a pure $E2$ character was adopted (although following the selection rules, those transitions can be of a mixed $M1 + E2$ character) and the $5_2^- \rightarrow 4_1^+$ transition was assumed to have an $E1$ character.

5.4.4 Lifetimes of excited nuclear states

Lifetimes of excited states in ^{106}Cd were previously measured using various techniques - the RDDS method in Ref. [50,65], direct timing [80] and Doppler-Shift Attenuation Method (DSAM [81]) following inelastic neutron scattering [60, 61]. Additionally, they were indirectly deduced from matrix elements obtained via safe Coulomb excitation in Refs. [71–75]. These literature sources were reviewed to select a set of lifetimes τ to be used in the current analysis. The adopted values are given in Table 5.1. The lifetimes marked with daggers in Table 5.1 – of the 2_1^+, 4_1^+, 2_2^+, 0_2^+, $(2^+, 3^+, 4^+)$ and 6_2^+ states - are calculated as a weighted average of the values reported in the references given in the fourth column. The averaging was performed following the general policies of Nuclear Data Sheets [82]:

$$\overline{\tau} = \sum_{n=1}^{N} w_i \tau_i, \tag{5.1}$$

where w_i is the weight of each of the N measurements τ_i, equal to $1/(\sigma\tau_i)^2$. The uncertainty of the averaged value is taken as the larger of the values given by Formulas 5.2 and 5.3:

$$\sigma(\overline{\tau}) = \sqrt{\sum_{n=1}^{N} w_i}, \tag{5.2}$$

$$\sigma(\overline{\tau}) = \sqrt{\sum_{n=1}^{N} w_i \sum_{n=1}^{N} \frac{w_i(\overline{\tau} - \tau_i)^2}{N-1}}. \tag{5.3}$$

An alternative lifetime measurement (not taken into account in the averaging) is presented in the last column of Table 5.1. Those will be commented on in the following.

- **The lifetime of the 2_1^+ state** is used for normalization of the cross sections in the present analysis, which will be discussed in Section 5.7.3. The $\tau(2_1^+)$ values, resulting from the two variants of the RDDS data analysis applied to the present dataset, were reported in Refs. [50, 65]. They were averaged

to obtain the value included in the analysis. Additionally, the $\langle 0_1^+||E2||2_1^+\rangle$ ME was measured in a number of previous Coulomb-excitation experiments [72–75]. The weighted average of 2_1^+ lifetimes deduced from these matrix elements is listed in Table 5.1 as an alternative solution.

- **The lifetime of the 4_1^+ state** obtained from the current data set using the RDDS method is $1.4(2)$ ps [50]. It is adopted in the present analysis. The evaluated $\tau(4_1^+)$ in ENSDF is $1.26(16)$ ps, obtained from a safe Coulomb-excitation study [72]. Two more recent safe Coulomb-excitation studies reported values with improved uncertainties [71, 75]. The weighted average of the lifetimes, calculated using all reported Coulomb-excitation results, yielded $\tau = 1.40(5)$ ps and is given as an alternative value of $\tau(4_1^+)$.

- The results for **the lifetime of the 2_2^+ state**, obtained by applying the RDDS method to the current data set [50], and those reported in Ref. [60], obtained with the DSAM technique, were averaged and adopted in the analysis. Alternatively, from the results of the Coulomb-excitation studies [71, 72, 75] one can calculate $\tau(2_2^+) = 0.48(3)$, which is in a perfect agreement with the direct lifetime measurement.

- As already mentioned in Ref. [50] for **the lifetime of the 4_2^+ state** there are conflicting values in the literature. The result from the RDDS measurement based on the current data set ($\tau = 4.1(7)$ ps) is consistent with the limit given in Ref. [61] ($\tau > 1$ ps), but not with the limit given in Ref. [76] ($\tau < 2.9$ ps). It should be noted that the experimental branching ratios for this level from previous studies are also discrepant, as presented in Section 5.4.2.

- Only **a lower limit of $\tau(0_3^+)$** was previously obtained via DSAM [61]. This limit is consistent with the observation of both shifted and unshifted components of the 1511-keV peak in the present data (Section 4.3.1). Unfortunately, the collected statistics is insufficient to perform an RDDS analysis. An alternative value is calculated from a $\langle 0_3^+||E2||2_1^+\rangle$ matrix element obtained via Coulomb excitation [71].

- **The lifetime of the state at 2254 keV** is taken from Ref. [61] and is consistent with the observation of both shifted and unshifted components of the corresponding γ-ray peak (Section 4.3.1). Unfortunately, the positioning of the peak of interest on the background of the $2_1^+ \rightarrow 0_1^+$ peak from ^{92}Mo hinders the extraction of $\tau(2^+, 3^+)$ via RDDS.

- The first **measurement of $\tau(4_3^+)$** via RDDS is reported in the work of M. Siciliano [50] ($\tau = 1.1(1)$ ps). However, using DSAM, a limit of this

lifetime was obtained previously ($\tau < 0.36$ ps) [61], which is inconsistent with the adopted value.

- **The lifetime of the 5_1^+ state**, $\tau(5_1^+) = 0.87(29)$ ns, was taken from Ref. [59]. It is too long to be measured using the RDDS method, thus the previous measurement could not be confirmed using the present data set. Surprisingly though, if a γ-ray energy gate is set on the 226-keV transition depopulating the 5_1^+ state, both shifted and unshifted components are observed in the decay of some of the states fed by the 226-keV line. This is incompatible with the long lifetime of the 5_1^+ state - since its decay is expected to happen after the degrader, the states fed by it should also decay after the degrader. This suggests that the 226-keV γ ray may be due at least in part to another transition, so far unobserved, originating from a decay of a short-lived state. This will be further discussed in Section 6.2.

- **The lifetimes of the 3_1^-, 2_4^+ and 5_2^- states** were taken from the DSAM study of Ref. [61] and are fully consistent with the limits adopted in Ref. [50]. Those limits originate from the observation of only shifted components of the corresponding γ-ray peaks, suggesting a lifetime shorter than the capabilities of the RDDS technique.

- **The lifetime of the $2^+, 3^+, 4^+$ state at 2486 keV** was measured for the first time in the RDDS study based on the present data set [50]. The obtained value is consistent with a limit deduced using the DSAM technique [61].

- Only **an upper limit of the 6_1^+ level lifetime** was obtained from the current data set using RDDS due to an unresolved feeding contribution, suggested by the $6_1^+ \rightarrow 4_1^+$ decay curve [50]. A lower limit of $\tau(6_1^+)$ was obtained via DSAM in Ref. [61].

- **The lifetime of the 6_2^+ state** obtained via RDDS from the current data set [50] is at odds with the previous lifetime measurements. The DSAM study of Ref. [61] suggests a much shorter lifetime, as do two recent safe Coulomb-excitation studies [71, 75].

- **The $\tau(2_5^+)$** obtained via DSAM [61] using the most intense decay branch ($2_5^+ \rightarrow 2_1^+$) is $0.19(3)$ ps. The authors also report a longer alternative value deduced using a weaker decay branch ($2_5^+ \rightarrow 0_1^+$). Both results are consistent with the observation in the present data of only the shifted component of the $2_5^+ \rightarrow 2_1^+$ transition (Section 4.3.1).

- **The lifetimes of the states at 2711, 2718 and 2825 keV** were obtained using the DSAM technique [60, 61]. Based on the present observation

of only shifted components of the depopulating γ-ray transitions of those levels (see Section 4.3.1), it was concluded that they have short lifetimes outside of the sensitivity range of the RDDS technique. Furthermore, even though these states were not previously considered in the work of M. Siciliano [50], one can apply to them the same upper lifetime limit, $\tau < 0.3$ ps, that Ref. [50] assigned to those for which no unshifted components were observed in the decay.

5.4.5 Diagonal matrix elements

In Coulomb excitation the population and decay of the nuclear states is governed by a set of transitional and diagonal matrix elements of the electromagnetic operator, as explained in Section 3.2. Although diagonal matrix elements have a limited influence on the excitation cross sections, especially at small scattering angles (as in the present case), they should be considered in the analysis. A summary of the diagonal matrix elements adopted in the present analysis is given in Table 5.4. They are weighted averages of the results from Refs. [71, 73, 75] as discussed in the following. Formula 5.1, adapted for the diagonal matrix elements, was used for the averaging and the corresponding uncertainties were calculated via Formula 5.2 or 5.3.

As can be seen in Table 5.4, the value obtained for the 4_1^+ state in Ref. [75] is much larger than the one reported in Ref. [71], although they are consistent within their large uncertainties. The adopted $\langle 4_1^+||E2||4_1^+\rangle$ and $\langle 2_1^+||E2||2_1^+\rangle$ values are very similar. Only one measurement is reported for the 6_2^+ state [75]. Finally, the weighted average for the 2_2^+ state is dominated by the value communicated in Ref. [75], which has a much smaller uncertainty compared to the one reported in Ref. [71].

Table 5.4 – The adopted diagonal $E2$ matrix elements (weighted averages of available literature data) together with their values reported in Refs. [71, 73, 75].

$\langle I_i^\pi\|\|E2\|\|I_f^\pi\rangle$	Ref. [71] $[eb]$	Ref. [73] $[eb]$	Ref. [75] $[eb]$	Adopted $[eb]$
$\langle 2_1^+\|\|E2\|\|2_1^+\rangle$	$-0.38(17)$	$-0.37(11)$	$-0.25(5)$	$-0.28(4)$
$\langle 4_1^+\|\|E2\|\|4_1^+\rangle$	$-0.15(18)$	–	$-0.52(24)$	$-0.28(18)$
$\langle 6_2^+\|\|E2\|\|6_2^+\rangle$	–	–	$-1.3(8)$	$-1.3(8)$
$\langle 2_2^+\|\|E2\|\|2_2^+\rangle$	$0.81(38)$	–	$1.33(6)$	$1.32(8)$

The effects induced by the diagonal matrix elements on the experimental excitation cross sections obtained in this study will be addressed in Section 6.2.3.

5.4.6 Negative-parity states

As already discussed in Sections 5.4.2 and 5.4.3, for the negative-parity states a population path via $E3$ transitions has to be included. As shown in Fig. 5.1 one-step excitation from the ground state is assumed for the 3_1^- state, while the $5_{1,2}^-$ and

$1^{(-)}$ states are populated from below in a two-step excitation via the intermediate 2_1^+ state. The $\langle I_i^\pi||E3||I_f^\pi\rangle$ matrix elements are in general rather scarce in the literature. The $\langle 0_1^+||E3||3_1^-\rangle$ values obtained in two previous measurements are listed in Table 5.5. For the remaining negative-parity states assumptions have to be made in order to apply the approach proposed in Section 5.2. However, using the method described in Section 5.3 it is possible to obtain for the first time an evaluation of those matrix elements or at least provide their upper limits.

Table 5.5 – $\langle 0_1^+||E3||3_1^-\rangle$ values obtained in the previous measurements.

$\langle I_i^\pi||E3||I_f^\pi\rangle$	Ref. [75] $[e\mathrm{b}^{3/2}]$	Ref. [83] $[e\mathrm{b}^{3/2}]$
$\langle 0_1^+||E3||3_1^-\rangle$	$0.28(14)$	$0.40(5)$

5.5 Calculation of matrix elements from spectroscopic data

The reduced matrix elements of interest to the present analysis were calculated from the adopted spectroscopic data listed in Section 5.4 by applying formulas provided in Section 5.5.1. The error estimation procedure is described in Section 5.5.2.

5.5.1 Formalism

The reduced transition probability $B(\sigma L)$ * for a nucleus to undergo a transition of a particular multipolarity σL from an initial state I_i to a final state I_f with the emission of a γ ray of energy E_γ is related to the partial lifetime $\tau^{\gamma_j}(\sigma L)$ via [84]:

$$B(\sigma\lambda(I_i \to I_f)) = \frac{L\hbar[(2L+1)!!]^2}{8\pi\tau^{\gamma_j}(\sigma L)}\left(\frac{\hbar c}{E_\gamma}\right)^{2L+1}. \tag{5.4}$$

The unit of the transition probability depends on the transition type σ and multipolarity L as follows - $B(EL)$ values are given in $[e^2\mathrm{b}^L]$, while $B(ML)$ values in $[\mu_N^2\mathrm{b}^{L-1}]$, where μ_N is the nuclear magneton. The index j denotes a particular branch in the decay of the I_i state.

The reduced transition probabilities $B(\sigma L)$ are related to the reduced matrix elements via [2]:

$$B(\sigma L(I_i \to I_f)) = \frac{1}{2I_i+1}\left|\langle I_f||\sigma L||I_i\rangle\right|^2. \tag{5.5}$$

As each $\langle I_f||\sigma L||I_i\rangle$ matrix element enters Formula 5.5 squared, it is not possible to infer the sign of a ME from a lifetime measurement. Therefore, from now on the absolute values of the matrix elements will be used, unless specified otherwise.

If the nucleus decays via several branches, the partial lifetime for the j-th branch, $\tau^{\gamma_j}(\sigma L)$, is proportional to the lifetime of the initial decaying state $\tau(I_i)$

*. In this Section, to avoid confusion with the decay constant λ, the multipole order is denoted by L.

with a coefficient $1/\varepsilon(\gamma_j)$. The $\varepsilon(\gamma_j)$ value is defined as the fraction of the decay of I_i which proceeds via the particular γ_j transition:

$$\varepsilon(\gamma_j) = \frac{\lambda^{\gamma_j}}{\lambda^{TOT}} = \frac{\lambda^{\gamma_j}}{\sum_i (1+\alpha_i)\lambda^{\gamma_i}}, \tag{5.6}$$

where λ^{γ_j} is the relative partial decay constant for the γ_j transition related to the partial lifetime via:

$$\lambda^{\gamma_j} = 1/\tau^{\gamma_j}. \tag{5.7}$$

Apart from the emission of a γ ray, the nucleus can lower its energy also via internal conversion. In this process the excess energy is transferred to an atomic electron. The decay constant for internal conversion is directly proportional to the decay constant for the γ_j transition through the conversion coefficient α_j. Thus, the total decay constant for a j-th decay branch, including both γ-ray and conversion electron (CE) emission, is $(1+\alpha_j)\lambda\gamma_j$. Considering this, the right side of Formula 5.6 is obtained, where the summing is over all possible decay branches i. On the other hand, $\lambda\gamma_j$ is related to the total decay constant for the j branch via $\lambda^{(\gamma+CE)_j}/(1+\alpha_j)$ thus Formula 5.6 can be modified to:

$$\varepsilon(\gamma_j) = \frac{\lambda^{\gamma_j}}{\lambda^{TOT}} = \frac{\lambda^{(\gamma+CE)_j}}{(1+\alpha_j)\lambda^{TOT}} = \frac{BR^{(\gamma+CE)_j}}{1+\alpha_j}, \tag{5.8}$$

where $BR^{(\gamma+CE)_j}$ is the total branching ratio for the j-th transition.

As discussed in Section 5.4.3, certain excited nuclear states decay by competing γ-ray transitions with similar strengths, but different σL, e.g. $M1+E2$. Thus, part of the γ_j branch will correspond to a transition with multipolarity L, while another part - with multipolarity $L+1$. This will result in a modification of the partial lifetime τ^{γ_j} with a coefficient $(1+\delta^2)$ for the L and $(1+\delta^2)/\delta^2$ for the $L+1$ component of the transition. The mixing ratio δ is given by the ratio of the transition strengths of the $L+1$ and L components. For example, for a mixed $M1+E2$ transition, δ can be expressed using the reduced matrix elements via:

$$\delta = 0.835 E_\gamma[MeV] \frac{\langle I_f||E2||I_i\rangle}{\langle I_f||M1||I_i\rangle}. \tag{5.9}$$

By combining Formulas 5.4, 5.5 and 5.8 one can obtain the general formula for the squared reduced matrix elements related to the $I_i \to I_f$ transition:

$$\langle I_f||^E_M L||I_i\rangle^2 = \frac{L\hbar[(2L+1)!!]^2}{8\pi\tau(I_i)(1+\alpha)} \frac{(2I_i+1)BR}{\delta^2+1} \left(\frac{\hbar c}{E_\gamma}\right)^{2L+1}. \tag{5.10}$$

For the particular cases of $E1$, $E2$ and $M1$ matrix elements relevant for the present analysis, using E_γ expressed in keV and τ in seconds, Formula 5.10 can be reduced as following:

- **E1 transitions**: the dependence on the mixing ratio δ is omitted as $E1$ transitions rarely have a meaningful $M2$ admixture and as they practically have no influence on the Coulomb-excitation process, they were not considered in the present analysis. The $\langle I_f||E1||I_i\rangle$ matrix element is expressed in units of $e\mathrm{fm}$.

$$\langle I_f||E1||I_i\rangle = \sqrt{\frac{6.29\ BR\ (2I_i+1)\ 10^{-9}}{\tau E_\gamma^3\ (1+\alpha)}} \tag{5.11}$$

- **E2 transitions**: the dependence on the energy of the γ ray (E_γ) is stronger compared to the $E1$ case. $M1$ transitions are often mixed with $E2$ ones, thus the $\delta^2/(1+\delta^2)$ term is added in the formula. If the transition has a very large mixing ratio, this coefficient approaches 1, as in the case of a pure electric quadrupole transition. The $\langle I_f||E2||I_i\rangle$ matrix element is expressed in units of $e\mathrm{fm}^2$.

$$\langle I_f||E2||I_i\rangle = \sqrt{\frac{81.64\ BR\ (2I_i+1)\ \delta^2}{\tau E_\gamma^5\ (1+\alpha)(1+\delta^2)}} \tag{5.12}$$

- **M1 transitions**: if a $\langle I_f||M1||I_i\rangle$ matrix element is much larger than the $E2$ matrix element for the same transition, the mixing ratio approaches 0 and the term $1/(1+\delta^2)$ becomes equal to 1. The $\langle I_f||M1||I_i\rangle$ matrix element is expressed in units of μ_N.

$$\langle I_f||M1||I_i\rangle = \sqrt{\frac{5.69\ BR\ (2I_i+1)\ 10^{-5}}{\tau E_\gamma^3\ (1+\alpha)(1+\delta^2)}} \tag{5.13}$$

Using Formulas 5.11-5.13, a set of reduced matrix elements relevant for the Coulomb-excitation analysis was calculated from the spectroscopic data summarized in Tables 5.1-5.3.

5.5.2 Error estimation

If the relative uncertainties of all observables in Formula 5.10 were smaller than 15%, standard error propagation was used. For example, the relative uncertainty of an $E2$ matrix element, calculated using Formula 5.12, can be estimated using:

$$\frac{\sigma(\langle I_f||E2||I_i\rangle)}{\langle I_f||E2||I_i\rangle} = \frac{1}{2}\sqrt{\left(\frac{\sigma(BR)}{BR}\right)^2 + \left(\frac{\sigma(\tau)}{\tau}\right)^2 + \left(\frac{5\sigma(E_\gamma)}{E_\gamma}\right)^2 + \left(\frac{\sigma(\alpha)}{1+\alpha}\right)^2}, \tag{5.14}$$

where $\sigma(BR)$, $\sigma(\tau)$, $\sigma(E_\gamma)$ and $\sigma(\alpha)$ are the absolute uncertainties of the branching ratio, lifetime of the initial state, energy of the γ-ray transition and the conversion coefficient, respectively. If the transition is mixed, an additional term $\left(\frac{2\sigma(\delta)}{\delta(1+\delta^2)}\right)^2$ has to be added in the summation under the square root to account

for the uncertainty of the mixing ratio. The formula needed to calculate the uncertainty of a $M1$ matrix element is similar to Formula 5.14 with the coefficient in front of the relative uncertainty of E_γ changed to 3 and a term $\left(\frac{2\delta\sigma(\delta)}{1+\delta^2}\right)^2$ added.

If any of the relative uncertainties of the lifetime, E_γ, α, branching or mixing ratio were larger than 15%, a different procedure for the error estimation was adopted. The largest and the smallest possible matrix elements were calculated, considering the uncertainties of the spectroscopic data. The differences between the adopted matrix element and these two limits were taken to be its uncertainty interval. Usually such strategy results in asymmetric error bars, larger than those from a standard error propagation. The reduced matrix elements and their uncertainties, calculated following the described procedure, are summarized in the second columns ("Literature") of Tables 5.6-5.9.

Table 5.6 – Reduced transitional $E2$ matrix elements, corresponding to the transitions observed in the present experiment. The MEs calculated using the spectroscopic information summarized in Section 5.4 are given in the second column. They are compared to those obtained by fitting the experimental γ-ray yields using GOSIA (third column), as explained in Section 5.3. Note that the $\langle 2_1^+||E2||0_1^+\rangle$ matrix element is used for normalization, therefore the fitted ME is not a new result of the present study and consequently its value is given without uncertainty. The MEs marked with a dagger have a relative sign extracted from the current data set. Those marked with an asterisk were chosen to be positive, as discussed in Section 6.2.1. There was no sensitivity to the signs of the remaining MEs. The difference between the absolute values of the MEs, defined as the absolute difference between the literature and fitted ME, divided by the literature value, is given in the last column. The sign illustrates if the fitted ME is smaller (-) or larger (+) with respect to the literature one.

$\langle I_i^\pi\|\|E2\|\|I_f^\pi\rangle$	Literature $[eb]$	Fitted $[eb]$	Difference $[\%]$
$\langle 2_1^+\|\|E2\|\|0_1^+\rangle$	$0.622(5)$	$+0.623$ *	$-$
$\langle 4_1^+\|\|E2\|\|2_1^+\rangle$	$1.05(8)$	$+1.12(3)$ *	$+6.7$
$\langle 2_2^+\|\|E2\|\|0_1^+\rangle$	$0.168(7)$	$+0.157^{+0.006}_{-0.003}$ *	-6.5
$\langle 2_2^+\|\|E2\|\|2_1^+\rangle$	$0.42(2)$	$+0.41^{+0.02}_{-0.01}$ †	-2.4
$\langle 0_2^+\|\|E2\|\|2_1^+\rangle$	$0.173(7)$	$+0.125^{+0.028}_{-0.008}$ *	-28
$\langle 0_3^+\|\|E2\|\|2_1^+\rangle$	< 0.069	$+0.024^{+0.006}_{-0.001}$ *	$-$
$\langle 4_2^+\|\|E2\|\|2_1^+\rangle$	$0.093^{+0.011}_{-0.009}$	$+0.09(1)$ †	-3.2
$\langle 4_2^+\|\|E2\|\|4_1^+\rangle$	$0.35^{+0.06}_{-0.05}$	$0.21^{+0.03}_{-0.02}$	-40
$\langle 4_3^+\|\|E2\|\|4_1^+\rangle$	$0.22(6)$	$0.6(1)$	$+173$
$\langle 5_1^+\|\|E2\|\|4_2^+\rangle$	$0.55^{+0.23}_{-0.16}$	$5.5^{+0.7}_{-5.0}$	$-$
$\langle 2^+, 3^+, 4^+\|\|E2\|\|2_1^+\rangle$	$0.095(4)$	$+0.100(4)$ *	$+5.3$
$\langle (2^+, 3^+)\|\|E2\|\|2_1^+\rangle$	$0.25^{+0.06}_{-0.04}$	$+0.246^{+0.014}_{-0.010}$ *	0
$\langle 6_1^+\|\|E2\|\|4_1^+\rangle$	> 0.73	$+1.27^{+0.03}_{-0.18}$ *	$-$

Table 5.6 – Reduced transitional $E2$ matrix elements, corresponding to the transitions observed in the present experiment - continued.

$\langle 6_2^+ \| E2 \| 4_1^+ \rangle$	$0.91(6)$	$+1.45^{+0.06}_{-0.04}$ *	$+59$
$\langle 2_4^+ \| E2 \| 2_1^+ \rangle$	$0.115(13)$	$+0.11(2)$ *	-4.3
$\langle 2_5^+ \| E2 \| 2_1^+ \rangle$	$0.03(1)$	$0.018^{+0.009}_{-0.008}$	-40
$\langle 2^+, 3 \| E2 \| 2_1^+ \rangle$	$0.15^{+0.03}_{-0.02}$	$+0.16(1)$ *	$+6.7$
$\langle 2 - 6 \| E2 \| 4_1^+ \rangle$	$0.98^{+0.15}_{-0.13}$	$+0.64(5)$ *	-35

Table 5.7 – Same as Table 5.6, but for the reduced transitional $E2$ matrix elements, corresponding to the $E2$ transitions, which were not observed directly in the present experimental data. Without additional spectroscopic information (branching ratios), the "fitted" MEs could not be determined from the present data set. The MEs marked with a dagger have a relative sign extracted from the current data set, while those marked with an asterisk were chosen to be positive, as discussed in Section 6.2.1.

$\langle I_i^\pi \| E2 \| I_f^\pi \rangle$	Literature $[e\mathrm{b}]$	Fitted $[e\mathrm{b}]$	Difference $[\%]$
$\langle 0_3^+ \| E2 \| 2_2^+ \rangle$	< 0.99	$+0.35^{+0.08}_{-0.02}$ †	$-$
$\langle 4_2^+ \| E2 \| 2_2^+ \rangle$	$0.64^{+0.09}_{-0.07}$	$+0.37^{+0.05}_{-0.03}$ *	-42
$\langle 4_3^+ \| E2 \| 2_1^+ \rangle$	$0.071^{+0.006}_{-0.005}$	$+0.18(1)$ *	$+154$
$\langle 5_1^+ \| E2 \| 4_1^+ \rangle$	$0.005^{+0.003}_{-0.002}$	$0.046^{+0.012}_{-0.042}$	$-$
$\langle 2^+, 3^+, 4^+ \| E2 \| 4_1^+ \rangle$	$0.285(12)$	$0.30(2)$	$+5.3$
$\langle 2^+, 3^+, 4^+ \| E2 \| 2_2^+ \rangle$	$0.33(2)$	$+0.34(2)$ †	$+3$
$\langle 2^+, 3^+, 4^+ \| E2 \| 4_2^+ \rangle$	$1.02(6)$	$1.07(7)$	$+5$
$\langle 2_4^+ \| E2 \| 0_2^+ \rangle$	$0.19(4)$	$0.18^{+0.05}_{-0.06}$	-5.3
$\langle 2_4^+ \| E2 \| 2_2^+ \rangle$	$0.27(3)$	$+0.25^{+0.05}_{-0.03}$ †	-7.4
$\langle 2_5^+ \| E2 \| 0_1^+ \rangle$	$0.032^{+0.004}_{-0.003}$	$+0.022(4)$ †	-31
$\langle 2_5^+ \| E2 \| 0_2^+ \rangle$	$0.16^{+0.03}_{-0.02}$	$0.105^{+0.027}_{-0.024}$	-34
$\langle 2_5^+ \| E2 \| 0_3^+ \rangle$	$0.56^{+0.10}_{-0.09}$	$+0.38^{+0.10}_{-0.09}$ *	-32
$\langle 2_5^+ \| E2 \| 2_2^+ \rangle$	$0.51^{+0.06}_{-0.05}$	$0.34^{+0.07}_{-0.06}$	-33
$\langle 2^+, 3 \| E2 \| 2_2^+ \rangle$	$0.39^{+0.14}_{-0.13}$	$+0.42^{+0.05}_{-0.07}$ †	$+7.7$

The reduced transitional $E2$ matrix elements between low-lying states in ^{106}Cd, corresponding to the transitions that were directly observed in the present experiment (the $E2$ transitions marked in red in Fig. 5.1) are summarized in Table 5.6. The states are identified by their spin-parities in accordance with Table 5.2. Table 5.7 lists the transitional $E2$ MEs corresponding to the transitions, which were not directly observed in the present data set (plotted in black in Fig. 5.1), but the relevant branching ratios are known (Table 5.2). The reduced $M1$ matrix elements are summarized in Table 5.8. They were obtained using the literature values of the

mixing ratios listed in Table 5.3. Finally, the reduced $E1$ matrix elements, as well as the $E2$ MEs for the decay of the buffer state 8_1^+, are given in Table 5.9.

Table 5.8 – Same as Table 5.6, but for reduced transitional $M1$ matrix elements. Without additional spectroscopic information on mixing ratios, the "fitted" MEs could not be obtained from the present data set. The fitted MEs marked with a dagger have a relative sign extracted from the present analysis.

$\langle I_i^\pi \Vert M1 \Vert I_f^\pi \rangle$	Literature	Fitted	Difference
	$[\mu_N]$	$[\mu_N]$	[%]
$\langle 2_2^+ \Vert M1 \Vert 2_1^+ \rangle$	$-0.27(2)$	$-0.26^{+0.01}_{-0.02}$ †	-3.7
$\langle 4_2^+ \Vert M1 \Vert 4_1^+ \rangle$	$-0.57^{+0.05}_{-0.07}$	$-0.33^{+0.02}_{-0.04}$	-42
$\langle 4_3^+ \Vert M1 \Vert 4_1^+ \rangle$	$-0.87(5)$	$-2.18^{+0.13}_{-0.16}$	151
$\langle 5_1^+ \Vert M1 \Vert 4_1^+ \rangle$	$-0.018^{+0.003}_{-0.005}$	$-0.176^{+0.159}_{-0.006}$	–
$\langle 5_1^+ \Vert M1 \Vert 4_2^+ \rangle$	$-0.18^{+0.03}_{-0.05}$	$-1.80^{1.63}_{-0.09}$	–
$\langle 2_4^+ \Vert M1 \Vert 2_1^+ \rangle$	$0.59(4)$	$+0.56^{+0.11}_{-0.07}$ *	-5.1
$\langle 2_5^+ \Vert M1 \Vert 2_1^+ \rangle$	$-0.40^{+0.03}_{-0.04}$	$-0.27(5)$	-33

Table 5.9 – The reduced $E1$ matrix elements calculated using the spectroscopic information provided in Section 5.4 (second column) compared with the set of MEs obtained from a fit to the experimental γ-ray yields using GOSIA (third column). These matrix elements could not be determined from the present data set and have a limited influence on the values of other matrix elements. The $E2$ MEs related to the decay of the buffer state 8_1^+ are also given. To avoid an impression that they are new results of the present analysis, the values of these matrix elements adopted in the GOSIA fit are quoted without uncertainties.

$\langle I_i^\pi \Vert E1 \Vert I_f^\pi \rangle$	Literature	Fitted
	$[e\mathrm{b}^{1/2}]$	$[e\mathrm{b}^{1/2}]$
$\langle 1 \Vert E1 \Vert 0_1^+ \rangle$	$0.0052(1)$	0.0052
$\langle 1 \Vert E1 \Vert 2_1^+ \rangle$	$0.0013(1)$	0.0013
$\langle 1 \Vert E1 \Vert 0_2^+ \rangle$	$0.0054(2)$	0.0054
$\langle 3_1^- \Vert E1 \Vert 2_1^+ \rangle$	$0.0064^{+0.0005}_{-0.0004}$	0.0064
$\langle 5_1^- \Vert E1 \Vert 4_1^+ \rangle$	$0.00103(4)$	0.00103
$\langle 5_1^- \Vert E1 \Vert 4_2^+ \rangle$	$0.0067(2)$	0.0067
$\langle 5_1^- \Vert E1 \Vert 5_1^+ \rangle$	$0.0038(3)$	0.0038
$\langle 5_2^- \Vert E1 \Vert 4_1^+ \rangle$	$0.011(1)$	0.010
$\langle 2^+, 3 \Vert E1 \Vert 3_1^- \rangle$	$0.010^{+0.004}_{-0.003}$	0.010
$\langle I_i^\pi \Vert E2 \Vert I_f^\pi \rangle$	Literature	Fitted
	$[e\mathrm{b}]$	$[e\mathrm{b}]$
$\langle 8_1^+ \Vert E2 \Vert 6_1^+ \rangle$	$0.17^{+0.06}_{-0.03}$	0.174
$\langle 8_1^+ \Vert E2 \Vert 6_2^+ \rangle$	$0.14^{+0.05}_{-0.03}$	0.145

5.6 FRESCO calculations

Following the approach proposed in Section 5.1, an attempt was made to qualitatively describe the experimental excitation cross sections affected by the nuclear interaction using the coupled-channel code FRESCO [36]. FRESCO is a general-purpose reaction code based on the coupled-channel equations described in Section 3.4. Considering the qualitative character of the task, only a subset of the excited states in ^{106}Cd populated in the present study was included in the FRESCO analysis, as described in Section 5.6.1. The addressed physics problem is described using the namelist format explained in Section 5.6.2. The relevant input files can be found in Appendix A. The global optical potential employed in the study is described in Section 5.6.3. The obtained results are presented and discussed in Section 5.6.4.

5.6.1 Physics case

Using FRESCO, it is possible to calculate absolute cross sections for elastic and inelastic scattering involving both Coulomb and nuclear interaction acting between the colliding nuclei. Usually, an effective optical potential is employed to describe the processes beyond elastic scattering. The effective potential has both a Coulomb and a nuclear part and is typically obtained empirically. The different channels involved - elastic or inelastic (in which a particular state is excited) - are coupled via the differential equation system given by Formula 3.16. The couplings, Formula 3.17, describe the inner structure of the nucleus and can be taken either from theory of from experiment. However, a main drawback of this approach is often the lack of a reliable optical potential and/or information for the particular Coulomb and nuclear couplings involved.

Considering all of the above and the qualitative character of the present investigation, only a fraction of the level scheme presented in Fig. 5.1 was selected to explore the Coulomb-nuclear interference effects on the population of the low-lying excited states in ^{106}Cd. Namely, the strongly populated 2_1^+, 4_1^+, and 2_2^+ states were included in the analysis, together with the 0_2^+, 4_3^+ and 3_1^- states, as summarized in Fig. 5.3. Although their populations are much lower, the latter three states merit an investigation as the experimentally observed γ-ray intensities in their decay (shown in the insets of Figs. 5.6 B, 5.7 and 5.8 A) exhibit systematic deviations from Coulomb-excitation predictions. Second-order effects, such as simultaneous target and projectile excitation, cannot be considered within FRESCO. Thus, only the ground state of ^{92}Mo was treated in the analysis.

Optimally, all populated states should be included in the coupled-channel analysis. Limiting the number of studied states may introduce systematic deviations. Thus, this study should be viewed as a first approximation of the investigated physics problem.

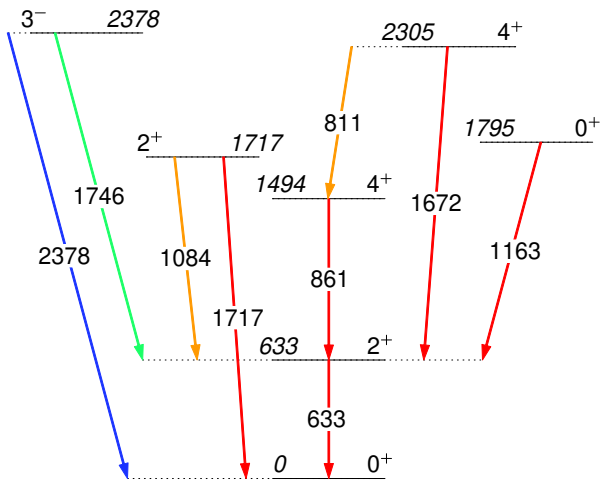

Figure 5.3 – Partial level scheme of ^{106}Cd considered in the FRESCO analysis. The colors of the arrows correspond to the transition multipolarity: $E1$ transitions are presented in green, pure $E2$ ones in red, $E3$ in blue and mixed $E2 + M1$ in orange. Level and transition energies are given in keV.

5.6.2 Preparation of the input file

The FRESCO input file (see Appendix A) starts with a heading that is not directly used in the calculations. It is followed by a "NAMELIST", that marks the beginning of the file and sets the preferred namelist format. The rest of the file is divided into a few sections : &FRESCO, &PARTITION, &STATES, &POT, &OVERLAP, and &COUPLING. The physics problem investigated in this work could be fully described using only the first four namelists, and they will be discussed in more details in the following. More detailed information on the specific parameters included in each namelist can be found in Ref. [36].

- **&FRESCO** - the general numerical parameters that control the calculation are described in this section. Namely, "hcm" (here 0.005 fm) - the step of the integration of the coupled-channel equations, "rmatch" (here 400 fm) - the radius at which the wave function is matched to its asymptotic form (as described in Section 3.4), and "jtmin" (here 0) and "jtmax" (here 5500) - initial and final total angular momentum J, which defines the number of used partial waves. "Rmatch" and "jtmax" should be large enough to adequately describe the safe Coulomb-excitation process at small scattering angles where the central long-range electromagnetic force dominates the process. The considered scattering angular range from "thmin" ($5°$) to "thmax" ($100°$) is also defined in this namelist, together with the angle step "thinc" ($1°$). Those angles are defined in the center-of-mass coordinate system. Another important variable which controls the convergence is "absend" (-1 mb). The calculation is terminated if the absorption in the

elastic channel is smaller than "absend" in calculations for three consecutive values of J. If this parameter is negative, the calculations are performed for the full range from jtmin to jtmax. Several parameters controlling the output are also defined here: "iblock", "smats" and "xstabl". Finally, an essential parameter of the calculation is the beam energy "elab" (here 756.7 MeV) in the laboratory frame. The adopted energy corresponds to the middle of the target (according to calculation with elo [58]).

- **&PARTITION** - this section describes the intrinsic properties of the colliding nuclei, including the mass of the projectile "massp" (106), of the target "masst" (92) and their atomic numbers - "zp" (48) and "zt" (42), respectively. Additionally, the Q-value of the first reaction channel "qval" (0 MeV for elastic scattering) and the number of channels "nex" corresponding to the number of considered states in ^{106}Cd (7) are provided.

- **&STATES** - this namelist defines the pairs of projectile and target states associated with each channel "nex". Within the &PARTITION namelist, the user defines "nex" &STATES namelists, which include the information on the spins - "jp", "jt", parities - "bandp" and "bandt", and energies - "ep", "et" of the coupled states in the projectile and the target, respectively. In each &STATES partition, one pair of projectile and target states is defined. For example, in the elastic channel, both nuclei are in their ground states with ep=et=0, jp=jt=0, and bandp=bandt=$+1$. In the first channel beyond elastic scattering, which corresponds to the population of the first excited state in ^{106}Cd, these parameters are as follows: jp=2, ep=0.633 MeV, and bandp=1, while the target nucleus stays in its ground state. Instead of explicitly defining the energy and spin-parity of the ground state of ^{92}Mo, copyt=1 is used, which automatically copies the previously defined state for the target. The last variable defined here is "cpot", indicating which effective potential governs the excitation and relative motion of the target and projectile in each channel. This variable refers to "kp", which is later defined for each potential explicitly.

- **&POT** - this section specifies the used Coulomb and nuclear potentials. One has to explicitly define the coupling potentials (Formula 3.17) that can be either calculated from experimentally measured transition probabilities or taken from theory, e.g., in the axially-symmetric rigid-rotor model framework. Each potential is labeled with an index "kp", corresponding to "cpot" used in &STATES namelist. All potentials with the same "kp" value are added together to form the total effective potential used in the calculation. Each potential is characterized by "type", "shape" and specific parameters "p$_i$". More details on the potentials used in the present calculation for ^{106}Cd are given in the following section.

5.6.3 Optical potentials in FRESCO

The effective potential used in a FRESCO calculation has both Coulomb and nuclear parts. In the first approximation, the Coulomb component can be assumed as the potential induced by uniformly charged spheres with radii R_T (target) and R_P (projectile). At large distances R it follows that of structureless charges and can be calculated with Formula 5.15 [45]. At distances smaller that the separation distance between the nuclear surfaces ($R_c = R_T + R_P$), the potential can be obtained with Formula 5.16. Uc_0 is a central potential that slowly decreases with the distance between the colliding nuclei, as shown in Fig. 5.4 with the solid blue curve.

$$Uc_0(R) = \begin{cases} \dfrac{e^2 Z_T Z_P}{4\pi\epsilon_0 R} & R > R_c \qquad (5.15) \\ \dfrac{e^2 Z_T Z_P e^2}{8\pi\epsilon_0 R_c}(3 - \dfrac{R^2}{R_c^2}) & R \leq R_c \qquad (5.16) \end{cases}$$

If the nucleus is not spherical, one can expand the Coulomb potential U_c into a series of multipoles as mentioned in Section 3.2. The monopole part corresponds to the potential generated by structureless charges (Formula 5.15), which governs the relative motion of the interacting nuclei. Higher-order multipoles depend on the internal structure of the nucleus and thus are responsible for transitions from one state to another. Within a collective model, excitations of the nucleus can be understood as reorganization of its charge. Those excitations are described by the coupled-channel system, Formula 3.16, where a transition of the nucleus from one state to another results in a redistribution of the flux between the involved channels. For example, for the excitations from the ground state, one can describe the process as shifting a part of the elastic channel flux to a particular inelastic channel. Those processes are controlled by the coupling potentials, which in this case are proportional to the matrix elements of the multipole electromagnetic operator.

Within FRESCO (see Appendix A), the monopole Coulomb potential by default corresponds to TYPE=0 and is always defined in the beginning of the &POT namespace. The mass numbers of the collision partners are provided (ap=106.0 and at=92.0), together with the reduced radius (r_c=1.200), which can be used to calculate the distance between the nuclear centers at touching nuclear surfaces ($r_c CC$, where $CC = A_P^{1/3} + A_T^{1/3}$). In the following, more potentials with TYPE> 0 are defined. First, a TYPE=12 potential is introduced, which corresponds to a deformed projectile nucleus. The parameters "$p1$", "$p2$", and "$p3$" are the strengths of the coupling factors with $E1$, $E2$, or $E3$ multipolarities, respectively. They are explicitly given in different &STEP lists for each two coupled states - final state "ib" with angular momentum I' and initial "ia" with angular momentum I. The state indices follow those defined in section &STATES. Both populating and depopulating transitions are explicitly included in the complete coupled-channel system. The "str" couplings of multipolarity "k"=λ are the reduced transitional

matrix elements $\langle I'||M(E\lambda)||I\rangle$ in units of $e\mathrm{fm}^{\lambda}$, which can be calculated from experimentally obtained transition probabilities $B(E\lambda; I \to I')$ [85]:

$$STR = (-1)^{\frac{I-I'+|I-I'|}{2}} \langle I'||M(E\lambda)||I\rangle = \pm\sqrt{(2I+1)B(E\lambda; I \to I')}. \quad (5.17)$$

The diagonal matrix elements ($I = I'$) can be included in the calculation in a similar way. The transitional matrix elements used in the present analysis were taken from the second columns of Tables 5.6 and 5.7. They were calculated from the measured lifetimes and other spectroscopic information, as explained in Section 5.5. The only exception is the $\langle 0_1^+||E3||3_1^-\rangle$ matrix element, which was taken from the Coulomb-excitation measurement of D. Rhodes [75]. As magnetic couplings cannot be defined within FRESCO, the mixed $4_3^+ \to 4_1^+$ and $2_2^+ \to 2_1^+$ transitions were solely described by their corresponding $E2$ matrix elements. The diagonal matrix elements for the 2_1^+, 4_1^+ and 2_2^+ states were taken from Table 5.4.

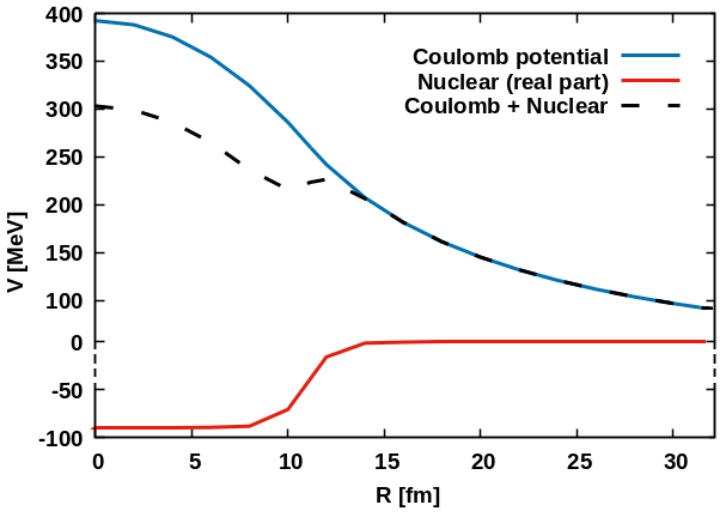

Figure 5.4 – Coulomb potential (in blue) and the real part of the nuclear (Woods-Saxon) potential (in red) as a function of the distance R between the nuclear centers. The effective potential, defined as the sum of the Coulomb and the nuclear potentials, is presented with the black dashed line. The Coulomb barrier of about 220 MeV appears in the effective potential at about 12 fm.

As a next step, the volume nuclear potential (TYPE=1) was defined. The nuclear part of the effective potential is usually modeled within the Woods-Saxon parametrization [45]. The nuclear potential $Un_0(R - R_0)$ between two spherical nuclei, where $R_0 = R_T + R_P$, follows the nuclear density and has a real and an imaginary part. The real part usually enters the description of the elastic scattering process, while the imaginary part accounts for absorption. In FRESCO this parametrization is realized by SHAPE=0, where the volume nuclear potential between two spherical nuclei as a function of the distance R between their centers is given by:

$$Un_0(R) = -\frac{p_1}{1+e^{\frac{R-CCp_2}{p_3}}} - i\frac{p_4}{1+e^{\frac{R-CCp_5}{p_6}}}. \quad (5.18)$$

The parameters p_1, p_2 and p_3 describe the real part of the potential and correspond to the potential depth (V_0), reduced radius and diffuseness, respectively [85]. The equivalent parameters p_4, p_5 and p_6 are used for the imaginary part of the potential. Preferably, these parameters are obtained by fitting experimental data from elastic and inelastic scattering for the investigated nuclei or an analogous system under similar kinematic conditions. If that is not possible, the required parameters can be calculated using global parametrizations, e.g., the parametrization of R. Broglia and A. Winther [86], which is often used to describe systems of heavy colliding partners, as in this particular case. In this parametrization, the depth of the nuclear potential (p_1) can be obtained via:

$$p_1 = V0 = 16\pi\gamma a_v \bar{R}_{TP} \quad [\mathrm{MeV}], \tag{5.19}$$

where the reduced radius $\bar{R}_{TP}$ is given by $R_T R_P/(R_T + R_P)$ and the radii of the projectile and the target (R_P, R_T) can be calculated as $1.2A_i^{1/3} - 0.09$ fm. Thus, parameter p_2 is then defined as $(1.2CC - 0.18)/CC$. The surface tension parameter γ is given by:

$$\gamma = 0.95\left(1 - 1.8\frac{N_P - Z_P}{A_P}\frac{N_T - Z_T}{A_T}\right) \quad [\mathrm{MeV\ fm^{-2}}], \tag{5.20}$$

where A_i, Z_i and N_i are the mass, atomic and neutron numbers of the projectile (P) and the target (T). The diffuseness a_v, which corresponds to p_3, can be calculated using

$$p_3 = a_v = \frac{1}{1.17\left[1 + 0.53\left(\frac{1}{A_P^{1/3}} + \frac{1}{A_T^{1/3}}\right)\right]} \quad [\mathrm{fm}]. \tag{5.21}$$

The real part of the volume nuclear potential, with parameters calculated using Formulas 5.19-5.21 – $V_0 = 89.2$ MeV, $r_c = 1.18$ fm and $a_v = 0.69$ fm – is plotted in Fig. 5.4 with a solid red curve. The sum of the Coulomb and nuclear potentials forms the effective potential presented with the dashed black line.

In addition to the real part, the imaginary part of the nuclear potential has to be provided. There is no clear rule how to handle this task, as the imaginary part describes the absorption channels, which depend in a complicated way on the beam energy and the particularities of the system. Often the same reduced radius and diffuseness as for the real nuclear part are adopted for the imaginary potential, while the potential depth is taken to be a quarter of V_0. This choice is arbitrary, and in general these parameters should be fitted to experimental data.

Similarly to the Coulomb case, if the nucleus is deformed, within a collective model (e.g. rotational), excitations related to the nuclear interaction can be interpreted in terms of changes in the mass distribution of the nucleus. The separation between the target and projectile surfaces will depend on the orientation of the deformed nucleus and so will the nuclear potential $Un_0(R)$. The potential can

be expanded in a multipole series, with the monopole part corresponding to the potential of a spherical nucleus, given by Formula 5.18. Higher-order multipoles result in couplings between different channels (excited nuclear states), which are described by the coupling potentials proportional to the reduced matrix elements of the corresponding deformation length operator δ_λ [45]. Those matrix elements are model dependent and in the current analysis they were calculated from the reduced electromagnetic matrix elements introduced in the definition of the deformed Coulomb potential within the rotational model framework. When K (the projection of the angular momentum I on the symmetry axis) is a good quantum number - as it is for axially symmetric nuclei - and the mass and charge distributions coincide, $\langle I'||\delta_\lambda||I\rangle$ can be calculated from $\langle I'||M\lambda||I\rangle$ by:

$$STR = RDEF = \langle I'||\delta_\lambda||I\rangle = \frac{4\pi}{3Z_P e R_0^{\lambda-1}}\langle I'||M\lambda||I\rangle, \qquad (5.22)$$

where $R_0 = 1.2A_P^{1/3}$ is an average radius of the deformed projectile. In the present calculation, a series of TYPE=12 potentials (deformed projectile) were defined for each pair of coupled states "ia" and "ib" with multipolarities "k" (see Appendix A) and strengths (reduced deformation lengths - RDEF) deduced from Formula 5.22. The adopted signs were as for the deformed Coulomb part.

All potentials with "kp=1" are finally summed together to form the effective potential, in which the projectile and the target nucleus move and exchange energy. It is important to stress that although the nuclear couplings alone may have a limited direct effect on the excitation cross sections, drastic changes may appear due to the Coulomb-nuclear interference effect (see Section 3.4).

5.6.4 Results and conclusions

Calculations employing both deformed Coulomb and nuclear potentials (using the input file in Appendix A) and only the deformed Coulomb potential (the first two &POT in the input file) were performed using FRESCO and the parametrization of Broglia and Winther [86]. Selected results are presented in the following.

The obtained absolute cross section for elastic scattering is presented in Fig. 5.5 with a solid red curve. It is evident that at small scattering angles ($\theta_{CM} < 46^\circ$, which corresponds to $\theta_{LAB} < 21^\circ$) there are only small oscillations present in the cross section and the red curve closely follows the black one (pure Coulomb interaction). The amplitude of the oscillations increases at higher angles and a systematic deviation from the pure Coulomb solution appears. The two calculations differ by less than 10% at angles below $\theta_{CM} = 46^\circ$, while at higher angles the difference becomes larger than 50%. The cross section in the Coulomb-nuclear solution decreases to zero faster than the pure Coulomb one, as at higher angles (smaller separation distances) the absorption increases. The behaviour presented in Fig. 5.5 is known as Fresnel scattering (rainbow), which appears when the beam energy is around the Coulomb barrier and the Sommerfeld parameter $\eta \gg 1$ [45], which is fulfilled in the current study ($\eta = 255$).

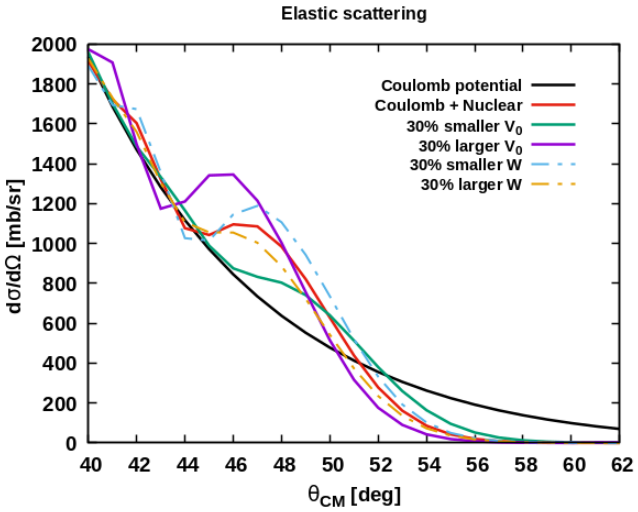

Figure 5.5 – Differential cross section for elastic scattering of ^{106}Cd on ^{92}Mo as a function of the scattering angle in the center-of-mass coordinate system, calculated with FRESCO using only a deformed Coulomb potential (in black) and both Coulomb and nuclear potentials (in red). Results of calculations using reduced/increased depths of the real (V_0) and imaginary (W) parts of the nuclear potential are also presented.

Typically, the parameters of the real part of the nuclear potential are adjusted to experimental elastic-scattering data with the goal to closely reproduce at least the main rainbow peak. This would reduce the number of free parameters involved in the problem and allow obtaining reliable quantitative results for the inelastic channels. As this was not possible in the present work, additional calculations using different values of the nuclear potential parameters (real (V_0) and imaginary (W_0) potential depth) were performed in order to illustrate the possible effects. As shown in Fig. 5.5, increasing or decreasing of the potential depth V_0 of the real nuclear potential results in larger or smaller amplitudes of the cross-section oscillations, respectively. The main rainbow peak moves towards smaller scattering angles when using a larger potential depth V_0. In addition, the amplitude of the cross-section oscillations depends also on the imaginary part of the potential. This demonstrates the complexity of the problem, as the obtained results strongly depend on the assumed potential.

Moreover, for the inelastic channel, in addition to the potential parameters, the reduced deformation lengths (RDEF) can also be varied to better describe the experimental data. It has been observed in other studies that the optimal RDEF values are usually $20-30\%$ smaller than the values calculated from the experimental transition probabilities with Formula 5.22 [87]. Therefore the calculations for the excited states in ^{106}Cd were carried out using the same potential parameters, but various RDEF values.

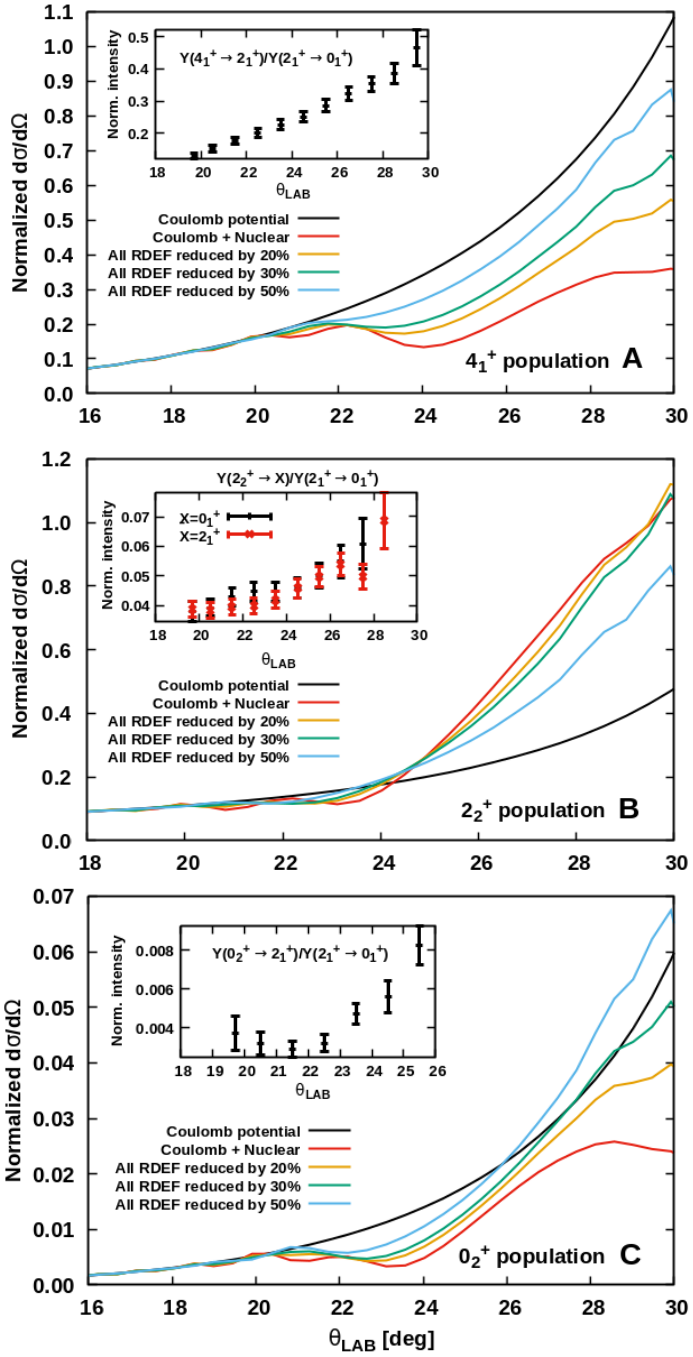

Figure 5.6 – Differential cross sections to populate the 4_1^+ (A), 2_2^+ (B) and 0_2^+ (C) states, normalized to the cross section for the first inelastic channel (2_1^+ excitation), as a function of the scattering angle θ_{LAB}. The calculations assumed various reduced deformation lengths (RDEF) - reduced by 20% (orange), 30% (green) or 50% (blue) with respect to the RDEF calculated from the experimental electromagnetic matrix elements using Formula 5.22. The experimentally measured γ-ray intensities of the transitions depopulating the states in question, normalized to the intensity of the $2_1^+ \rightarrow 0_1^+$ transition, are presented in the insets of each plot for a qualitative comparison.

In order to enable a more direct comparison between the results of the present measurement and the FRESCO calculations, Figs. 5.6-5.8 present the excitation cross sections to populate the 4_1^+, 2_2^+, 0_2^+, 3_1^- and 4_3^+ states, normalized to that for the first inelastic channel (excitation of the 2_1^+ state), as a function of the scattering angle in the laboratory frame. The present experiment provided γ-ray intensities of transitions depopulating the states in question, normalised to the 2_1^+ decay. In order to relate them to absolute excitation cross sections, a model would need to be imposed. To avoid that, no attempt was made to quantitatively compare the experimental observables and the results of the FRESCO calculation, but a general comparison with the predicted trends is still possible. Thus, the experimental γ-ray intensities normalized to that of the $2_1^+ \rightarrow 0_1^+$ transition are presented in the inset of each figure. It is also important to note that the trends observed for the experimental intensities (as a function of the scattering angle) will be smeared in comparison with the calculated cross sections due to the integration over the target thickness, scattering angle, etc.

As it can be observed in Fig. 5.6 (A), at small scattering angles ($\theta_{LAB} < 21^\circ$), the population of the 4_1^+ state closely follows the one calculated assuming a pure Coulomb process. At $\theta_{LAB} = 22^\circ$ the Coulomb-nuclear cross sections are reduced by $13 - 20\%$ (depending on the RDEF values) with respect to the pure Coulomb solution, while at 30° (at almost touching nuclear surfaces), a reduction of $18 - 66\%$ is observed, strongly dependent on the used RDEF values. In contrast, the experimental intensities in the inset of Fig. 5.6 (A) show a smooth trend consistent with a pure Coulomb-excitation prediction, which suggests that the effects of the nuclear influence on the excitation process were minimal even at high scattering angles. Similarly, in Fig. 5.6 (B) it can be seen that for the population of the 2_2^+ state the differences between the two solutions are minimal up to about $\theta_{LAB} \approx 24^\circ$ ($5 - 13\%$ reduction at $\theta_{LAB} = 22^\circ$ with respect to the pure Coulomb solution). A rather rapid increase in the Coulomb-nuclear cross section appears at higher angles (up to almost 130% difference between the solutions at $\theta_{LAB} = 30^\circ$). Finally, Fig. 5.6 (C) presents the population of the 0_2^+ state. Evidence for a destructive Coulomb-nuclear interference, which reduces the cross section, can be found in both the FRESCO calculation and the experimentally observed γ-ray intensities. For $\theta_{LAB} < 21^\circ$ the differences between the two solutions are minimal, while already at $\theta_{LAB} = 22^\circ$ the Coulomb-nuclear cross section is reduced by about 40% with respect to the pure Coulomb prediction.

The results presented above involved states populated via $E2$ transitions. The observed trends of the cross sections suggest that for those states both calculations with and without a nuclear potential produced similar results for $\theta_{LAB} < 22^\circ$. However, if transitions of higher multipolarities are involved in the excitation process, the deviation from pure Coulomb excitation appears at smaller scattering angles. This is illustrated in Fig. 5.7, presenting the calculated cross section to populate the 3_1^- state (normalized to that of the 2_1^+ state). The 3_1^- state is populated mostly

via a direct $E3$ transition from the ground state. As can be seen in Fig. 5.7, the Coulomb-nuclear interference induces fluctuations of the excitation cross section around the pure Coulomb solution. For $\theta_{LAB} < 22°$, their amplitude is larger in comparison with those observed for states in Fig. 5.6, which are populated via $E2$ transitions. At higher angles, the cross section strongly increases, reaching values a few times larger than the pure Coulomb cross section. Moreover, at smaller angles, the calculation is almost independent of the RDEF values, in contrast to the results for $\theta_{LAB} > 22°$. The experimentally measured γ-ray intensities exhibit a similar oscillatory behaviour, with a minimum observed around $\theta_{LAB} = 22°$, followed by a maximum at higher angles.

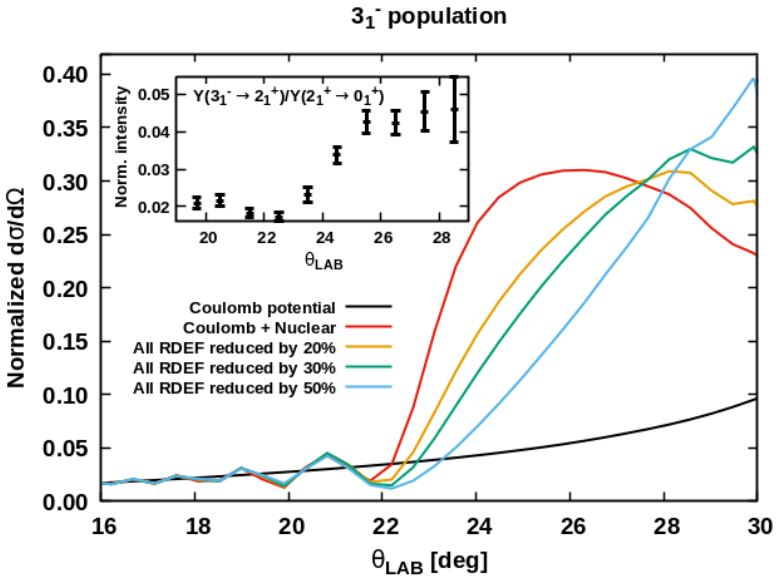

Figure 5.7 – Same as Fig. 5.6 but for the 3_1^- state.

Finally, the results of a similar calculation for the population of the 4_3^+ state are shown in Fig. 5.8 (A). The deviation from pure Coulomb excitation is rather small and strongly depends on the RDEF values, with a similar trend as for the 2_2^+ and 0_2^+ states. However, the measured intensity of the $4_3^+ \rightarrow 4_1^+$ transition has a trend significantly different from the calculated one. The sudden increase in intensity, starting at $\theta_{LAB} = 22°$, can be attributed to additional population of the state of interest via an $E4$ transition from the ground state. Deformed Coulomb and nuclear potentials were included in the calculation of an additional $4_3^+ \rightarrow 0_1^+$ $E4$ transition. Their parameters were calculated assuming a $B(E4; 0_1^+ \rightarrow 4_3^+)$ transition probabilities of 1, 5 and 10 W.u. From Formula 5.17 for the Coulomb part, STR parameters of 377, 844 and 1193 efm^4 were obtained, respectively. Using Formula 5.22 for the nuclear part, the corresponding RDEF values were calculated to be 0.18, 0.40 and 0.57 fm. It is visible from Fig. 5.8 (B) that the cross section changes drastically when the additional $E4$ coupling potential is included.

Strong fluctuations appear and a rapid cross-section increase is observed above $\theta_{LAB} = 22°$, in line with the behaviour of the experimental intensities.

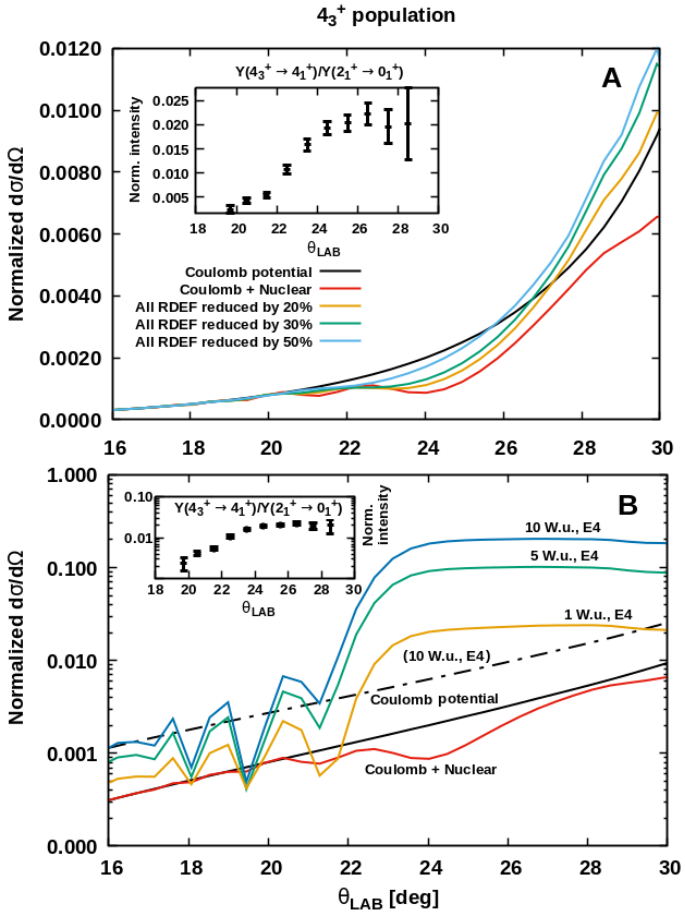

Figure 5.8 – Cross section to populate the 4_3^+ state, normalized to that for the 2_1^+ state. (A) Various reduced deformation lengths RDEF are used (as given in the legend). Experimental normalized intensities for the $4_3^+ \rightarrow 4_1^+$ transition are presented in the inset. (B) Calculations assuming different $E4$ reduced transition probabilities - 10 W.u. (blue), 5 W.u. (green), 1 W.u. (orange) and zero (red). The pure Coulomb solution without any $E4$ transition is presented with a black solid line, while a Coulomb calculation assuming $B(E4; 0_1^+ \rightarrow 4_3^+)$ = 10 W.u. is given with a dotted-dashed black line. Note the logarithmic scale.

Based on the observed trends of the calculated cross sections, it can be concluded that the experimentally observed intensities of transitions depopulating the 4_1^+ and 2_2^+ states (and possibly other 2^+ and 4^+ states that are populated by $E2$ transitions) should be minimally affected by the Coulomb-nuclear interference at θ_{LAB} scattering angles below $22°$. For the 0_2^+ state, a deviation from the Coulomb-excitation prediction appears earlier, but the cross sections for $\theta_{LAB} < 21°$ seem to follow the pure Coulomb trend. The negative-parity states, predominantly populated via higher-order multipolarity transitions ($E3$), may be affected to a greater

extent by the nuclear excitation process, but for $\theta_{LAB} < 22^{\circ}$ the Coulomb-nuclear interference induces only small fluctuations of the cross section around the pure Coulomb solution. A considerable gain in the cross section for $\theta_{LAB} > 22^{\circ}$ was observed for the positive-parity states, which have a $E4$ contribution to their population. The experimental data for the 4_3^+ state are consistent with such a contribution.

5.7 GOSIA calculations

GOSIA is a coupled-channel code developed to handle Coulomb-excitation data, allowing both realistic simulations of the experimental observables and extraction of matrix elements of the electromagnetic operator. The latter is achieved via a multi-dimensional χ^2 fit of a set of MEs to the experimental γ-ray yields and additional spectroscopic information, provided as independent data points. This allows extracting nuclear-structure properties such as electromagnetic transition probabilities and spectroscopic quadrupole moments of excited states. Various effects, which can influence the γ-ray yields are accounted for, e.g. detector geometry, deorientation effect, attenuation due to the finite size of the detector, de-excitation via the competing internal conversion process, etc. [88]. A basic introduction to the code is provided in Section 5.7.1, with a more detailed description of specific GOSIA functions presented in Appendix B. The procedure applied in the present work to obtain a realistic intensity simulation is discussed in Section 5.7.2 and the fitting procedure, providing a set of MEs describing the nucleus of interest, is presented in Section 5.7.3. Sample input files used in the present work are given in Appendices C and D.

5.7.1 Introduction to the GOSIA code

The main input file of GOSIA consists of a sequence of option commands. The option names start by "OP," followed by four characters which indicate the specific command. For more information on the options used in the particular work, see Appendix B. Full descriptions of all possible options can be found in the GOSIA manual [88].

First, in OP,GOSI the user defines the studied nucleus and the experiments to be used in the fitting procedure. The spin, parity and excitation energy are provided for each state in the considered level scheme. In total 22 states were defined, following the level scheme in Fig. 5.1. Subsequently, the reduced matrix elements used in the fitting procedure are defined. It is possible to declare electric matrix elements of multipolarities $E1$-$E6$, including diagonal $E2$ (I_I=I_F), as well as magnetic ones ($M1$,$M2$). For each matrix element, the lower and upper limits in which the matrix element can be varied during the fitting procedure are also given. The limits are provided in order to avoid unphysical solutions of the least-square search. The limits used in the present analysis were chosen in line with the recommendations in Ref. [89] - it is very unlikely for $E1$ reduced transition

probability to exceed 0.01 W.u., for $E2$ - 300 W.u., for $E3$ - 100 W.u. and finally for $M1$ - 1 W.u. The initial values of the transitional matrix elements were taken from the second column of Tables 5.6-5.9, and those of the diagonal ones from Table 5.4. The only exception are the $E3$ MEs, which will be discussed in Section 6. The previously known signs of the matrix elements can also be provided accordingly. In the present analysis, they were only known for diagonal matrix elements (Table 5.4). In total 58 matrix elements were defined - 9 of $E1$, 38 - $E2$, 4 - $E3$ and 7 of $M1$ multipolarity.

Subsequently, the user defines the experiments to be analysed. Each experiment corresponds to a particular combination of bombarding energy, scattering angle and geometry of the particle and γ-ray detectors. In this work, the defined experiments correspond to different slices of the particle-γ spectra with respect to the scattering angle θ_{LAB} (Fig. 4.9). For each experiment, the atomic and mass numbers of the collision partner are provided (^{92}Mo; $A = 92$, $Z = 42$), as well as the average beam energy E_{LAB} and average projectile scattering angle θ_{LAB}. As the former, the energy of the beam in the middle of the target was adopted (756.7 MeV). The mean scattering angle θ_{LAB} is taken to be the middle of each $\Delta\theta_{LAB}$ region (Fig. 4.9). The first three mean θ_{LAB} correspond to 19.7°, 20.5° and 21.5°. The azimuthal angular limits of the detector at the middle of each $\Delta\theta_{LAB}$ slice are also provided. They were deduced from Fig. 4.9 - for example, at the smallest mean scattering angle θ_{LAB}=19.7°, the particle detector stretches between ϕ_L=-11.6° and ϕ_U=12.0°.

For a calculation of the de-excitation γ-ray yields following Coulomb excitation, information on the competing internal-conversion process is necessary, as well as the geometry of the γ-ray detectors. These are provided in GOSIA's OP,YIEL, see Appendix B. The internal conversion coefficients at specific energies (mesh points) were provided for each of the multipolarities present in the declared coupling scheme. In the present analysis, 23 energy mesh points were used, ranging from 0.1 MeV to 3.2 MeV in uneven steps. The internal conversion coefficients for $E1$, $E2$, $E3$ and $M1$ transitions were calculated using the online BRICC calculator [91]. By interpolating between those mesh points, GOSIA is able to calculate the internal conversion coefficient at any specific transition energy. Subsequently, the geometry of the γ-ray detection system is described. The θ_{LAB} and ϕ_{LAB} angles for each of the 21 AGATA detectors were provided for each experiment. Detector sizes and their distances from the target were specified, as described in Appendix B.

For each experiment, the number of data sets per experiment (i.e. the number of individual γ-ray spectra that were analysed), the detection upper limits and the relative normalization factors of the γ-ray detectors have to be provided. The upper limit is described as the lowest possible intensity, normalized to that of the $2_1^+ \rightarrow 0_1^+$ transition, which could be observed in the γ-ray spectrum. An upper limit of 0.1% of the intensity of the normalization transition was deduced from the experimental γ-ray spectra.

Additional spectroscopic information, including branching and mixing ratios, lifetimes, known transitional and diagonal MEs, needed for the least-square fitting is then provided. In this work 22 branching ratios were considered. They are calculated from the relative γ-ray intensities (I_γ), summarized in Table 5.2. Their uncertainties are determined using standard error propagation. Lifetimes can also be provided as constraints of the fit. This was done differently for the two approaches adopted in this work. For a calculation of the γ-ray intensities based solely on the spectroscopic data found in the literature (the approach described in Section 5.2), all known lifetimes were provided (20 values taken from Table 5.1). For the lifetime of the 6_1^+ state a value of $1(1)$ ps was adopted as only an upper limit of $\tau < 2$ ps was previously reported in the literature. Only a lower limit is known for the lifetime of the 0_3^+ state, $\tau > 1.58$ ps [61], thus no lifetime was provided for this state. Instead, the $\langle 2_2^+||E2||0_3^+\rangle$ matrix element was fixed at a value of 0.35 eb, which was taken from the beyond-mean-field (BMF) calculations of T. Rodriguez [50].

When fitting experimental γ-ray intensities (approach from Section 5.3) the lifetimes that entered the fit were limited to that used for normalization ($\tau(2_1^+)$), lifetime of the unobserved 8_1^+ state and those of the negative-parity states (3_1^-, 5_1^-, 5_2^-, $1^{(-)}$). The latter are related to the matrix elements describing the $E1$ decay of these states, and do not affect the excitation process. Finally, the lifetime of the 5_1^+ state was provided as a part of error estimation discussed in Section 6.2.

Seven literature values of $\delta(E2/M1)$ mixing ratios were considered in the analysis. These mixing ratios are summarized in the second column of Table 5.3. Finally, previously measured matrix elements can also be included in the least-square fit. In the current work, those were the diagonal matrix elements given in Table 5.4. For the intensity simulations, the $\langle 0_1^+||E3||3_1^-\rangle$ matrix element was added as well. However, when fitting a set of MEs to the experimental γ-ray intensities no additional constraints were imposed on the $\langle 0_1^+||E3||3_1^-\rangle$ matrix element in order to be able to extract its value from the fit.

5.7.2 Simulating intensities

An important feature of GOSIA is the possibility to calculate γ-ray intensities of transitions depopulating Coulomb-excited states, registered in coincidence with scattered particles, in the geometry of the experimental setup. Using GOSIA's OP,POIN the so-called "point-like" γ-ray yields can be calculated. These are the yields calculated for the mean beam energy E_{LAB} and mean laboratory scattering angle θ_P characterizing each experiment:

$$Y((I_i \to I_f), \theta_P, E_{LAB}) = \sin(\theta_P) \int_{\phi_P} \frac{d^2\sigma(I_i \to I_f)}{d\Omega_\gamma d\Omega_P}\, d\phi_P, \tag{5.23}$$

where $\sin(\theta_P)$ is a solid angle factor and the double differential cross section for the transition $I_i \to I_f$ is proportional to the Rutherford cross section. The differential cross section describes the angular distribution of the γ rays assuming a point-

like γ-ray detector, with additional attenuation factors included to account for the finite size of the detectors.

GOSIA's OP,INTI option can be used to perform integration over the finite scattering angle range covered by the particle detector $d\Omega_P$ and over the bombarding energies resulting from the projectile energy loss over the target thickness. Using this option, one can realize the approach proposed in Section 5.2, namely simulate realistic γ-particle coincidence intensities based on the set of matrix elements fitted to the spectroscopic data. The input for OP,INTI for the first three ranges of scattering angles considered in the analysis is given in Appendix D. In the first stage of the calculation, an integration over the azimuthal angle ϕ is performed at specific energy and scattering angle θ_P mesh points, similar to OP,POIN. An integration over the bombarding energy and scattering angle follows, relying on an interpolation between the calculated γ-ray yields at energy and θ_P mesh points at which a full Coulomb-excitation calculation is performed. The integrated γ-ray yields are calculated as:

$$Y(I_i \rightarrow I_f) = \int_{E_{MIN}}^{E_{MAX}} dE \frac{1}{\frac{dE}{dx}} \int_{\theta_{MIN}}^{\theta_{MAX}} Y((I_i \rightarrow I_f), \theta_P, E)\, d\theta_P, \tag{5.24}$$

where E_{MIN}, E_{MAX} correspond to the limits of incident energy, θ_{MIN} and θ_{MAX} to the θ_P scattering angle limits, and dE/dx are the stopping powers provided by the user. The minimum incident energy E_{MIN} was calculated with the program "elo" [58], assuming a target thickness of 0.715 mg/cm^2. It is important to note that if another model, e.g. another program, is used for the calculation, the obtained stopping powers may differ. Indeed, they were found to be about 6.5% smaller when LISE++ [92] was used and about 14% smaller for a VTL [93] calculation. This resulted in calculated normalized γ-ray intensities differing by up to 2% between those that relied on stopping powers calculated with elo, LISE++, VTL, and SRIM [94]. Consequently, this source of systematic errors was taken into account by increasing the uncertainties of the experimental normalized γ-ray intensities by 2%. The simulated intensities are subject to the same systematic uncertainty.

The γ-ray yields obtained with OP,INTI are not directly comparable with the absolute experimental γ-particle coincidence intensities. In order to obtain a realistic number of γ-particle coincidence counts N, one has to take into account the beam intensity and detector efficiency [88]:

$$N = 10^{-30} \left[\frac{Q}{qe}\right] \left[\frac{N_A}{A_T}\right] Y(I_i \rightarrow I_f)\ \epsilon_P\ \epsilon_\gamma\ \Delta\Omega_\gamma\ t, \tag{5.25}$$

where Q is the integrated beam charge in [C], q is the average charge state of the beam, N_A is the Avogadro number, ϵ_P is the absolute particle detection efficiency, ϵ_γ is the energy dependent γ-ray detection efficiency per unit solid angle, $\Delta\Omega_\gamma$ is the total solid angle subtended by the γ-ray detectors and t is the measurement time (accounting for possible acquisition dead time). The integrated γ-particle coincidence yield $Y(I_i \rightarrow I_f)$ in Formula 5.25 is taken from the output of OP,INTI.

If in the data analysis only relative numbers of counts are used, all factors in Formula 5.25 that multiply the calculated γ-ray yield cancel out, apart from the energy-dependent γ-ray detection efficiency. This strategy was employed in the present work: the experimentally measured γ-ray intensities in coincidence with the projectiles registered in each range of scattering angles $\Delta\theta_P$ were corrected for γ-ray detection efficiency and normalized to the number of counts observed in the $2_1^+ \rightarrow 0_1^+$ peak. The normalized intensities could then be directly compared to the corresponding normalized γ-ray yields calculated with OP,INTI.

5.7.3 Fitting experimental γ-ray yields

Sets of transitional and diagonal electromagnetic matrix elements can be extracted by performing a multi-dimensional χ^2 fit to the experimental data using GOSIA's OP,MINI. The χ^2 function used by the code consists of three components [69], accounting for the reproduction of the experimental γ-ray yields, other spectroscopic data and an user-defined upper limit for γ-ray yields, respectively:

$$\chi^2 = S_{YLD} + S_{SPEC} + S_{UPL}. \tag{5.26}$$

The fitting procedure consists in simulating γ-ray yields, based on the initial set of MEs, and comparing them to the experimental intensities. The MEs are then modified, until an optimal reproduction of experimental data is achieved.

Instead of using integrated γ-ray intensities, in order to shorten the computational time, the experimental γ-ray yields Y_{exp} are "translated" to "point-like" yields Y_{exp}^{corr} and are then compared to simulated γ-ray intensities calculated for a specific energy and a specific scattering angle. The modification of the experimental intensities is done by introducing a correction factor $CF^i = Y^i_{poin}/Y^i_{inti}$ for each transition i, calculated by comparing the γ-ray intensities resulting from a full OP,INTI procedure (Y_{inti}) with those resulting from a point-like calculation with OP,POIN (Y_{poin}). The correction factors CF are then applied to the experimental γ-ray yields Y_{exp}:

$$(Y_{exp}^{corr})^i = CF^i \cdot Y^i_{exp}. \tag{5.27}$$

This correction procedure, implemented in GOSIA's OP,CORR, depends on the used set of matrix elements, thus during the minimization it should be repeated periodically until a self-consistent solution is found.

In the GOSIA minimization routine, normalized γ-ray intensities are used rather than absolute cross sections. In order to measure absolute cross sections, information such as the absolute particle-detection efficiency, beam intensity, dead time, etc., has to be provided (see Formula 5.25). However, such data are not always known with a good precision. For example, the beam intensity may fluctuate during the experiment, which is hard to quantify and account for. Thus, to avoid such problems, GOSIA uses normalization constants, which include the Rutherford cross section, particle detector solid-angle factor, absolute efficiency, integrated beam current, etc., to relate the experimental and calculated intensities. Instead

of calculating and providing the normalization coefficients by hand, the normalization is usually performed internally by the code. In the present analysis, since the data from all γ-ray detectors were summed together, one normalization constant C_m for each experiment m is introduced. To obtain C_m, GOSIA fits the experimental γ-ray yields of all observed transitions in the experiment m by minimizing the sum of $(C_m Y_c^{m,i} - (Y_{exp}^{corr})^{m,i})/\sigma_{m,i}^2$, where Y_c is the calculated γ-ray yield. However, both the normalization constants and the matrix elements are fitted to the experimental data, which can result in an ambiguity: changes in the MEs can be compensated by modifying the normalization constant. Therefore, additional constraints are needed to obtain reliable results. This can be achieved by providing additional spectroscopic information such as a known lifetime of a state that is observed to decay via an intense transition. In the present work, the lifetime of the 2_1^+ state, known with a good precision, was used for this aim. Based on the lifetime, GOSIA calculates the expected intensity of the corresponding transition(s) for each experiment. From a comparison between the simulated and experimental yields, the normalization constants can be extracted.This procedure is part of the least-square search and is implemented by including the S_{YLD} component in the χ^2 function:

$$S_{YLD} = \sum_m \omega_m \sum_i \frac{(C_m Y_c^{i,m} - (Y_{exp}^{corr})^{i,m})^2}{\sigma_{i,m}^2}, \tag{5.28}$$

where ω_m are the user-defined weights with which the experimental yields are considered for each experiment (1.0 in this work).

The other components of the χ^2 function are given by Formulas 5.29 and 5.30. S_{SPEC} accounts for how well the additional spectroscopic data (lifetimes, branching and mixing ratios, etc.) are reproduced with the obtained set of MEs. Their experimental values, D_{exp}, are compared to the calculated ones, D_c, considering the experimental uncertainties for all n data points:

$$S_{SPEC} = \sum_d \omega_d \sum_n \left(D_c^n - D_{exp}^n\right)^2 / \sigma_n^2, \tag{5.29}$$

where ω_d is the weight given by the user for each group of spectroscopic data (e.g. 1.0 for lifetimes).

A S_{UPL} term is added to the χ^2 function if GOSIA predicts observation of a transition, which is not present in the experimental data. In such a case, for each transition i in experiment m that exceeds the upper limit and has not been observed, its calculated intensity $Y_c^{i,m}$, divided by the intensity of the normalising transition Y_{cN}^m, is compared to the user-defined upper limit $u(m)$:

$$S_{UPL} = \sum_m \sum_i \left(\frac{Y_c^{i,m}}{Y_{cN}^m} - u(m) \right)^2 \times \frac{1}{u^2(m)} \, . \tag{5.30}$$

It is important to note that the χ^2 function used in GOSIA is normalized to the number of data points (experimental γ-ray yields and spectroscopic data), rather

than to the number of degrees of freedom. This is due to the impossibility to clearly define the exact number of fitted parameters (MEs), as they have very different influence on the χ^2 fit [69].

The statistical errors of the fitted matrix elements can be evaluated using GOSIA's OP,ERRO by probing the probability distribution around the χ^2 minimum after the global χ^2 minimum has been found. First, GOSIA calculates uncorrelated uncertainties by sampling each matrix element until a point in the χ^2 surface corresponding to $\chi^2_{min} + 1$ is found. In the second step, to account for possible correlations between the MEs, a "maximum correlation path" is defined for each ME, i.e. a curve in the matrix-element space $\bar{x}$, for which the effect of varying the matrix element in question is balanced by changes in the other matrix elements to the largest extent. The uncertainty is then found by requesting the integral of the normalised probability distribution contained within error bars to be equal to the confidence limit of 68.3% [88]:

$$\frac{\int\limits_{l} \exp\left(-\frac{1}{2}\chi^2(\bar{x})\right) d\bar{x}}{\int \exp\left(-\frac{1}{2}\chi^2(\bar{x})\right) d\bar{x}} = 68.3\% \,, \tag{5.31}$$

where the integration in the numerator is performed along the maximum correlation path l, and in the denominator over all possible values of $\bar{x}$, i.e. the entire variation range of matrix elements defined in OP,GOSI.

6 - GOSIA analysis and results

Although a qualitative description of the behaviour of the measured cross sections was achieved with FRESCO, a quantitative analysis was attempted using GOSIA as proposed in Sections 5.2 and 5.3. As a first step of these two approaches, an initial set of matrix elements was determined. In order to avoid any mistakes while calculating the initial set of matrix elements and to cross check the results obtained with Formulas 5.11, 5.12 and 5.13, a GOSIA minimization procedure was used to obtain a set of MEs, which optimally fits the provided literature information on lifetimes, branching and mixing ratios, given in Tables 5.2-5.3, and previously measured matrix elements, including the quadrupole moments given in Table 5.4. As the lifetime of the 0_3^+ state was not known, a value of 0.35 eb was assumed for the $\langle 2_2^+||E2||0_3^+\rangle$ matrix element, taken from the beyond-mean-field (BMF) calculations of T. Rodriguez [50]. The $\langle 0_1^+||E3||3_1^-\rangle$ matrix element was taken from the experimental work of D. Rhodes [75] (Table 5.5). The remaining $E3$ matrix elements relevant for this study were not previously measured, thus values of 0.2 $e\text{b}^{3/2}$ for the $\langle 2_1^+||E3||5_1^-\rangle$ matrix element (equivalent to 5 W.u.) and 0.3 $e\text{b}^{3/2}$ for the $\langle 2_1^+||E3||5_2^-\rangle$ and $\langle 2_1^+||E3||1_1^-\rangle$ matrix elements (12 and 45 W.u., respectively) were adopted as initial values. These matrix elements were sufficient to reproduce the observed intensities at the smallest scattering angles.

For purely technical reasons, in the first step of the minimization procedure point-like intensities have to be simulated using OP,POIN for each transition in the level scheme of the nucleus of interest.Those intensities were calculated using the initial set of MEs defined in the sub-option ME (see Appendix B). Defining one experiment in the EXPT sub-option (e.g. at the smallest mean scattering angle) is sufficient for this calculation. The simulated point-like intensities were saved in an external file. The weight with which they are taken in the least-square procedure can be changed within the external file. It was set to 0.0 and thus they did not enter into the χ^2 function.

A χ^2 minimization was carried out next (using OP,MINI) and a new set of matrix elements, better reproducing the spectroscopic data, was saved in the corresponding external file. Subsequently, OP,REST was additionally called to replace the initial set of matrix elements with those from this file. This was followed by a multiple-step minimization, at each step of which a new set of MEs was found and saved to an external file. The minimization was terminated when a satisfying reduced χ^2 was obtained (of the order of 10^{-5}). The final set of matrix elements, corresponding to this minimum, was used in the next step of the analysis - both for simulating the γ-ray intensities and as an initial set of matrix elements to be used when fitting experimental data.

6.1 GOSIA simulations based on spectroscopic data

As the first step, the strategy proposed in Section 5.2 was implemented. Using the matrix elements obtained from the spectroscopic data, realistic γ-ray intensities in coincidence with projectiles scattered into each $\Delta\theta_{LAB}$ region were simulated and compared to the experimental ones, using a normalisation to the $2_1^+ \rightarrow 0_1^+$ transition intensity. This task was handled using the GOSIA input file given in Appendix D in addition to the GOSIA input file given in Appendix C. From the comparison of simulated and observed intensities, one can evaluate the extent of the nuclear-induced effects.

OP,INTI, together with OP,REST were called to perform a simulation of γ-particle coincidence intensities for all eleven $\Delta\theta_{LAB}$ regions ($19.4^\circ < \theta_{LAB} < 30^\circ$). The obtained γ-ray yields, normalized to those of the $2_1^+ \rightarrow 0_1^+$ transition at a given angle, were written to the main output file. These can be directly compared to the experimental normalized intensities, which were corrected for the γ-ray detection efficiency, as explained in Section 5.7.2. The obtained simulated intensities as a function of the scattering angle for each experimentally observed transition were plotted in Figs. 6.2-6.9 and compared to the experimental normalized yields.

The uncertainties of the simulated γ-ray yields were evaluated. The adopted procedure was relatively simple for states, which decay by a single transition. Two additional yield simulations had to be performed, in which the maximum and minimum values of the transitional matrix element governing the depopulating transition were assumed. The upper and lower limits of each matrix element were taken from the second columns of Tables 5.6-5.9. Subsequently, the calculated largest and smallest γ-ray yields were used to plot the uncertainty corridor, as presented for example in Fig. 6.2 (A) for the $4_1^+ \rightarrow 2_1^+$ transition. Only an upper limit of the $\langle 2_1^+ || E2 || 0_3^+ \rangle$ matrix element and a lower limit of the $\langle 4_1^+ || E2 || 6_1^+ \rangle$ matrix element were previously known, therefore only upper/lower intensity limits were calculated for the corresponding transitions and plotted with dashed lines in Figs. 6.6 (B) and 6.2 (B), respectively. The adopted procedure for calculating the error corridors takes into account only the major source of the uncertainty - the variations of the MEs related to the transitions involved in the decay of each state. Effects on the population of the state of interest, resulting from changes in all other matrix elements (including diagonal MEs), i.e. correlation effects, have not been considered. Therefore the presented error corridors may be slightly underestimated in favour of computational time and are plotted for illustrative purposes.

A more sophisticated calculation of the uncertainty corridor is needed when the state of interest decays by multiple branches. In such a case, its excitation proceeds via competing paths involving different matrix elements. Therefore, a combination of matrix elements has to be carefully selected for each branch, considering their uncertainties (limits), which would result in a maximum or minimum observed intensity of the transition of interest. This is illustrated for the experimentally observed $(2^+, 3^+, 4^+) \rightarrow 2_1^+$ transition. The state at 2486 keV decays via four

transitions, namely to the 2_1^+, 4_1^+, 2_2^+ and 4_2^+ states as shown with green arrows in the partial level scheme in Fig. 6.1.

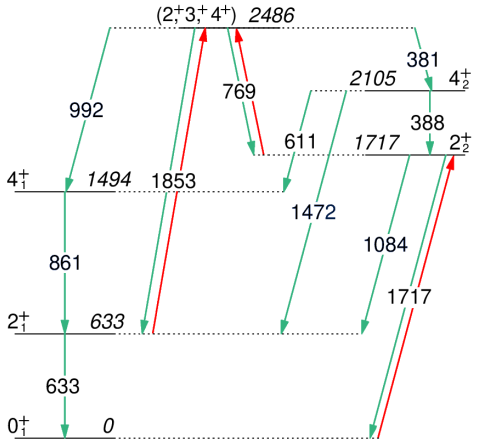

Figure 6.1 – Partial level scheme presenting the decay branches of the $(2^+, 3^+, 4^+)$ state (in green). The populating transitions discussed in the text are marked with red arrows.

It was found that the highest intensity of the $(2^+, 3^+, 4^+) \rightarrow 2_1^+$ transition is observed when the $\langle 2_1^+||E2||(2^+, 3^+, 4^+)\rangle$ and $\langle 2_2^+||E2||(2^+, 3^+, 4^+)\rangle$ matrix elements are at their maximum (considering their uncertainties), while the $\langle 4_1^+||E2||(2^+, 3^+, 4^+)\rangle$ and $\langle 4_2^+||E2||(2^+, 3^+, 4^+)\rangle$ matrix elements are at their minimum. To explain this, the role of each transition in both the excitation and de-excitation process has to be considered. Naturally, maximal de-excitation intensity requires the maximal value of the transitional matrix element $\langle 2_1^+||E2||(2^+, 3^+, 4^+)\rangle$. Naively, it can be expected that to maximize the intensity of this branch, all other possible decay branches should have minimal matrix elements. However, the state of interest is populated from below via all four branches. Thus reducing any of their matrix elements will result in a smaller population of the state. Those two processes are competing and highly state dependent. In the discussed case, maximizing the $\langle 2_2^+||E2||(2^+, 3^+, 4^+)\rangle$ matrix element results in a higher overall observed intensity of the $(2^+, 3^+, 4^+) \rightarrow 2_1^+$ transition, because additional population of the $(2^+, 3^+, 4^+)$ state proceeds via the 2_2^+ state, which is excited directly from the ground state (as marked with a red arrow in Fig. 6.1). The 4_1^+ and 4_2^+ states are excited predominantly in a two-step process through the 2_1^+ state, and thus the role of the corresponding excitation paths is much smaller than those involving intermediate states populated in one-step excitation from the ground state. Consequently, they influence mostly the decay pattern and minimizing the $\langle 4_1^+||E2||(2^+, 3^+, 4^+)\rangle$ and $\langle 4_2^+||E2||(2^+, 3^+, 4^+)\rangle$ matrix elements leads to maximizing the de-excitation proceeding via the $2_1^+ \rightarrow (2^+, 3^+, 4^+)$ transition.

Similar tests were performed for all of the observed transitions. This included simulating the yields for all possible combinations of transitional matrix elements

describing the decay of the states of interest. It was observed that $M1$ transitions had a very limited influence on the obtained error corridors. Moreover, the components of a mixed transition had to be treated similarly - both $M1$ and $E2$ matrix element had to be either maximized or minimized.

Additionally, in some cases by comparing the experimental observables with the normalized γ-ray yields simulated based on the known spectroscopic data it was possible to distinguish between discrepant literature information, such as previously measured matrix elements, branching and mixing ratios. Examples are given in Fig. 6.4. A few remarks for selected states are provided in the following. A more extensive discussion will be presented in Section 6.5.

- **Fig. 6.4 (A)** - simulation of the $6_2^+ \rightarrow 4_1^+$ transition intensity, obtained assuming different values of the $\langle 4_1^+ || E2 || 6_2^+ \rangle$ matrix element. The simulated γ-ray yields, based on the matrix element calculated from $\tau(6_2^+) = 1.22(15)$ ps, obtained via RDDS from the present data set [50] (presented with the red curve), significantly underestimate the measured intensities. However, if a ME calculated from $\tau(6_2^+) = 0.26^{+0.44}_{-0.14}$ ps, obtained in a DSAM lifetime measurement [61], is used instead, the simulated yields (in yellow) are in agreement with the experimental ones (within the large error corridor), with a tendency to overestimate them. Finally, a simulation with $\langle 4_1^+ || E2 || 6_2^+ \rangle = 1.37(10)$ eb, taken from a recent Coulomb-excitation measurement [75], corresponding to $\tau(6_2^+)$ of $0.54(8)$ ps, seems to best describe the experimental data. This suggests that there may be a problem with the RDDS measurement [50]. A possible explanation for obtaining an overestimated lifetime using the RDDS method is a feeding of the state of interest from a long-lived state, which was not taken into account in the lifetime calculation. According to Ref. [50], no feeding transitions to the 6_2^+ state were experimentally observed. However, a possible long-lived direct feeder is the 8_1^+ state with $\tau(8_1^+) \approx 0.6$ ns. Its decay would only contribute to the unshifted component of the $6_2^+ \rightarrow 4_1^+$ peak as the nuclei excited to the 8_1^+ state would decay only after the degrader foil. This illustrates the importance of using complementary data to verify lifetime measurements using a different experimental technique.

- **Fig. 6.4 (B)** - simulation of the $(2^+, 3^+, 4^+) \rightarrow 2_1^+$ transition intensities, obtained assuming different branching ratios in the decay of the $(2^+, 3^+, 4^+)$ state. According to the the ENSDF database [59], the state of interest decays via two equally strong branches to the 2_1^+ and 4_1^+ states. The blue curve in Fig. 6.4 (B) was obtained using this branching ratio. However, completely different decay patterns are proposed in Refs. [61,62]. Assuming the branching ratios reported in Ref. [62], summarized in Table 5.2, produces the red curve, which describes much better the experimental observables. This example illustrates that when discrepancies are present in

the literature, it is possible to favour one branching ratio over another, using the Coulomb-excitation data.

- **Fig. 6.4 (C)** - simulation of the $2_4^+ \rightarrow 2_1^+$ transition intensities, obtained assuming different mixing ratios. The blue curve in the inset of Fig. 6.4 is simulated using a mixing ratio taken from Ref. [59], $\delta = 2.5(2)$, which suggests a dominant $E2$ component of the mixed transition. In contrast, a δ of $0.312(33)$ is reported in Ref. [61], supporting a completely different interpretation that the transition is dominated by $M1$. Using the latter mixing ratio, one obtains the red curve in Fig. 6.4 (C). It is clear from the comparison of the two simulations that the smaller δ value [61] is consistent with the experimental data, thus it was adopted in the following analysis.

- **Fig. 6.4 (D)** - simulation of the $2_5^+ \rightarrow 2_1^+$ transition intensities. This figure again illustrates the possibility of differentiating between discrepant spectroscopic data. In this particular case, two different solutions for the mixing ratio of the $2_5^+ \rightarrow 2_1^+$ transition were obtained from the same γ-ray angular distribution study following the ^{106}Cd$(n, n'\gamma)$ reaction induced by fast neutrons [95]. The blue curve in the inset of Fig. 6.4 (D) is obtained using the larger one ($\delta = 3.2(4)$). Using the other solution ($\delta = -0.11(4)$) yields the red curve. By comparing these two results it becomes clear that the smaller δ value describes better the experimental points, thus this one has been used in the subsequent analysis. One should note that a more recent measurement [61] reports a mixing ratio in line with the conclusions of this test, listed in Table 5.3 as an alternative solution.

- **Fig. 6.9 (A)** - the last example of discrepant literature information resolved within the current work. Two different values of the $\langle 0_1^+ || E3 || 3_1^- \rangle$ matrix element are reported in the literature: $0.40(5)$ eb$^{3/2}$ [83] and $0.28(14)$ eb$^{3/2}$ [75]. The γ-ray yields, simulated assuming these two values, are presented in blue and red in Fig. 6.9 (A), respectively. Although the two matrix elements are consistent within their uncertainties (and so are the simulated yields), a much better agreement with the experimental data is obtained by using the value of Ref. [75]. On the other hand, it can be argued that the reduction of the experimental excitation cross section with respect to the predicted one may be due to the Coulomb-nuclear interference effects. However, the FRESCO calculations presented in Section 5.6 predict that only small oscillations in the 3_1^- excitation cross section are present at small scattering angles (θ_{LAB} below 22°), while at larger angles the normalized γ-ray yields will increase, which is inconsistent with such an argument.

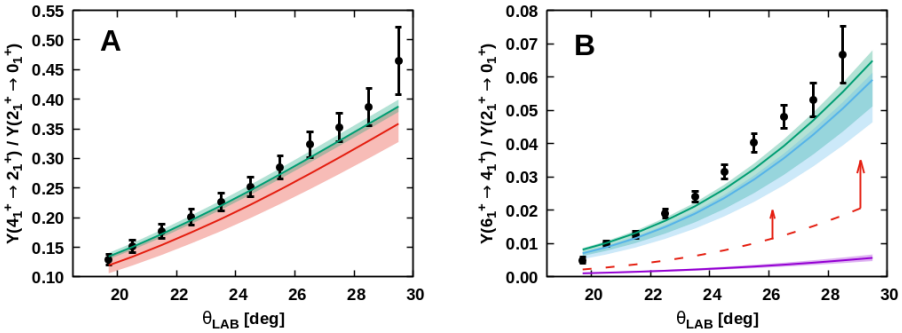

Figure 6.2 – (A) γ-ray intensity of the $4_1^+ \rightarrow 2_1^+$ transition, normalized to that of the $2_1^+ \rightarrow 0_1^+$ transition, as a function of the θ_{LAB} scattering angle. The measured intensities are presented in black. In red: γ-ray yields simulated using MEs resulting from a fit to the spectroscopic data; in green - those simulated assuming the set of MEs obtained by fitting the first three experimental points. (B) Same, but for the two components of the 998-keV peak: $6_1^+ \rightarrow 4_1^+$ (blue), $(2^+, 3^+, 4^+) \rightarrow 4_1^+$ (purple) and their sum (green), simulated using MEs fitted to the first six experimental points. The uncertainty corridors are determined considering fits to the first three and first six experimental points. The lower limit based on spectroscopic data is given in red.

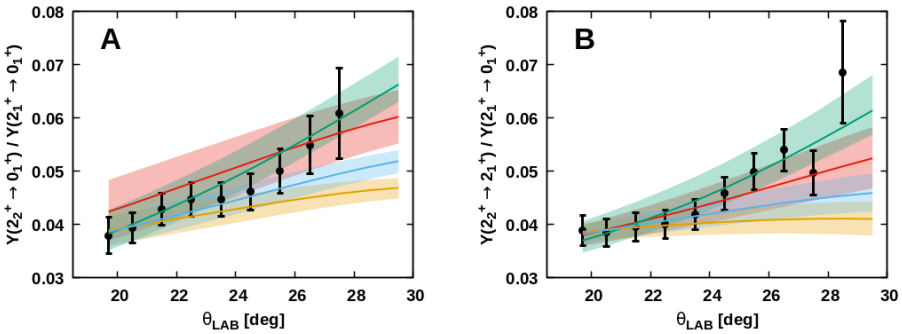

Figure 6.3 – Same as Fig. 6.2 (A), but for the γ-ray intensities of the $2_2^+ \rightarrow 0_1^+$ (A) and $2_2^+ \rightarrow 2_1^+$ (B) transitions. The normalized yields simulated using MEs obtained from a fit to the spectroscopic data are given in red. The yields simulated assuming the set of MEs obtained by fitting the first three experimental points including all diagonal E2 matrix elements listed in Table 6.3 are presented in green, those with $\langle 2_2^+ || E2 || 2_2^+ \rangle$=0 eb in blue, and those with all diagonal MEs set to zero are in orange.

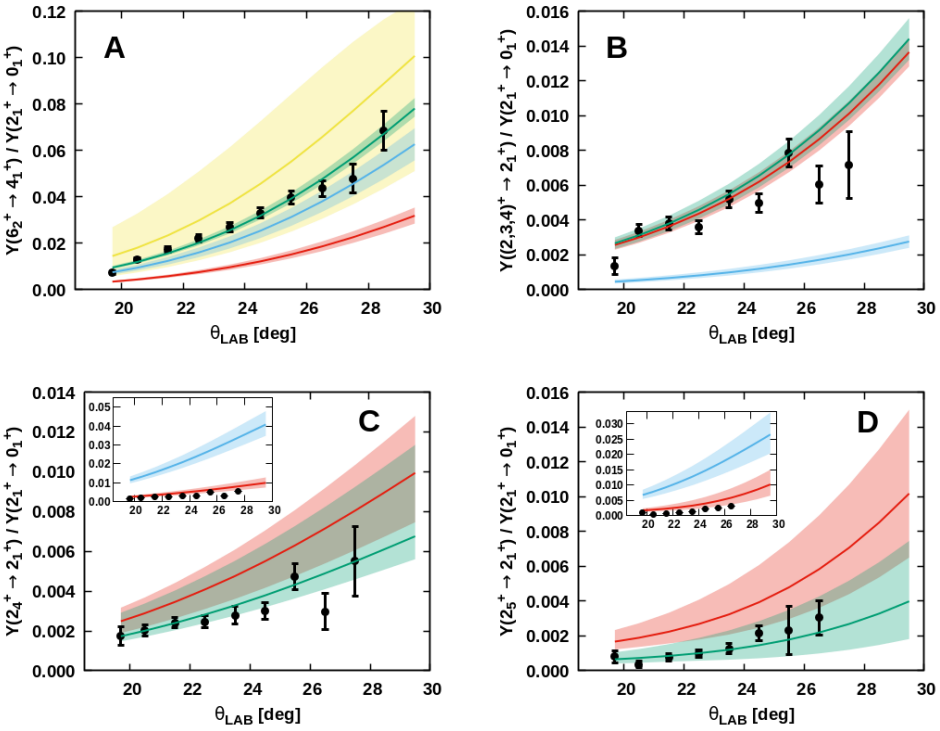

Figure 6.4 – Same as Fig. 6.2 (A) but for the γ-ray intensities of the $6_2^+ \rightarrow 4_1^+$ (A); $(2^+, 3^+, 4^+) \rightarrow 2_1^+$ (B); $2_4^+ \rightarrow 2_1^+$ (C) and $2_5^+ \rightarrow 2_1^+$ (D) transitions. (A) - additional simulations using alternative $\tau(6_1^+)$ values are presented in yellow [61] and in blue [75]. (B) - a simulation using an alternative set of branching ratios [59] is presented in blue. (C, D) - the blue curves in the insets are simulated using alternative mixing ratios. See text for more details.

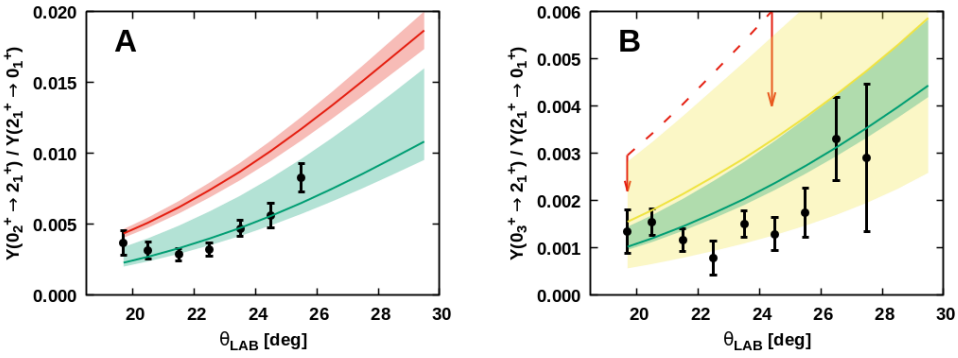

Figure 6.5 – Same as Fig. 6.2 (A) but for the γ-ray intensities of the $0_2^+ \rightarrow 2_1^+$ (A) and $0_3^+ \rightarrow 2_1^+$ (B) transitions. (B) - an upper limit deduced from literature spectroscopic data is indicated with the red dashed line. The γ-ray yields simulated assuming the $\langle 2_{1,2}^+ || E2 || 0_3^+ \rangle$ values from Ref. [71] are presented in yellow.

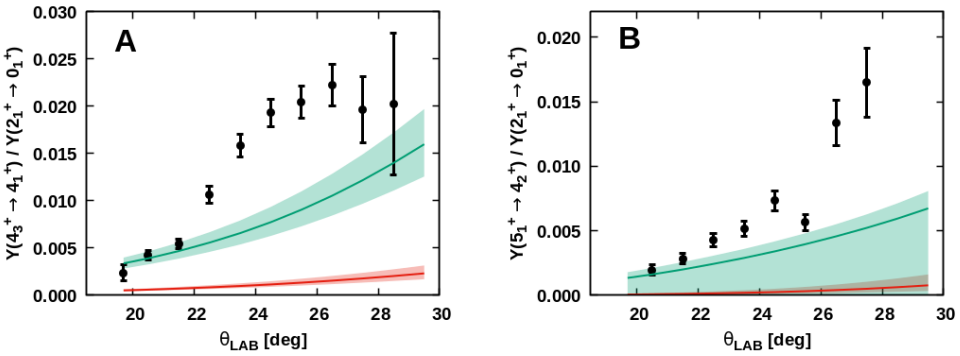

Figure 6.6 – Same as Fig. 6.2 (A) but for the $4_3^+ \rightarrow 4_1^+$ (A) and $5_1^+ \rightarrow 4_2^+$ (B) transitions.

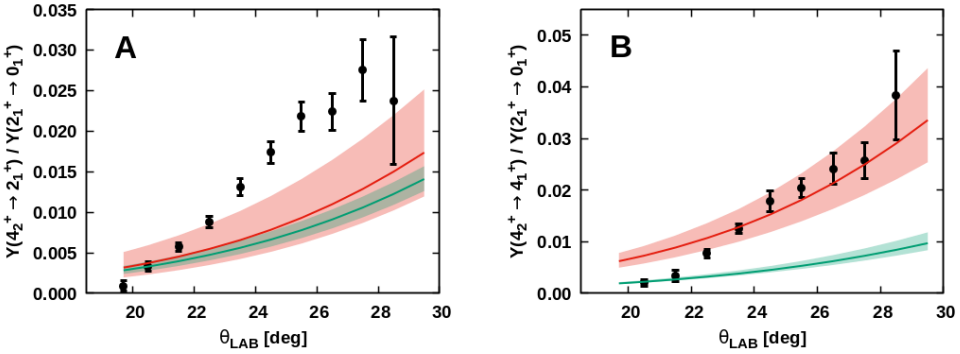

Figure 6.7 – Same as Fig. 6.2 (A) but for the $4_2^+ \rightarrow 2_1^+$ (A) and $4_2^+ \rightarrow 4_1^+$ (B) transitions.

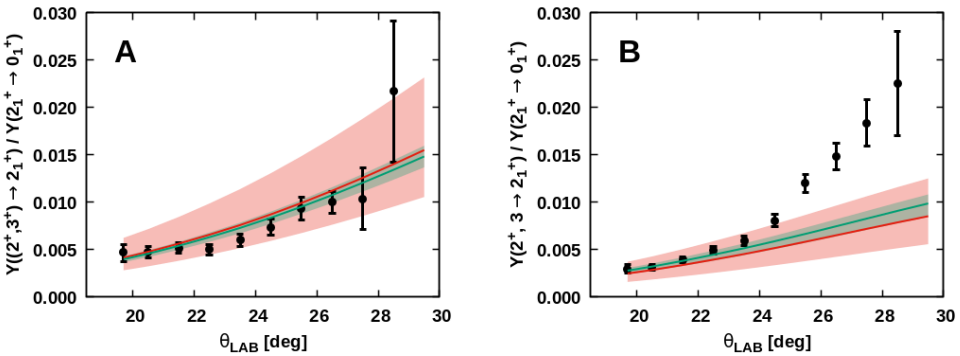

Figure 6.8 – Same as Fig. 6.2 (A) but for the $(2^+, 3^+) \rightarrow 2_1^+$ (A) and $2^+, 3 \rightarrow 2_1^+$ (B) transitions.

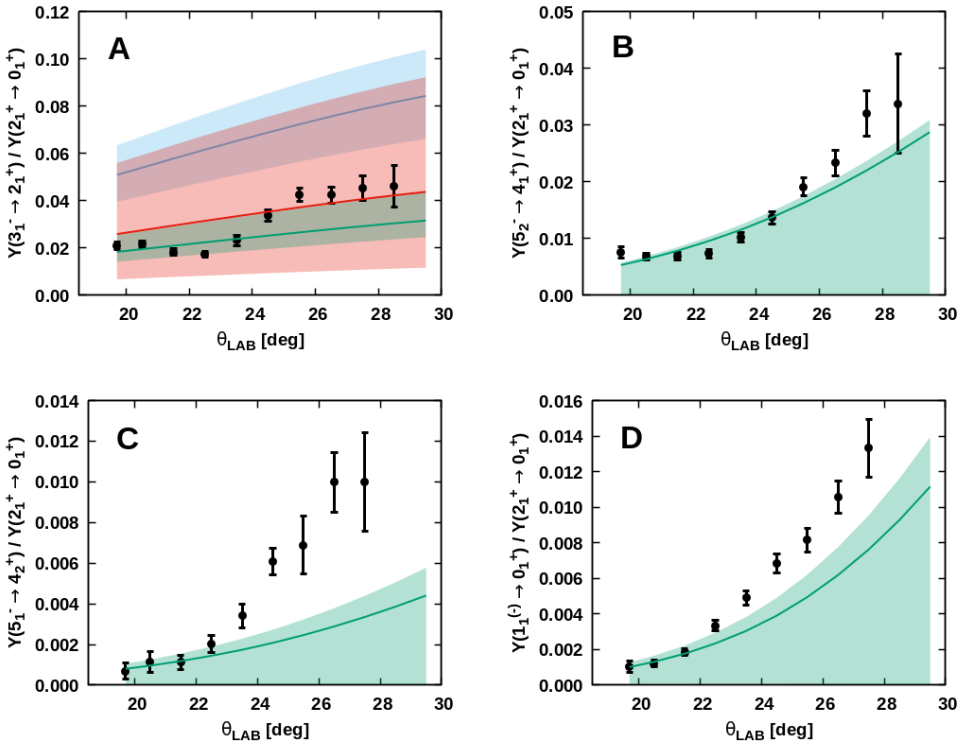

Figure 6.9 – Same as Fig. 6.2 (A) but for the $3_1^- \rightarrow 2_1^+$ (A); $5_2^- \rightarrow 4_1^+$ (B); $5_1^- \rightarrow 4_2^+$ (C) and $1^- \rightarrow 0_1^+$ (D) transitions. (A) - the γ-ray yields simulated using MEs obtained from a fit to the spectroscopic data, including the adopted $\langle 0_1^+ || E3 || 3_1^- \rangle$ value (Table 5.5) are presented in red, while those based on an alternative $\langle 0_1^+ || E3 || 3_1^- \rangle$ value reported in Ref. [83] are in blue.

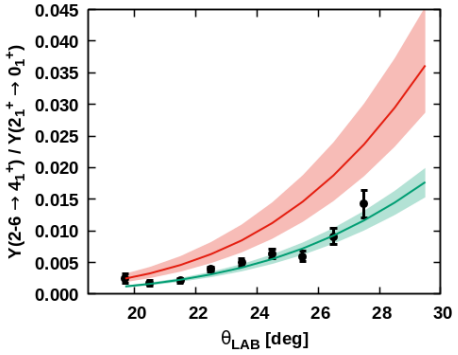

Figure 6.10 – Same as Fig. 6.2 (A) but for the $2 - 6 \rightarrow 4_1^+$ transition.

6.2 Fitting unsafe Coulomb-excitation data

Another approach to the unsafe Coulomb-excitation data was proposed in Section 5.3. Namely, GOSIA can be used to fit a set of matrix elements to the measured γ-ray intensities in coincidence with particles scattered at a specific $\Delta\theta_{LAB}$ range, assuming that those observed for the smallest scattering angles are not influenced by the Coulomb-nuclear effects in a significant way. Indeed, as it was shown in Section 5.6.4, under the conditions of the present study, only small deviations from the pure Coulomb solution are expected at scattering angles below 22°, which are in fact comparable with the experimental uncertainties of the relative γ-ray intensities measured at those angles. A GOSIA fit was therefore performed using as an input the measured γ-ray intensities corresponding to mean θ_{LAB} of 19.7°, 20.5° and 21.5°. Subsequently, the obtained set of MEs was used to predict the intensities at higher scattering angles.

The measured γ-ray intensities had first to be transformed to point-like γ-ray intensities, as explained in Section 5.7.2. The MEs fitted to the spectroscopic data were used in this procedure and also served as an initial set of MEs in the GOSIA fit. The point-like experimental intensities resulting from the correction procedure were written to an external file. In contrast to the procedure described in the beginning of Section 6, the weights of those γ-ray yields in the χ^2 function (Formula 5.29) were set to 1.0 as they were considered in the fit. The relevant input files are presented in Appendices C and D.

The following fitting procedure was realized by calling GOSIA's functions OP, MINI and OP,REST (see Appendix D). The point-like experimental yields were read from the external file and compared to the simulated point yields at each step of the minimization. In addition, certain spectroscopic information was also included in the least-square function, namely all branching and mixing ratios, taken from the second column of Table 5.3, all diagonal matrix elements, taken from Table 1.7, and a few lifetimes (that of the 2_1^+ state used for normalization and those of the negative parity states). An exception was made for the branching ratio $I_\gamma(4_2^+ \rightarrow 2_1^+)/I_\gamma(4_2^+ \rightarrow 4_1^+)$, whose uncertainty was strongly increased, since a discrepancy was observed between the literature value and the current data set, as explained in Section 5.4.2. The minimization was repeated until a satisfactory convergence was obtained, with a reduced χ^2 value of 0.74. In total, GOSIA was called 500 times, performing three subsequent minimizations with 30 steps each. As a next step, the uncertainties of the fitted matrix elements were evaluated using OP,ERRO, considering all possible correlations between the matrix elements. A number of additional tests were performed in order to account for other possible sources of uncertainty, as described in the following.

- **The unexpected strong population of the 5_1^+ state** can be clearly seen in Fig. 6.6 (B), which shows that the γ-ray yields calculated on the basis of the spectroscopic data (in red) strongly underestimate the experimen-

tal ones. This suggests that the observed 226-keV γ ray, assigned to the $5_1^+ \rightarrow 4_2^+$ transition, may originate from another state. However, from the present γ-γ coincidence data it was evident that the adopted placement of this transition fits well with the one previously proposed. On the other hand, a coincidence with the 226-keV line reveals both shifted and unshifted components of the transitions depopulating states fed by the 5_1^+ state. This is incompatible with the literature value of $\tau(5_1^+)$, which is of the order of 1 ns [59] and suggests instead a much shorter lifetime (few ps). Such an observation can be explained in a few different ways. For example, the measured intensities may be strongly affected by the γ-ray background in this energy region; the spin assignment of the 5_1^+ state can be wrong or there may be an unresolved doublet state, which has a similar decay pattern to that of the 5_1^+ state. An attempt was made to account for these possible scenarios by performing the fitting procedure twice: (i) using the experimental intensity of the $5_1^+ \rightarrow 4_2^+$ transition ($\tau(5_1^+)$ not provided as an additional constraint) and (ii) providing the lifetime of the state, but not the experimental γ-ray yields for this transition. In this way, two sets of matrix elements were obtained and by comparing them, the effects related to the 5_1^+ overpopulation could be accounted for.

Following this procedure, a value of $\langle 4_2^+||E2||5_1^+\rangle = 5.5$ eb was obtained by fitting the $5_1^+ \rightarrow 4_2^+$ transition intensities measured for the first three ranges of scattering angles. The same matrix element must be equal to 0.55 eb in order to be consistent with the literature lifetime. Therefore, a ten-fold increase of the ME was needed to properly describe the experimental data at the smallest $\Delta\theta_{LAB}$ ranges. Similar conclusions were reached for all other matrix elements governing the decay of the 5_1^+ state - $\langle 4_2^+||M1||5_1^+\rangle$, $\langle 4_1^+||M1||5_1^+\rangle$ and $\langle 4_1^+||E2||5_1^+\rangle$. The only other matrix elements which were strongly affected by the performed tests were those related to the decay of the 4_2^+ state, directly fed by the 5_1^+ state. Reproducing the experimental γ-ray yields of the $5_1^+ \rightarrow 4_2^+$ transition resulted in a 10% increase of $\langle 2_1^+||E2||4_2^+\rangle$, a 12% increase of $\langle 4_1^+||E2||4_2^+\rangle$, and in a 13% increase of $\langle 2_2^+||E2||4_2^+\rangle$ and $\langle 4_1^+||M1||4_2^+\rangle$ matrix elements. The remaining matrix elements (i.e. those not involving the 5_1^+ and 4_2^+ states) were affected by less than 5%, which is well within their relative uncertainties.

- **The 6_1^+ state** decays by a γ ray with an energy of 998 keV. Its shifted component overlaps with the $(2^+, 3^+, 4^+) \rightarrow 4_1^+$ transition (992 keV). Therefore those transitions had to be treated as a doublet in order to obtain the related matrix elements. The experimentally extracted intensity of the γ-ray peak at about 992 keV was defined in the present analysis as resulting from the summing of the intensities of both possible transitions. In addi-

tion, the fitting procedure was performed considering different numbers of experimental points - either the first three or the first six. In the latter case only the intensities of the $6_1^+ \rightarrow 4_1^+$, $4_1^+ \rightarrow 2_1^+$ and $2_1^+ \rightarrow 0_1^+$ transitions were provided for the larger three angles. Such a test was attempted in order to obtain a better description of the experimental points at higher angles. It was performed only for the 6_1^+ state, as it was expected that the cross section to populate the yrast 6^+ state would be well described by the Coulomb interaction up to rather large scattering angles, similarly to the 4_1^+ state. Two minimization procedures, each with a large number of iterations, were performed. The obtained two sets of matrix elements were rather similar - a change of less than 3% was observed for most MEs, with the only exception of the $\langle 4_1^+||E2||6_1^+\rangle$ ME, which increased by 11% once the experimental points at larger scattering angles were also considered. The larger value of the $\langle 4_1^+||E2||6_1^+\rangle$ matrix element was adopted and the observed difference between the two solutions was taken into account in the error estimation.

- As discussed in Section 5.6.4, the FRESCO calculations suggested that the γ-ray intensities measured in coincidence with projectiles scattered at the smallest angles will be negligibly affected by the nuclear interaction for most of the states. However, **for the 0^+ excited states, non-negligible Coulomb-nuclear effects were predicted to appear already at $\theta_{\mathbf{LAB}} = \mathbf{22}^\circ$**. In order to take this into account, a GOSIA fit with the same number of minimization steps was performed using the first three experimental points for all transitions, except for $0_2^+ \rightarrow 2_1^+$ and $0_3^+ \rightarrow 2_1^+$. For these two transitions, the intensities measured for $\theta_{LAB} = 22^\circ$ were effectively excluded from the χ^2 fit by setting their experimental uncertainties to very large values. The only MEs which differed significantly from the previous solution, in which the first three experimental points were considered for all transitions, were $\langle 2_1^+||E2||0_2^+\rangle$ (increased by 14%), and $\langle 2_1^+||E2||0_3^+\rangle$ and $\langle 2_2^+||E2||0_3^+\rangle$ (increased by 17%). These changes are consistent with the effects from the destructive Coulomb-nuclear interference predicted with FRESCO to increase with the scattering angle (Fig. 5.6 (C)). Additionally, the MEs related to transitions depopulating the 2_5^+ state, built on the 0_3^+ state, were also slightly affected - a change of about 3% was observed. The remaining MEs were not affected by this test.

- Another series of tests were performed in order to determine **the relative signs of the matrix elements**. It was found that using the current data set only a few signs of matrix elements can be determined. For the remaining MEs, the solutions involving different combinations of signs, which resulted in similar absolute χ^2 values, had to be considered in the error estimation procedure. This will be further described in the following section.

6.2.1 Relative signs of the matrix elements

As already discussed in Section 3.3.1, the relative signs of the matrix elements can affect the observed cross sections. In order to take this into account and possibly deduce the relative signs of certain matrix elements, a number of fits to the experimental data were performed assuming different sign combinations. First, necessary assumptions were made about the signs of "benchmark" matrix elements, with respect to which the relative signs of the remaining matrix elements could be extracted. These benchmark matrix elements were selected as follows:

- Only one matrix element in the decay of each state was chosen to be positive.
- The transitional matrix elements for the in-band transitions were assumed to be positive, for example $\langle 4_1^+||E2||2_1^+\rangle$, $\langle 4_2^+||E2||2_2^+\rangle$, etc.
- If a state did not belong to a well-developed band, one of the matrix elements, governing its decay to the ground-state band was selected to be positive, for example $\langle 2_2^+||E2||0_1^+\rangle$.

Following the adopted convention, the transitional matrix elements marked in red in Fig. 6.11 were selected to be positive by default. To ensure that they remain positive during the minimization, their lower limits in the minimization procedure were set to zero. In addition, the signs of the diagonal matrix elements were previously measured to be negative for the 2_1^+, 4_1^+ and 6_2^+ states and positive for the 2_2^+ state, and thus their limits were set accordingly.

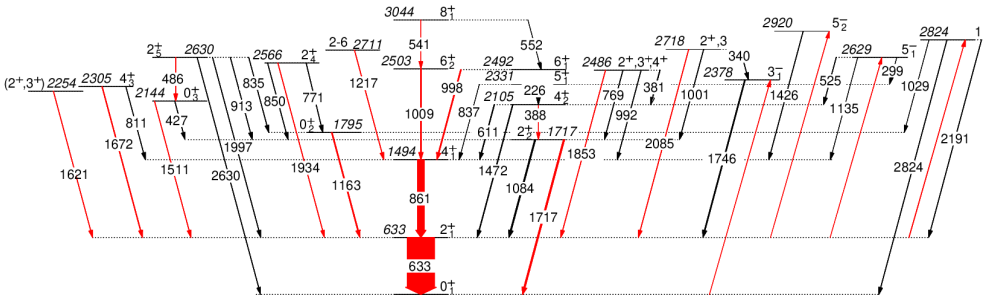

Figure 6.11 – The matrix elements related to the transitions marked in red were set to be positive by definition. The relative signs of the remaining matrix elements were investigated in the fit to the experimental data.

In order to extract the signs of the remaining matrix elements, first the experimental intensities were fitted without imposing any restrictions on the signs. The obtained result favoured all unsigned $E2$ matrix elements to be positive. However, it is naturally hard to flip the sign of a matrix element during the fitting procedure, when starting from a positive initial value. Thus, a series of minimizations were performed to the first three experimental points imposing a negative sign, and corresponding limits, for each matrix element one by one. If the transition was mixed

and the mixing ratio was known to be negative, the matrix element of the $M1$ component was set to be positive. Although probing the sign of each ME separately neglects correlations between the matrix elements, it can be viewed as an approximate procedure to deduce the signs that the data set is sensitive to. Each fitting procedure for testing the sign of a specific ME was performed with a fixed number of minimization steps (3x30x500) and using the set of MEs determined from the fit to the spectroscopic data as a starting point. This enabled a comparison between the obtained absolute χ^2 values. A summary of the performed tests can be found in Table 6.1. In the first column is the matrix element for which a negative value was imposed. The second column gives the difference between the absolute χ^2 value from the solution with all positive $E2$ MEs (referred to as "standard") and the one obtained assuming a negative sign for the considered ME. If the χ^2 difference was smaller than unity, it was concluded that this data set has no sensitivity to the sign of the particular matrix element, unless the new solution was excluded due to other criteria, as discussed in the following. However, the absolute values of the obtained MEs with a different sign combination may differ from the "standard" set of MEs. This has been taken into account in the error estimation procedure presented in Section 6.2.2.

The majority of the tests resulted in absolute $\Delta\chi^2 \leq 1$. However, the sign change of some matrix elements resulted in a large increase of the χ^2 value. Those were the $\langle 2_2^+||E2||(2^+,3^+,4^+)\rangle$ and $\langle 2_1^+||E2||2_2^+\rangle$ MEs, for which an increase of the χ^2 value by 3 was observed. The experimental data appeared to be sensitive to the relative signs of those MEs, supporting their positive signs. Sensitivity to specific signs may also be reflected in other ways. As a consequence of imposing an incorrect sign combination, certain MEs may take non-physical values. Alternatively, a change in the corresponding lifetime and its drastic deviation from the literature value may be observed, or a non-physical simulated γ-ray intensity distribution as a function of the scattering angle. For example, when the $\langle 0_1^+||E2||2_5^+\rangle$ ME is imposed to be negative, the obtained χ^2 value changes insignificantly, however, the obtained new set of MEs corresponds to a lifetime of the 2_5^+ state which is about 10 times larger than that measured with DSAM [61] ($0.19(3)$ ps). A lifetime of the order of 2 ps would result in the observation of both shifted and unshifted components of the corresponding peak, which was not supported by the present experimental data. Thus the investigated matrix element $\langle 0_1^+||E2||2_5^+\rangle$ should be positive. The advantage of using byproduct data from an RDDS experiment in the present analysis is the existence of such additional criteria with regards to the observed structure of each γ-ray peak. Using a similar strategy, a positive sign was also favoured for the $\langle 2_1^+||E2||4_2^+\rangle$ matrix element (although the obtained χ^2 value for its negative sign was significantly smaller), and for $\langle 2_2^+||E2||(2^+,3^+,4^+)\rangle$. Experimentally, the corresponding transitions had both shifted and unshifted components, while the lifetimes calculated assuming negative signs were too short, compatible with the observation of only a shifted component. The $\langle 2_2^+||E2||2_4^+\rangle$

and $\langle 2_2^+||E2||(2^+,3)\rangle$ MEs were also deduced to be positive, as the 2_4^+ and $(2^+,3)$ lifetimes obtained assuming their negative signs differed significantly from the literature values in Table 5.1.

In some of the tests, although the obtained χ^2 value was similar or even smaller than that for the "standard" solution, particular matrix elements became unphysically large. For example, imposing a negative sign of the $\langle 2_2^+||E2||0_3^+\rangle$ matrix element resulted in a $B(E2;2_2^+ \rightarrow 0_3^+)$ value of the order of 200 W.u. Thus, a positive sign for this ME was adopted. Another possible approach to gain more information about the relative signs of the investigated MEs is by simulating γ-particle coincidence intensities using the MEs with different signs and comparing them to the experimental data. Using this strategy, it was observed that a negative sign of the $\langle 2_1^+||E2||2_2^+\rangle$ ME yields a decreasing trend of the $2_2^+ \rightarrow 2_1^+$ and $2_2^+ \rightarrow 0_1^+$ transition intensities as a function of θ_{LAB}, which is not consistent with the experimental data.

As already mentioned, the assignments so far were only tentative as the possible correlations between the matrix elements were not accounted for. For example, a reduction in the cross section may be observed if the sign of a particular matrix element is negative, however, the effect might be compensated by changing the signs of other MEs. Thus additional tests were performed imposing changes of signs for different combinations of matrix elements that the data were found to be sensitive to. As all of the MEs for which positive signs were found were somewhat related to the 2_2^+ state, see Table 6.1, combinations of sign flips for the $\langle 2_1^+||E2||2_2^+\rangle$ ME together with each of the investigated MEs - $\langle 2_1^+||E2||4_2^+\rangle$, $\langle 4_1^+||E2||4_2^+\rangle$, $\langle 2_2^+||E2||(2^+,3^+,4^+)\rangle$, $\langle 2_2^+||E2||0_3^+\rangle$, $\langle 2_2^+||E2||2_4^+\rangle$, $\langle 2_1^+||E2||2_5^+\rangle$ and $\langle 4_2^+||E2||(2^+,3^+,4^+)\rangle$ - were investigated. In addition, selected combinations of three or more sign flips were tested. The obtained χ^2 values were always larger by at least 2.5 with respect to the "standard" solution. This supports further the sign assignments in Table 6.1.

Finally, one should comment that the relative signs of the $E1$ and $E3$ matrix elements were not probed within this work. Their influence on the Coulomb-excitation data is typically much lower than that of the $E2$ matrix elements, and only in one case it was possible to observe a weak sensitivity to a relative $E1/E3$ sign [90]. Moreover, in the present work only upper limits for most of the $E3$ MEs could be extracted. The signs of MEs related to the 8_1^+ state had no significant effect on the obtained results. Sign assignments for the MEs related to the transitions depopulating the 5_1^+ state were not attempted due to the problems regarding the large population of this state, discussed above.

6.2.2 Adopted matrix elements and error estimation

Following all of the tests described above, a final set of $E2$ and $M1$ matrix elements, obtained by fitting the first three experimental points ($\theta_{LAB} < 22^\circ$), was determined. It is summarized in the third columns of Tables 5.6 - 5.9. The corresponding signs, either assumed as presented in Fig. 6.11 (marked with an

asterisk in Tables 5.6 - 5.8) or extracted from the present data set (marked with a dagger), are also given. The sensitivity to diagonal $E2$ matrix elements will be discussed in Section 6.2.3, while Section 6.2.4 is focused on the obtained $E3$ matrix elements.

Table 6.1 – A summary of the tests performed in order to deduce the relative signs of the $E2$ matrix elements. One matrix element at a time, given in the first column, was imposed to be negative and a fit to the experimental data was performed. The difference in the absolute χ^2 value between the resulting solution and the solution assuming all positive MEs is given in the second column. Comments and conclusions on the signs are given in the last column.

Negative ME	Abs. $\Delta\chi^2$	Comments
$\langle 4_1^+ \|\| E2 \|\| (2^+, 3^+, 4^+) \rangle$	$+1.4$	**No sensitivity** to the sign
$\langle 2_2^+ \|\| E2 \|\| (2^+, 3^+, 4^+) \rangle$	$+2.7$	$\tau((2^+, 3^+, 4^+))$ five times shorter than τ_{LIT} [50]; **Positive sign**
$\langle 4_2^+ \|\| E2 \|\| (2^+, 3^+, 4^+) \rangle$	$+1.0$	**No sensitivity** to the sign
$\langle 4_1^+ \|\| E2 \|\| 4_3^+ \rangle$	$+0.1$	$\langle 4_1^+ \|\| M1 \|\| 4_3^+ \rangle$ positive; **No sensitivity** to the sign
$\langle 2_2^+ \|\| E2 \|\| 0_3^+ \rangle$	$+0.7$	Unphysically large ME; **Positive sign**
$\langle 2_2^+ \|\| E2 \|\| (2^+, 3) \rangle$	$+0.9$	$\tau((2^+, 3))$ becomes six times shorter than τ_{LIT}; **Positive sign**
$\langle 2_1^+ \|\| E2 \|\| 2_2^+ \rangle$	$+3$	Unphysical trends of the simulated γ-ray intensities; **Positive sign**
$\langle 2_1^+ \|\| E2 \|\| 4_2^+ \rangle$	-8	$\tau(4_2^+)$ is 10 times shorter than τ_{LIT} [50]; **Positive sign**
$\langle 4_1^+ \|\| E2 \|\| 4_2^+ \rangle$	$+2$	$\langle 4_1^+ \|\| M1 \|\| 4_2^+ \rangle$ positive; **No sensitivity** to the sign
$\langle 2_2^+ \|\| E2 \|\| 2_4^+ \rangle$	-0.3	$\tau(2_4^+)$ becomes five times smaller; **Positive sign**
$\langle 0_2^+ \|\| E2 \|\| 2_4^+ \rangle$	0.1	**No sensitivity** to the sign
$\langle 0_1^+ \|\| E2 \|\| 2_5^+ \rangle$	0.2	$\tau(2_5^+)$ becomes 10 times larger; **Positive sign**
$\langle 2_1^+ \|\| E2 \|\| 2_5^+ \rangle$	-0.3	$\langle 2_1^+ \|\| M1 \|\| 2_5^+ \rangle$ positive; **No sensitivity** to the sign
$\langle 0_2^+ \|\| E2 \|\| 2_5^+ \rangle$	0.4	**No sensitivity** to the sign
$\langle 2_2^+ \|\| E2 \|\| 2_5^+ \rangle$	0.2	**No sensitivity** to the sign

The transitional $E2$ MEs, which were extracted from the current data set on the basis of directly measured γ-particle coincidence yields for the corresponding transitions, are given in Table 5.6. The MEs, which were obtained by combining known branching and mixing ratios with the measured γ-ray yields, are given in Tables 5.7 and 5.8, respectively. Without additional spectroscopic information, these MEs

could not be determined from the present data set. The transitional $E2$ matrix elements involving states unobserved in the present study are given in Table 5.9. The same table lists the $E1$ matrix elements, which rely on the additional spectroscopic information (lifetimes) provided during the fitting procedure. Those matrix elements cannot be determined from the present data set and consequently their values obtained from the fit are provided without quoting uncertainties to avoid an impression that they are new results of the present study. They are presented here in the sole purpose of demonstrating that they adopted correct values in the fit. All MEs listed in Table 5.9 reproduced very well the spectroscopic data that they were fitted to. It was found, however, that they have rather limited influence on the extraction of matrix elements presented in Tables 5.6 - 5.8.

The uncertainties of the remaining MEs were calculated taking into account all possible sources of systematic uncertainty discussed in Section 6.2: fitting experimental $5_1^+ \rightarrow 4_2^+$ transition intensities (referred to as the "5_1^+ solution" from now on), fitting more experimental points for the $6_1^+ \rightarrow 4_1^+$ transition (called the "6_1^+ solution" from now on), using different relative signs of matrix elements. The latter has been done only for alternative solutions with χ^2 values similar to the one of the standard solution (resulting from the fit to the experimental data at the smallest scattering angles, assuming all positive $E2$ MEs), which were not excluded due to other criteria. It was found that changing the sign of a particular ME resulted in a significant change in only a small number of MEs, therefore this effect was taken into account only in the calculation of their uncertainties.

- The MEs related to the decay of the 4_1^+, 2_2^+, 5_1^+, 6_1^+, 6_2^+, 8_1^+, $(2^+, 3^+)$, $(2^+, 3)$ and $2-6$ states were adopted to be those resulting from the standard solution. The MEs corresponding to the alternative "5_1^+" and "6_1^+" solutions and their errors (from OP,ERRO) were used to estimate the limits of each matrix element, covering its maximum and minimum values obtained in all considered scenarios.

- The $\langle 2_1^+ || E2 || 0_2^+ \rangle$ ME obtained within the standard solution was adopted. In the corresponding uncertainty, the results of the alternative fits (the "5_1^+" and "6_1^+" solutions) were included, as well as those obtained by fitting only two experimental points for the $0_2^+ \rightarrow 2_1^+$ transition. This resulted in asymmetric error bars, favouring larger absolute values of the $\langle 2_1^+ || E2 || 0_2^+ \rangle$ ME.

- The MEs related to the decay of the 4_2^+ state were taken to be a weighted average of the MEs obtained in the standard, "5_1^+" and negative $\langle 4_1^+ || E2 || 4_2^+ \rangle$ solutions. Uncertainties covering the minimum and maximum MEs resulting from all of the considered solutions were adopted.

- The MEs related to the decay of the 4_3^+ state were taken to be a weighted average of the MEs obtained in the standard and negative $\langle 4_1^+ || E2 || 4_3^+ \rangle$

solutions. The uncertainties cover those resulting from both possible solutions.

- The MEs related to the decay of the $(2^+, 3^+, 4^+)$ state were adopted to be a weighted average of the MEs obtained in the standard, negative $\langle 4_1^+||E2||(2^+, 3^+, 4^+)\rangle$ and negative $\langle 4_2^+||E2||(2^+, 3^+, 4^+)\rangle$ solutions. The uncertainties were calculated accordingly.

- The MEs related to the decay of the 2_4^+ state were taken to be a weighted average of the MEs obtained within the standard and the negative $\langle 0_2^+||E2||2_4^+\rangle$ solution.

- The MEs related to the decay of the 2_5^+ state were calculated as weighted averages of the MEs obtained within the standard solution and the negative $\langle 2_1^+||E2||2_5^+\rangle$, $\langle 2_2^+||E2||2_5^+\rangle$, and $\langle 0_2^+||E2||2_5^+\rangle$ solutions, which had similar absolute χ^2 values. The adopted uncertainties incorporated all possible solutions, including an additional test performed using fewer experimental points for the transitions depopulating excited 0^+ states. Moreover, if the alternative branching ratios from Ref. [61] are used, a rather different set of transitional MEs related to the 2_5^+ state is obtained. In particular, the $2_5^+ \rightarrow 0_2^+$ transition was not observed in Ref. [61]. The largest change is recorded for the $\langle 0_3^+||E2||2_5^+\rangle$ ME, as the $I_\gamma(2_5^+ \rightarrow 0_3^+)/I_\gamma(2_5^+ \rightarrow 2_1^+)$ ratio is almost three times larger in the alternative solution, which will be further discussed in Section 7.1. The two sets of MEs describing the 2_5^+ decay, with uncertainties calculated considering similar sign tests, are given in Table 6.2.

- The $\langle 2_1^+||E2||0_3^+\rangle$ ME obtained within the standard solution was adopted. The uncertainties of this ME account for the results of the alternative "5_1^+" and "6_1^+" solutions, as well as those obtained by fitting only two experimental points for the $0_3^+ \rightarrow 2_1^+$ transition.

With this, the error estimation procedure was completed for the fitted $E2$ and $M1$ matrix elements. The resulting MEs with their relative signs are summarized in the third columns of Tables 5.6, 5.7 and 5.8.

6.2.3 Sensitivity to diagonal matrix elements

It would normally be expected that within the current data set, collected only at small scattering angles, the sensitivity to relative signs and spectroscopic quadrupole moments will be very limited. However, as it was shown in Section 6.2.1, it was possible to extract some information regarding the signs of specific MEs, mostly those related to the 2_2^+ state. Similarly, it can be tested whether performing the analysis without including the previously measured spectroscopic quadrupole moments would significantly affect the cross sections obtained under the kinema-

tic conditions of the present study. Since the diagonal $E2$ matrix elements of the 2_1^+, 4_1^+, 6_2^+ and 2_2^+ states were provided as additional literature information in OP,YIEL, the values of these MEs were treated as fit parameters, similarly to the $E1$ MEs. A comparison between the literature and fitted diagonal matrix elements is given in Table 6.3. The MEs provided in the third column of Table 6.3 are not new results of the present study, but should be viewed as fit parameters, which were correctly reproduced in the fitting procedure. For this reason, as it was done in the case of $E1$ matrix elements listed in Table 5.9, the diagonal matrix elements resulted from the present fit are quoted without uncertainties.

Table 6.2 – Matrix elements related to the decay of the 2_5^+ state obtained using different branching-ratio sets taken from Refs. [61, 62].

$\langle I_i^\pi \|\|E2\|\| I_f^\pi \rangle$	Fitted ME $[eb]$	
	BR from Ref. [62]	BR from Ref. [61]
$\langle 0_1^+ \|\|E2\|\| 2_5^+ \rangle$	$0.022(4)$	$0.026^{+0.007}_{-0.006}$
$\langle 0_2^+ \|\|E2\|\| 2_5^+ \rangle$	$0.105^{+0.027}_{-0.024}$	–
$\langle 0_3^+ \|\|E2\|\| 2_5^+ \rangle$	$0.38^{+0.10}_{-0.09}$	$0.57^{+0.20}_{-0.15}$
$\langle 2_1^+ \|\|E2\|\| 2_5^+ \rangle$	$0.018^{+0.009}_{-0.008}$	$0.016^{+0.009}_{-0.006}$
$\langle 2_2^+ \|\|E2\|\| 2_5^+ \rangle$	$0.34^{+0.07}_{-0.06}$	$0.30^{+0.09}_{-0.06}$
$\langle I_i^\pi \|\|M1\|\| I_f^\pi \rangle$	Fitted ME $[\mu_N]$	
	BR from Ref. [62]	BR from Ref. [61]
$\langle 2_1^+ \|\|M1\|\| 2_5^+ \rangle$	$-0.27(5)$	$-0.23^{+0.01}_{-0.09}$

To further test the sensitivity of the data set to the diagonal matrix elements, two additional fits to the first three experimental points were performed: one in which no diagonal MEs were defined and one in which only $\langle 2_2^+ \|\|E2\|\| 2_2^+ \rangle$ was excluded. The obtained absolute χ^2 value differed by less than 1 from the χ^2 value obtained for the standard solution (all positive signs, all diagonal MEs included). In both tests, certain matrix elements changed significantly with respect to the standard solution, considering their relative uncertainties, namely those related to the decay of the 2_2^+ $(14-23\%)$, 0_3^+ (16%), 2_5^+ $(21-22\%)$ and $2^+,3$ (7%) states. It was found that this change can be attributed mostly to the constructive effects induced by the positive quadrupole moment of the 2_2^+ state. Thus it was concluded that the present data set has a certain sensitivity to the $\langle 2_2^+ \|\|E2\|\| 2_2^+ \rangle$ matrix element. To illustrate this, the γ-ray yields at higher scattering angles were simulated (with a similar procedure as in Section 6.1) using different sets of MEs. The results are shown in Fig. 6.3. For the green curve, the MEs from the standard solution were used; the blue curve was based on the MEs obtained when the

quadrupole moment of the 2_2^+ state was set to zero; the orange curve - on the MEs obtained with all diagonal $E2$ matrix elements set to zero. As it is visible from both Fig. 6.3 (A) for the $2_2^+ \rightarrow 0_1^+$ transition and Fig. 6.3 (B) for the $2_2^+ \rightarrow 2_1^+$ transition, setting the diagonal MEs to zero has a significant effect on the simulated distributions. The largest effect originates from the $\langle 2_2^+||E2||2_2^+\rangle$ ME as it can be seen from the comparison of the blue and orange curves. At small scattering angles (θ_{LAB} below $22°$), the differences between the green and the blue curves are minimal (with overlapping error corridors) and there is only a 3.6% difference at $\theta_{LAB} = 22.5°$. At larger scattering angles, the intensities of the $2_2^+ \rightarrow 2_1^+$ transition simulated within the standard solution are larger with respect to the solution in which $\langle 2_2^+||E2||2_2^+\rangle$ was set to zero - by 16% at $26.5°$ and 25% at $29.5°$. This comparison illustrates the effects induced by the large positive quadrupole moment of the 2_2^+ state on the excitation cross section. Regarding the remaining transitions, no significant changes were found in the observed intensities, nor in the matrix elements involving the 4_1^+ or 6_2^+ states. It should be stressed that the performed tests were not considered in the error estimation, as one relies on the literature data for the signs and absolute values of the diagonal matrix elements.

Table 6.3 – Comparison of the diagonal matrix elements taken from the literature (Table 5.4) and those fitted to the experimental data (including the literature diagonal matrix elements). To avoid an impression that the latter are new results of the present analysis, they are quoted without uncertainties.

$\langle I_i^\pi\|\|E2\|\|I_f^\pi\rangle$	Literature ME $[eb]$	Fitted ME $[eb]$
$\langle 2_1^+\|\|E2\|\|2_1^+\rangle$	$-0.28(4)$	-0.28
$\langle 4_1^+\|\|E2\|\|4_1^+\rangle$	$-0.28(18)$	-0.29
$\langle 2_2^+\|\|E2\|\|2_2^+\rangle$	$+1.32(8)$	$+1.32$
$\langle 6_2^+\|\|E2\|\|6_2^+\rangle$	$-1.3(8)$	-1.3

6.2.4 Negative-parity states

As already discussed, it was assumed that the negative-parity states were predominantly populated by E3 transitions - 3_1^- in one step from the ground state, $5_{1,2}^-$ and 1^- in two steps via the 2_1^+ state, as shown in Fig. 6.12 in blue. The matrix elements, obtained by fitting the experimental data collected at $19.4° < \theta_{LAB} < 22°$, assuming such excitation paths, are given in the first row of Table 6.4 and will be referred to as a "standard solution" in the following. The value obtained for the $\langle 0_1^+||E3||3_1^-\rangle$ ME agrees with that reported in Ref. [75], but is much smaller than the one communicated in Ref. [83]. The remaining MEs have not been measured before. The obtained value of the $\langle 2_1^+||E3||5_1^-\rangle$ ME corresponds to a $B(E2)$ strength of 8.5 W.u, while those for the $\langle 2_1^+||E3||5_2^-\rangle$ and $\langle 2_1^+||E3||1^-\rangle$ MEs to 40 and 45 W.u., respectively. The latter MEs appear rather large, which suggests that important population paths have been omitted.

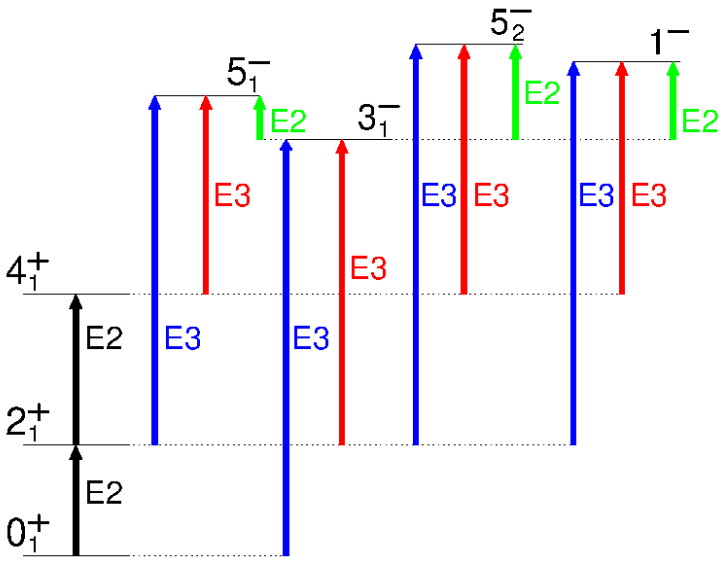

Figure 6.12 – Coupling schemes considered in the population of the negative-parity states in ^{106}Cd.

As a first step, additional $E3$ population paths with one extra step were included - from the 2_1^+ state for the 3_1^- state and from the 4_1^+ state for the remaining negative-parity states (presented in red in Fig. 6.12). The additional matrix elements were introduced in the sub-option ME of OP,GOSI and were fixed at specific values in the LCK section (see Appendix B). Subsequently, a full minimization was performed with the same number of minimization steps as for the standard solution. First, a conservative value for the $\langle 2_1^+||E3||3_1^-\rangle$ ME was adopted - two times larger than that of the $\langle 0_1^+||E3||3_1^-\rangle$ ME obtained in the standard solution ($0.466\ e\text{b}^{3/2}$), which corresponds to 46.5 W.u. A fitting procedure was performed and the only observed change in the obtained set of MEs was a reduction of the $\langle 0_1^+||E3||3_1^-\rangle$ ME by about 9%. As a next step, the $\langle 4_1^+||E3||5_2^-\rangle$ ME was introduced with a value of $0.584\ e\text{b}^{3/2}$, which corresponds to the same 46.5 W.u. transition probability. Even though the introduced $E3$ strength seemed larger than it is reasonable to expect in ^{106}Cd, the addition of such a coupling had no significant effect on the obtained MEs. A similar test was performed for the 5_1^- state and resulted in a reduction of the $\langle 2_1^+||E3||5_1^-\rangle$ ME by 8%. Finally, an additional ME $\langle 4_1^+||E3||1^-\rangle = 0.305\ e\text{b}^{3/2}$ was introduced, also corresponding to a transition probability of 46.5 W.u, which resulted in an increase of the $\langle 2_1^+||E3||1^-\rangle$ ME by 7%. Therefore, the matrix elements resulting from the standard solution (first row of Table 6.4) remained practically unchanged by introducing additional $E3$ excitation paths, considering their uncertainties.

Another possible population path was investigated for the $5_{1,2}^-$ and 1^- states, namely via an $E2$ transition from the 3_1^- state. In a quadrupole-octupole coupling scenario, discussed in Section 7.3, a multiplet of negative-parity states is

coupled to the 3_1^- state by $E2$ transitions of the same strength as that of the $2_1^+ \rightarrow 0_1^+$ transition. The analysis was performed under this assumption. First, the $\langle 3_1^- || E2 || 5_2^- \rangle$ ME was defined in the GOSIA input file and was fixed at a value of 0.92 eb, which is equivalent to a reduced transition probability of 26 W.u, i.e. equal to $B(E2; 2_1^+ \rightarrow 0_1^+)$. The full minimization procedure was carried out using the set of matrix elements resulting from the fit to spectroscopic data as initial values. Only the obtained $\langle 2_1^+ || E3 || 5_2^- \rangle$ ME differed significantly with respect to the standard solution - a reduction of about 56% was observed, leading to a value similar to that of the $\langle 2_1^+ || E3 || 5_1^- \rangle$ ME. In addition, the $\langle 0_1^+ || E3 || 3_1^- \rangle$ ME increased by 12%. This test shows that it is likely that the 5_2^+ state is built on the 3_1^- state, as even a rather strong $E2$ transition between them cannot fully compensate the large $\langle 2_1^+ || E3 || 5_2^- \rangle$ ME. On the contrary, a similar value of the $\langle 3_1^- || E2 || 5_1^- \rangle$ ME (0.92 eb) was already large enough to fully explain the entire population of the 5_1^- by a two-step process involving excitation of the 3_1^- state via an $E3$ transition, followed by the $E2$ transition. Finally, including a $\langle 3_1^- || E2 || 1^- \rangle$ ME of 0.48 eb, corresponding to an equivalent transition strength as that of the $2_1^+ \rightarrow 0_1^+$ transition, resulted in the $\langle 2_1^+ || E3 || 1^- \rangle$ matrix element decreasing by about 50%. In addition, the $\langle 0_1^+ || E3 || 3_1^- \rangle$ ME increased by 4%, as summarized in the last row of Table 6.4.

Table 6.4 – Summary of the obtained reduced transitional $E3$ matrix elements of the negative-parity states in ^{106}Cd. They result from GOSIA fits of the experimental γ-ray yields adopting different coupling schemes, as discussed in the text. To obtain the solutions presented in each row, the ME specified in the first column was included in the input file and fixed at a value corresponding to $B(E3) = 46.5$ W.u. (asterisk) or $B(E2) = 26$ W.u. (dagger). Bold font is used to indicate matrix elements that differ with respect to the solution presented in the first row. All values are given in eb$^{3/2}$.

Condition	$\langle 0_1^+ \|\| E3 \|\| 3_1^- \rangle$	$\langle 2_1^+ \|\| E3 \|\| 5_2^- \rangle$	$\langle 2_1^+ \|\| E3 \|\| 5_1^- \rangle$	$\langle 2_1^+ \|\| E3 \|\| 1^- \rangle$
–	$0.233(5)$	$0.54(2)$	$0.25(3)$	$0.30(1)$
$\langle 2_1^+ \|\| E3 \|\| 3_1^- \rangle^*$	$\mathbf{0.211(6)}$	$0.54(2)$	$0.25(3)$	$0.30(1)$
$\langle 4_1^+ \|\| E3 \|\| 5_2^- \rangle^*$	$0.233(5)$	$\mathbf{0.535(18)}$	$0.25(3)$	$0.30(1)$
$\langle 4_1^+ \|\| E3 \|\| 5_1^- \rangle^*$	$0.233(5)$	$0.54(2)$	$\mathbf{0.23(3)}$	$0.30(1)$
$\langle 4_1^+ \|\| E3 \|\| 1^- \rangle^*$	$0.233(5)$	$0.54(2)$	$0.25(3)$	$\mathbf{0.32(2)}$
$\langle 3_1^- \|\| E2 \|\| 5_2^- \rangle^\dagger$	$\mathbf{0.261(6)}$	$\mathbf{0.24(2)}$	$\mathbf{0.24(3)}$	$0.30(1)$
$\langle 3_1^- \|\| E2 \|\| 5_1^- \rangle^\dagger$	$\mathbf{0.245(6)}$	$0.54(2)$	$\mathbf{0^{+0.01}_{-0.12}}$	$0.30(1)$
$\langle 3_1^- \|\| E2 \|\| 1^- \rangle^\dagger$	$\mathbf{0.243(6)}$	$0.54(2)$	$\mathbf{0.24(3)}$	$\mathbf{0.16(2)}$

The addition of an $E2$ transition between each negative-parity state and the 3_1^- state resulted in drastic changes of the investigated matrix elements. Thus, this two-step $E3$-$E2$ population path cannot be neglected. However, some assumptions were made for the transition strengths, which leaves room for ambiguity. Using the current data set, without any additional information on the possible $E2$ transition

(i.e. a known branching ratio or its direct observation in the present experiment), it is not possible to extract both $E2$ and $E3$ matrix elements involved in the population of any of the investigated negative-parity states. On the other hand, each $E3$ ME can be described as a function of the assumed $E2$ ME and their upper limits can be obtained.

The adopted procedure for each of the states included performing a series of fits to the experimental data with $19.4^\circ < \theta_{LAB} < 22^\circ$ for different values of the additional $E2$ ME. The MEs obtained within the standard solution were taken as initial values in the minimization. For each fit, the $\langle 3_1^- || E2 || X \rangle$ ME was increased with a fixed step of 0.05 eb (starting from zero), fixed and then a minimization with $3\text{x}3\text{x}30$ steps was carried out. Additionally, the MEs which had a limited effect on the investigated $E3$ transition (i.e. on the population of each negative-parity state), were fixed at their standard values in order to limit the computational time. The normalized χ^2 value was saved for each value of the $\langle 3_1^- || E2 || X \rangle$ ME, together with the relevant $E3$ and $E2$ matrix elements. Only the transitions relevant for the population and decay of the 1^- state are presented in the partial level scheme in Fig. 6.13. The matrix elements related to those transitions were left free to vary during the minimization. The remaining MEs were fixed at the values corresponding to the standard solution.

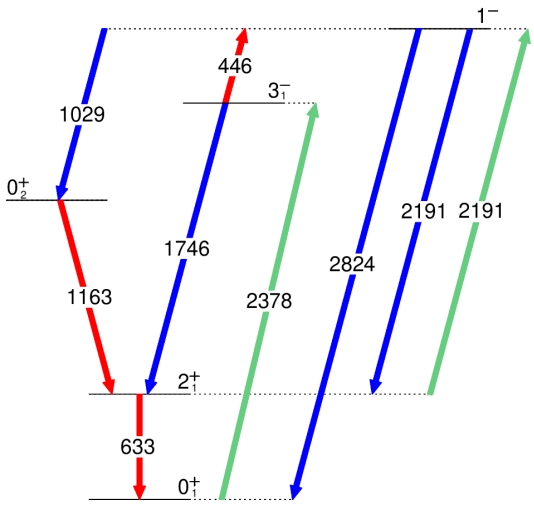

Figure 6.13 – Partial level scheme including the transitions relevant for the population and depopulation of the 1^- state in ^{106}Cd. Color code: blue - $E1$ multipolarity; red - $E2$; green - $E3$. The transitions not observed in the decay but involved in the population of the 1^- and 3_1^- states are presented with arrows in the corresponding direction.

The obtained $\langle 2_1^+ || E3 || 1^- \rangle$ ME as a function of the additional $\langle 3_1^- || E2 || 1^- \rangle$ ME is presented in the upper panel of Fig. 6.16 with a solid green line. The corresponding $\langle 0_1^+ || E3 || 3_1^- \rangle$ ME is presented with a dashed green line. As can be seen, in the region of roughly constant normalized χ^2 (see the lower panel of

Fig. 6.16, in green), the $\langle 0_1^+||E3||3_1^-\rangle$ ME remained almost unchanged with a tendency to slowly increase. A $\langle 3_1^-||E2||1^-\rangle$ ME of about 0.85 eb was found sufficient to account for the total population of the 1^- state, while the strength of the corresponding $E3$ transition, needed to solely explain the observed 1^- population is about 45 W.u., corresponding to $\langle 1^-||E3||2_1^+\rangle = 0.30$ eb$^{3/2}$. By fitting the obtained distribution with a second order polynomial, one obtains the relation: $\langle 2_1^+||E3||1^-\rangle = -0.155(8)A^2 - 0.217(7)A + 0.30(1)$, where $A = \langle 3_1^-||E2||1^-\rangle$. Thus, if either the $E2$ or the $E3$ ME needed to populate the 1^- state is determined in the future, it will be possible to also extract the other of the two matrix elements from this relation.

Similar calculations were performed for the 5_1^- state, varying the MEs which govern the transitions presented in Fig. 6.14. The remaining MEs were fixed at their values obtained in the standard solution and the 5_1^- population via the $2_1^+ \rightarrow 5_1^-$ transition was probed as a function of the assumed $\langle 3_1^-||E2||5_1^-\rangle$ value.

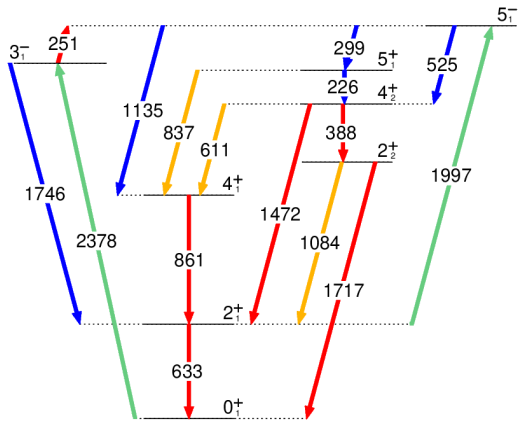

Figure 6.14 – Partial level scheme including the transitions relevant for the population and depopulation of the 5_1^- state in ^{106}Cd. Color code: blue - $E1$ multipolarity; red - $E2$; green - $E3$; orange - mixed $E2+M1$ character. The transitions not observed in the decay but involved in the population of the 5_1^- and 3_1^- states are presented with arrows in the corresponding direction.

The obtained results as a function of the $\langle 3_1^-||E2||5_1^-\rangle$ value are presented in the upper panel of Fig. 6.16 with a blue solid line for $\langle 2_1^+||E3||5_1^-\rangle$ and a blue dashed line for $\langle 0_1^+||E3||3_1^-\rangle$. The latter was not largely affected by the addition of the $E2$ population path. It was found that the upper limit of the $\langle 2_1^+||E3||5_1^-\rangle$ ME corresponds to 0.24 eb$^{3/2}$, while a $\langle 3_1^-||E2||5_1^-\rangle$ ME of 0.75 eb is large enough to account for the total observed population of the 5_1^- state. An $\langle 3_1^-||E2||5_1^-\rangle$ matrix element larger than 0.85 eb resulted in a significantly larger χ^2 value, as the observed population of the 5_1^- state could no longer be reproduced. The relation between the $E2$ and $E3$ matrix elements of interest is as follows: $\langle 2_1^+||E3||5_1^-\rangle = -0.113(3)B^2 - 0.237(3)B + 0.25(3)$, where $B = \langle 3_1^-||E2||5_1^-\rangle$.

The $\langle 2_1^+||E3||5_2^-\rangle$ ME as a function of the $\langle 3_1^-||E2||5_2^-\rangle$ ME was investigated in a similar manner. The MEs related to the transitions presented in Fig. 6.15 were left free to vary during the minimization, with the only exception being the $\langle 3_1^-||E2||5_2^-\rangle$ ME, which was increased in even steps for each separate fit. The obtained results are presented in red in Fig. 6.16. The observed γ-ray yields can be reproduced solely by two-step population via an $E2$ transition to the 2_1^+ state and a subsequent $E3$ transition with a matrix element of 0.54 eb$^{3/2}$. A similar population of the 5_2^- state can also be obtained in the alternative two-step process involving the 3_1^- state and an $E2$ transition with a matrix element of 1.5 eb. The relation between the two competing transitions is given by: $\langle 2_1^+||E3||5_2^-\rangle = -0.0615(7)C^2 - 0.263(1)C + 0.54(2)$, where $C = \langle 3_1^-||E2||5_2^-\rangle$.

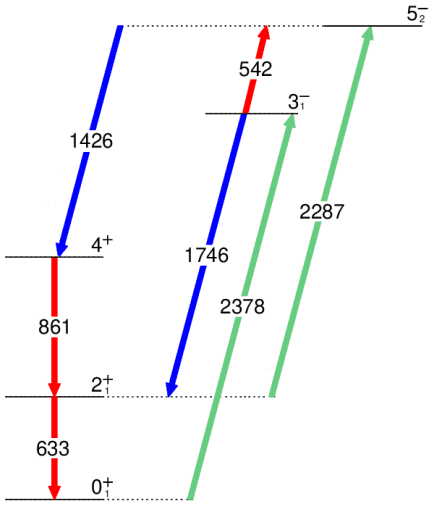

Figure 6.15 – Partial level scheme including the transitions relevant for the population and depopulation of the 5_2^- state in ^{106}Cd, which were varied during the fitting procedure. Color code: blue - $E1$ multipolarity; red - $E2$; green - $E3$. The transitions not observed in the decay but involved in the population of the 3_1^- and 5_2^- states are represented with arrows pointing upwards.

In conclusion, relations between the assumed $\langle 3_1^-||E2||X\rangle$ matrix elements and the $\langle 2_1^+||E3||X\rangle$ ME were extracted, where X is 1^-, 5_1^- or 5_2^-, which can be used in the future if additional information on the corresponding transitions becomes available. Upper limits for the discussed $E3$ matrix elements were extracted for the first time from the current Coulomb-excitation data and they are summarized in Table 6.5. Moreover, it was shown that the $\langle 0_1^+||E3||3_1^-\rangle$ ME was not strongly affected by the performed tests, thus considering all possible scenarios, a value of $0.23^{+0.04}_{-0.03}$ eb$^{3/2}$ has been adopted for this matrix element. This value has a much better precision than the measurement of Ref. [75].

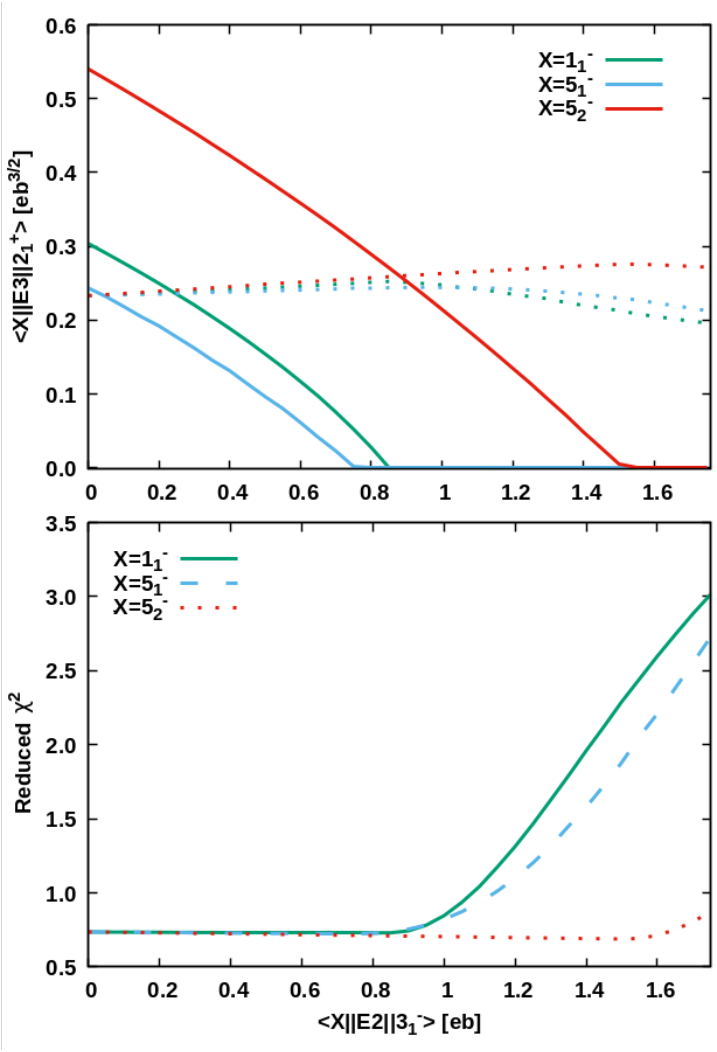

Figure 6.16 – Upper panel: the $\langle 2_1^+||E3||X\rangle$ ME as a function of the assumed $\langle 3_1^-||E2||X\rangle$ ME, where X is 1^- (green), 5_1^- (blue) or 5_2^- (red). The corresponding value of the $\langle 0_1^+||E3||3_1^-\rangle$ matrix element is presented with dotted lines. Lower panel: the reduced χ^2 value obtained from a GOSIA fit assuming the corresponding $\langle 3_1^-||E2||X\rangle$ value.

Table 6.5 – Upper limits of the transitional $E3$ and $E2$ MEs describing the population of the 1^- and $5_{1,2}^-$ states, resulting from the current analysis, as well as corresponding $B(E2)$ and $B(E3)$ limits expressed in W.u.

X	$\langle 2_1^+\|\|E3\|\|X\rangle$ [eb$^{3/2}$]	$B(E3; X \to 2_1^+)$ [W.u.]	$\langle 3_1^-\|\|E2\|\|X\rangle$ [eb]	$B(E2; X \to 3_1^-)$ [W.u.]
1^-	< 0.34	< 58	< 0.85	< 81
5_1^-	< 0.28	< 11	< 0.75	< 17
5_2^-	< 0.54	< 40	< 1.6	< 78

6.3 Calculation of lifetimes

The lifetimes of the populated states can be extracted using the obtained set of matrix elements, based on the present experimental data, and the literature branching and mixing ratios. An exception is the lifetime of the 2_1^+ state, which was used for normalization, as well as the lifetimes of the negative-parity states and the unobserved 8_1^+ state, which were provided as additional constraints of the GOSIA fit and thus they cannot be determined from it.

As a first step, the transition probabilities, corresponding to each of the obtained MEs, were calculated using Formula 5.5. The upper and lower limits of the transition probabilities were also calculated, considering the uncertainties of each ME. Subsequently, using Formula 5.4, the partial lifetimes $\tau^j = 1/\lambda^{\gamma_j}$ for each decay branch j were calculated together with their limits, and then combined together:

$$\lambda^{TOT} = 1/\tau = \sum (1 + \alpha_j)\lambda^{\gamma_j}. \tag{6.1}$$

The lifetime uncertainty limits were calculated using the corresponding maximum and minimum transition probabilities. The uncertainties of the transition energy were taken from the third column of Table 5.2, while the internal conversion coefficients α_j were calculated using the online BRICC calculator [91]. The uncertainties of α_j were not taken into account.

In this way, it was possible to extract the lifetimes of the populated states in ^{106}Cd from the measured γ-ray intensities, in a way that is independent and complementary to the RDDS analysis of Ref. [50]. The obtained results are summarized in Table 6.6. Certain discrepancies can be noticed, as discussed in the following.

- The obtained $\tau(0_2^+)$ is almost twice as large as the lifetime reported in Ref. [50]. However, considering the large uncertainty of the current result, the two measurements agree within 2σ.

- The $\tau(0_3^+)$ obtained from the present Coulomb-excitation data could not be determined via the RDDS technique due to the insufficient statistics at different target-degrader distances. The current result agrees within 1σ with the lifetime calculated using the ME from another Coulomb-excitation study [71], equal to 11^{+32}_{-6} ps.

- The lifetimes of the 2_2^+ state obtained via unsafe Coulomb excitation and via RDDS agree within 1σ. The present result agrees with those obtained in previous Coulomb-excitation measurements (mean value of $\tau(2_2^+) = 0.48(3)$ ps, Table 5.1) within 1σ as well.

- The $\tau(2_4^+)$ obtained in the current analysis is consistent with the lifetime limit deduced from the RDDS study. Moreover, it agrees within 1σ with the result reported in Ref. [61] ($0.10(1)$ ps). This shows that using the byproduct data it was possible to access information beyond the limitations of the RDDS technique.

Table 6.6 – Lifetimes calculated from the MEs summarized in Tables 5.6, 5.7 and 5.8. The lifetimes extracted using the RDDS method from the same data set are given in the third column. The values marked with asterisks are a weighted average of the values reported in Ref. [50].

I^π	E_x [keV]	τ [ps] Current work	τ [ps] Ref. [50]
0_2^+	1795	$2.46^{+0.35}_{-0.82}$	$1.32(10)^*$
0_3^+	2144	13^{+1}_{-5}	–
2_2^+	1717	$0.55^{+0.03}_{-0.05}$	$0.50(2)^*$
2_4^+	2566	$0.11^{+0.04}_{-0.03}$	< 0.3
2_5^+	2630	$0.45^{+0.23}_{-0.13}$	–
$(2^+, 3^+)$	2254	$0.60^{+0.05}_{-0.06}$	–
$2^+, 3$	2718	$0.33^{+0.05}_{-0.04}$	–
$2 - 6$	2711	$0.37^{+0.07}_{-0.05}$	–
4_1^+	1494	$1.23(7)$	$1.4(2)$
4_2^+	2105	$7.6^{+1.6}_{-1.5}$	$4.1(7)$
4_3^+	2305	$0.17(2)$	$1.1(1)$
$2^+, 3^+, 4^+$	2486	$2.12^{+0.23}_{-0.20}$	$2.34(17)^*$
5_1^+	2331	9^{+976}_{-1}	–
6_1^+	2492	$0.66^{+0.24}_{-0.03}$	< 2
6_2^-	2503	$0.48^{+0.03}_{-0.04}$	$1.22(15)^*$

- The lifetime of the 2_5^+ state was not obtained in the RDDS analysis of the current data set. The present result agrees within 2σ with the measurement of Ref. [61].

- It was possible to obtain the lifetimes of several states, which were not previously measured in Ref. [50]: $(2^+, 3^+)$ at 2254 keV, $(2^+, 3)$ at 2718 keV and $2 - 6$ at 2711 keV. However, assumptions were needed regarding the spins of these states. Moreover, there was some ambiguity regarding the origin of the relevant γ-ray peaks, which could be attributed to the de-excitation of other excited states or to a sum of more than one transition. Thus, the obtained lifetimes should be viewed as lower limits, rather than absolute measurements. Nevertheless, the values reported in Table 6.6 are in agreement (well within 1σ) with those reported for the $(2^+, 3^+)$ and $(2^+, 3)$ states in Ref. [61]. A discrepancy is observed for the obtained lifetime of the $2-6$ state, which is almost twice the value reported in Ref. [61], although the two agree within 3σ.

- The lifetime of the strongly populated 4_1^+ state obtained from the present analysis is also in agreement with the result of the RDDS measurement within 1σ, although it is slightly shorter. It is important to note that if the cross section to populate this state was strongly affected by Coulomb-nuclear effects, the obtained lifetime would be longer with respect to the literature value. This is due to the Coulomb-nuclear destructive interference, predicted with FRESCO (Fig. 5.6 (A)), which would result in a reduction of the excitation cross section, therefore a reduction of the corresponding ME, and an increase of the lifetime. When compared to other Coulomb-excitation studies, the obtained result shows an agreement within 1σ with Ref. [72] and within 2σ with the more recent studies [71, 75].

- The lifetime obtained for the 4_2^+ state disagrees with the measurement of Ref. [50] by more than 3σ. However, considering the discrepant branching ratios in the decay of this state, it was difficult to make firm conclusions regarding its character and the obtained lifetime.

- The obtained lifetime of the 4_3^+ state is much smaller than the value reported in Ref. [50]. A possible reason behind this can be the effects of the nuclear interaction, which would result in an increased excitation cross section if an $E4$ population path is considered. However, according to the FRESCO calculation the first few experimental points were not strongly affected by the nuclear interaction (Fig. 5.8). Moreover, an additional GOSIA fit was performed, in which a $\langle 0_1^+||E4||4_3^+\rangle$ ME corresponding to a $B(E4)$ of 5 W.u. was included. The obtained $\tau(4_3^+)$ of about 0.26 ps is still much smaller than the one extracted with the RDDS technique. Another reason could be an incorrect mixing ratio for the $4_3^+ \rightarrow 4_1^+$ transition. Finally, it is possible that the obtained new value is correct, while the RDDS measurement was affected by unobserved feeding. In line with the latter, another study using the DSAM technique yielded an upper limit of 0.36 ps [61], which is in good agreement with the current value, while it excludes the value from the RDDS measurement.

- The obtained lifetime of the $(2^+, 3^+, 4^+)$ state is in a good agreement (within 1σ) with the RDDS result [50].

- The strong population of the 5_1^+ state cannot be easily explained both within the safe and the unsafe Coulomb-excitation scenario. If the first few experimental points are fitted with GOSIA, a lifetime about 100 times smaller than the literature value is obtained. This corresponds to non-physical values of the $B(E2; 5_1^+ \rightarrow 4_2^+)$ transition probability of over 900 W.u., which suggests that there may be a doublet state with a similar de-excitation pattern. Moreover, the observed discrepancies related to the 4_2^+ state, which is directly fed by the decay of the 5_1^+ state, further complicate the problem.

- The obtained $\tau(6_1^+)$ can be viewed as a first measurement of this lifetime, as previously only upper and lower limits were extracted via RDDS [50] (< 2 ps) and via DSAM [61] (> 0.35 ps), respectively. The present result is in a good agreement with both limits.

- The value of $\tau(6_2^+)$ reported in Ref. [50] is more than twice as large as the current value. However, another study [61], using the DSAM technique, yielded a value of $0.26^{+0.44}_{-0.14}$ ps, almost two times smaller than the current $\tau(6_2^+)$, although they are in agreement within 1σ. Using the matrix elements reported in the Coulomb-excitation study of Ref. [75], the corresponding lifetime was calculated to be $0.54(8)$ ps, which is in line with the present work. A more recent Coulomb-excitation study reports a larger value of $\tau(6_2^+) = 0.73(13)$ ps, agreeing within 2σ with the present measurement. Thus, it is possible that the RDDS measurement suffered from unobserved feeding, which resulted in an overestimation of the 6_2^+ lifetime.

6.4 Comparison with previous Coulomb-excitation studies

The MEs obtained using the unsafe Coulomb-excitation data can also be compared with those extracted from previous safe Coulomb-excitation studies (Table 6.7). The obtained $\langle 4_1^+||E2||2_1^+\rangle$ value determined in the current work is larger than the values reported in Refs. [71, 75] and agrees with them within 2σ. It is also consistent with an older safe Coulomb-excitation study [72] within 1σ. The $\langle 6_2^+||E2||4_1^+\rangle$ value extracted from the current analysis is consistent within 1σ with the value reported in Ref. [75] and within 3σ with that obtained in Ref. [71]. The obtained $\langle 2_2^+||E2||0_1^+\rangle$ and $\langle 2_2^+||E2||2_1^+\rangle$ matrix elements agree within 2σ and 1σ, respectively, with the values reported in Refs. [71, 75]. The remaining matrix elements in Table 6.7 were measured only in Ref. [71] and they are in excellent agreement with the MEs obtained in the current work, however they are subject to much larger uncertainties (up to 50%). This comparison illustrates once again that analysis of Coulomb-excitation data from an experiment that does not fulfill Cline's safe criterion can yield results that are fully consistent with those obtained under "safe" conditions.

6.5 Cross-section distributions – positive-parity states

As a final step one can also simulate with GOSIA the intensities of the experimentally observed transitions at all scattering angles, using the set of MEs resulting from a fit to the first three experimental points (Tables 5.6-5.9). Usually, if a good agreement between the experimental and the simulated intensities is observed, one can consider that the set of MEs describes well the electromagnetic properties of the nucleus of interest. In the present work, discrepancies may result not only from an incorrect nuclear-structure input, but also from effects of the nuclear interaction.

Table 6.7 – Selected matrix elements obtained in the current work compared with those reported in Refs. [71, 72, 75]. All MEs are given in units of eb.

ME	Current work	Ref. [75]	Ref. [72]	Ref. [71]
$\langle 4_1^+ \|\|E2\|\|2_1^+\rangle$	$1.12(3)$	$1.044(25)$	$1.11(7)$	$1.05(3)$
$\langle 6_2^+ \|\|E2\|\|4_1^+\rangle$	$1.45^{+0.06}_{-0.04}$	$1.37(10)$	–	$1.18(9)$
$\langle 2_2^+ \|\|E2\|\|0_1^+\rangle$	$0.157^{+0.006}_{-0.003}$	$0.169(4)$	–	$0.195(15)$
$\langle 2_2^+ \|\|E2\|\|2_1^+\rangle$	$0.41^{+0.02}_{-0.01}$	$0.415(15)$	–	$0.44(3)$
$\langle 2^+, 3^+, 4^+ \|\|E2\|\|2_1^+\rangle$	$0.100(4)$	–	–	$0.09(4)$
$\langle 2^+, 3^+, 4^+ \|\|E2\|\|2_2^+\rangle$	$0.34(2)$	–	–	$0.26(12)$
$\langle 0_3^+ \|\|E2\|\|2_1^+\rangle$	$0.024^{+0.006}_{-0.001}$	–	–	$0.026(13)$
$\langle 0_3^+ \|\|E2\|\|2_2^+\rangle$	$0.35^{+0.08}_{-0.02}$	–	–	$0.4(2)$

Using FRESCO, it was shown than at scattering angles below $22°$, negligible effects would be observed from the Coulomb-nuclear interference (Section 5.6.4). However, at higher angles larger discrepancies are expected and by comparing the measured transition intensities with the simulation based on the MEs fitted to the $19.4° < \theta_{LAB} < 22°$ range, we can deduce their magnitude. The green curves in Figs. 6.2-6.9 and their error bands were obtained with a procedure similar to the one described in Section 6.1 but using as an input the matrix elements fitted to the first three experimental points. In the following, these curves are compared to those simulated using the MEs corresponding to the spectroscopic data summarized in Tables 5.1-5.3 for each transition.

- For **strongly populated states** decaying with an experimentally observed intensity of at least 1% of that of the $2_1^+ \rightarrow 0_1^+$ transition, a good agreement between the simulated intensities using both sets of MEs is generally observed.
  - — **The $4_1^+ \rightarrow 2_1^+$ transition** [Fig. 6.2 (A)]. The experimentally obtained intensities as a function of the scattering angle are well reproduced by both literature values of the matrix elements and the results of the fit to the data from the first three angular ranges. The $\langle 4_1^+ \|\|E2\|\|2_1^+\rangle$ matrix element resulting from the fit agrees with the literature value within 1σ, although it is about 7% larger, see Table 5.6. The distribution seems rather smooth with no clear oscillations or a decrease of the intensity with angle, which was predicted by the FRESCO calculation, see Fig. 5.6 (A). This is rather unexpected, as the largest scattering angles correspond to almost touching nuclear surfaces.

  - — **The $2_2^+ \rightarrow 0_1^+$ and $2_2^+ \rightarrow 2_1^+$ transitions** [Fig. 6.3]. The experimental trends seem to be slightly better reproduced using the MEs obtained by

fitting the current experimental data. However, this can be explained by the influence of other matrix elements on the population of the 2_2^+ state, such as e.g. $\langle 4_2^+||E2||2_2^+\rangle$ and $\langle 2_5^+||E2||2_2^+\rangle$, which adopt considerably different values in the fit to the literature data and that to the measured transition intensities. Nevertheless, both simulations agree well within the uncertainties with the experimentally obtained intensities for all scattering angle ranges. The obtained distributions are in line with the predictions of FRESCO, suggesting that a small deviation from the pure Coulomb-excitation solution will appear for scattering angles above 24°. The matrix elements describing the decay of the 2_2^+ state obtained from fits of the intensities of both depopulating transitions in the $19.4^\circ \leq \theta_{LAB} \leq 22^\circ$ range agree within 1σ with the literature values (Table 5.6). The MEs obtained from this fit are a few percent smaller than the literature values, see last column of Table 5.6.

— **The $6_2^+ \rightarrow 4_1^+$ transition** [Fig. 6.4 (A)]. As already commented in Section 6.1, the intensities predicted on the basis of the matrix elements fitted to the literature data, namely using the lifetime from the RDDS study based on the current data set [50], are underestimated with respect to the experimentally observed values. The experimental trend can be well reproduced at all scattering angles by assuming a significantly different $\langle 6_2^+||E2||4_1^+\rangle$ matrix element (60% larger, see Table 5.6), resulting from the fit to the first three experimental points. This result is in a good agreement (1.3σ) with $\langle 6_2^+\|E2\|4_1^+\rangle = 1.37(10)$ eb, obtained in a recent Coulomb-excitation study [75] (note that Ref. [75] refers to the state in question as 6_1^+, but their level scheme reveals that it is in fact the 6_2^+ state at 2503 keV). On the other hand, the fitted $\langle 6_2^+||E2||4_1^+\rangle$ matrix element disagrees with that deduced from the measured lifetime by more than 8σ. For the $6_2^+ \rightarrow 4_1^+$ transition, pure Coulomb-excitation process is sufficient to account for the measured cross sections up to at least $\theta_{LAB} = 25^\circ$. Above $\theta_{LAB} = 26^\circ$, if there is a systematic deviation from the trend predicted with GOSIA, it is smaller than the uncertainties on the experimental points, which are larger in this angular range.

- The experimental intensities of transitions depopulating the **excited 0^+ states** have a decreasing trend with a minimum at about 23°, as predicted with FRESCO, resulting from the destructive Coulomb-nuclear interference (see Fig. 5.6 (C)).

  — **The $0_2^+ \rightarrow 2_1^+$ transition** [Fig. 6.5 (A)]. As suggested by FRESCO calculations presented in Section 5.6.4, nuclear influence is not negligible already at 22°, thus another GOSIA fit to the first two experimental

points was performed and the difference between its result and that of the standard analysis (using $19.4^\circ < \theta_{LAB} < 22^\circ$ data) was incorporated in the obtained uncertainties. The individual experimental points deviate by less than 2σ from the pure Coulomb-excitation prediction resulting from the fit to the $19.4^\circ \leq \theta_{LAB} \leq 22^\circ$ data. In contrast, the intensities simulated on the basis of the MEs calculated from the spectroscopic data are much larger with respect to the experimental values, with the exception of the very first data point. The $\langle 0_2^+ || E2 || 2_1^+ \rangle$ matrix element determined from this fit is about 30% smaller than that corresponding to the lifetime of the 0_2^+ state obtained in Ref. [50], although the two are in agreement within 2σ, considering the large uncertainty of the present result.

— **The $\mathbf{0_3^+ \rightarrow 2_1^+}$ transition** [Fig. 6.5 (B)]. The uncertainties of the measured intensities are rather large, however, the third experimental point seems significantly lower than the first two, in line with the FRESCO prediction for the 0_2^+ state. Similar procedure as for the 0_2^+ state was used to obtain the uncertainty of the $\langle 0_3^+ || E2 || 2_1^+ \rangle$ matrix element. It was fitted to the experimental data from $19.4^\circ \leq \theta_{LAB} \leq 22^\circ$ range, but its uncertainty accounts for the difference with the result of the fit performed to the first two experimental points ($19.4^\circ \leq \theta_{LAB} \leq 21^\circ$). The obtained $\langle 0_3^+ || E2 || 2_1^+ \rangle$ matrix element is in a perfect agreement with the literature lower limit [61] as well as with the value reported in Ref. [71]. The experimental points are consistent with the results of the GOSIA calculations assuming the literature upper limit for the 0_3^+ lifetime [61] and the $B(E2)$ values for the 0_3^+ decay obtained in Ref. [71], but the measured intensities seem to be lower with respect to the results of the simulation assuming the set of MEs fitted to the experimental data, although an agreement within 2σ is observed.

- **Relatively good agreement between the two approaches** is observed for some of the less strongly populated states:

  — **The $\mathbf{2^+, 3^+, 4^+ \rightarrow 2_1^+}$ transition** [Fig. 6.4 (B)]. The experimental points look more randomly scattered around the pure Coulomb-excitation solution in comparison to those for other transitions and in general follow well the trends predicted with both sets of MEs. The two simulations agree well within their uncertainties, and so do the $\langle 2^+, 3^+, 4^+ || E2 || 2_1^+ \rangle$ matrix elements derived using the two approaches.

  — **The $\mathbf{2_4^+ \rightarrow 2_1^+}$ transition** [Fig. 6.4 (C)]. A good agreement between the two simulations (within 1σ) and the experimental data is achieved assuming a pure Coulomb-excitation process. The $\langle 2_4^+ || E2 || 2_2^+ \rangle$ matrix

elements resulting from the two approaches agree within 1σ and differ by only 4%. The intensities calculated using the set of matrix elements resulting from the fit to the spectroscopic data seem to slightly overestimate the measured values. Small deviations of the experimental points from the simulation start to appear at higher angles (above 25°), although they resemble a random scatter rather than a systematic effect.

— **The $\mathbf{6_1^+ \rightarrow 4_1^+}$ transition** [Fig. 6.2 (B)]. Only upper and lower limits of the lifetime of the 6_1^+ state were previously reported (0.35 ps$< \tau(6_1^+) <$ 2 ps), which are consistent with the present result. Thus, the intensity simulated assuming the MEs obtained from a fit to the experimental data is also in agreement with the lower limit shown with the dotted line in Fig. 6.2 (B). However, fitting only the first three experimental points was not sufficient to reproduce well the data at higher angles. This was rather unexpected, as the decay of the 6_2^+ state, which has a similar distribution, was well fitted. Thus it was attempted to perform a fit to data from the entire $19.4^\circ \leq \theta_{LAB} \leq 26^\circ$ range. This resulted in an improved agreement (2σ) between the experimental and simulated intensities for $\theta_{LAB} > 25^\circ$. The uncertainties in Fig. 6.2 (B) cover the solutions obtained by fitting the first three and the first six ranges of θ_{LAB}. One should also note that the measured intensity of the 998-keV γ-ray peak includes a small contribution from the (2^+, 3^+, 4^+) $\rightarrow 4_1^+$ transition, plotted in purple, which is accounted for in the analysis. Another observation is that the populations of the 6_1^+ and 6_2^+ states measured in the present experiment are very similar, while in the "safe" Coulomb-excitation study with a ^{48}Ti target [75] only the 6_2^+ state has been observed.

— **The $\mathbf{2^+, 3 \rightarrow 2_1^+}$ transition** [Fig. 6.8 (B)]. The $\langle 2^+, 3 \| E2 \| 2_1^+ \rangle$ matrix elements obtained from the fits to the $19.4^\circ \leq \theta_{LAB} \leq 22^\circ$ data and to the literature values are in a good agreement considering their uncertainties, with the former being 7% larger (Table 5.6). Therefore, both simulations of the intensities describe equally well the experimental data below $\theta_{LAB} = 24^\circ$. A linear increase of the measured intensity is observed at higher angles, which resembles the distribution predicted with FRESCO for the 2_2^+ state, see Fig. 5.6 (B).

— **The $\mathbf{(2^+, 3^+) \rightarrow 2_1^+}$ transition** [Fig. 6.8 (A)]. No deviation from the pure Coulomb-excitation prediction is observed and both sets of MEs describe equally well the experimental data. As it was already discussed in Section 4.3.1 the γ ray at about 1620 keV can be attributed to the decay of both the $(2^+, 3^+)$ state at 2254 keV and the (4^+) state

at 2252 keV, which has a lifetime shorter by 30% than the $(2^+, 3^+)$ state [61]. If both states were populated in the present experiment, one would expect a combined intensity over a factor of two higher than that experimentally observed. On the other hand, the experimental data are well reproduced using the measured lifetime of the 2254-keV $(2^+, 3^+)$ level. This hints that the $2252-$keV state was probably not populated in the Coulomb-excitation process, although it appears more collective. A possible reason behind this could be the spin of the state at 2252 keV, firmly assigned as a 3^+ in Ref. [61]. This would provide a consistent explanation of the measured cross-section distribution: out of the two collective states forming the doublet only that at 2254 keV was populated, with the excitation of the 2252-keV 3^+ state being hindered due to its odd spin. For the same reason, a 2^+ spin-parity would be favoured for the 2254-keV level. One should note that these conclusions rely on the level lifetimes [61] and should definitely be verified by complementary measurements.

- **Discrepancies** between the intensities simulated with the two approaches and/or the experimental data are observed for the following transitions:

  — **The $\mathbf{2_5^+ \rightarrow 2_1^+}$ transition** [Fig. 6.4 (D)]. The intensities simulated using the matrix elements based on the literature spectroscopic data have a similar overall trend as the experimentally observed ones but significantly overestimate them (by more than 3σ). On the other hand, the MEs obtained by fitting the data collected at the smallest scattering angles describe the experimental data well in the full range of scattering angles. The $\langle 2_5^+ || E2 || 2_1^+ \rangle$ matrix element resulting from this analysis is 40% smaller then the literature value, although the two agree within 1σ, considering the large uncertainties (Table 5.6). The rather large uncertainties of the matrix elements involving the 2_5^+ state are a consequence of their unknown relative signs, as it was discussed in Section 6.2.2.

  — **The $\mathbf{2-6 \rightarrow 4_1^+}$ transition** [Fig. 6.10]. Using the lifetime of the $2-6$ state reported in Ref. [61] and assuming a spin of 2^+, which implies a pure E2 character for its decay, results in the simulated intensities overestimating the experimental data. If the first three experimental points are fitted, the obtained $\langle 2-6 || E2 || 4_1^+ \rangle$ matrix element is 35% smaller than the literature value. The simulated intensities using the latter ME and assuming a pure Coulomb-excitation process are in a good agreement with the experimental data for all scattering angles. One should note, however, that if an $M1$ admixture was introduced, it would be possible to reproduce both the measured transition intensi-

ties and the level lifetime at the same time. The $\langle 2-6||E2||4_1^+\rangle$ value resulting from the fit agrees with the literature value within 2σ.

— **The $5_1^+ \rightarrow 4_2^+$ transition** [Fig. 6.6 (B)]. The peak corresponding to the $5_1^+ \rightarrow 4_2^+$ transition was not observed at the smallest scattering angle, but a rather strong population of the 5_1^+ state is observed at higher angles, which cannot be easily explained assuming neither pure Coulomb excitation, nor the nuclear influence on the population process if the spin-parity assignment is correct. As shown in Section 6.2 the $E2$ matrix element necessary to reproduce the measured cross sections assuming a pure Coulomb-excitation process corresponds to a $B(E2; 5_1^+ \rightarrow 4_2^+)$ value of about 900 W.u., which is clearly nonphysical and discrepant with the known lifetime of this state (Table 5.1). The intensities predicted using the spectroscopic data are an order of magnitude smaller than those experimentally measured. Even the matrix elements fitted to the first two experimental points do not provide a correct reproduction of the intensities at larger scattering angles. Therefore the 5_1^+ state constitutes a puzzle which requires more investigation.

- **Signature of higher-order multipolarities** involved in the excitation process was observed for some of the 4^+ states. The experimental distributions of the transitions depopulating $4_{2,3}^+$ states may be explained by the presence of a non-negligible $E4$ strength carried by these levels, which has a very limited influence on the pure Coulomb-excitation cross sections, but, in contrast, becomes important when nuclear interaction starts to play a role. The effect of an $E4$ excitation on the measured cross section was discussed on the basis of FRESCO calculations in Section 5.6.4. Moreover, from inelastic scattering of protons and deuterons on $A \approx 100$ nuclei [96] it was concluded that the $E4$ strength tends to be fragmented between states around $2.5-3$ MeV, which would be consistent with the current data for the $4_{2,3}^+$ states in ^{106}Cd.

— **The $4_2^+ \rightarrow 2_1^+$ and $4_2^+ \rightarrow 4_1^+$ transitions** [Fig. 6.7]. Both simulations are in a good agreement with the experimental data at the smallest scattering angles for $4_2^+ \rightarrow 2_1^+$ decay. A disagreement between the two solutions is observed for the other depopulating transition, which can be linked to the discrepancy between the literature value of the branching ratio for the decay of the 4_2^+ state and the intensities measured in the present experiment, discussed in Section 5.4.2. The experimental data for both transitions exhibit a rather rapid increase in the cross section at scattering angles higher than 22°, which hints at possible contributions from higher-order multipolarities in the excitation process. The

distributions resemble an oscillation with a very large amplitude, departing from pure Coulomb excitation by more than 5σ. One should note, however, that the 4_2^+ state is fed by the decay of the 5_1^+ state, whose unusual features make it more difficult to draw conclusions regarding the character of the 4_2^+ state and the role of the nuclear effects in its excitation. The $\langle 4_2^+||E2||2_1^+\rangle$ matrix element determined from the fit to the $19.4^\circ \leq \theta_{LAB} \leq 22^\circ$ data is consistent within 1σ with the value deduced from the literature data, while for the $\langle 4_2^+||E2||4_1^+\rangle$ values the agreement is worse (within 2σ).

— **The $4_3^+ \rightarrow 4_1^+$ transition** [Fig. 6.6 (A)]. Similar conclusions as for the 4_2^+ state can be drawn for the 4_3^+ state. The intensities simulated using the literature value of the $\langle 4_3^+||E2||2_1^+\rangle$ matrix element differ by more than 2σ from the values obtained using the MEs fitted to the measured γ-ray intensities. The former strongly underestimate the experimental data, while the latter can describe only the very first few experimental points. Interestingly, the transition strength deduced from the present data for the 4_3^+ state is larger than that corresponding to the lifetime, while it is smaller for the 4_2^+ state. The $\langle 4_3^+||E2||2_1^+\rangle$ matrix element obtained from the present data is about three times larger than the literature value, however the two agree within 3σ.

7 - Discussion and outlook

Based on the excitation energy pattern of the low-lying states, stable cadmium isotopes were considered textbook examples of spherical vibrational nuclei [2, 104]. As an example, a partial level scheme of ^{112}Cd organized into one-, two- and three-phonon multiplets is presented in Fig. 7.1.

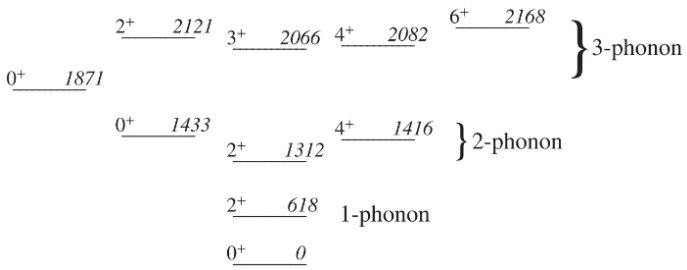

Figure 7.1 – Low-energy excited states in ^{112}Cd organized into one-, two- and three-phonon multiplets. Figure adapted from Ref. [105].

However, a large difference between the reduced transition probabilities of the transitions connecting each of the proposed two-phonon states with the one-phonon 2_1^+ state is present. The $B(E2; 4_1^+ \rightarrow 2_1^+)$ value follows the expectation for a harmonic vibration, while $B(E2; 2_2^+ \rightarrow 2_1^+)$ is substantially lower than twice the $B(E2; 2_1^+ \rightarrow 0_1^+)$ value and $B(E2; 0_3^+ \rightarrow 2_1^+)$ is almost vanishing. This decay pattern could be explained by strong mixing with a shape-coexisting deformed intruder structure that was systematically observed in the cadmium isotopes [106]. This scenario was questioned following e.g. the multi-step Coulomb-excitation study of ^{114}Cd [107]. From a comparison of an extensive set of $E2$ matrix elements determined in this study with the results of a mixing calculation it was concluded that the strong mixing hypothesis could not provide a consistent description of the measured $E2$ strengths.

A good reproduction of the observed transition probabilities could be achieved within an IBM configuration mixing calculation with a partial dynamical symmetry [108]. This calculation introduced terms resulting in mixing of phonon states. The mixing was needed to distribute the $E2$ strength among several levels and thus explain the small $B(E2)$ values for the transitions connecting the two- and three-phonon 0^+ states to the 2_1^+ state. However such a redistribution of the $E2$ strength would require its enhancement in higher-lying levels, which, as pointed out by Garrett et al. [11], is not experimentally observed. As an alternative, a reorganisation of the level schemes of $^{110-116}$Cd was proposed [105] in terms of rotational structures.

Following the proposed rearrangement of the level scheme, Garrett et al. performed a series of experiments utilizing β^+/electron-capture decay of ^{110,112}In and

β^- decay of ^{112}Ag to populate excited states in ^{110,112}Cd [10, 11]. Several low-intensity γ rays, depopulating key states, were observed. Transition probabilities were calculated using the extracted branching ratios in combination with previously measured lifetimes [103, 109]. The obtained $B(E2, 2_5^+ \rightarrow 0_4^+) = 34(15)$ W.u. and $B(E2, 4_6^+ \rightarrow 2_5^+) = 77(30)$ W.u. in ^{112}Cd demonstrated the increased collectivity of the structure built on the 0_4^+ state, presented in Fig. 7.2. Additionally, a γ band $(K = 2)$ associated with the ground state, built on the presumed two-phonon 2^+ state, was proposed. Moreover, a rotational structure built on the reinterpreted 0_3^+ two-phonon state and a γ band associated with the established "intruder" band were proposed (Fig. 7.2).

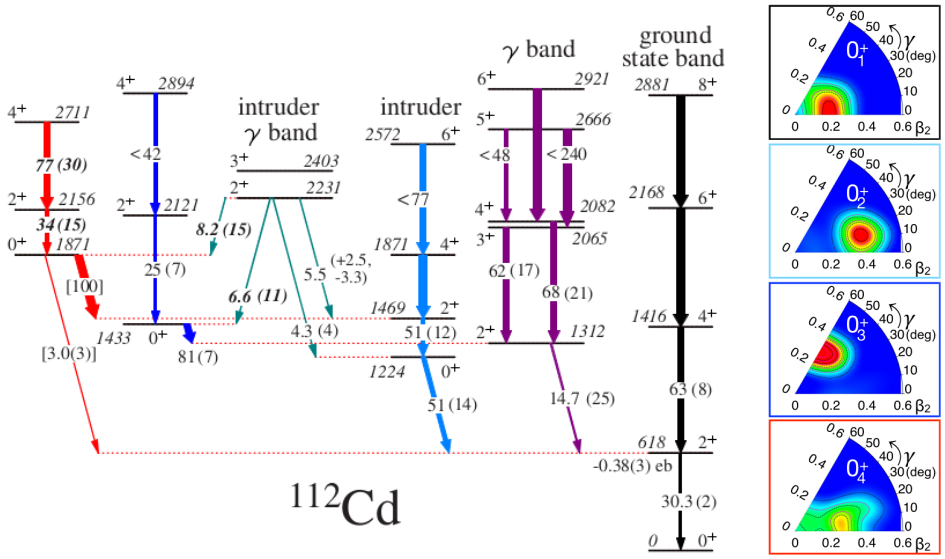

Figure 7.2 – Left: partial experimental level scheme of ^{112}Cd, presenting the collective, low-lying, positive-parity bands with their in-band and band-head decays. The experimental transition probabilities are given in W.u. (values in square brackets are relative $B(E2)$ values). Right: the collective wave functions of the band-heads in the (β_2, γ) plane, calculated using the SCCM method, with color coding corresponding to that used for the bands in the experimental level scheme. Figure adapted from Ref. [10].

Similar results were obtained for ^{110}Cd. The observed similarities between ^{110}Cd and ^{112}Cd hinted that the neutron degrees of freedom affected minimally the observed structure, favouring an interpretation invoking multiparticle-multihole proton excitations. This scenario is supported by the energy systematics of the excited 0^+ states as a function of the mass number, presented in Fig. 7.3. The observed parabolic shape with a minimum near the mid-shell is typical for multiparticle-multihole excitations, which are the main mechanism behind shape coexistence [13]. The idea of low-lying coexisting structures with different intrinsic shapes was explored using beyond-mean-field (BMF) calculations, based on the symmetry conserving configuration mixing (SCCM) method with the Gogny D1S energy density functio-

nal [110]. Within this model the nuclear states in the laboratory frame are obtained by mixing intrinsic states with well-defined deformations, which makes it a perfect tool for studying nuclear collectivity (vibrations, rotations, shape evolution, shape coexistence, shape mixing). As a downside, due to computational limitations in the implementation of the variational principle, parity and time-reversal symmetry breaking was not allowed, which resulted in stretched excitation-energy spectra with respect to the experimental ones [111,112]. In the calculated potential energy surfaces (PES) for ^{110}Cd projected on angular momentum 0 (see Fig. 15 (a) in Ref. [11]), a clear minimum at a prolate deformation $\beta_2 \approx 0.15$ is present. This is not consistent with a vibrational interpretation. Moreover, two more shallow minima were observed, corresponding to different deformation parameters ($|\beta_2|$ about 0.4 and 0.1) [11]. Further insight in the structure of the different bands was obtained by analysing the collective wave functions calculated within the SCCM method [110]. As an example, the results for the first four 0^+ states in ^{112}Cd are presented on the right side of Fig. 7.2 [11]. The model predicts the existence of a prolate ground state with $\beta_2 \approx 0.2$, a more deformed ($\beta_2 \approx 0.4$) triaxial 0^+_2 state, an oblate 0^+_3 state and a shape-mixed, evolving towards prolate 0^+_4 state. Based on the calculated transition probabilities, the levels of ^{110,112}Cd were organized into bands, strikingly similar to those suggested by experimental data, see Figs. 2 and 3 in Ref. [10]. In addition to the bands built on the 0^+ states, two γ bands were predicted. The two γ bands were strongly mixed, resulting in enhanced $E2$ transitions between the band members, which was in line with the experimentally observed transition probabilities. Generally, the predicted $B(E2)$ values were well reproduced for the decays of the band heads, while those for the in-band transitions were overestimated, as were the quadrupole moments.

The structure of Cd isotopes can also be described in the framework of shell-model calculations. Unfortunately, for isotopes heavier than ^{104}Cd a model space including proton orbitals beyond the $Z = 50$ shell gap becomes prohibitively large. Among the recent shell-model calculations for Cd nuclei, that of Ref. [113] focused on the deformation of low-spin states in $^{98-108}$Cd. The model space included the $2d_{5/2}$, $3s_{1/2}$, $2d_{3/2}$, $1g_{7/2}$ and $1h_{11/2}$ neutron orbitals and the $2p_{1/2}$ and $1g_{9/2}$ proton orbitals with an inert core of ^{88}Sr. An effective realistic nucleon-nucleon interaction originating from the CD-Bonn [114] potential was used, resulting in a G matrix called the v3sb effective interaction [115]. The effective proton charge ($e_\pi = 1.7e$) was determined by fitting the calculated $B(E2; 8^+_1 \rightarrow 6^+_1)$ value in ^{98}Cd to the known experimental value [116], while that for the neutrons ($e_\nu = 1.1e$) by comparing experimental and calculated $B(E2; 2^+_1 \rightarrow 0^+_1)$ values in ^{102,104}Cd [117]. The calculations were conducted in the full model space without any additional truncations. However, the model space did not permit proton excitations across the $Z = 50$ shell gap, even though such correlations were implicitly included by the use of proton and neutron effective charges. Therefore, the model could not accurately describe the shape-coexisting states arising from multi-particle multi-

hole excitations. Nevertheless, the calculation predicted a non-zero β_2 deformation parameter for the ground state ($\beta_2 \approx 0.18$ for ^{106}Cd) as well as its certain triaxiality. Very similar β_2 values were reported for the excited $0^+_{2,3}$ states.

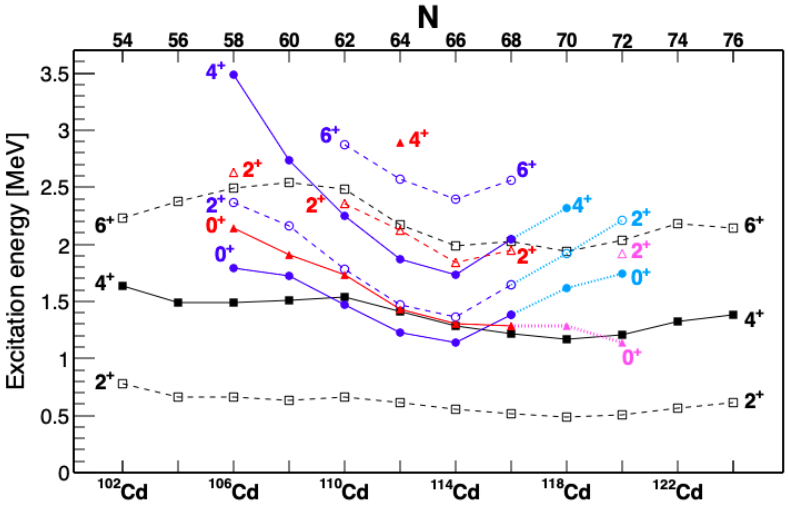

Figure 7.3 – Systematics of the excitation energies of low-lying excited states in $^{102-124}$Cd as a function of the neutron number N. The ground-state band is presented in black. The members of the intruder structure are presented in blue and those of the presumably oblate structure in red. Lighter colors and dotted lines are used for tentative assignments. Figure adapted from Ref. [4] with the new data from Ref. [62].

The scenarios discussed above differ in their predictions of shapes of specific states in Cd nuclei, which can be explored via low-energy Coulomb excitation. A series of experiments focused on the ^{110}Cd nucleus has been performed at HIL, Warsaw [118], LNL Legnaro [119] and Argonne National Laboratory (ANL). From the collected data it will be possible to determine the β and γ deformation parameters of the 0^+_1, 0^+_2 and 0^+_3 states via the quadrupole sum rules approach [5, 6].

While ^{110,112}Cd were and are still extensively studied, there are not many recent experiments addressing the structure of ^{108}Cd, especially in terms of transition probabilities. Based on the $B(E2)$ values resulting from a DSAM lifetime measurement [98], the 2^+_3 state in ^{108}Cd was ruled out as a three-phonon state and instead assigned as a band member of the rotational band built on the intruder 0^+ state. The decays out of this band were found to be very weak, suggesting a high purity of the intruder configuration. Based on comparison with the neighboring ^{110,112}Cd nuclei, it was concluded that the intruder band is moving towards higher excitation energies, while the members of the presumed two- and three-phonon structures are spread over a larger energy range. In addition to an IBM-based interpretation similar to those proposed for ^{110,112}Cd, an arrangement of the observed levels into collective bands was suggested, including notably a $K = 2$ γ band. An earlier study [120] identified a potential 6^+ member of this band.

7.1 Shape coexistence in ^{106}Cd

In contrast to ^{108}Cd, a large number of recent works were focused on ^{106}Cd. Two low-energy Coulomb-excitation studies were performed, yielding quadrupole moments of the 2_1^+, 4_1^+, 6_2^+ and 2_2^+ states (summarized in Table 5.4) [71, 75] and $|\beta_2|$ deformation parameters of the 0_1^+ and 2_1^+ states [71]. The RDDS measurement of Siciliano et al. [50] obtained the lifetimes or lifetime limits of a number of low-lying excited states, some of which for the first time. They were investigated with a guidance from a SCCM calculation performed along the lines of those for ^{110,112}Cd [10, 11], which predicted a number of low-energy coexisting structures [50]. The collective wave functions of the first few members of these structures are presented in Fig. 7.4. The ground state of ^{106}Cd was predicted to have a well-defined prolate shape ($\beta_2 = 0.2$), which is consistent with the measured $B(E2; 2_1^+ \rightarrow 0_1^+)$ value that corresponds to $\beta_2 \approx 0.17$. The calculated 0_2^+ and 0_3^+ states have a larger oblate ($\beta_2 \approx 0.27$) and prolate ($\beta_2 \approx 0.35$) deformation, respectively.

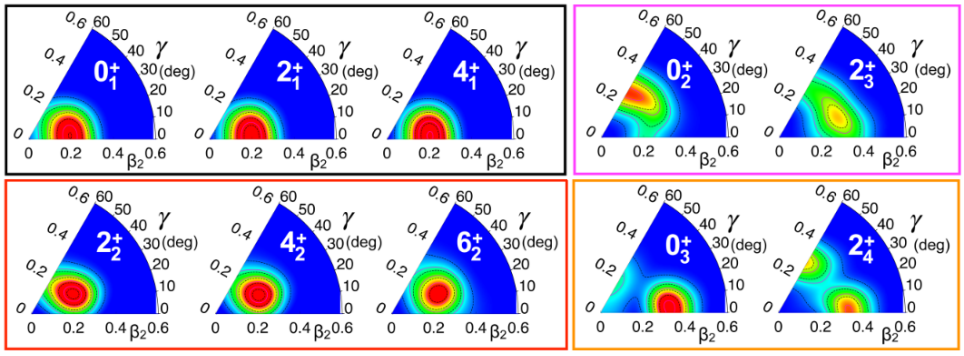

Figure 7.4 – Collective wave functions as a function of the deformation parameters (β, γ). Color-coded rectangles: black - the ground state band ; red - even-spin states from the $K = 2$ band associated with the ground state; magenta - oblate shape-mixing 0^+ and triaxial shape-mixing 2^+ states; orange - prolate shape-mixing band.

The partial level schemes of ^{106,110,112}Cd resulting from the SCCM calculation, presenting decay properties of the $0_{1,2,3}^+$ states and the 2^+ states built on them, are compared in Fig. 7.5. The transition probabilities, given in W.u., are taken from Refs. [10, 11, 50]. In the BMF calculations the oblate configuration is the 0_3^+ state in ^{110,112}Cd, and the 0_2^+ state in ^{106}Cd. However, from the experimental point of view, the oblate band-head in ^{106}Cd seems to be the 0_3^+ state. A clear indication for this is the preferential decay of the 0_3^+ state to the 2_2^+ state, which is consistent with the decay patterns of the presumably oblate structures in heavier Cd isotopes (presented e.g. in Figs. 36,39 in Ref. [4]). Moreover, the $B(E2)$ value corresponding to the decay of the oblate deformed 0^+ state in the BMF calculation agrees with the value obtained in the present Coulomb-excitation study,

$B(E2;0_3^+ \rightarrow 2_2^+)$= 41^{+19}_{-5} W.u., as it is the case in the heavier Cd isotopes, see Figs. 7.5 and 7.6. The obtained $\langle 0_3^+||E2||2_2^+\rangle$ matrix element is also in a perfect agreement with the result of a previous measurement [71], although the latter has a large experimental uncertainty (50%).

Based on the decay pattern of the 2_5^+ state, it was assigned as part of the band built on the 0_3^+ state. The $2_5^+ \rightarrow 0_3^+$ transition was observed for the first time in Ref. [61] and later confirmed in Ref. [62]. However, a discrepancy in the reported branching ratios is present. Using those from the most recent study [62] in the Coulomb-excitation analysis yields a $B(E2;2_5^+ \rightarrow 0_3^+)$ value of 10^{+6}_{-5} W.u. If one uses the alternative branching ratios from an older study [61], a value of 22^{+18}_{-10} W.u. is obtained. Both these values are smaller than the one predicted by the theory (52 W.u.), suggesting a smaller collectivity of the band built on the 0_3^+ state. One should note that while the BMF calculations predict that the collectivity of the oblate structure (built on the calculated 0_3^+ state in ^{112,114}Cd and on the 0_2^+ state in ^{106}Cd) decreases with N, an inverse trend seems to be observed in the $B(E2)$ data, even though the energy spacing in the band in question suggests the opposite. Both in the experiment and in the calculation, the $B(E2;0_3^+ \rightarrow 2_2^+)$ value in ^{106}Cd is less enhanced than its counterparts in the heavier Cd nuclei, which is in line with the higher excitation energy of the 0_3^+ state. One should also note that a 2_5^+ lifetime of $0.19(3)$ ps was obtained from a DSAM measurement following inelastic neutron scattering [61]. This lifetime, together with the branching ratios reported in Ref. [62], corresponds to a larger transition probability (21^{+8}_{-6} W.u.), which is still smaller than the value predicted by theory. To provide a firm conclusion on the collectivity of the band built on the 0_3^+ state, the relevant branching ratio needs to be remeasured.

A transition connecting the 0_2^+ state with the ground-state band was previously observed and from the current Coulomb-excitation analysis a $B(E2;0_2^+ \rightarrow 2_1^+)$ value of $5.2^{+2.3}_{-0.7}$ W.u. was obtained. According to the BMF prediction (Fig. 7.5) a much smaller $B(E2)$ value is expected between the prolate deformed 0^+ state and the 2_1^+ state (again, note that the 0_2^+ and 0_3^+ states seem inverted in the calculation). The experimentally obtained value suggests a stronger coupling between the presumed prolate-deformed structure and the ground-state band compared to the calculation, which is in line with the lower excitation energy of the 0_2^+ state. An even larger $B(E2;0_2^+ \rightarrow 2_1^+)$ value was obtained in the Coulomb-excitation study [71]. However, the lifetime of the 0_2^+ state from the RDDS study based on the current data set [50] was used to constrain the GOSIA fit in Ref. [71], therefore the obtained MEs reproduced the provided lifetime, which is discrepant with the value obtained in the current work. Unfortunately, the 2_3^+ state at 2370 keV, which based on its decay properties [61] is interpreted as built on the 0_2^+ state, has not been populated in the present experiment. Hence, the key $\langle 2_3^+||E2||0_2^+\rangle$ matrix element reflecting the collectivity of the band built on the 0_2^+ state could not be determined.

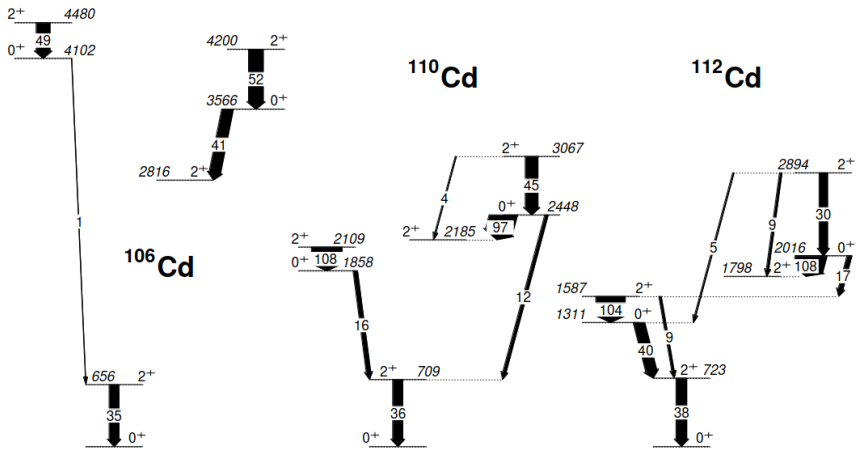

Figure 7.5 – Partial level schemes of ^{106,110,112}Cd, presenting the decay of the $0^+_{1,2,3}$ states and the 2^+ states build on them, resulting from the SCCM calculation [10, 11, 50, 121]. The arrow widths and labels represent the $B(E2)$ values expressed in Weisskopf units. Only transitions with $B(E2)$ values of at least 1 W.u. are plotted.

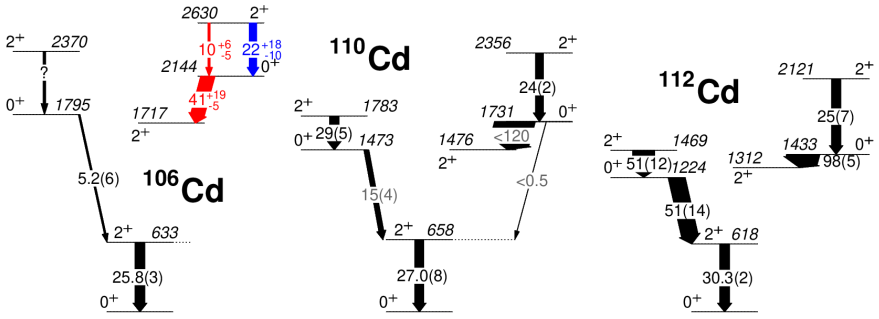

Figure 7.6 – Same as Fig. 7.5, but presenting experimental data. The $B(E2)$ values in ^{106}Cd are from the present study, with the exception of the $B(E2; 2^+_1 \rightarrow 0^+_1)$ value, which was taken from ENSDF [59]. Two alternative values of $B(E2; 2^+_5 \rightarrow 0^+_3)$, obtained using the branching ratios reported in Ref. [62] (in red) and in Ref. [61] (in blue), are given. The $B(E2; 2^+_3 \rightarrow 0^+_2)$ value in ^{106}Cd is not known. The transition probabilities in ^{110,112}Cd are taken from Ref. [10] with the exception of the values given in gray which are from Ref. [122].

As one can deduce from the comparison of Figs. 7.5 and 7.6, the in-band transitions in the ground-state band are less collective than those predicted within the SCCM calculation. Siciliano et al. [50] attempted to evaluate the deformation of the ground state. Using the transition probabilities obtained in Ref. [50] and adopting the axially-symmetric rigid-rotor model (Formulas 1.8 and 1.11), β_2 was calculated to be about 0.17, in reasonable agreement with the SCCM prediction ($\beta_2 \approx 0.2$). The beyond-mean-field calculations predicted rather constant deformation within the ground-state band ($\beta_2 \approx 0.2$). However, a smaller $\beta_2 \approx 0.12$ was obtained from the $B(E2; 6^+_2 \rightarrow 4^+_1)$ value, which was explained by possible mixing

between the closely lying 6_1^+ and 6_2^+ states [50]. The LSSM calculation performed by Schmidt et al. [113] also investigated the evolution of the deformation within the bands built on the ground state and on the 0_2^+ state in ^{106}Cd. A small increase of β_2 was reported for both bands between the 0^+ and 2^+ states, followed by a slow decrease of the β_2 parameter with increasing spin (see Fig. 5 in Ref. [113]). The reported deformation of the 6_2^+ state ($\beta_2 \approx 0.175$), although smaller than the deformation of the ground state ($\beta_2 \approx 0.185$), is still much larger than the value reported in Ref. [50]. However, within the axially-symmetric rigid-rotor model, the $\langle 6_2^+ || E2 || 4_1^+ \rangle$ extracted in the current study (Table 5.6) corresponds to $\beta_2 \approx 0.18$, which is in line with both discussed theoretical calculations.

The properties of the ground-state band were also discussed by Gray et al. [71] by comparing the ratio of the $\langle Q^2 \rangle$ quadrupole invariants [5, 6] for the 2_1^+ and 0_1^+ states with the predictions of various models. The experimentally obtained value (presented in red in Fig. 7.7) was shown to be lower than those predicted by all models. The observed decrease of $\langle Q^2 \rangle$ with spin is in contrast with the trend observed for ^{114}Cd [107]. Based on this result, the vibrational interpretation was ruled out and it was concluded that the Cd isotopic chain can be described as evolving from seniority to a rotational character with the influence of intruder states on the properties of other structures increasing towards midshell.

The $\langle Q^2 \rangle$ quadrupole invariants for several states were evaluated by applying Formula 1.14 to $E2$ matrix elements obtained in the current study. In this evaluation, $E2$ matrix elements reported in the last columns of Tables 5.6 and 5.7 were used in addition to the diagonal $E2$ MEs taken from Table 5.4. The deformation parameters β_2 were calculated using Formula 1.16. The results are presented in Table 7.1 together with the experimental values reported in Ref. [71] and those resulting from the BMF [50] and the LSSM calculations [113].

Table 7.1 – Rotational invariants $\langle Q^2 \rangle$ and deformation parameters $|\beta_2|$ calculated from the matrix elements obtained in the current work, in Ref. [71] and those resulting from the SCCM [50, 121] and LSSM calculations [113].

	This work	Ref. [71]	BMF	This work	BMF	LSSM
I^π	$\langle Q^2 \rangle [e^2\mathrm{b}^2]$	$\langle Q^2 \rangle [e^2\mathrm{b}^2]$	$\langle Q^2 \rangle [e^2\mathrm{b}^2]$	$\lvert\beta_2\rvert$	$\lvert\beta_2\rvert$	$\lvert\beta_2\rvert$
0_1^+	$0.413(8)$	$0.443(13)$	0.575	$0.174(2)$	0.205	0.186
2_1^+	$0.411(28)$	$0.375(29)$	0.574	$0.173(5)$	0.205	0.192
4_1^+	$0.66^{+0.08}_{-0.10}$	$> 0.28(3)$	0.838	$0.22^{+0.01}_{-0.02}$	0.248	0.190
2_2^+	$0.53^{+0.10}_{-0.07}$	$> 0.21(13)$	0.661	$0.20^{+0.02}_{-0.01}$	0.220	–
0_3^+	$0.27^{+0.15}_{-0.07}$	–	1.03	$0.14^{+0.04}_{-0.02}$	0.27	0.176

The $\langle Q^2 \rangle$ values obtained for the 0_1^+ and 2_1^+ states from the current data suggest a ratio identical with unity ($1.00(7)$), which is in a perfect agreement with the results of the BMF calculation and in contradiction with the decreasing trend reported in Ref. [71] (see Fig. 7.7). The $\langle Q^2 \rangle$ for the 4_1^+ state is also larger than

the value obtained in the work of Gray et al. [71] and the corresponding ratio $\langle Q^2 \rangle_{4_1^+} / \langle Q^2 \rangle_{0_1^+}$ of $1.6^{+0.02}_{-0.03}$ follows the increasing trend predicted by the BMF calculation as illustrated in Fig. 7.7. However, the obtained $\langle Q^2(4_1^+) \rangle$ should be viewed as a lower limit, as some key matrix elements were not considered in the sum, for example those relating the 4_1^+ state to the 3^+ and 5^+ states in the $K = 2$ band. Similarly, the $\langle Q^2 \rangle$ invariant for the 2_2^+ band-head of the γ band should be treated as a lower limit, although the current value is already large compared to the theory and previous measurements. Finally, a similar calculation was performed for the 0_3^+ state. The obtained result is much smaller than the value predicted by the SCCM calculation, suggesting a smaller deformation. However, the actual value depends strongly on the adopted branching ratio for the $2_5^+ \rightarrow 0_3^+$ decay (if the branching ratio from Ref. [61] is used, $\langle Q^2(0_3^+) \rangle = 0.45^{+0.33}_{-0.16}$ eb is obtained instead). Evaluation of $\langle Q^2 \rangle$ for the 0_2^+ state was not attempted, as the key $\langle 2_3^+ || E2 || 0_2^+ \rangle$ and $\langle 2_2^+ || E2 || 0_2^+ \rangle$ matrix elements could not be deduced from the present data set.

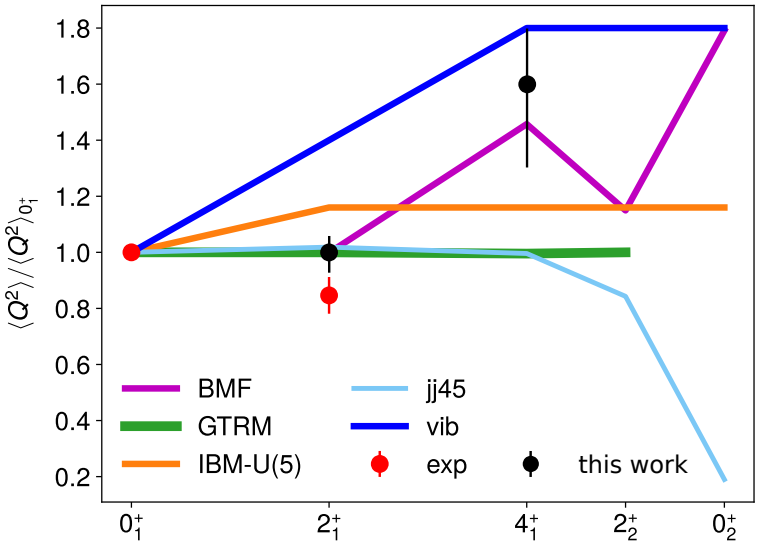

Figure 7.7 – The $\langle Q^2 \rangle$ quadrupole invariants for low-lying states in ^{106}Cd obtained in Ref. [71] (red) and in this work (black), normalized to the $\langle Q^2 \rangle_{0_1^+}$ value, compared to the predictions of several theoretical models including beyond-mean-field calculations (BMF) [50], generalized triaxial rotor model (GTRM), IBM calculations in the U(5) limit (IBM-U(5)), shell-model (jj45) [75] and surface vibrations about a spherical shape (vib). For more details see Ref. [71] and the references therein. Figure adapted from Ref. [71].

A common feature for all discussed states is that the deformation parameters β_2 obtained from the current experimental data are smaller than those predicted with BMF, which is typical for this type of calculations, as discussed in Ref. [10, 11].

However, the general trend of the deformation within the ground state band seems to be correctly reproduced. Although the β_2 values predicted for the 0_1^+ and 2_1^+ states by the LSSM calculation [113] are in overall good agreement with the experimental data, $\beta_2(4_1^+)$ seems underestimated and the predicted trend of β_2 values within the ground-state band is different than the one experimentally observed. On the contrary, the β_2 of the 0_3^+ state obtained within the framework of LSSM describes better the experimentally obtained deformation (if the branching ratio from Ref. [61] is used for the $2_5^+ \rightarrow 0_3^+$ transition, the obtained $\beta_2 = 0.18^{+0.06}_{-0.04}$ is in perfect agreement with the prediction of the LSSM calculation). One should note, however, that the LSSM calculation did not include proton excitations through the $Z = 50$ shell gap, and most probably the microscopic structure of the 0_3^+ state and the band built upon it is not correct.

7.2 Triaxiality in ^{106}Cd

According to the BMF calculation, the $K = 2$ band associated with the ground state has a very similar overall deformation as that of the ground state and $\gamma = 25°$, as it can be deduced from the collective wave functions presented in Fig. 7.4. The properties of this band resulting from the calculation are presented in the left panel of Fig. 7.8. By comparing the predicted and experimental transition probabilities, Siciliano et al. [50] proposed the level scheme in the right panel of Fig. 7.8. A main drawback of this arrangement is the lack of a possible candidate for the 3^+ member of the γ band. The lowest 3^+ state in ^{106}Cd is the 2252-keV level, according to the assignment in Ref. [61]. As discussed in Section 5.4, the 2254-keV and 2252-keV states form a doublet, however based on the analysis of the experimental γ-ray yields, it was concluded that predominately the decay of the state at 2254 keV was observed in the current data set. This is in line with the spin assignment of the state at 2252 keV as a 3^+, as typically the odd-spin members of the $K = 2$ bands are much less populated in low-energy Coulomb excitation than their even-spin counterparts. This is due to cancellations between the competing excitation paths, as discussed e.g. in Refs. [107, 123]. Considering the state at 2252-keV as a possible γ-band member, the level scheme was rearranged as proposed in Fig. 7.9. The $B(E2)$ values describing the decay of the 3^+ state were calculated using the lifetime measured in Ref. [61] combined with the branching and mixing ratios taken from Refs. [62] and [61], respectively. The strongest observed branch is going to the $K = 2$ band-head, followed by a decay to the 4_1^+ state. The strong $3^+ \rightarrow 2_2^+$ decay is consistent with the pattern predicted by the BMF calculation, although the actual $B(E2)$ value is underestimated by the theory. One should note however, that for the decay of the 3^+ state to the 4_1^+ and 2_2^+ states, out of two possible mixing ratios reported in Ref. [61] values corresponding to a stronger $E2$ character were adopted.

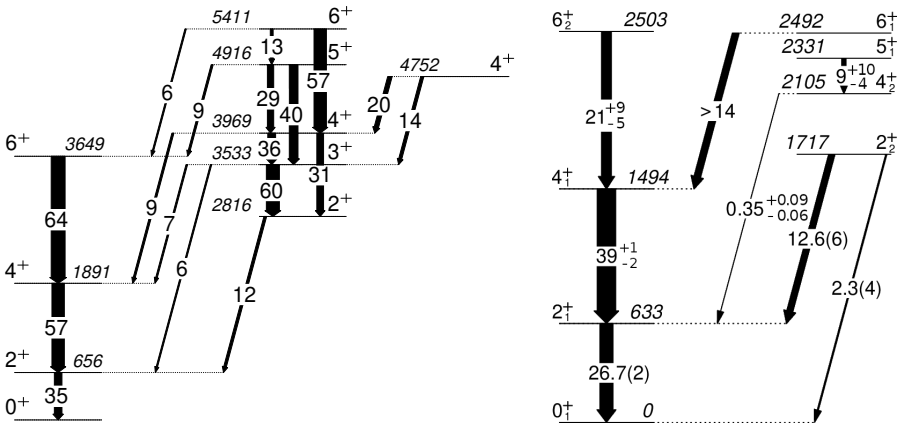

Figure 7.8 – Partial level schemes of ^{106}Cd presenting the ground-state band and the γ band. Transition probabilities are given in W.u. and level energies in keV. Left panel: BMF calculation. The band-head of the $K = 4$ band is also shown. Only the transitions with reduced transition probabilities larger than 5 W.u. are plotted [50, 121]. Right panel: level scheme organization proposed in Ref. [50].

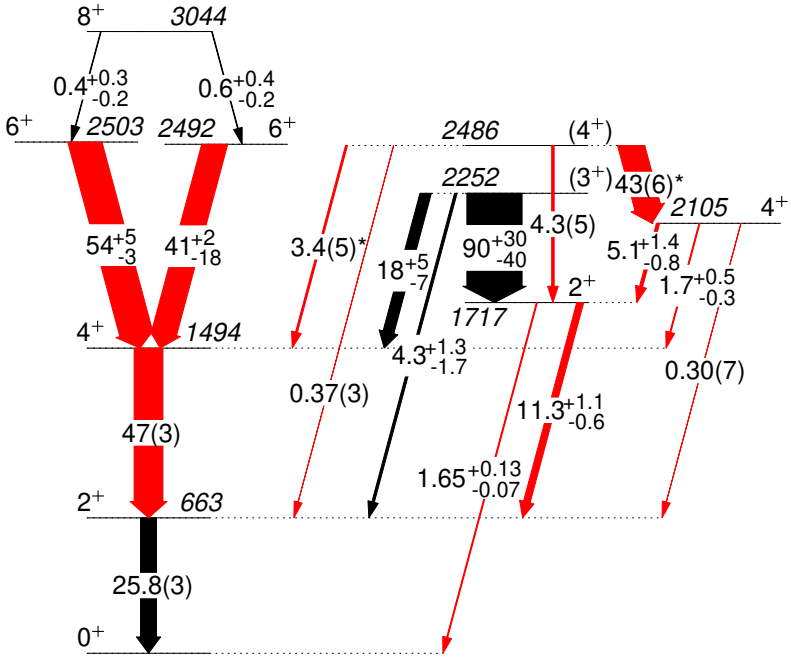

Figure 7.9 – Proposed arrangement of selected levels in ^{106}Cd into bands. Arrow widths and labels represent the experimental $B(E2)$ values in W.u. Red colour indicates that the corresponding information was obtained from the current measurement. For the transitions marked with asterisks pure $E2$ multipolarity was assumed. Level energies are given in keV.

A possible candidate for the 4^+ member of the γ band is then the 2486-keV state, which agrees with the assignment of Ref. [71]. Based on the trend of the measured $2^+, 3^+, 4^+ \rightarrow 2_1^+$ transition intensities, Fig. 6.4 (B), no direct $E4$ transition to the ground state would be expected from the state at 2486 keV, making it a good candidate for a member of the $K = 2$ band. One should note however, that an unexpectedly strong branch is observed to the 4_2^+ state, which can be due to the assumption that this transition has a pure $E2$ character. Furthermore, the transition connecting the $2^+, 3^+, 4^+$ state with the 2_2^+ band-head is also rather weak, although one should note that a larger branching ratio for this decay branch was measured in Ref. [61]. Subsequently, the previously proposed 4^+ γ-band member can be reinterpreted as a band-head of the $K = 4$ band associated with the ground state. The collectivity of the 4_2^+ state is supported by its strong population in the current experiment, and the $K = 4$ assignment is consistent with its preferred decay to the $K = 2$ band-head. A $K = 4$ character would also be in line with a presence of a non-negligible $E4$ matrix element coupling this state with the ground state, suggested by the enhancement of the 4_2^+ excitation cross sections observed for higher scattering angles, see Fig. 6.7. Moreover, a strong transition connecting the 4^+ states in the $K = 2$ and $K = 4$ bands is observed, in line with the BMF prediction, although the $B(E2; (4^+) \rightarrow 4_2^+)$ value presented in Fig. 7.9 may be overestimated as already mentioned.

The proposed assignment of $K = 2$ band members in ^{106}Cd can be further discussed in the context of the energy systematics of $K = 2$ structures in the neighbouring Cd isotopes, presented in Fig. 7.10. The excitation energy of the 2_2^+ state increases monotonically with decreasing mass number A. The 3^+ and the 4^+ γ-band members follow a similar pattern, with the spacing between the two gradually decreasing with A. The currently proposed 3^+ and 4^+ γ-band members in ^{106}Cd fit well with these energy systematics. The previously assigned 6^+ γ-band member in ^{106}Cd [50] is at a rather low energy, resulting in a narrow energy spacing in the $K = 2$ band. Another possible 6^+ candidate in ^{106}Cd would be the level at 2924.8 keV, which is the only other firmly assigned 6^+ state in ^{106}Cd. However, following the systematics, one would expect a 6^+ $K = 2$ band member at an even higher excitation energy. Thus, further studies are needed to extend the level scheme of ^{106}Cd. A rather large $B(E2; 6_1^+ \rightarrow 4_1^+)$ value is obtained from the current Coulomb-excitation analysis, which would agree well with the interpretation of the state as a member of the $K = 2$ band proposed by Ref. [50]. However, another possible explanation of this observation is that the $6_{1,2}^+$ states in ^{106}Cd result from a strong mixing between a seniority state and a member of the rotational ground-state band. Long-lived 6^+ seniority states were indeed observed in the lighter Cd nuclei, e.g. ^{102}Cd [124]. As the result of the mixing, both $6_{1,2}^+$ states would have a collective character, consistent with the large $B(E2; 6_{1,2}^+ \rightarrow 4_1^+)$ values obtained in the present analysis. Similarity in the structure of the two 6^+ states is also supported by the fact that the $B(E2; 8_1^+ \rightarrow 6_{1,2}^+)$ values agree within

error bars. The observed pattern cannot be reproduced by the SCCM calculations as the seniority states are outside of the model space.

The 5^+ states in $K = 2$ bands should follow a similar trend as a function of A as lower-spin band members. Such a behaviour is observed in ^{110,112}Cd, while the systematics reveal a sudden decrease of the 5^+ energy in ^{108}Cd. This casts doubt on the assignment of the 5^+_1 level as a part of the $K = 2$ band proposed in Ref. [98]. In fact, there is another 5^+ state identified in ^{108}Cd at 2906 keV excitation energy [125] that would fit better with the energy systematics, as presented in Fig. 7.10, and has a dominating decay to the 4^+ and 3^+ states from the γ band. This suggests that the 5^+_1 state in ^{108}Cd has a different configuration, which may be similar to that of the 5^+_1 state in ^{106}Cd.

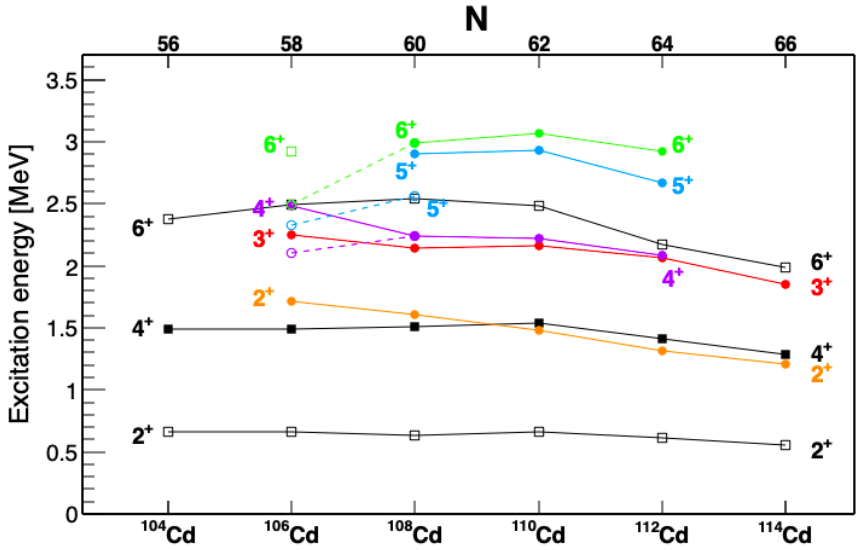

Figure 7.10 – Systematics of the ground-state band members (in black) and those of the $K = 2$ bands in $^{104-114}$Cd. The solid lines and filled circles correspond to the level scheme presented in Fig. 7.9, while dashed lines and open circles indicate the K=2 band members proposed in Ref. [50]. For ^{108}Cd, the filled circle corresponds to the 5^+_2 state which seems a better candidate for a $K = 2$ band member than the 5^+_1 state (open circle) proposed in Ref. [98], as discussed in the text. The open green square denotes a possible candidate for the 6^+ member of the γ band in ^{106}Cd.

7.3 Negative-parity states

Data on $E3$ transition strengths are in general difficult to obtain. The present study provided a new $B(E3; 3^- \rightarrow 0^+_1)$ value, which is more precise than those resulting from previous experiments, as well as information about the properties of the 5^-_1, 5^-_2 and 1^- states in ^{106}Cd. The intensity simulation using the $\langle 0^+_1 || E3 || 3^-_1 \rangle$

matrix element obtained by fitting the data from the first three ranges of scattering angle [Fig. 6.9 (A)] resembles an average of the experimental points, which have an oscillatory behaviour, as predicted with FRESCO (Fig. 5.7). The simulation assuming the $\langle 0_1^+||E3||3_1^-\rangle$ value from Ref. [83] strongly overestimates the measured intensities, although an agreement within 2σ between the result of the present fit and the value of Ref. [83] is observed. Using the ME from Ref. [75] yields a better agreement with the experimental data, however, the uncertainty of this measurement is rather large.

The experimental yields for the $5_2^- \rightarrow 4_1^+$ transition presented in Fig. 6.9 (B) display an oscillatory behaviour around the pure Coulomb-excitation cross section. This trend is very similar to the cross-section distribution observed for the $3_1^- \rightarrow 2_1^+$ transition. Such a behaviour is expected when the main population path involves an $E3$ transition (see Fig. 5.7 obtained with FRESCO). The dependence of the $5_1^- \rightarrow 4_2^+$ transition intensity on scattering angle, Fig. 6.9 (C), is similar to those observed for the $4_{2,3}^+$ states, for which it was postulated that higher-order multipolarities (i.e. $E4$) are important in the excitation process. In the case of the 5_1^- state one can hypothesize that the observed sudden departure from the pure Coulomb-excitation prediction for $\theta_{LAB} > 23^\circ$ is caused by the Coulomb-nuclear interference involving an $E5$ transition. This suggestion is supported by the fact that substantial $E5$ components in the wave functions of several 5^- states in ^{110,112}Cd were reported following inelastic proton and deuteron scattering [97]. Finally, a much smaller deviation from the pure Coulomb-excitation prediction is observed for the $1^- \rightarrow 0_1^+$ transition, Fig. 6.9 (D). It can be speculated that this deviation is caused by the Coulomb-nuclear interference, which has a constructive character.

The limit extracted in the current work for the $\langle 5_1^-||E3||2_1^+\rangle$ matrix element (Table 6.5) corresponds to a reduced transition probability smaller than 10.7 W.u. Much larger $E3$ strengths are required if the population of the 5_2^- and 1^- states is linked solely to $E3$ transitions from the 2_1^+ state: $B(E3; 5_2^- \rightarrow 2_1^+) = 40(3)$ W.u. and $B(E3; 1^- \rightarrow 2_1^+) = 45(3)$ W.u. (calculated using the MEs reported in the first row of Table 6.4). Therefore, it seems more realistic that the population of the 5_2^+ and 1^- states involves other excitation paths. Moreover, Linnemann et al. [60] suggested the 1^- state as a candidate for the quadrupole-octupole coupled (QOC) 1^- state in ^{106}Cd, based on the measured large $B(E1; 1^- \rightarrow 0_1^+)$ value as well as its excitation energy and decay pattern, which are similar to those of other known quadrupole-octupole candidates in the even-even stable cadmium isotopes. Coupling of one-phonon quadrupole and one-phonon octupole surface vibrations would result in the appearance of five negative-parity states (1^-, 2^-, 3^-, 4^-, 5^-), which have excitation energy equal to approximately the sum of the single-phonon energies ($E(2_1^+) + E(3_1^-)$). In heavier Cd isotopes, i.e. $^{108-114}$Cd, candidates for all five members of the quintuplet were found, see Ref. [98] for ^{108}Cd, Ref. [99] for ^{112}Cd, and Ref. [100] for ^{114}Cd. In the case of ^{106}Cd the expected $E_{QOC} = 632.6 + 2378.5 = 3011.1$ keV. The excitation energy

of the 1^- and 5_2^- states are 2824.6 keV and 2920.1 keV, respectively. Thus, both states fit well the energy criterion. In the decay of the members of the quintuplet, a destruction of the quadrupole phonon results in an $E2$ transition to the 3_1^- state with a transition strength comparable to that of the $2_1^+ \rightarrow 0_1^+$ transition. Connecting $E2$ transitions between the proposed QOC states and the 3_1^- state were previously reported in ^{114}Cd (except for the 1^- quintuplet candidate) [100], and a strong $E2$ transition was observed between the 5_1^- and 3_1^- states in ^{112}Cd [99]. Similarly, transitions to the one-phonon quadrupole state involve the destruction of an octupole phonon, thus the associated $E3$ transition strength should be similar to the $B(E3)$ strength of the $3_1^- \rightarrow 0_1^+$ transition [100]. Therefore, one can further test the QOC hypothesis for the 1^- and 5_2^- states using the results of the tests summarized in Table 6.4.

Assuming a value of the $\langle 1^-||E2||3_1^-\rangle$ matrix element, which corresponds to a $B(E2)$ value of 26 W.u. (similar to the $2_1^+ \rightarrow 0_1^+$ strength), results in a reduction of the $\langle 1^-||E3||2_1^+\rangle$ matrix element to $0.16(2)$ $e\text{b}^{3/2}$, which corresponds to $13(3)$ W.u. The adopted $\langle 3_1^-||E3||0_1^+\rangle$ matrix element, Section 6.2.4, corresponds to a transition strength of 11^{+4}_{-3} W.u., which perfectly fits the QOC expectation of $B(E3; 3_1^- \rightarrow 0_1^+) \approx B(E3; 1^- \rightarrow 2_1^+)$ and further supports the suggestion of Ref. [60]. However, to this date no direct $E2$ transition connecting the 1^- and 3_1^- states has been observed.

On the other hand, an alternative explanation can be offered if one considers the ground state of Cd to be deformed. Then it is possible that the 1^- state originates from the coupling of the octupole vibration to the static quadrupole deformation. This coupling would give rise to four octupole-vibrational bands with K$= 0, 1, 2, 3$ [101]. Both bands with K$= 0$ and K$= 1$ have band-heads with spin-parity 1^-. The states in the K$= 0$ band have odd spin $(1, 3, 5, ..)$, while those in the K$= 1$ band follow no spin restrictions $(1, 2, 3, ..)$ [101]. Therefore, it is also possible that the 1_1^- state in ^{106}Cd is the band-head of a K$= 0$ or a K$= 1$ band and if so, one should observe a rotational-like structure built on it. This hypothesis merits an investigation in a future experiment. Moreover, a new dedicated study is needed to measure the small unobserved decay branch to the 3_1^- state, essential to firmly extract the $\langle 1^-||E3||2_1^+\rangle$ matrix element.

Similarly, if one assumes an $\langle 5_2^-||E2||3_1^-\rangle$ matrix element corresponding to a transition probability as large as the $B(E2; 2_1^+ \rightarrow 0_1^+)$ value, a significant reduction of $B(E3; 5_2^- \rightarrow 2_1^+)$ is observed, to a value of $8(1)$ W.u. This value also agrees well with the adopted $B(E3; 3_1^- \rightarrow 0_1^+)$ value (Section 6.2.4). Thus, one can speculate that the 5_2^- state is also a member of the quadrupole-octupole quintuplet. In addition, one should mention that the $5_2^- \rightarrow 3_1^-$ transition was previously reported in Ref. [61], however in a more recent study of the same group it was not confirmed. From the reported $I_\gamma(5_2^- \rightarrow 3_1^-)/I_\gamma(5_2^- \rightarrow 2_1^+) = 0.09(1)$ and the adopted 5_2^- lifetime (Table 5.2), one can calculate $\langle 3_1^-||E2||5_2^-\rangle = 2.8$ eb, which corresponds to a transition strength of 239 W.u. This value does not seem reasonable.

The systematics of the excitation energies of the 3^-_1, 1^-_1 and $5^-_{1,2}$ states in the $^{106-114}$Cd isotopes are presented as a function of the mass number in Fig. 7.11. As the energy of the 2^+_1 state is approximately constant, one would expect that the energies of quadrupole-octupole coupled states follow a trend that is similar to that of the 3^-_1 state. As one can see in Fig. 7.11, this is indeed true for the 1^-_1 and 5^-_1 states in $^{110-114}$Cd. An inversion between the 5^-_1 and 5^-_2 states taking place between ^{108}Cd and ^{110}Cd would be necessary to maintain the same trend of the 5^- states in ^{106,108}Cd as suggested in Ref. [102].

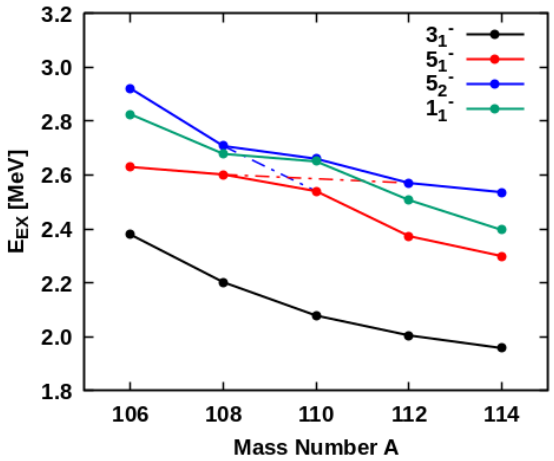

Figure 7.11 – Excitation energy systematics of the 3^-_1, 1^-_1, 5^-_1 and 5^-_2 states in $^{106-114}$Cd [59]. The inversion of configurations of the 5^-_1 and 5^-_2 states, suggested in Ref. [102], is schematically presented with the dashed lines.

If the proposed inversion is adopted, the presumed second configuration in Fig. 7.11 corresponds to the 5^-_1 states in ^{106,108}Cd and the 5^-_2 states in heavier Cd nuclei. This state appears at a roughly constant excitation energy in $^{106-114}$Cd. Moreover, if an additional transition relating the 5^-_1 and 3^-_1 state with a $B(E2; 5^-_1 \rightarrow 3^-_1) = 26$ W.u. is included in the coupling scheme, the entire observed population of the 5^-_1 state is accounted for without any $\langle 5^-_1 || E3 || 2^+_1 \rangle$ matrix element needed (Table 6.4).

Although the quadrupole-octupole coupling scheme fits well the experimental findings for the 5^-_2 state, another possible interpretation exists. Questions about the validity of the QOC character of the presumed 5^- member of the QOC quintuplet in ^{112}Cd were raised following one-neutron transfer study [102]. In this work, the second largest spectroscopic strength was observed for the 5^-_1 state in contrast to the weak or non population of the remaining members of the quintuplet. Considering this observation in combination with a previously known enhanced B(E2,$5^-_1 \rightarrow 3^-_1$) value [103], Jamieson et al. [102] suggested that the 5^-_1 state in ^{112}Cd is part of a rotational band based on the 3^-_1 state. Similar interpretation can be adopted in the present study. The members of rotational negative-parity

bands would also be connected via strong $E3$ transitions to positive-parity states. In fact, the present data do not permit discriminating between the two scenarios. Observation of higher-spin members of the band built on the 3_1^- state could resolve the issue.

7.4 Outlook - future β^+/EC decay study of ^{104,106}In

The current study raised a number of questions regarding discrepant spectroscopic data in ^{106}Cd. Although in some cases it was possible to differentiate between the discrepant branching or mixing ratios using the unsafe Coulomb-excitation data, there are many remaining structural puzzles in ^{106}Cd to be solved.

The lack of spectroscopic information for certain states resulted in assumptions on their spins, parities, multipolarities of de-exciting transitions, etc. Some of the structural conclusions of the current analysis were hindered by the missing or discrepant literature information concerning decay properties of the states in question. For example, the discrepant literature information on the branching ratios in the decay of the 2_5^+ state prevented from drawing firm conclusions on the collectivity of the presumably oblate structure built on the 0_3^+ state.

Questions have also arisen following the unexpected observation of certain levels in this study, e.g. the 5_1^+ state, which has a lifetime suggesting its much lower collectivity. Moreover the branching ratio for the decay of the 5_1^+ state is unusual, with the 226-keV decay to the 4_2^+ state being twice as intense as the 837-keV transition to the 4_1^+ state. In the neighbouring ^{108}Cd, the 5_1^+ state is known at a similar energy (2565 keV, compared to 2331 keV in ^{106}Cd) and decays, as one would expect, preferentially to the 4_1^+ state, even though the energy difference between the $5_1^+ \rightarrow 4_1^+$ and $5_1^+ \rightarrow 4_2^+$ transitions in ^{108}Cd (1037 keV and 326 keV, respectively) is smaller than in ^{106}Cd. In the current work, it was investigated if other possible placements of the 226-keV transition in the level scheme of ^{106}Cd can explain its observed large intensities. It was concluded that a decay of a hypothetical new state at about 2.5 MeV or higher (i.e. where one could assume that an excited state has avoided observation), yields equally unphysical $E2$ strengths. On the other hand, a coincidence with the 226-keV γ ray revealed shifted (i.e. corresponding to γ-ray emission in flight) components of the transitions de-exciting the 4_2^+, 2_2^+ and 2_1^+ states, which is inconsistent with the measured long lifetime of the 5_1^+ state. Therefore the 226-keV transition may be a doublet, either de-exciting a collective state close in energy to the 5_1^+ state or with an entirely different placement in the level scheme. Its placement and the properties of the level at 2331-keV excitation energy clearly require re-investigation.

In Section 7.2, a proposed reorganization of the low-energy level scheme of ^{106}Cd was discussed, regarding in particular the $K = 2$ and $K = 4$ bands associated with the ground state. In heavier Cd isotopes, the 2_2^+ states are band heads of well developed γ bands. In ^{106}Cd, due to non-conclusive spin assignments and discrepant literature information on transition probabilities, such a structure is not

firmly established. For example, based on previous spin assignments, there are several candidates for the first 3^+ state, including the 2252-keV, 2254-keV, 2710-keV and 2718-keV states. Although the current work argues that the state at 2252 keV is a good candidate for the 3^+ member of the γ band, one has to confirm its spin unambiguously. Previous studies yield mutually exclusive spin assignments for this state, namely $(2^+, 3)$ or 3^+ from a (n,n'γ) study [61], and (4^+) from a (p,p'γ) study [62]. The higher-spin members of the γ band are also controversial. Due to the strong population of the 2486-keV $(2^+, 3^+, 4^+)$ state in the safe Coulomb-excitation experiment of Gray et al. [71], it was postulated to be a γ-band member. In contrast, Siciliano et al. [50] proposed the 2107-keV 4_2^+ state, together with the 2331-keV 5_1^+ states as γ-band members.

Moreover, the branching ratio $I_\gamma(4_2^+ \rightarrow 2_1^+)/I_\gamma(4_2^+ \rightarrow 4_1^+)$ obtained from the current data set differs significantly from the literature value of $0.611(19)$ [59], however our data seem to be internally consistent, as presented in Fig. 5.2. The $I_\gamma(4_2^+ \rightarrow 2_1^+)/I_\gamma(4_2^+ \rightarrow 4_1^+)$ intensity ratios obtained from γ singles are approximately constant, within error bars, as a function of θ_{LAB} (a deviation is observed for $\theta_{LAB} < 22^\circ$, where the statistics is low). Summing the data from all scattering angles and gating on a transition below (633 keV, $2_1^+ \rightarrow 0_1^+$) and above (226 keV, $5_1^+ \rightarrow 4_2^+$) yielded very similar results, although with considerably larger uncertainties. It is worth noting that the present study represents the first measurement where the 2105-keV state was observed following inelastic scattering of heavy ions. This reaction mechanism preferentially populates excited states of a collective character. It is therefore possible that previous experiments on ^{106}Cd, which used β decay, inelastic neutron and proton scattering and fusion-evaporation reactions, observed in fact a doublet of states at 2105 keV, while in the present measurement one member of the doublet is populated more strongly than the other. Similar scenario was already observed in ^{112}Cd, where inconsistent branching ratios in the decay of a 1871-keV state, populated using various reaction mechanisms [106, 126], were the first hint of the presence of a doublet of 4^+, 0^+ states at this excitation energy. Finally, discrepancies in the literature are also evident for the decay of the 2_2^+ γ band-head. Those reported in Ref. [62] are dominated by the branch to the 2_1^+ state, while a direct ground-state decay was found to dominate in all other available studies.

Therefore, one would benefit largely from a new β-decay study of ^{106}Cd to resolve the existing ambiguities. Such a measurement would make it possible to pin down the structure of the γ band by firmly assigning the spins of key states and possibly observing low-intensity branches in and out of band, connecting it to other existing structures. Moreover, it would be possible to extend to higher spin the rotational bands built on the excited 0^+ states, and possibly identify more 0^+ states at higher energies. A precise determination of the $2_5^+ \rightarrow 0_3^+$ decay branch is necessary to compare the collectivity of the structure built on the 0_3^+ state with the model predictions, as mentioned in Section 7.1. Additionally, such an experiment would

allow searching for low-intensity $E2$ transitions between negative-parity states, e.g. $5^-_2 \rightarrow 3^-_1$. As it was discussed in Section 6.2.4, the excitation cross sections of the 5^-_1, 5^-_2 and 1^- states strongly depend not only on the corresponding $E3$ matrix elements, but also on the $B(E2)$ values between the state in question and the 3^-_1 state. The hypothesis of a strong $E2$ coupling between the 3^-_1 and 5^-_2, and/or the 3^-_1 and 1^- states would explain the enhanced population of the 5^-_2 and 1^- states, otherwise the excitation uniquely via the 2^+_1 state would require a $B(E3; 5^-_2 \rightarrow 2^+_1)$ value of $40(3)$ W.u. and a $B(E3; 1^- \rightarrow 2^+_1)$ value of $45(3)$ W.u., Table 6.4, drastically different from e.g. $B(E3; 3^-_1 \rightarrow 0^+_1)$ and close to the largest $B(E3)$ values known in the nuclear chart. A verification of this scenario can be provided by a direct observation of the weak $5^-_2 \rightarrow 3^-_1$ and $1^- \rightarrow 3^-_1$ transitions. Moreover, the possible observation and assignment of other negative parity states in ^{106}Cd can contribute greatly to the discussion on the character of the 5^-_2 and 1^- states, suggested as possible members of the quadrupole-octupole coupled quintuplet. Finally, fast-timing measurements with $LaBr_3$ detectors would help resolving the issue with the 5^+_1 lifetime. In addition, one would be able to directly measure the lifetime of the 0^+_3 state, which is in the sensitivity range of the fast-timing method. There is also a possibility that lifetimes of other less-collective states in ^{106}Cd would be extracted, giving further insight into their structures.

For these reasons, a β-decay experiment to study ^{106}Cd at the ISAC facility at TRIUMF was recently proposed (S2313, spokespersons: P. Garrett, D. Kalaydjieva, M. Zielińska) aiming to extend the work presented in the current manuscript. At the July 2023 meeting, the TRIUMF Nuclear Physics Experiments Evaluation Committee recommended 11 shifts with high priority for this project, which should be scheduled within three years. For this study, a setup identical to that described in Part II of the present thesis will be used, namely GRIFFIN [127] together with its ancillary detectors (PACES and eight $LaBr_3$ detectors with BGO shielding). This will allow performing γ-γ angular correlations [128] to firmly establish the spins of key states. The spins of the decaying ^{106}In nuclei (7^+ for the ground state and (2^+) for the isomeric state) will allow populating a wide range of spins in ^{106}Cd, thus enabling a search for possible 6^+ and higher-spin members of the γ band. Furthermore, as presented in Fig. 7.3, the detailed information on low-spin states across the Cd isotope chain, and in particular about the excited 0^+ states, ends abruptly at ^{106}Cd; in fact, there are no excited non-yrast low-spin states assigned in ^{104}Cd. Thus, within the S2313 project an investigation of the structure of ^{104}Cd via the ^{104}In $\beta+$/EC decay was also proposed. Ten shifts with medium priority were recommended for this study.

Part II

β-decay study of ^{100}Zr

8 - Shape coexistence in nuclei with $A \approx 100$

The changes in the ground-state mean-square charge radii $\delta\langle r^2\rangle$ as a function of the neutron number for nuclei with mass $A \sim 100$ are presented in Fig. 8.1 [4]. A sudden increase of $\delta\langle r^2\rangle$ is observed for the Rb, Sr, Y and Zr isotopes at $N = 60$. Moreover, at the same time their binding energy increases, as can be concluded from the two-neutron separation energies [129]. These observations were related to a sudden onset of deformation appearing at $N = 60$. While usually deformation changes gradually within an isotopic chain, a rapid change of the ground-state shape is observed for those nuclei. This interpretation is also supported by the vast reduction of the energy of the 2_1^+ states in the even-even Zr and Sr isotopes, which is related to an increase of collectivity. As can be seen in Fig. 8.2 (A), this phenomenon has a well localized character as a much more gradual shape transition is observed in both lighter (Kr) and heavier (Mo, Ru) nuclei. Furthermore, the systematics of the $B(E2; 2_1^+ \rightarrow 0_1^+)$ values expressed in single particle units, normalized to the number of nucleons A [presented in Fig. 8.2 (B)] indicate that almost all nucleons contribute to the collectivity at $N = 60$, i.e. the $B(E2; 2_1^+ \rightarrow 0_1^+)/A$ value is saturated at unity resembling a perfect rigid rotor.

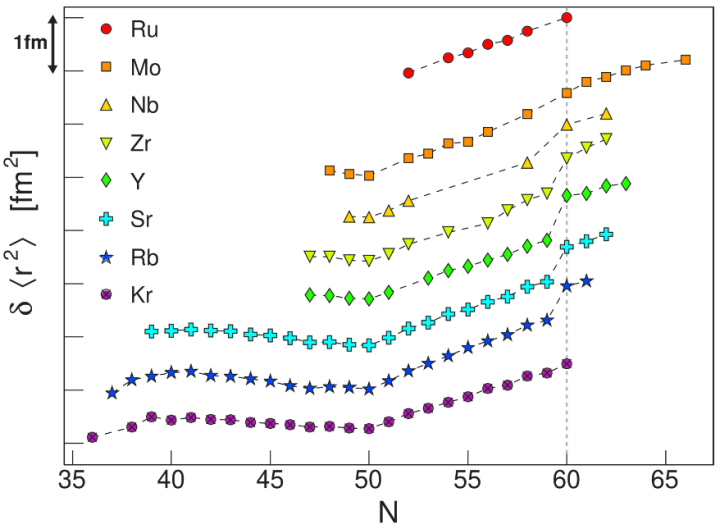

Figure 8.1 – Changes in the mean-square charge radii as a function of the neutron number for the ground states of the Kr–Ru nuclei. Figure adapted from Ref. [4].

Various theoretical models attempted to reproduce the sudden change of the ground-state deformation occurring at $N = 60$ in Zr and Sr nuclei. As an example, Figure 8.3 presents experimental $B(E2; 2_1^+ \rightarrow 0_1^+)$ values for Zr isotopes with $52 < N < 66$ compared to the results of relativistic beyond-mean-field calculations

with the PC-PK1 force [130], nonrelativistic BMF using SLy4 [130] and Gogny-D1S [131] interactions, interacting boson model (IBM) with self-consistent mean-field approximation based on the Gogny-D1M energy density functional [132], shell model [133] and the large-scale Monte-Carlo shell model (MCSM) [134]. While all BMF and IBM calculations reproduce rather satisfactorily the $B(E2; 2_1^+ \rightarrow 0_1^+)$ values in the well-deformed $N = 60, 62$ Zr nuclei, they fail to describe the properties of lighter Zr isotopes. In contrast, "standard" shell-model calculations accurately reproduced the $B(E2; 2_1^+ \rightarrow 0_1^+)$ values for Zr isotopes with $52 < N < 58$, however, due to the limitations of the valence space, they could not be extended towards heavier Zr isotopes. A successful description of the evolution of collectivity on both sides of the shape transition at $N = 60$ has only been achieved via the MCSM calculations.

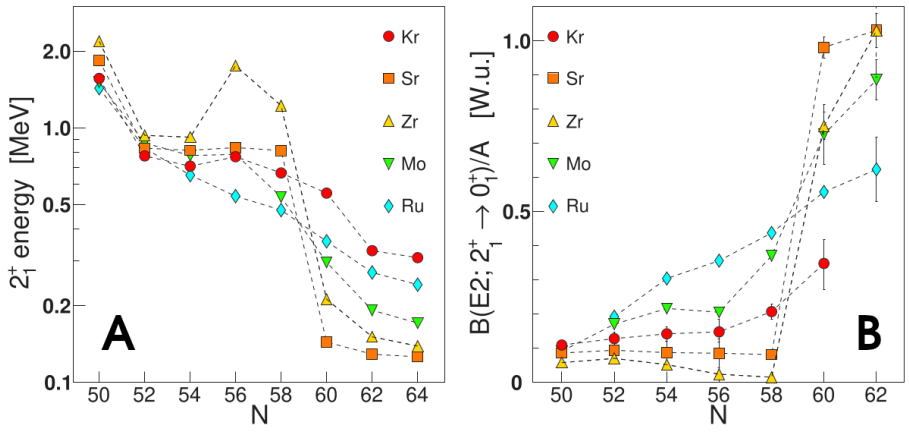

Figure 8.2 – Left: Systematics of the excitation energies of the 2_1^+ states in Kr, Sr, Zr, Mo and Ru isotopes as a function of the neutron number. Right: Systematics of the $B(E2; 2_1^+ \rightarrow 0_1^+)$ values in W.u., normalized to the mass A, for Kr, Sr, Zr, Mo and Ru isotopes. Figure adapted from Ref. [4].

A sudden change of the ground-state configuration may be explained by the coexistence of two configurations with distinct shapes which interchange at $N = 60$. A shape-coexistence scenario in Zr and Sr nuclei is supported by the appearance of low-energy excited 0^+ states in both ^{98}Sr and ^{100}Zr nuclei. An interpretation has therefore been proposed that the 0_2^+ states in the Sr and Zr isotopes with $N < 60$ correspond to a deformed configuration that interchange with the nearly spherical ground state at $N = 60$, which becomes non-yrast for $N \geq 60$. For example, the ground state of ^{96}Sr is believed to be spherical and its first excited 2_1^+ state was suggested to have a vibrational character [135, 136], as its spectroscopic quadrupole moment is compatible with zero and a rather low reduced transition probability is measured for its decay to the ground state. On the other hand, two closely-spaced excited 0^+ states were established at low excitation energy in ^{96}Sr. They are connected by a strong $E0$ transition [137, 138], suggesting both a considerable

mixing and a shape difference between their configurations. Excited 2^+ states were identified as possible candidates for members of rotational bands built on these collective structures.

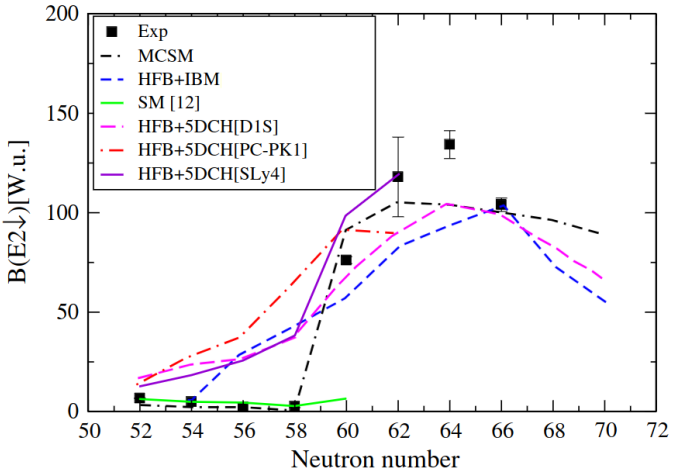

Figure 8.3 – Experimental $B(E2; 2_1^+ \rightarrow 0_1^+)$ values for Zr isotopes with $52 < N < 66$ compared with results of several theoretical approaches (see text for references). Figure adapted from Ref. [131].

In contrast to the ground-state band of ^{96}Sr, that in ^{98}Sr has a rotational character with large in-band transition probabilities. Large negative quadrupole moments were measured via Coulomb excitation [135, 136] for the ground-state band members indicating prolate deformation with $|\beta_2| \approx 0.5$. At the same time, the spectroscopic quadrupole moment of the 2_2^+ state in ^{98}Sr is compatible with zero and the in-band $2_2^+ \rightarrow 0_2^+$ transition has a reduced transition probability very similar to the $B(E2; 2_1^+ \rightarrow 0_1^+)$ value in ^{96}Sr. This shape-coexistence scenario between the well-deformed prolate ground-state band and a weakly deformed excited structure in ^{98}Sr was put on firm ground in Ref. [136] by extracting the quadrupole invariants $\langle Q^2 \rangle$ for both 0_1^+ and 0_2^+ states via Coulomb excitation.

Far less precise information is available in the literature regarding the shapes of ^{98}Zr and ^{100}Zr nuclei. Two RDDS measurements were carried out to determine lifetimes of low-lying excited states in ^{98}Zr, populated via fission [131] and in a two-neutron transfer reaction [139]. Based on the measured lifetimes of the first excited 2^+, 4^+ and 6^+ states, Singh et al. [131], proposed the existence of two deformed configurations coexisting with a spherical ground state. The obtained $B(E2; 2_1^+ \rightarrow 0_2^+)$ value (corresponding to $\beta_2 \approx 0.21$ within the rigid rotor model) suggested that the 2_1^+ state is a part of the moderately deformed structure built on the 0_2^+ state. Based on the large $B(E2; 6_1^+ \rightarrow 4_1^+)$ and $B(E2; 4_1^+ \rightarrow 2_2^+)$ values, the 2_2^+, 4_1^+ and 6_1^+ states were proposed to be members of a rotational band built on the highly deformed 0_3^+ state. The measured large $B(E2; 4_1^+ \rightarrow 2_1^+)$ value supported a strong mixing between the moderately and strongly deformed configurations, in

line with the large $E0$ transition strength between the 0_2^+ and 0_3^+ states [140]. This triple shape coexistence interpretation was guided by MCSM calculations and explained by the type-II shell evolution (see Section 13.1 for further details). According to these calculations, a prolate 0_2^+ state and a strongly deformed triaxial 0_3^+ state coexist with the nearly spherical ground state in ^{98}Zr. The model, however, predicted larger collectivity in the prolate band with respect to the experimental findings, and failed to reproduce the strong mixing between the two deformed configurations.

A different interpretation of the ^{98}Zr structure was offered in Ref. [139] based on calculations within the framework of configuration mixing in the interacting boson model (IBM-CM). The 0_1^+ and 2_3^+ states were proposed to be spherical single-particle states. The remaining low-lying states were organized into multi-phonon structures built on the weakly-deformed intruder 0_2^+ state: the 2_1^+ state being the one-phonon state, the 0_3^+, 2_2^+ and 4_1^+ states members of the two-phonon triplet and the 6_1^+ state a three-phonon state. The measured lifetimes of the 2_1^+ and 4_1^+ states, longer with respect to those in Ref. [131], pointed to significantly reduced collectivity. The $B(E2; 2_2^+ \rightarrow 2_1^+)$ value of 46^{+35}_{-14} W.u., obtained for the first time in Ref. [139], is in line with both interpretations. On one hand, a strong $E2$ transition is expected between the two-phonon and one-phonon states, on the other hand, this can also be interpreted in terms of strongly mixed deformed configurations built on the 0_2^+ and 0_3^+ states as proposed in Ref. [131]. Both MCSM and IBM-CM approaches yielded an overall good description of the experimental transition probabilities in ^{98}Zr. However, there are certain major differences between the predictions of the two models, which may allow to disentangle the structural puzzle of ^{98}Zr in the future. For example the $B(E2; 2_2^+ \rightarrow 0_3^+)$ value predicted by MCSM is almost 10 times larger than the value obtained in the IBM-CM calculation. The $\tau(2_3^+)$ measured in Ref. [139] combined with the currently known branching ratio for this transition [141] yields an unphysically large transition probability (over 500 W.u.), which suggests that these two observables should be remeasured. Moreover, a measurement of the quadrupole moments of the 2^+ states would also discriminate between the two interpretations.

Although much less is known about ^{100}Zr in comparison to its lighter isotone ^{98}Sr, their structures seem strikingly similar. The states in the ground-state bands are closely spaced and linked by strong $E2$ transitions. The observation of an enhanced $E0$ transition between the 0_2^+ state and the ground state, and a much smaller moment of inertia of the rotational structure built upon it, compared to the ground-state band, suggest the existence of a low-energy configuration with a different shape [13]. In order to confirm whether the sudden ground-state shape transition in Zr is due to the interchange between configurations in ^{98}Zr and ^{100}Zr, as it seems to be the case for the Sr isotopes, precise information on the decay properties of ^{98,100}Zr is needed. The structure of ^{100}Zr was previously investigated mostly following fission or β decay. The lifetimes of the ground-state band members

were measured up to spin 12 using various techniques as summarized in Ref. [147]. In contrast, apart from that of the 0_2^+ state, lifetimes of non-yrast states are not known, and therefore the conclusions regarding collectivity of the structure built on the 0_2^+ state rely solely on level energies. A third low-lying 0^+ state in ^{100}Zr was identified, but contrary to ^{98}Zr there is no rotational structure known to be associated with it. On the other hand, Ref. [146] proposed a $K = 2$ "proto-γ" band, suggesting that the triaxial degree of freedom may influence the structure of ^{100}Zr. There is no equivalent of this structure in the ^{98}Sr isotone, however Ref. [136] related the observed reduction of the spectroscopic quadrupole moment of the 2_1^+ state in ^{98}Sr with respect to the rigid-rotor expectation to a certain degree of triaxiality.

The current knowledge of the low-energy part of the ^{100}Zr level scheme seems insufficient. In order to firmly establish low-spin levels, and in particular assign the structures built on states with presumably different shapes, a study of β decay into ^{100}Zr has been proposed and perfomed at TRIUMF, Canada. The collected data have been partially analysed within this PhD project. Among the goals of this experiment was a search for possible candidates for the band-head of the "proto-γ" band proposed in Ref. [146], as well as a measurement of lifetimes of non-yrast states in ^{100}Zr via the fast-timing technique.

To firmly establish shape coexistence in ^{100}Zr, a direct measurement of the deformation of excited states is required. This is possible only by employing the Coulomb-excitation technique to determine their spectroscopic quadrupole moments, or even better, to extract a complete set of transitional and diagonal electromagnetic matrix elements which can be further analysed using the quadrupole sum rules approach [5, 6] in order to obtain a model-independent information on the shape parameters. To this aim, a low-energy Coulomb-excitation measurement to study ^{100}Zr has been proposed and approved by the PAC of the Argonne National Laboratory. It currently awaits scheduling within the nuCARIBU project [142]. As shown in Section 5.4 for ^{106}Cd, Coulomb-excitation studies require a precise knowledge of various spectroscopic information on the nucleus of interest. Thus, the established level scheme and precisely measured branching and mixing ratios in ^{100}Zr resulting from the present analysis will greatly enhance the sensitivity of the future Coulomb-excitation measurement to key nuclear-structure parameters such as spectroscopic quadrupole moments.

9 - β decay

The radioactive β^- decay in a nucleus consists of the conversion of a neutron to a proton (or vice-versa for the β^+ decay). Both Z and N change by one unit, while the total mass number A is preserved. In addition, an electron (positron) and anti-neutrino (neutrino) are emitted:

$$\beta^- : \quad {}^A_Z X_N \rightarrow {}^A_{Z+1} Y_{N-1} + e^- + \tilde{\nu}_e, \tag{9.1}$$

$$\beta^+ : \quad {}^A_Z X_N \rightarrow {}^A_{Z-1} W_{N+1} + e^+ + \nu_e. \tag{9.2}$$

The β^+ decay competes with the electron capture process ϵ, in which an orbital electron, usually from the K shell, is captured by the nucleus and a neutrino is emitted:

$$\epsilon : \quad {}^A_Z X_N + e^- \rightarrow {}^A_{Z-1} W_{N+1} + \nu_e. \tag{9.3}$$

The latter two processes are energetically forbidden for free protons or for protons in hydrogen atoms.

9.1 Energy release in β decay

The particles emitted in β decay have a continuum of energies from zero up to an upper limit given by the difference between the initial and the final nuclear states. The experimentally obtained continuous electron spectra remained a puzzle for more than a decade after its first observation [1]. It was finally explained in 1931 by Pauli by the existence of a third body in the process. This unknown particle was named neutrino by Fermi and due to the conservation of electric charge, it was concluded that the neutrino has to be electrically neutral. The conservation of the angular momentum on the other hand implied that the spin of ν is $1/2$, as for the electron.

The Q value is defined as the difference between energies corresponding to the initial and final nuclear masses. Therefore, Q value of the β^- process, relevant for this study, is given by:

$$Q_{\beta^-} = m_N({}^A_Z X_N)c^2 - m_N({}^A_{Z+1} Y_{N-1})c^2 - m_e c^2, \tag{9.4}$$

where m_N denotes the nuclear masses, m_e is the mass of the emitted electron and the antineutrino is treated as massless. The mass of the nucleus and the mass of the atom $M({}^A_Z X_N)$ are related via:

$$M({}^A_Z X_N) = m_N({}^A_Z X_N)c^2 + Z m_e c^2 - \sum_{i=1}^{Z} B_i, \tag{9.5}$$

where Bi represents the binding energy of the i-th electron. If the differences in binding energies are negligible, the following formula is obtained by substituting Formula 9.5 into Formula 9.4:

$$Q_{\beta^-} = M(^A_Z X_N)c^2 - M(^A_{Z+1}Y_{N-1})c^2. \tag{9.6}$$

Note that if $^A_{Z+1}Y_{N-1}$ is an excited nuclear state, the Q value has to be decreased by its excitation energy.

9.2 Fermi theory of the process of β decay

Half-lives in β decay are typically far longer than the characteristic nuclear times (10^{-20} s). Therefore, in the description of the β-decay process, in order to enable transitions between the nuclear states, a potential V is introduced that can be treated as a weak perturbation of the nuclear interaction W. The nuclear states are eigenstates of W, and approximate eigenstates of $V + W$. The transition rate between these quasi-stationary states can be evaluated using Fermi's Golden Rule:

$$\lambda = \frac{2\pi}{\hbar}|V_{fi}|^2\rho(E_f), \tag{9.7}$$

where $\rho(E_f)$ is the density of the final states (that can also be written as dn_f/dE_f) and the matrix element V_{fi} is the integral of the interaction V between the initial and final quasi-stationary states of the system, which for β^- decay is given by:

$$V_{fi} = \int \psi_f^* V \psi_i d\mathrm{V} = g \int \psi_D^* \psi_e^* \psi_{\tilde{\nu}}^* O_x \psi_P d\mathrm{V}, \tag{9.8}$$

where g, referred to as a coupling constant, is a scalar quantity describing the strength of the weak interaction, x indicates the form of the mathematical operator (V (vector) - A (axial vector)), and $\psi_{D,e,P,\nu}$ are the wave functions of the daughter nucleus, the emitted electron, the parent and the antineutrino, respectively [1].

Within the "allowed approximation", the nuclear matrix element M_{if}, given by $\int \psi_f^* O_x \psi_i d\mathrm{V}$, does not depend on the electron and the antineutrino momenta. Therefore, the dependence of λ in Formula 9.7 on the e^- and $\tilde{\nu}$ energies originates only from the density of the final states $\rho(E_f)$ and the following formula can be obtained [1]:

$$\lambda = \frac{g^2|M_{fi}|^2}{2\pi^3\hbar^7c^3}\int_0^{p_{MAX}} F(Z_D, p)p^2(Q - T_e)^2 dp, \tag{9.9}$$

where p is the momentum of the electron, $F(Z_D, p)$ is the Fermi function accounting for effects appearing due to the Coulomb interaction between the β particle and the daughter nucleus and $p^2(Q - T_e)^2$ is a statistical factor depending on the number of final states. Formula 9.9 can be further reduced to:

$$\lambda = \frac{g^2 m_e^5 c^4 |M_{fi}|^2}{2\pi^3\hbar^7} f(Z_D, Q), \tag{9.10}$$

where the latter is known as the Fermi integral, often expressed using the half-life $t_{1/2}$ instead of the transition rate:

$$ft_{1/2} = \frac{2\pi^3\hbar^7 \ln(2)}{g^2 m_e^5 c^4 |M_{fi}|^2}. \tag{9.11}$$

The $ft_{1/2}$ values can be used to compare β-decay probabilities in different nuclei. As they cover a very wide range ($10^3 - 10^{20}$), their logarithms are often used instead. The transitions with the lowest $\log ft$ values are the fastest ones.

9.3 Angular momentum and parity selection rules

Conservation of the total angular momentum in β decay requires that:

$$\vec{I_P} = \vec{I_D} + \vec{L} + \vec{S}, \tag{9.12}$$

where $\vec{I_{P,D}}$ are the total angular momentum of the parent/daughter nucleus, and $\vec{L}$ ($\vec{L_e} + \vec{L_{\tilde{\nu}}}$) and $\vec{S}$ ($\vec{s_e} + \vec{s_{\tilde{\nu}}}$) are the total orbital and spin angular momentum of the emitted electron-antineutrino pair. As the intrinsic spin of e^- and $\tilde{\nu}$ are both $1/2$, the total spin of the pair is either 0 or 1.

There are two types of classification of decays corresponding to $S = 0$ (Fermi decays) or $S = 1$ (Gamow-Teller decays). If the total lepton angular momentum is $L = 0$, then $\Delta I = 0$ for Fermi decays, and $\Delta I = 0$ (but no $0 \to 0$ decays) or $\Delta I = \pm 1$ for Gamow-Teller decays.

The change of the parity between the initial and final states is given by $\pi_P = \pi_D(-1)^L$. In principle, all transitions satisfying this condition should be considered, i.e. $|M_{fi}|^2 = \sum_L |M_{fi}^L|$. However, lower values of L are typically dominant and with the increase of L, the transition rate λ decreases dramatically, while the half-life increases. This is a result of the reduced overlap of the $e^-\tilde{\nu}$ wavefunctions with the nucleus at higher L values. The most probable transitions correspond to $L = 0$, and they are referred to as superallowed or allowed, following the classification in Table 9.1. Note that a superallowed transition between two nuclei with 0^+ states is only possible via a Fermi decay. If the initial and final states have opposite parities, the parity selection rule is violated and the $e^-\tilde{\nu}$ pair must carry an odd orbital momentum. The decays with the lowest odd orbital momentum $L = 1$ are classified as "first-forbidden". The next possible decay involving parity change is with $L = 3$ and is the third-forbidden decay, etc. The $ft_{1/2}$ value giving the relative intensity of those transitions is presented in the last column on Table 9.1 and decreases by a factor of $\approx 10^4$ for each increase of L by a unit.

Table 9.1 – A classification of transitions that may occur in a β decay process: superallowed (the nucleon that transformed did not change its shell-model orbital), allowed ($L = 0$) and n^{th} forbidden (the $e^{-}\tilde{\nu}$ pair carry an orbital angular momentum of $n\hbar$). The "unique" transitions are Gamow-Teller transitions where $\vec{L}$ and $\vec{S}$ are aligned.

Type of the transition	Selection rules	$L_{e^{-}\tilde{\nu}}$	$\Delta\pi$	$ft_{1/2}$ [s]
Superallowed	$\Delta I = 0, \pm 1$	0	no	$10^3 - 10^4$
Allowed	$\Delta I = 0, \pm 1$	0	no	$2 \cdot 10^3 - 10^6$
1^{st}forbidden	$\Delta I = 0, \pm 1$	1	yes	$10^6 - 10^8$
Unique 1^{st} forbidden	$\Delta I = \pm 2$	1	yes	$10^8 - 10^9$
2^{nd}forbidden	$\Delta I = \pm 1, \pm 2$	2	no	$2 \cdot 10^{10} - 2 \cdot 10^{13}$
Unique 2^{nd} forbidden	$\Delta I = \pm 3$	2	no	10^{12}
3^{rd}forbidden	$\Delta I = \pm 2, \pm 3$	3	yes	10^{18}
Unique 3^{rd} forbidden	$\Delta I = \pm 4$	3	yes	$4 \cdot 10^{15}$
4^{th}forbidden	$\Delta I = \pm 3, \pm 4$	4	no	10^{23}
Unique 4^{th} forbidden	$\Delta I = \pm 5$	4	no	10^{19}

10 - γ-γ angular correlations

Each excited nuclear state with angular momentum I has $(2I+1)$ substates with projections of the angular momentum $m = -I,\ -I+1, ..., I-1, I$, which in the absence of external fields have nearly degenerate energies [1]. The angular distribution $W(\theta)$ of γ rays emitted in the decay of an excited state I to a particular final substate m_f is given by:

$$W(\theta) = \sum_{m_i} p(m_i) W_{m_i \to m_f}(\theta), \tag{10.1}$$

where the sum is over all possible initial substates m_i, $p(m_i)$ is the population of the initial substate and $W_{m_i \to m_f}(\theta)$ is a characteristic anisotropic angular distribution for the $m_i \to m_f$ transition, depending on the transition multipolarity.

For example, let us assume dipole transitions in a $1^+ \to 0^+ \to 1^+$ decay cascade. The initial state has three possible substates with projection of the angular momentum $+1,\ 0$, and -1, while the intermediate state has only one substate (0). The angular distributions of transitions de-exciting individual substates of the spin-1 state would be $W(\theta)_{+1\to 0} = W(\theta)_{-1\to 0} = \frac{1}{2}(\cos^2(\theta)+1)$ and $W(\theta)_{0\to 0} = \sin^2(\theta)$. If all substates are equally populated ($p(m_i) = 1/3$), as in the case of β decay, the total angular distribution $W(\theta)$ has no dependence on θ:

$$W(\theta) = \frac{2}{3}\left(\frac{1}{2}(\cos^2(\theta)+1)\right) + \frac{1}{3}\sin^2(\theta) = const. \tag{10.2}$$

Therefore, the angular distribution of an unpolarized sample is isotropic, due to the random orientation of the ensemble of nuclei in the sample. In order to observe the individual angular distributions, it is necessary to create an uneven population of the initial substates. Such alignment may be due to the reaction mechanism (e.g. in heavy-ion induced fusion-evaporation reactions). However, even if there is no initial alignment, angular correlations between subsequent γ-ray decays can be investigated. If the radiation populating the initial state m_i is registered in coincidence with the $m_i \to m_f$ transition, the direction of the first emitted γ ray can be used to define a Z axis and therefore an orientation axis for the magnetic substates. This way, a polarization of the nucleus is effectively generated and the population of magnetic substates is unequally distributed. For example, in a cascade $0^+ \to 1^+ \to 0^+$, if the first transition is registered, the Z axis can be defined along the emission axis, i.e. $\theta_1 = 0$ by definition and $W(\theta_1)_{0\to 0} = \sin^2(0) = 0$. Therefore, $m_f = 0$ can not be populated in this cascade, while m_f of 1 and -1 are equally populated resulting in total $W(\theta_2) \propto (1+\cos^2(\theta_2))$. This way the anisotropic spatial distribution of the second γ ray with respect to the first one can be observed.

The angular correlations depend on the spins of the nuclear states in the cascade and multipolarities of the emitted γ rays (including multipole mixing ratios). For an arbitrary cascade, $W(\theta)$ can be expressed as:

$$W(\theta) = \sum_{i=0,\ even} B_{ii} A_{ii} P_i(\cos(\theta)), \tag{10.3}$$

where B_{ii} is the initial nuclear orientation, $P_i(\cos(\theta))$ are Legendre polynomials of order i, A_{ii} are coefficients depending on the spins of the involved states, multipolarities and mixing ratios [148] and the sum only includes even i values to conserve parity. Since the states of interest are populated in β decay the initial nuclear orientation is isotropic, i.e. $B_{ii} = 1$. The A_{ii} coefficients can be calculated using angular momentum algebra [148–151]. Note that A_{ii} do not depend on the parity of the involved states, therefore it is not possible to obtain direct information on the parity from angular-correlation measurements.

For cascades involving low transition multipolarities, usually only the first few terms of Formula 10.3 are necessary:

$$W(\theta) = A_{00} \left[1 + a_2 P_2(\cos(\theta)) + a_4 P_4(\cos(\theta))\right], \tag{10.4}$$

where A_{00} is a normalizing factor, $a_i = A_{ii}/A_{00}$ and θ is the angle between the two successive γ rays in the investigated cascade. The dependence of angular correlations on the spins of the involved states is illustrated in Fig. 10.1, presenting $W(\theta)$ for $I \to 2^+ \to 0^+$ cascades calculated assuming different spins I of the initial state. For transitions that can be mixed, mixing ratios $\delta = 0$ were assumed. The observed angular correlations have distinct patterns and are symmetric with respect to $\theta = 90^\circ$. The corresponding a_2 and a_4 coefficients are given in Table 10.1.

Table 10.1 – Theoretical a_2 and a_4 coefficients describing angular correlations for the cascades specified in the first column. Mixing ratios are assumed to be equal to 0.

Cascade	a_2	a_4
$0 \to 2^+ \to 0^+$	0.357	1.143
$1 \to 2^+ \to 0^+$	-0.25	0
$2 \to 2^+ \to 0^+$	0.25	0
$3 \to 2^+ \to 0^+$	-0.071	0
$4 \to 2^+ \to 0^+$	0.102	0.009

On the other hand, the coefficients a_2 and a_4 depend strongly on the mixing ratio, as shown in Figure 10.2 for a $2^+ \to 2^+ \to 0^+$ cascade, although the sensitivity to δ effectively disappears for large δ values. Similar a_2 and a_4 combinations can result from cascades involving different spin sequences, therefore additional spectroscopic information is required to assign definite spins.

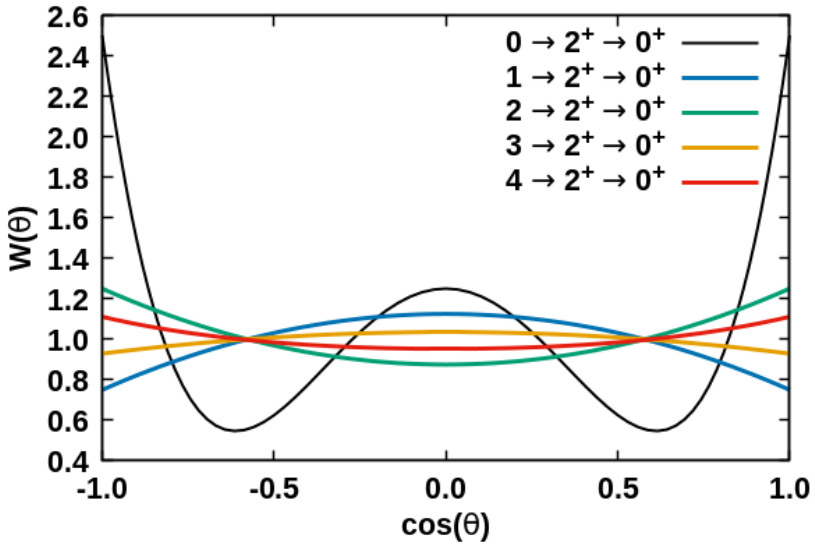

Figure 10.1 – Angular correlations $W(\theta)$ calculated for a cascade $I \to 2^+ \to 0^+$ assuming different initial spins I and mixing ratios equal to 0.

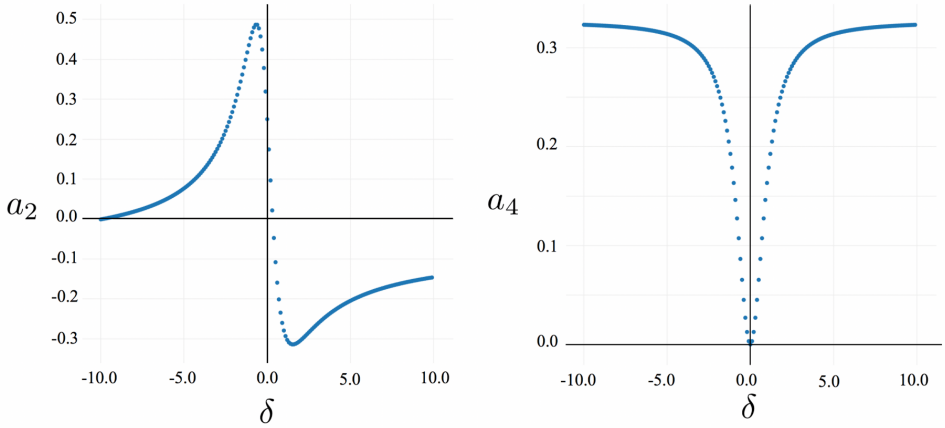

Figure 10.2 – The $a_{2,4}$ coefficients as a function of the mixing ratio for a $2^+ \to 2^+ \to 0^+$ cascade. Figure adapted from Ref. [152].

As will be discussed in Section 12.3, the measured angular correlations are attenuated with respect to those calculated with Formula 10.3 due to various experimental effects. This is usually accounted for by introducing suitable attenuation coefficients multiplying terms in $W(\theta)$.

11 - Experimental details

This work is based on a β-decay measurement performed in November 2021 at the TRIUMF facility [153, 154], Canada. The instrumentation used for this study is introduced in Section 11.1, while the initial data processing is presented in Section 11.2.

11.1 Experiment S1790

A beam mixture of ^{100}Rb and ^{100}Sr, produced using the Isotope Separation On-Line (ISOL) technique [155], was delivered to the GRIFFIN decay station [127] situated in the ISAC I experimental hall [156]. Excited states in ^{100}Zr were populated in the β^- decay of ^{100}Y and studied using GRIFFIN and its ancillary detectors.

11.1.1 Beam production

The world's largest cyclotron [157] is situated at TRIUMF. It is capable of accelerating proton beams up to 520 MeV. First, H^- ions are produced from H_2 gas using hot-filament ionization. They are then transported through an electrostatic beam line to the cyclotron, where they are accelerated using high-frequency alternating electric fields. Finally, the negative ions are stripped of their electrons by passing through thin graphite extraction foils. The extracted H^+ ions are next delivered onto a thick production target. A cocktail of radioactive ions is produced in the induced spallation and fission reactions. The products diffuse to the surface of the heated target and effuse to the ion source where they are ionized, and subsequently accelerated and mass separated.

In the present experiment a 9.8 μA beam of 480-MeV protons was focused on a UC_X primary target coupled with a rhenium surface-ion source, heated to $\approx$ 2200°C. The effused ions, mostly singly charged, were accelerated through a potential difference of ≈ 30 kV and mass separated based on their charge-to-mass ratio, using a high-resolution mass separator providing $\Delta m/m$ mass resolution of the order of $1/1000$ - $1/2000$ [158].

The nucleus of interest, ^{100}Zr, is populated via β^- decay of the $(1)^-$ ground state of ^{100}Y ($T_{1/2} = 732(5)$ ms [147]). However, using the described technique, ^{100}Y has a prohibitively low production yield due to its refractory nature (high melting temperature and high ionisation energy). On the other hand, the grand-mother and mother nuclei of ^{100}Y, i.e. ^{100}Rb and ^{100}Sr, are easily surface-ionized and could be extracted with relatively high yields – $5\text{x}10^4$/s and $2\text{x}10^4$/s, respectively. The β^--decay chain used to populate ^{100}Zr in the present experiment is highlighted in red in Fig. 11.1. The (4^-) ground state of ^{100}Rb with a half-life of $52(2)$ ms decays predominately to ^{100}Sr ($T_{1/2} = 200(2)$ ms). However, a weaker β^--n branch to ^{99}Sr was also observed in the present data set (marked in blue in Fig. 11.1).

^{100}Mo 7.3E+18 y 2β⁻=100 %	^{101}Mo 14.61 min β⁻	^{102}Mo 11.3 min β⁻	^{103}Mo 67.5 s β⁻	^{104}Mo 60 s β⁻	^{105}Mo 36.3 s β⁻
^{99}Nb 15.0 s β⁻=100 %	**^{100}Nb 1.4 s β⁻=100 %**	^{101}Nb 7.1 s β⁻	^{102}Nb 4.3 s β⁻	^{103}Nb 1.5 s β⁻	^{104}Nb 4.9 s β⁻, β⁻n
^{98}Zr 30.7 s β⁻	**^{99}Zr 2.1 s β⁻=100 %**	**^{100}Zr 7.1 s β⁻=100 %**	^{101}Zr 2.3 s β⁻	^{102}Zr 2.9 s β⁻	^{103}Zr 1.3 s β⁻, β⁻n
^{97}Y 3.75 s β⁻, β⁻n	^{98}Y 548 ms β⁻, β⁻n	**^{99}Y 1.484 s β⁻=100 % β⁻n=1.77 %**	**^{100}Y 732 ms β⁻=100 % β⁻n=1.02 %**	^{101}Y 450 ms β-, β-n	^{102}Y 360 ms β⁻, β⁻n
^{96}Sr 1.07 s β⁻	^{97}Sr 429 ms β⁻, β⁻n	^{98}Sr 653 ms β⁻, β⁻n	**^{99}Sr 269 ms β⁻=100 % β⁻n=0.10 %**	**^{100}Sr 200 ms β⁻=100 % β⁻n=1.11 %**	^{101}Sr 118 ms β⁻, β⁻n
^{95}Rb 378 ms β⁻, β⁻n	^{96}Rb 203 ms β⁻, β⁻n	^{97}Rb 169 ms β⁻, β⁻n	^{98}Rb 115 ms β⁻, β⁻n, β⁻2n	^{99}Rb 54 ms β⁻, β⁻n	**^{100}Rb 52 ms β⁻=100 % β⁻n=5.6 % β⁻2n=0.15 %**

Figure 11.1 – The main β^--decay chain used to populate ^{100}Zr in the present experiment (in red) and a weaker ($5.6(12)\%$ [159] or $26(8)\%$ [160]) β^--n branch to $A = 99$ isotopes (in blue). The half-lives and decay modes are taken from Ref. [159].

The Q values of the β^- decay of ^{100}Rb, ^{100}Sr, ^{100}Y and ^{100}Zr are as follows: $13574(21)$ keV, $7506(13)$ keV, $9050(14)$ keV, $3420(11)$ keV [159].

11.1.2 Beam deposition and decay

The beam mixture of ^{100}Rb and ^{100}Sr was transported to the low-energy experimental area of the ISAC I (Isotope Separator and ACcelerator) hall and delivered onto a mylar tape of the Moving Tape Collector at the center of the GRIFFIN spectrometer, marked as (2) in Fig. 11.2.

The Moving Tape Collector enabled the removal of the source of activity from the center of the GRIFFIN array, and typically operates in a cycling mode. Each cycle starts with a background measurement, then the beam is implanted onto the tape for a certain period of time ("beam on"). Subsequently, the beam is deflected by an electrostatic kicker and the subsequent measurement period is labelled as "beam off". The decay of the implanted radioactive ions can be observed throughout the cycle, or in selected periods. At the end of every cycle the beam deposition spot on the tape is moved outside of the array behind a thick (5 cm) lead shielding wall, labelled as (1) in Fig. 11.2.

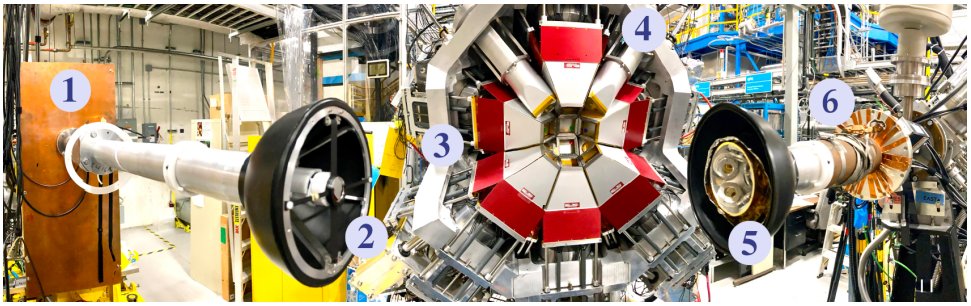

Figure 11.2 – Experimental setup, including the Moving Tape Collector with related lead shielding (1); mylar tape for beam deposition placed inside a vacuum reaction chamber (2); GRIFFIN HPGe clover detectors (one hemisphere shown, (3)); $LaBr_3$ detectors (4); PACES (5); beam line (6).

In the experiment two main cycle lengths were used referred to as "short" and "long" cycle. Most of the data were collected using the short cycle: 0.25s background measurement; 3.5s "beam on"; 1s "beam off" and 1s for the tape movement. The "beam on" period is approximately equal to five half-lives of ^{100}Y and was chosen to effectively saturate the ^{100}Y activity, while keeping the ^{100}Zr activity suppressed ($T_{1/2}(^{100}\text{Zr}) = 7.1(4)$ s), see Fig. 11.3. A small portion of the data were also collected with a longer "beam on" (20 s) and "beam off" (30 s) periods to observe the decay of ^{100}Zr into ^{100}Nb and ^{100}Mo.

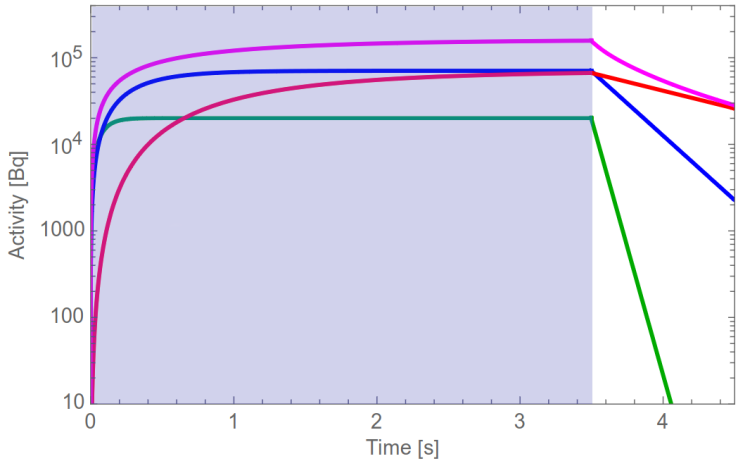

Figure 11.3 – Simulation of the activity build up of ^{100}Y (red), ^{100}Sr (blue), ^{100}Rb (green) and total (magenta) as a function of time [161]. The "beam on" period in the "short" cycle is illustrated with the shaded blue area.

11.1.3 GRIFFIN spectrometer

The daughter nuclei, produced in a β^- (or β^--n) decay, can be in an excited nuclear state and subsequently they de-excite through several γ decays. A large number of γ rays were observed, originating from all of the nuclei in the investigated

decay chains. They were registered by the high-efficiency HPGe clover detectors of the GRIFFIN (Gamma-Ray Infrastructure For Fundamental Investigation of Nuclei) spectrometer, labelled (3) in Fig. 11.2.

GRIFFIN consists of 64 HPGe crystals organized into 16 clover detectors. They are installed at 16 of the 18 available positions in a frame with a rhombicuboctahedral geometry. The remaining two positions are for the beam line and the tape system ((6) and (1) in Fig. 11.2, respectively). The frame consists of mechanical substructures - two "coronas", each holding four GRIFFIN detector units at $90°$, and four "lampshades" that each hold two GRIFFIN detector units at either $45°$ or $135°$ relative to the beam line [127].

Each GRIFFIN clover detector can be equipped with a set of bismuth germanate (BGO) Compton-suppression shields composed of separate front, side and back segments. The setup can be operated in two main configurations – a "high-efficiency" mode, in which the HPGe detectors are positioned 11 cm away from the tape and the front BGO shields are retracted, or an "optimized peak-to-total" mode, in which the HPGe crystals are placed 14.5 cm away from the beam spot and are fully Compton suppressed, see Fig. 1 in Ref. [127]. In the latter mode, a delrin absorber can also be placed around the vacuum chamber in order to suppress neutrons and electrons interacting with the HPGe detectors.

During the S1790 experiment the detectors were arranged in the "optimized peak-to-total" configuration, with 10-mm thick delrin absorber, and one of the clovers was removed to make space for the cooling system of PACES. The coordinates of the center of each crystal are given in Table E.1 in Appendix E. The large number of crystals and high γ-ray detection efficiency of the GRIFFIN spectrometer make it a perfect tool for performing γ-γ angular correlations [128]. Each two crystals can be organized into a pair with a specific opening angle, resulting in a total of 52 unique opening angles (see the last two columns of Table E.1 in Appendix E) that can be used for an angular-correlation analysis.

11.1.4 Ancillary detectors

In the present study, GRIFFIN was complemented by a set of ancillary detectors [127]:

- **Pentagonal Array for Conversion Electron Spectroscopy (PACES)** is an array of 5 lithium-drifted silicon (Si(Li)) detectors with approximately 5 mm thickness each. PACES has a combined solid angle coverage of 8% [144]. The detector can be used for registration of conversion electrons and alpha particles and is cooled to liquid nitrogen temperature in order to improve its resolution. In the present experiment, PACES was used for the registration of conversion electrons emitted in the decay of the excited daughter nuclei. The detector is placed inside the vacuum reaction chamber at backward angles, as marked with (5) in Fig. 11.2.

- **7 $LaBr_3$(Ce)** fast scintillator detectors (doped with 5% cerium) coupled to Photo Multiplier Tubes (PMT) were placed in the ancillary triangular positions on the GRIFFIN frame. Triangular BGO shields were used to reduce the amount of Compton-scattered γ rays. Due to their good timing resolution, the $LaBr_3$(Ce) detectors were used for fast-timing lifetime measurements in ^{100}Zr, reported in the PhD thesis of H. Bidaman [163], University of Guelph, Canada.

- **Zero Degree Scintillator (ZDS)** is a 1-mm thick BC422Q fast plastic scintillator. It is mounted inside the vacuum chamber, just behind the mylar tape (Fig. 11.2 (2)) and has a maximum solid angle coverage of 25% [144]. Thanks to its great timing properties, the ZDS can be used together with the $LaBr_3$ detectors for fast-timing measurements, or to select events that involve emission of β particles. In the analysis of the present experimental data the information from the ZDS was not used as due to the high rates and purity of the delivered radioactive ion beam the background level was low and tagging on β particles was not necessary.

The signals from all GRIFFIN HPGe detectors and ancillary detectors were processed by a custom-built digital electronics modules designed to operate at high counting rates (up to 50 kHz/crystal) [127] read out by the Maximum Integrated Data Acquisition System (MIDAS) [165]. Using the described setup, a large amount of data (40 TB) was collected in a triggerless mode within about two days of active data taking.

11.2 Data processing and calibration

The raw data from the data acquisition system were saved in a specific MIDAS format and had to be first "translated" to a format readable within the GRSISort framework [164]. GRSISort is an environment based on ROOT [64], designed to facilitate the analysis of GRIFFIN data sets.

11.2.1 From raw data to histograms

As a first step, the raw data were unpacked and organized in "TFragments" with the help of a GRSISort macro prepared following the examples given in Ref. [164]. Subsequently, the fragments were organized into ROOT trees containing "events". An event is a sequence of single detector hits registered in a given time window. Each hit contains information about the channel (i.e. detector), integrated charge of the pulse, timestamp, etc. [164]. The beginning of an event is given by a single detector hit. An event may contain multiple hits from different detector types - HPGe, $LaBr_3$, etc.

In the present study a static time window of 2 μs was used for the event building. About six weeks were needed to unpack and sort the collected raw data.

Multiple checks were performed at each step to ensure no data were lost or corrupted. As the final step, the events were filled into histograms following various coincidence conditions using the GRSIProof framework [164]. An energy calibration of the detectors was required at this stage, which was obtained as described in the following section.

11.2.2 Energy calibration of GRIFFIN

An initial energy calibration of GRIFFIN detectors was performed using data collected with five standard sources: ^{56}Co, ^{60}Co, ^{133}Ba, ^{152}Eu and ^{207}Bi. The source data were unpacked, sorted and organized into two-dimensional charge-channel histograms. The raw spectra obtained from the ^{60}Co data are shown in Fig. 11.4 (A). Each bin on the X axis represents a single crystal with its specific label used in the program, while the charge on the Y axis is given in arbitrary units. It is possible to obtain a one-dimensional spectrum of each HPGe crystal by projecting this two-dimensional histogram for a specific detector.

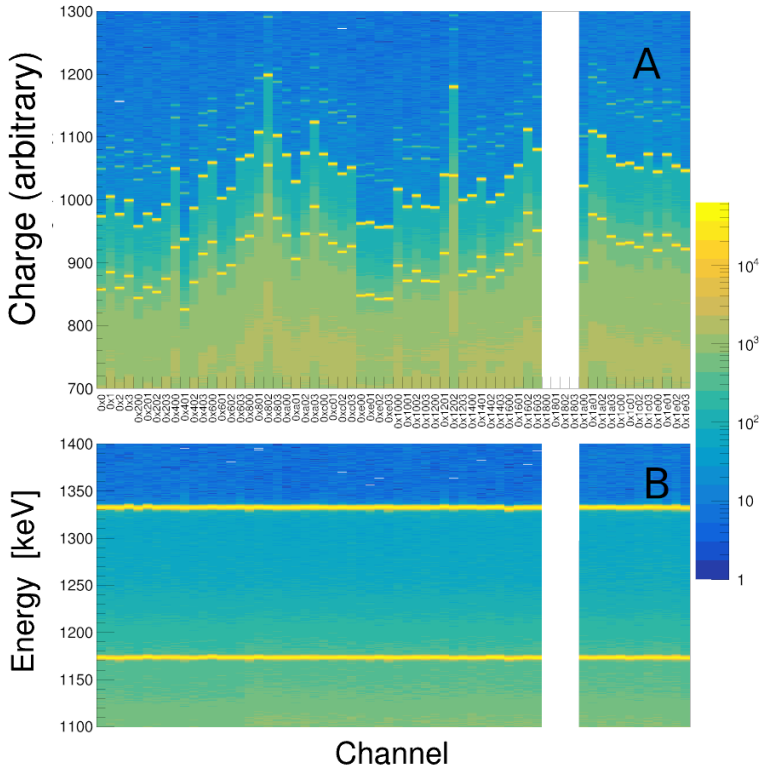

Figure 11.4 – Two-dimensional histograms obtained from the ^{60}Co source data before (A) and after (B) energy calibration. Each bin on the X axis corresponds to a single GRIFFIN crystal. On the Y axis, the raw charge is given in arbitrary units (panel A) and the calibrated energy in keV (panel B). The two lines in panel B correspond to the 1173-keV and 1333-keV γ rays emitted by the ^{60}Co source. The missing four crystals were removed from the setup to put the cooling system of PACES.

The charge peak positions were extracted from the one-dimensional spectra for each crystal using a semi-automatic procedure based on the newly-implemented feature of GRSISort TSourceCalibration [164], as shown in the left side of Fig. 11.5. The procedure reads energies and relative intensities of calibration peaks for each source from external files. The fitting procedure was controlled through two parameters: threshold (peak height relative to the largest peak) and sigma (peak width). They were varied to obtain satisfactory results. The data collected with all five sources were treated simultaneously. The extracted peak positions in arbitrary units were compared to their literature energies E_{LIT} and fitted with a polynomial function. The goodness of the calibration was tested by calculating the differences between the calculated (E_{CAL}) and literature energies as shown on the right side of Fig. 11.5. A linear calibration function was used for the majority of the crystals with only a few exceptions, where a higher-order (quadratic or cubic) polynomial was preferred. Additionally, the calibration of several detectors had to be performed "by hand" as the automatic procedure failed or did not reach satisfactory results. The obtained calibration functions for all 60 crystals of the GRIFFIN clover detectors were applied to the sorted data. The calibrated ^{60}Co data are presented in Fig. 11.4 (B) where the 1173-keV and 1333-keV γ-ray peaks are well aligned in all crystals.

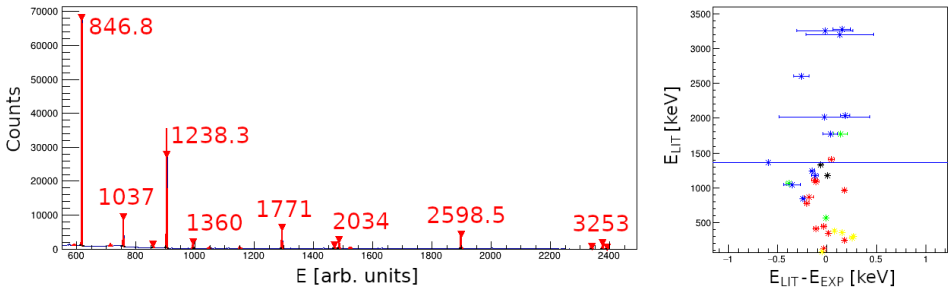

Figure 11.5 – Part of the TSourceCalibration interface. Left: Spectrum obtained with a ^{56}Co source. The marked peaks were automatically identified and fitted. Right: Residuals, i.e. $(\mathrm{E_{LIT}} - \mathrm{E_{CAL}})$, as a function of the γ-ray energy. Data points obtained with the ^{56}Co (blue), ^{60}Co (black), ^{133}Ba (yellow), ^{152}Eu (red) and ^{207}Bi (green) sources are presented.

The residuals (differences between the experimental and literature energies) obtained by fitting the spectra of a single crystal (in red) and the total summed spectra for all sixty crystals (in black) are compared in Fig. 11.6 (A). Although the energy calibration of a few crystals resulted in residuals larger than 0.5 keV, overall, the applied calibration leads to deviations from the literature data smaller than 0.2 keV. However, summing the spectra of all individual crystals results in a broadening of the γ-ray peaks, i.e. an increase of their full width at half maximum (FWHM). This effect increases with the energy and at energies higher than 3 MeV, the FWHM$_{ALL}$ of a peak in the summed spectrum is larger by more than 0.5 keV

than the FWHM$_{single}$ of the same peak in single-crystal spectra, as demonstrated in Fig. 11.6 (B).

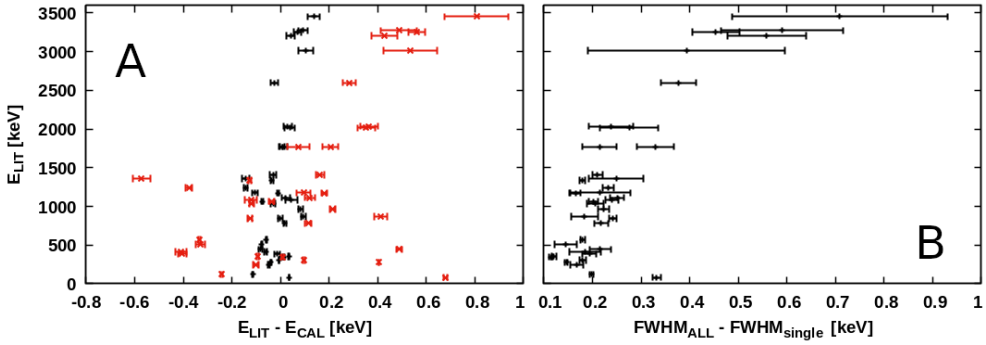

Figure 11.6 – (A) Difference between the literature E_{LIT} and experimental E_{CAL} peak positions, obtained from the calibrated source spectra of a random single crystal (in red) and the summed spectra of all HPGe detectors (in black). (B) The difference between the FWHM of the peaks in the summed spectra and in the spectra of a single crystal. An increase of the FWHM with E_{LIT} is observed.

The energy calibration procedure described above should be understood as an initial alignment of energy spectra, which needed to be further refined using in-beam data, as the gain was observed to be slightly rate dependent. However, no significant "gain drift" was observed in the in-beam data over the duration of the experiment, suggesting that the electronics of GRIFFIN detectors was very stable.

11.2.3 Add-back procedure and cross-talk correction

When γ rays interact with the detector material, they may deposit only a part of their energy if a Compton-scattering event occurs (γ ray scattering from a charged particle, mostly atomic electrons). Such events do not contribute to the main photo-peak and instead contribute to the background at lower energies. This results in a deterioration of the energy resolution and peak-to-total ratio, especially for low-energy γ-ray peaks. Thus, Compton scattering degrades data quality and measures need to be taken to suppress it. As discussed in Section 11.1.3, active anti-Compton BGO shielding was used during the experiment and anti-coincidences between the HPGe and the BGO detectors were required when sorting the data.

It is possible to further reduce the effects from Compton scattering and recover some of the lost events when clusters of HPGe detectors are employed by using add-back algorithms. A γ ray may deposit its total energy in a HPGe clover through a series of Compton scatterings between individual crystals forming the clover. The energy of the original γ ray may be recovered if the signals from the individual crystals registered within a fixed add-back time window are summed together. However, when interactions occur close in time in neighbouring crystals within the same clover, cross-talk effects start to play an important role, i.e. the signals from individual crystals may interfere with and distort each other. This leads to a

shift of the energy resulting from the add-back procedure, and a worsened energy resolution. The effect depends on the particularities of the experimental setup, on the energy deposited in the neighbouring crystals and the time differences between the events. A detailed discussion of several methods used for cross-talk correction can be found in Ref. [168].

Selected peaks in the total (all HPGe detectors) spectrum of the ^{56}Co source, obtained using the add-back procedure, are shown in Fig. 11.7 with (blue) and without (red) cross-talk corrections applied. The effects are rather small at energies below 1 MeV. However, at higher energies the applied correction significantly improves the quality of the spectra. A reduction of the peak broadening towards lower energy is observed, and the peak energies are slightly shifted and reproduce better the literature energy values. Furthermore, the separation of doublet peaks is facilitated (see the region around 2610 keV in Fig. 11.7). The described procedures are crucial for disentangling complex data sets with many observed transitions as in the case of the present study.

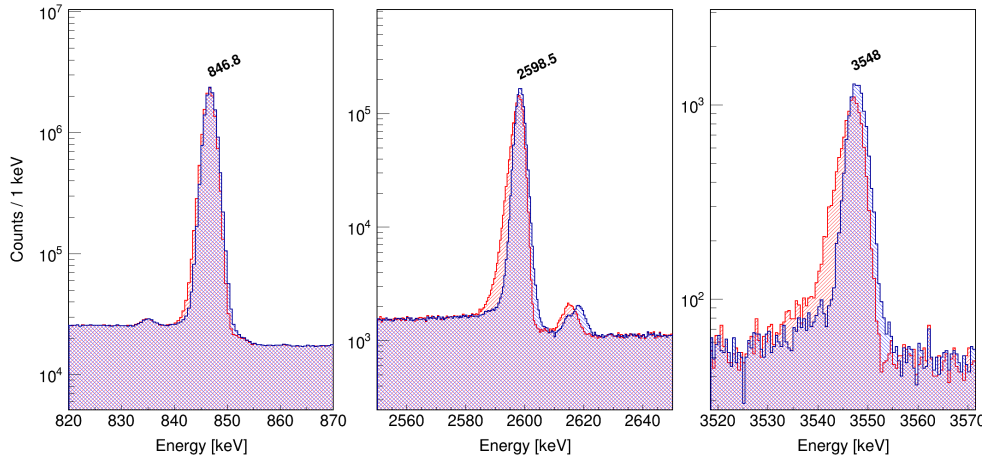

Figure 11.7 – Selected γ-ray peaks observed in the total ^{56}Co source spectrum obtained with the add-back procedure with (blue) and without (red) a cross-talk correction.

11.2.4 Efficiency calibration

An efficiency calibration has to be performed to allow for a comparison to be made between the intensities of γ-ray peaks with different energies. The differences in the detector response as a function of the energy were investigated using ^{152}Eu, ^{56}Co and ^{133}Ba sources placed at the center of GRIFFIN. The energies (E_γ) and relative intensities (I_γ) of the observed γ rays are known with good precision. The measured values were compared to the literature E_γ and I_γ to obtain the relative efficiency ($\varepsilon(E_\gamma)$) in arbitrary units, i.e. the likelihood of detecting γ rays of a particular energy E_γ relative to another reference energy.

If γ-ray detectors cover large solid angles, summing effects may strongly influence the observed energy spectra, including those of calibration sources emitting γ rays in cascades. In "summing out", the photo-peak efficiency is reduced due to summing of the γ ray of interest with other γ rays depositing their full or partial energy in the same crystal. Summing effects in GRIFFIN data can be evaluated making use of the fact that γ-ray angular correlations are symmetric about 90°, which means that the number of coincident γ rays observed in pairs of crystals separated by 180° is equal to the number of those which are summed in a single crystal (i.e. an angular difference of 0° between the two emitted γ rays). Therefore, the magnitude of the summing effects for each transition can be determined from the experimental data by using γ-γ coincidences between detectors separated by 180° [168].

Due to prolonged unavailability of coincidence source data from the S1790 experiment following a failure of a server at the University of Guelph, summing correction factors C_{sum} determined from ^{56}Co, ^{133}Ba, and ^{152}Eu source data in Ref. [169] were used in the present work. The values reported in Table 3.1 of Ref. [169] were extracted for the high-efficiency configuration of GRIFFIN used in the experiment, thus had to be scaled (as $0.57(C_{sum}-1)+1$) to account for the difference in the solid angle in the present work.

To obtain the efficiency calibration, in total 30 experimental points with energies between 81 and 3273 keV were fitted with the function:

$$\ln(\varepsilon(E_\gamma)) = [(A + Bx + Cx^2)^{(-G)} + (D + Ey + Fy^2)^{(-G)}]^{(-1/G)}, \qquad (11.1)$$

where $x = \ln(E_\gamma/100)$, $y = \log(E_\gamma/1000)$ and E_γ is given in keV. The fit was carried out with the EFFIT program from the RadWare package [170]. The data from different sources were scaled until the points overlapped to obtain the relative efficiency curve presented in Fig. 11.8. The corresponding coefficients are: $A = 8.05(9)$, $B = 1.4(3)$, $C = 0$, $D = 6.792(1)$, $E = -0.407(3)$, $F = -0.044(3)$, $G = 15$. A 3% relative uncertainty was conservatively adopted for the efficiency based on the analysis of residuals presented in Fig. 11.9.

Using the nominal activity of the sources the total absolute efficiency of the setup was estimated to be $\approx 9\%$ at 1 MeV. This value is slightly smaller than the efficiency predicted using the GRIFFIN efficiency calculator [167], which yields 10% absolute efficiency at 1 MeV for a setup consisting of 15 GRIFFIN clusters and a 10 mm delrin absorber.

11.2.5 γ-γ coincidences

Among the main goals of this study is to extend the existing level scheme of ^{100}Zr and obtain the relative intensities of different decay branches with a better precision than previously reported [147]. This can be achieved by analysing γ-γ coincidence data. Only γ rays registered in a narrow time window can be considered correlated in time. Thus, as a first step, signals of the individual GRIFFIN crystals were time-aligned. [163].

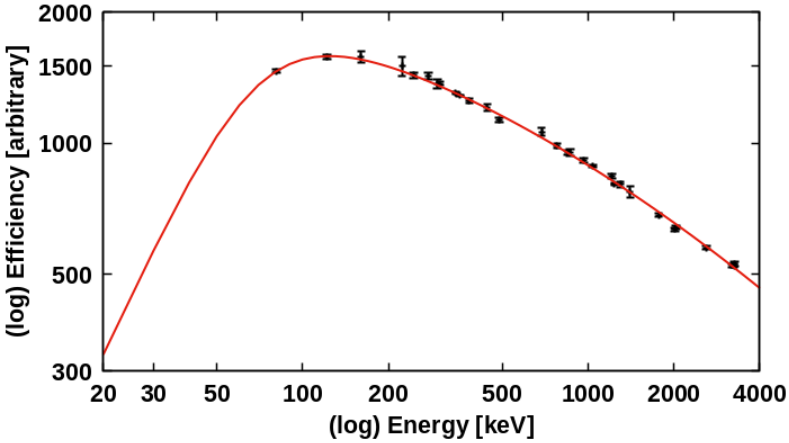

Figure 11.8 – Relative efficiency as a function of the γ-ray energy, presented in doubly-logarithmic scale. Efficiencies deduced from experimental data, with scaling factors for each source applied, are presented in black and the relative efficiency curve in red.

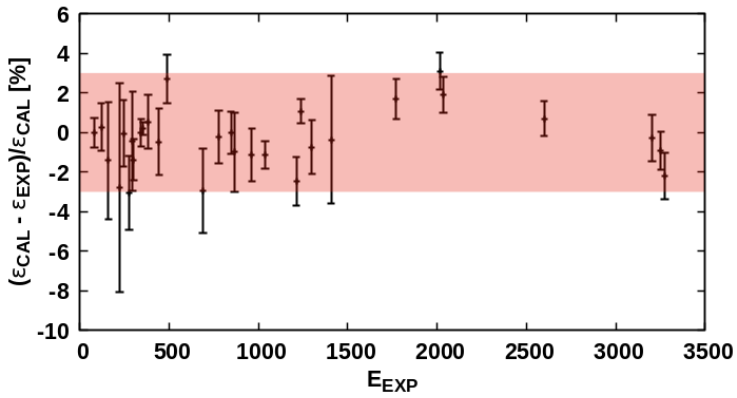

Figure 11.9 – Relative differences in percent between the efficiency ε_{CAL} calculated using the curve obtained with EFFIT and the experimentally measured values ε_{EXP} as a function of the energy of the γ ray. The shaded area corresponds to the 3% uncertainty adopted in the analysis.

On the basis of the HPGe-HPGe time difference spectra it was possible to select a "prompt" coincidence time window of 300 ns. If the time difference between two γ rays registered by GRIFFIN is smaller than 300 ns, they can be considered to be emitted in a cascade. However, some of those events may still be due to random coincidences, i.e. time-uncorrelated events. In order to correct for that, two-dimensional γ-γ matrices were created for both prompt (time difference $\Delta t <$ 300ns) and time-random events (350ns $< \Delta t < 713$ns). The time-random matrix was scaled with a coefficient of 0.83 (calculated as the ratio of the widths of the two Δt regions) and subtracted from the prompt matrix. The resulting time-

random-subtracted matrix was gated on several γ rays of different energies and the obtained energy spectra were investigated for possible over-subtraction of time randoms or large self-coincidence peaks. Although this procedure resulted in a small self-coincidence peak for the most intense γ ray (212 keV), it was confirmed to perform correctly for less intense peaks (e.g. 1108 keV).

If the counting rates during the experiment are high, a loss of data may occur due to pile-up events. These are events in which a second γ ray hits a detector before the charge collection related to the previous γ ray is completed, and consequently the new signal is superimposed on top of the first one. The GRIFFIN DAQ is capable of separating some of the pile-up signals and recovering information on the individual γ rays that were added together. Pulses that exhibit a systematic increase of the amplitude during sampling are recognized, and flagged as pile-ups [166]. The amplitude of each signal is sampled KValue times. In the current experiment, events without pile-up corresponded to $\mathrm{KValue} = 379$, while for the recovered pile-up events, which amounted to about 11% of the obtained data, the number of samples is lower, thus $0 < \mathrm{KValue} < 379$. Due to the shorter integration time, the recovered pile-up events correspond to a worse energy resolution. Thus, they were excluded from the γ-γ coincidence matrices by requiring a $\mathrm{KValue} = 379$.

Finally, only the data collected with the "short" tape cycle were used to investigate the structure of ^{100}Zr. However, it was found that the information on the cycle time was not properly stored for many among the data runs. Thus, an effort was made to recover this information by calculating it on a sub-run-by-sub-run basis from the saved data of the PPG (Programmable Pattern Generator), which was used to control the movement of the tape. The possibility to exclude part of the data collected in a cycle is crucial in the angular-correlation analysis, as it will be explained in Section 12.3.

12 - Analysis and results

A γ-γ matrix was built using all data collected with the short-cycle tape movement setting using a 300 ns prompt coincidence window. After implementing all of the procedures described in Section 11.2, the total number of Compton-suppressed coincidence events was $\approx 4\text{x}10^9$ (with add-back implemented and after the subtraction of time-random events). Although the richness of the current data set makes it possible to largely extend the level scheme of ^{100}Zr with respect to earlier measurements presented in Section 12.1, this manuscript is focused mainly on the low-lying excited states in ^{100}Zr with excitation energy below 2.2 MeV. The obtained results have a preliminary character and the analysis will be refined and extended in the future.

12.1 Information from previous β-decay studies of ^{100}Zr

The work of Wohn et al. [145] is the most detailed previous study of the β decay of the ^{100}Y ground state. It has confirmed and largely extended the level scheme of ^{100}Zr proposed in the earlier works [143, 171].

The primary beam was produced with a Re surface ionization source containing enriched ^{235}U bombarded with neutrons. A beam of ions with mass 100 (predominately ^{100}Sr) was mass separated by the TRISTAN facility at Brookhaven National Laboratory and delivered onto a mylar tape connected to a moving tape station. Decay data were collected in several different tape movement modes to enable separation between long- and short-lived decay products. The γ rays emitted from the excited products of the decay were registered with either one (for γ-ray singles measurements), or two or four (for γ-γ coincidence and angular correlation measurements) Ge(Li) detectors. A thin plastic scintillator was used to register β particles, which helped improving the quality of γ-ray singles spectra by applying a β-coincidence gate. In addition a Si(Li) detector with 200 mm^2 area and 3 mm depletion depth was used for detection of conversion electrons.

Based on the collected data, 64 γ-ray transitions were placed between 20 levels in ^{100}Zr. The highest reported state had an excitation energy of 4288 keV, while the weakest transition placed in the decay scheme ($2_2^+ \rightarrow 4_1^+$) amounted to 0.09% of the intensity of the $2_1^+ \rightarrow 0_1^+$ transition. Several rather intense lines remained unplaced, some of which will be further discussed in Section 12.2. The authors also reported that due to the close detector geometry ($5-7$ cm from the tape) coincidence summing was not negligible. While the summing corrections have been applied to the measured intensities, it seems that the branching ratios were extracted from singles spectra, and thus the results should be taken with caution and possibly verified using coincidence data. The level scheme proposed by Wohn et al [145] is presented in Fig. 12.1 for states below 2.2 MeV excitation energy.

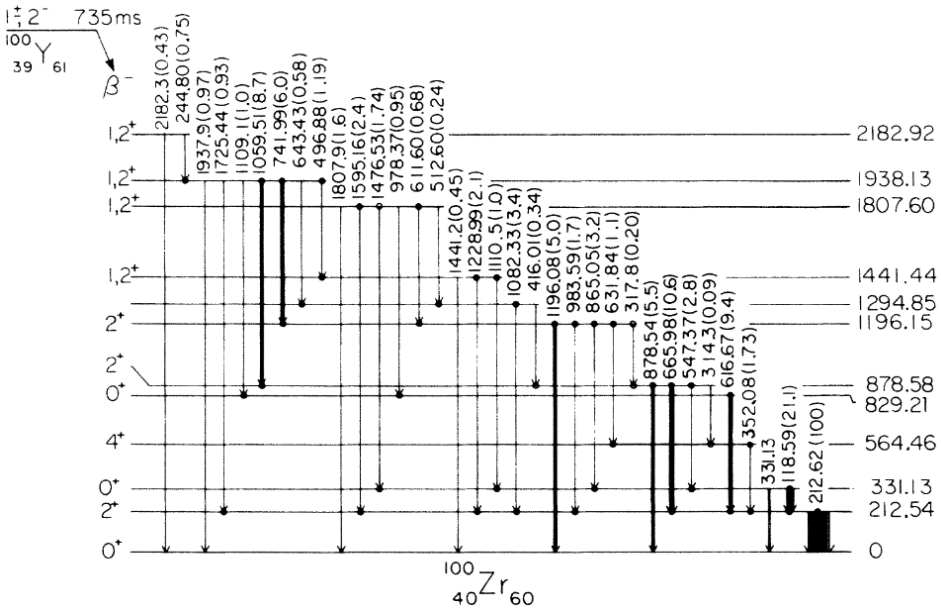

Figure 12.1 – Low-energy part of the decay scheme for the ground state of ^{100}Y, obtained in Ref. [145]. Energies (in keV) and relative intensities of γ-ray transitions are given and illustrated by arrow widths. Figure adapted from Ref. [145].

The half-lives of ^{100}Sr $(193$ ms) and ^{100}Y $(735$ ms) were measured and the spin-parity of the ground state of ^{100}Y was constrained to $1^{\pm}$ or 2^{-}. The four Ge(Li) detectors were positioned to form 6 distinct opening angles between each two crystals - $90°$, $105°$, $120°$, $135°$, $150°$ and $165°$. Using γ-γ angular correlations for $I_i \rightarrow 2_1^+ \rightarrow 0_1^+$ cascades, the spin assignment of the 0_2^+ state at 331 keV, previously reported in Ref. [143], was confirmed. In addition, the 0_3^+ state was identified for the first time and a mixing ratio for the $2_2^+ \rightarrow 2_1^+$ transition was extracted. However, due to a low coincidence statistics, the latter was subject to a large uncertainty. The spin-parities of the remaining populated states were proposed to be $1^{\pm}$ or 2^+ (based on the spin-parity of the parent nucleus) if a transition to the ground state was observed.

Finally, using triple coincidences between a β particle, a γ ray and a conversion electron registered in the Si(Li) detector, the K and $L+M$ conversion-electron intensities related to the 118-keV $(0_2^+ \rightarrow 2_1^+)$ $E2$, 212-keV $(2_1^+ \rightarrow 0_1^+)$ $E2$ and 331-keV $(0_2^+ \rightarrow 0_1^+)$ $E0$ transitions were measured. The branching ratio of the $E0$ and $E2$ transitions de-exciting the 331-keV 0_2^+ level was determined.

12.2 Level scheme of ^{100}Zr obtained from the present data

The γ-ray spectrum up to 2 MeV energy obtained by projecting the time-random-subtracted γ-γ coincidence matrix is presented in Fig. 12.2. A large number of γ-ray peaks is observed, mostly originating from the decay of excited states

in ^{100}Zr (indicated with black asterisks). Only the most intense lines in ^{100}Zr, previously reported and summarized in the ENSDF database [147], are marked. Some of the γ rays, originating from other nuclei in the β-decay chain of ^{100}Rb, are marked as well: ^{100}Sr (red), ^{100}Y (blue) and ^{100}Nb (green) [159].

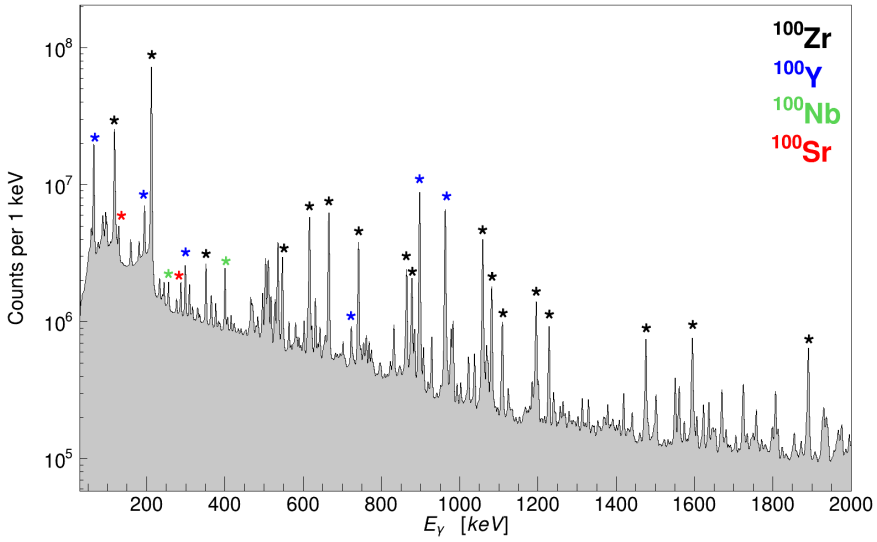

Figure 12.2 – Part of a projection of the γ-γ coincidence matrix for γ-ray energies up to 2 MeV. Most intense γ rays among those previously known in ^{100}Sr (red), ^{100}Y (blue), ^{100}Zr (black), and ^{100}Nb (green) [159] are marked.

The decay scheme of ^{100}Zr was constructed by gating on the obtained γ-γ matrix using the ESCL8R program from the RadWare package [170]. The γ-γ histogram was projected with the help of the SLICE program [170]. A smooth background was simulated using the GF3 RadWare program [170] and used as an input for ESCL8R. As a first step, the low-energy levels reported in previous β-decay studies [145, 171] were investigated.

Using the current coincidence data the placement of all γ rays proposed by Wohn et al. [145] resulting from decay of states up to an excitation energy of 2.2 MeV (summarized in Fig. 12.1) was confirmed. The 1606.8 keV γ ray connecting the 0_2^+ state and the $(1, 2^+)$ state at 1938 keV, which was previously reported only in Ref. [171] and listed as "uncertain" by the ENSDF evaluators, was also confirmed. In addition, a 1670.8-keV γ ray, which was observed in Ref. [145], but not placed in the level scheme, has been placed in the current work. Moreover, five new transitions between the states reported in Ref. [145] were observed in the current data set: a γ-ray doublet at $\approx$ 366 keV and γ rays at 375.4(2) keV, 612.2(2) keV, and 929.0(6) keV. The latter was found to connect the $(1, 2^+)$ state at 1807.7 keV and the 2_2^+ state. It can be speculated that Wohn et al. have also observed this line, as indicated in Fig. 12.3 in green. However, their coincidence

data were probably insufficient to resolve the 929-keV line from the $928.34(3)$-keV γ ray, originating from the decay of the 2_3^+ state in ^{100}Mo. Similarly, the low-intensity 366-keV doublet in ^{100}Zr was obscured by the $365.31(4)$-keV γ ray originating from the $(1^+, 2, 3^+)$ state at 376.1 keV in ^{100}Y, marked in Fig. 12.3 in red.

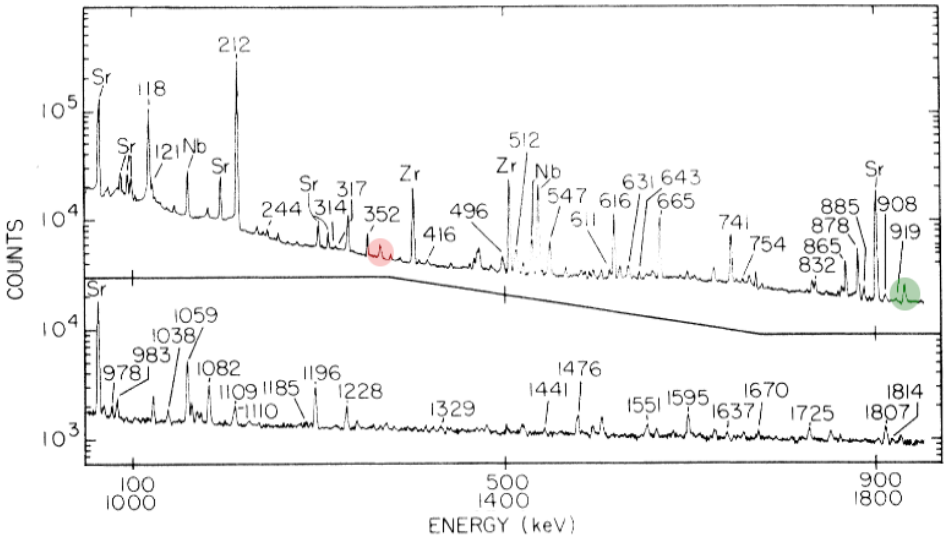

Figure 12.3 – γ-ray singles spectra from the decay of $A = 100$ isotopes observed in Ref. [145]. The lines from the decay of ^{100}Y (transitions de-exciting states in ^{100}Zr) are labelled with their energies. Some of the lines from the decay of ^{100}Sr, ^{100}Zr and ^{100}Nb are also labelled with the corresponding element symbol. See the text for the discussion of the peaks indicated in red and green. Figure adapted from Ref. [145].

In the current work it was possible to resolve the 366-keV doublet in ^{100}Zr and separate it from the 365-keV line in ^{100}Y by using suitable coincidence conditions. Fig. 12.4 illustrates the effects of using different gates and demonstrates that the centroids of the three resulting peaks correspond to distinct energies, i.e. different transitions. The spectrum of ^{100}Y was obtained by gating on the 484.7-keV γ ray depopulating the state at 860.60 keV [147]. To observe the 366.2-keV transition in ^{100}Zr connecting the $(1, 2^+)$ state at 1808 keV and the $(1, 2^+)$ state at 1441.5 keV, coincidences were required with the 1229-keV γ ray depopulating the latter, as illustrated on the right side of Fig. 12.4. The 366.9-keV line in ^{100}Zr is also clearly observed in the spectra obtained by gating on the 742-keV γ ray originating from the 1938-keV state.

Another doublet at 612 keV was resolved. In Ref. [145] the 612-keV line was attributed solely to the transition connecting the states at 1808 and 1196 keV. However, as demonstrated in Fig. 12.5, if a gate is set on the 497-keV γ ray depopulating the $(1, 2^+)$ state at 1938 keV to the state at 1441 keV, a 612.2-keV line is clearly observed (in red). Therefore, the observed 612-keV γ ray corresponds to the decay of the 1441-keV state to the 829-keV 0_3^+ state. On the other hand,

if a gate is set on the 885-keV γ ray originating from the state at 2693 keV [145], the observed intensity of the 611.5-keV line is too large to be solely attributed to the new transition from the 1441-keV state to the 0_3^+ state, thus the previously reported transition between the states at 1808 and 1196 keV is indeed present as well. These new findings suggest the existence of a pair of doublet cascades with $611-367$-keV and $366-612$-keV γ rays. The large number of coincidence events was crucial for disentangling these γ rays.

Finally, a new 375.4-keV γ ray was found connecting the states at 2183 keV and 1807 keV. This placement was confirmed by gating on a transition directly populating the state at 2183 keV, as further explained in Section 12.2.1.

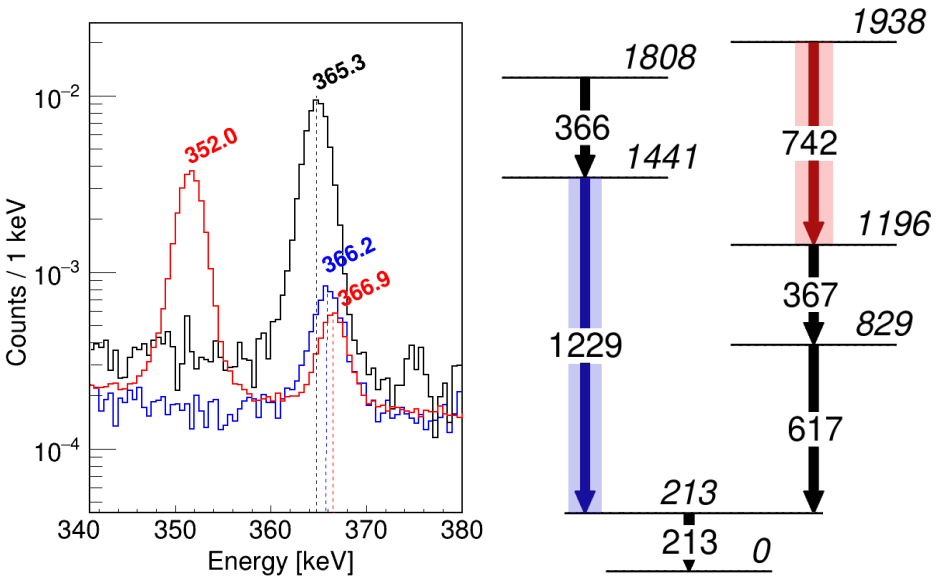

Figure 12.4 – Energy spectra obtained by applying gates on the 484.7-keV γ ray depopulating the state at 860.6 keV in ^{100}Y (black), and on the 1229-keV (blue) and 742-keV (red) γ rays originating from excited states in ^{100}Zr. The observed peaks are labeled with their energy given in keV. The 352-keV line originates from the decay of the 4_1^+ state in ^{100}Zr.

Thanks to the high coincidence statistics, several new states up to about 2.2 MeV excitation energy were identified:

- **A state at 1773.99(7) keV** was proposed based on the observation of an intense γ-ray transition with an energy of $1561.42(6)$ keV in coincidence with the transition depopulating the 2_1^+ state, see Fig. 12.6. In addition, a weaker $577.94(5)$-keV branch decaying out of the proposed state to the 2_3^+ state was found. Gating on the 1561.4-keV line revealed an intense feeding transition with an energy of $1072.0(2)$ keV, connecting the proposed state at 1774 keV with a previously reported state at $2846.34(7)$ keV [145].

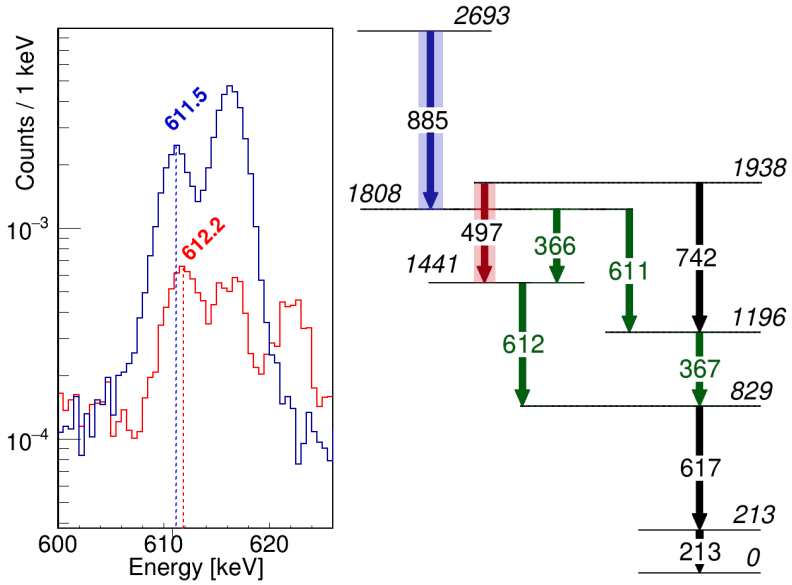

Figure 12.5 – Energy spectra obtained by applying gates on the $885.06(6)$-keV γ ray depopulating the state at $2692.84(9)$ keV (blue) and on the $496.63(9)$-keV (red) transition originating from the $1937.97(6)$-keV excited state in ^{100}Zr. The observed peaks are labelled with their energy given in keV. The corresponding gating transitions are marked in the partial level scheme in the right panel using the same color code. The doublet cascades with $611-367$-keV and $366-612$-keV γ rays are indicated in green.

- Similarly, **a state at $1883.16(6)$ keV** was placed due to the observation of an intense $1670.63(5)$-keV line, which was previously reported in Ref. [145], but remained unplaced, in a 212.6-keV gated spectrum shown in Fig. 12.6. Two other decay branches of the new state were identified: to the 0_2^+ state via a $1552.07(7)$-keV γ ray and to the 0_3^+ state via a $1053.83(7)$-keV transition. Gating on any of these transitions revealed an intense feeding transition with an energy of $962.9(1)$ keV, suggesting that the new state is also connected to the $2846.34(7)$-keV state.

- The existence of **a state at $1970.75(7)$ keV** was deduced following the observation of $775.08(8)$-keV and $1758.4(2)$-keV γ rays in the spectra gated on the $1195.98(9)$-keV and $212.59(2)$-keV γ rays, respectively. Another branch depopulating the state at 1970.8 keV to the 1441.4 keV state was observed with an energy of $529.39(3)$ keV. A feeding $799.6(3)$-keV γ ray, originating from the state at $2770.76(8)$ keV [145] was observed in coincidence with all three γ rays depopulating the proposed state at 1970 keV.

- **A state at $2068.09(15)$ keV** was proposed following the observation of an intense $1855.53(11)$-keV transition in coincidence with the 212.6-keV

$2_1^+ \rightarrow 0_1^+$ transition. Rather intense transitions from the new 2068.1-keV state to the 2_2^+ state ($E_\gamma = 1189.8(2)$ keV) and to the 2_3^+ state ($E_\gamma = 872.0(3)$ keV) were observed as well. A feeding γ-ray transition with an energy of $777.9(3)$ keV, originating from the decay of the $2846.34(7)$-keV state [145] was identified.

- **A new state at $2143.70(4)$ keV** was proposed based on the observation of a $1931.00(5)$-keV γ ray in coincidence with the transition depopulating the 2_1^+ state, see Fig. 12.6. Several other decay branches of the new state were found, namely to the state at 1807.5 keV ($E_\gamma = 336.23(3)$ keV), to the state at 1938 keV ($260.50(7)$-keV γ ray), to the 2_2^+ and 2_3^+ states ($1265.26(4)$ keV and $947.62(7)$ keV, respectively). A feeding transition with an energy of $702.55(3)$ keV was observed in coincidence with all five transitions de-exciting the proposed state at 2143.7 keV. It originates from the decay of the $2846.34(7)$-keV state, previously reported in Ref. [145].

- Finally, **a new state at $2208.51(5)$ keV** was found due to the observation of an intense $1995.97(8)$ keV line in the spectrum obtained by gating on the 212.6-keV line. The new state was found to decay to the 0_2^+, 0_3^+, 2_2^+, 4_1^+ states, to the states at 1441.4 and 1294.8 keV, as well as via a direct transition to the ground state, as reported in Ref. [172]. A feeding transition with an energy of $637.6(1)$ keV, originating from the state at $2846.34(7)$ keV [145], was observed in coincidence with all eight depopulating γ rays. It is interesting to note that a (5^+) state with an almost identical energy ($2208.40(8)$ keV) was previously proposed in Ref. [146] following fission of ^{248}Cm and ^{252}Cf. This state cannot be populated in the present experiment due to the low spin of the parent nucleus. The decay pattern of the (5^+) state differs significantly from that of the new $2208.51(5)$-keV state with the only exception being the 1644-keV γ ray to the 4_1^+ state. Based on its decay pattern, including transitions to the 4_1^+ and several 0^+ states, as summarized in Table 12.1, this state was assigned to have spin 2 [172].

The spectrum presented in Fig. 12.6 was obtained by gating the total γ-γ matrix on the 212.6-keV γ ray. The γ-ray peaks which indicated the existence of the above-mentioned new states are labelled in red. Previously observed γ-ray transitions at 1551.4 keV (between the states at 2846.3 and 1294.8 keV [145]), 1595.0 keV (between the state at 1807.5 keV and the 2_1^+ state), 1725.3 keV (between the state at 1938.0 keV and the 2_1^+ state), and 1891.8 keV (between the state at 2770.8 keV and the 2_2^+ state [145]) are labelled in black.

The excitation energies of the identified states in ^{100}Zr were obtained via a least-squares fit to the set of measured γ-ray energies, performed using GLS [170]. These level and transition energies are listed in Table 12.1. The transitions observed for the first time in this work are presented in red in the proposed partial level

schemes of ^{100}Zr summarized in Figs. 12.7 (up to 1.8 MeV) and 12.8 (up to 2.2 MeV). The states and transitions in black were reported already in Ref. [145] and are confirmed in the present study. The proposed new states are also marked in red.

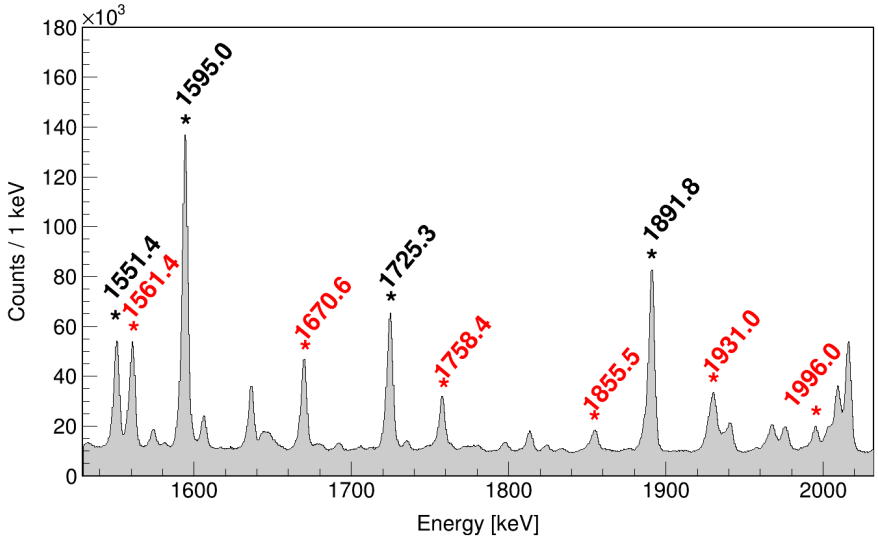

Figure 12.6 – Part of the energy spectrum obtained by gating the total γ-γ matrix on the 212.6-keV $2_1^+ \rightarrow 0_1^+$ transition in ^{100}Zr. Selected transitions are labelled with their energies in keV. Red colour is used for those reported for the first time in the present work.

The γ-ray energies in Table 12.1 and their uncertainties were obtained using an additional in-beam calibration. It was found that although the energy calibration resulting from a fit to the source data yielded very small residuals (< 0.2 keV) for the source peaks (see Fig. 11.6), certain systematic discrepancies from the literature were observed for the measured energies in the in-beam decay data. This gain change was found to depend on the counting rate, i.e. it was largest for the decay of ^{100}Sr and ^{100}Y, and vanishing for the decay of ^{100}Nb. Therefore, it was necessary to refine the energy calibration applied to ^{100}Zr data using well known intense lines in ^{100}Zr. The γ rays used for this calibration are summarized in Table 12.2, where the literature values of the γ-ray energies E_γ^{LIT} are taken from Ref. [147], while the experimental ones E_γ^{INI} were obtained by fitting the corresponding peaks in the total projection of the γ-γ matrix with the initial energy calibration applied (see Section 11.2.2). The peaks of interest were fitted with a combination of a Gaussian function, a skewed Gaussian, and the background of a step function with a constant. The uncertainties of E_γ^{INI} in Table 12.2 originate from the peak fitting procedure and account for the systematic effects evaluated by using different fitting functions and performing the fit to different regions of the spectrum around the peak of interest.

Table 12.1 – Excited states of ^{100}Zr with spin-parities I_i^π (marked with daggers if extracted via γ-γ angular correlations in the present work, or with double daggers if deduced from the observed decay pattern) and excitation energies E_x^i, decaying to states with energies E_x^f via γ rays with energies E_γ. The intensities relative to the most intense transition depopulating the state of interest, extracted from the current analysis, are given in the fifth column, while those taken from literature [147] are presented in the last column for comparison. Energies are given in keV. Transitions used for the in-beam calibration are marked with asterisks.

I_i^π	E_x^i[keV]	E_x^f[keV]	E_γ[keV]	I_γ	I_γ [147]
2_1^+	212.53(3)	0	212.60(2)*	100	100
0_2^+	331.08(4)	212.53(3)	118.58(3)*	100	100
4_1^+	564.54(7)	212.53(3)	352.05(5)*	100	100
0_3^+	829.28(6)	212.53(3)	616.74(5)*	100	100
2_2^+	878.49(4)	564.54(7)	314.2(5)	0.83(9)	0.9(3)
		331.08(4)	547.54(7)*	31.2(13)	30(4)
		0	878.47(11)*	54(2)	52(4)
		212.53(3)	665.98(4)*	100(4)	100(6)
2_3^+	1196.08(5)	829.28(6)	366.9(4)	3.03(13)	–
		878.49(4)	317.61(6)	6.2(3)	4.0(8)
		564.54(7)	631.66(10)*	23.9(10)	21.4(20)
		212.53(3)	983.5(2)	36.3(15)	34(4)
		331.08(4)	865.04(5)*	84(4)	65(4)
		0	1195.98(9)*	100(4)	100(6)
$0_4^{+\dagger}$	1294.77(5)	878.49(4)	416.36(7)	7.4(4)	10.0(12)
		212.53(3)	1082.26(4)*	100(4)	100(9)
$2^{+\dagger}$	1441.36(4)	829.28(6)	612.2(2)	3.6(2)	–
		0	1441.23(11)*	16.9(7)	21(4)
		331.08(4)	1110.33(3)	58(3)	65(20)
		212.53(3)	1228.85(3)*	100(4)	100(10)
$0_5^{+\dagger}$	1773.99(7)	1196.08(5)	577.94(5)	6.3(3)	–
		212.53(3)	1561.42(6)	100(4)	–
$1^\dagger$	1807.49(4)	1441.36(4)	366.23(11)	2.1(3)	–
		1294.77(5)	512.73(5)	15.8(7)	10(3)
		878.49(4)	929.00(6)	21.9(10)	–
		1196.08(5)	611.5(5)	29.3(13)	28(3)
		0	1807.41(5)*	42.8(18)	67(13)
		829.28(6)	978.1(2)	55(2)	40(4)
		331.08(4)	1476.55(5)*	91(4)	73(8)
		212.53(3)	1594.98(4)	100(4)	100(13)
$(1,2^+)^\ddagger$	1883.16(6)	829.28(6)	1053.83(7)	14.4(7)	–
		331.08(4)	1552.07(7)*	25.2(8)	–
		212.53(3)	1670.63(5)	100(3)	–

Table 12.1 – Excited states in ^{100}Zr - continued

I_i^π	E_x^i[keV]	E_x^f[keV]	E_γ[keV]	I_γ	I_γ [147]
$1^{(-)\dagger}$	1937.97(6)	331.08(4)	1606.77(12)	3.1(2)	–
		0	1937.66(11)	4.8(3)	11.2(14)
		1294.77(5)	643.40(13)*	6.7(3)	6.7(9)
		829.28(6)	1109.2(2)	9.4(4)	11(3)
		212.53(3)	1725.3(2)*	11.1(5)	10.7(17)
		1441.36(4)	496.93(9)	14.3(8)	13.7(20)
		1196.08(5)	741.95(9)*	70(3)	69(5)
		878.49(4)	1059.44(5)*	100(4)	100(7)
$(1,2,3)^\dagger$	1970.75(7)	1441.36(4)	529.39(3)	11.4(7)	–
		1196.08(5)	775.08(8)	81(4)	–
		212.53(3)	1758.4(2)	100(4)	–
$0_6^{+\dagger}$	2068.09(15)	1196.08(5)	872.0(3)	65(4)	–
		212.53(3)	1855.53(11)	94(5)	–
		878.49(4)	1189.8(2)	100(5)	–
$(0^+,2^+)^\dagger$	2143.71(4)	1196.08(5)	947.62(7)	2.8(2)	–
		1883.16(6)	260.49(7)	4.1(2)	–
		1807.49(4)	336.23(3)	22(3)	–
		878.49(4)	1265.26(4)	41.0(18)	–
		212.53(3)	1931.01(5)	100(4)	–
$(1,2^+)$	2182.67(8)	1807.49(4)	375.4(2)	6.5(11)	–
		0	2182.57(13)	8.3(5)	57(15)
		1937.97(6)	244.70(4)	100(5)	100(8)
$2^{+\ddagger}$	2208.51(5)	1441.36(4)	767.30(5)	6.7(4)	–
		1294.77(5)	913.78(7)	9.2(7)	–
		0	2208.04(11)	9.4(5)	–
		829.28(6)	1379.10(10)	18.8(9)	–
		331.08(4)	1877.34(10)	23.0(11)	–
		564.54(7)	1644.01(12)	50(4)	–
		878.49(4)	1329.99(5)	58(3)	–
		212.53(3)	1995.97(8)	100(5)	–

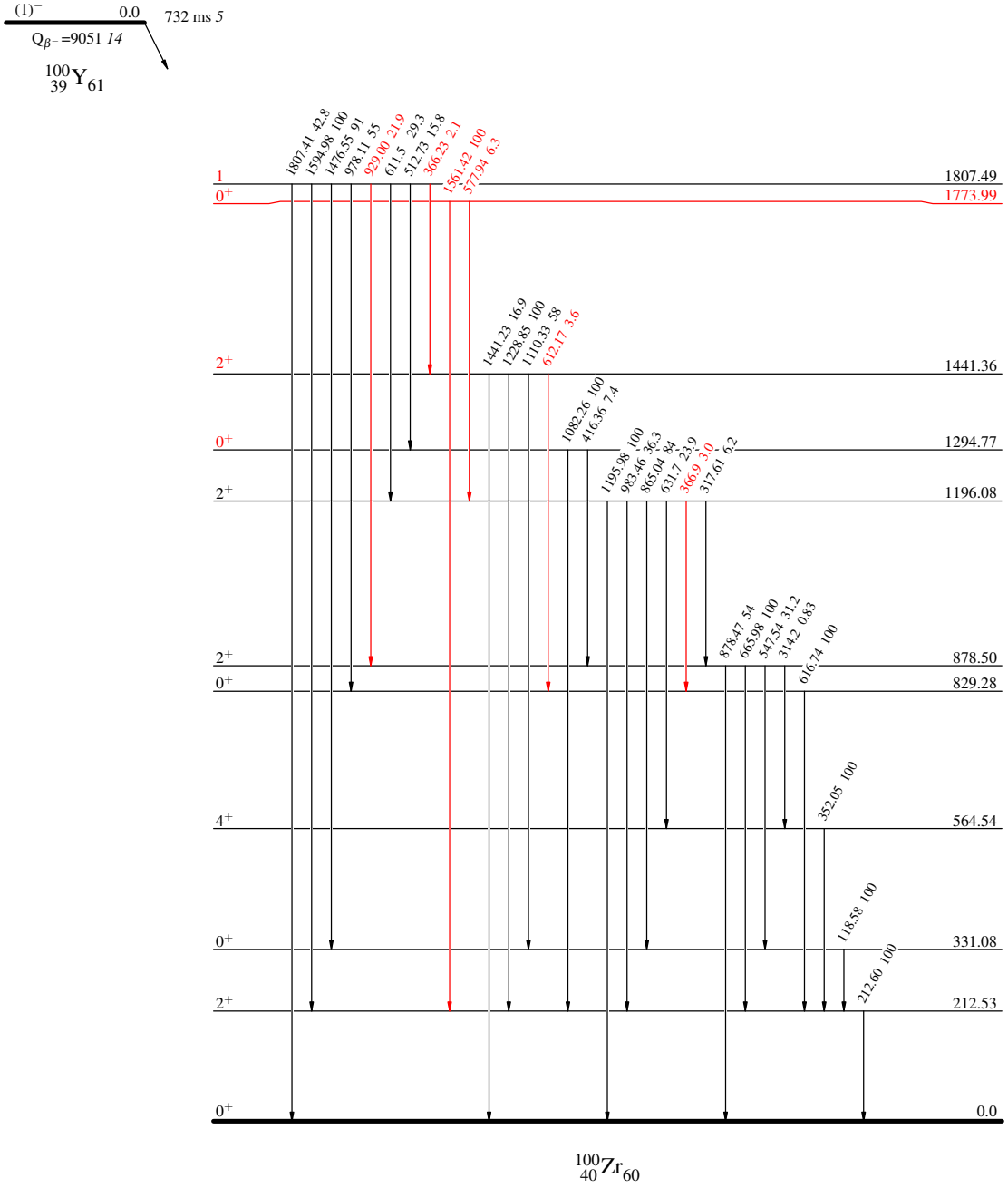

Figure 12.7 – Partial level scheme of ^{100}Zr obtained in the present study. The levels and transitions marked in red have been observed for the first time. The spin assignments in red result from the γ-γ angular correlation analysis described in Section 12.3.

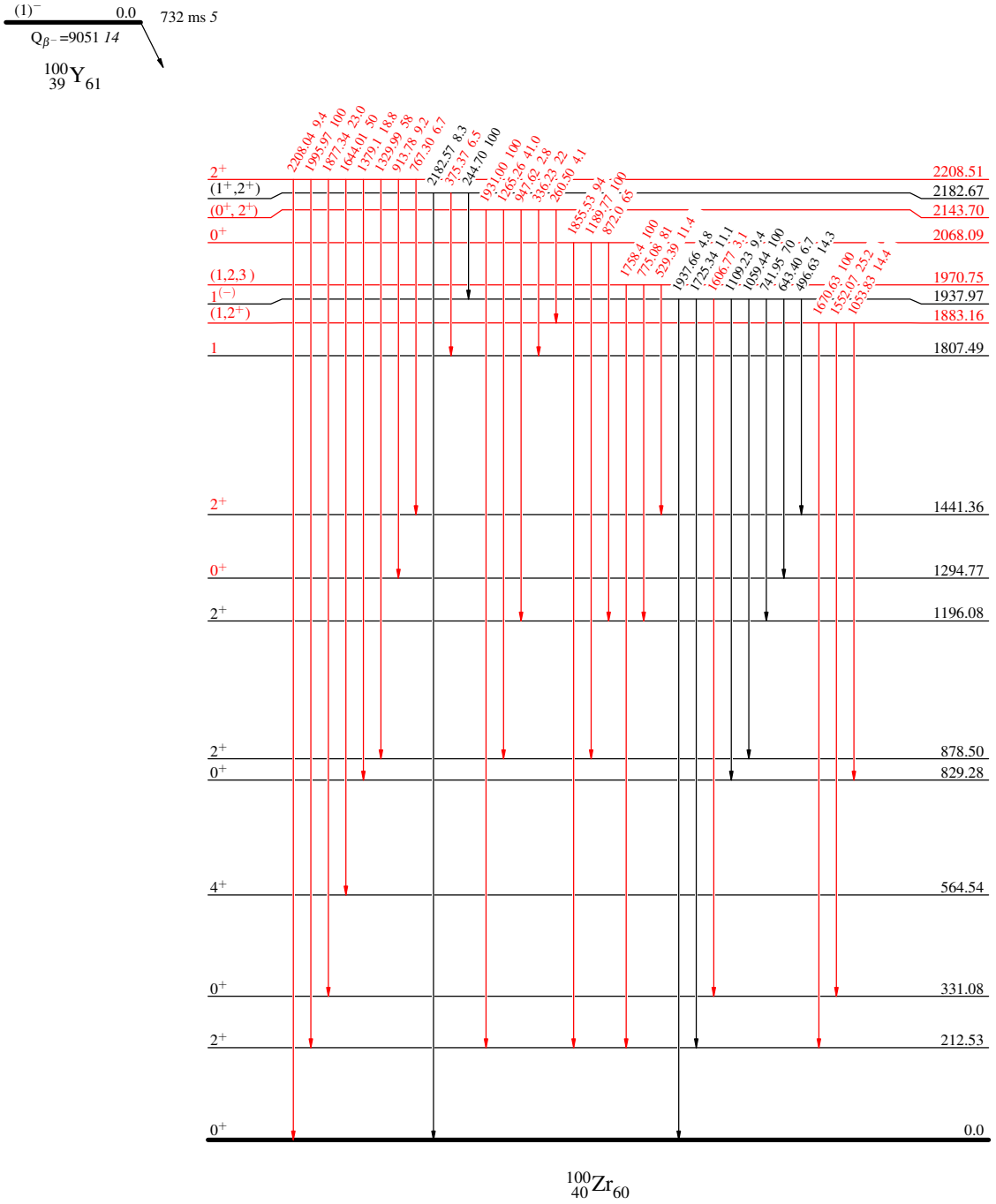

Figure 12.8 – Continuation of Fig. 12.7. The spin assignments in red result from the γ-γ angular correlation analysis described in Section 12.3 or were deduced from the decay pattern observed in the present work.

Table 12.2 – Energies of γ rays in ^{100}Zr used for the refined energy calibration. Literature values E_γ^{LIT} [147] are compared with those obtained from S1790 data using the initial energy calibration described in Section 11.2.2 (E_γ^{INI}).

E_γ^{INI}[keV]	E_γ^{LIT}[keV]	$E_\gamma^{INI} - E_\gamma^{LIT}$[keV]
118.313(4)	118.63(5)	−0.32(5)
212.314(1)	212.61(4)	−0.30(4)
351.75(5)	351.966(13)	−0.21(5)
547.16(8)	547.41(7)	−0.25(11)
616.40(4)	616.67(7)	−0.27(8)
631.38(2)	631.81(8)	−0.43(8)
642.95(1)	643.43(12)	−0.48(12)
665.696(6)	666.00(12)	−0.30(12)
741.63(4)	741.99(7)	−0.36(8)
864.724(3)	865.04(8)	−0.32(8)
878.22(8)	878.64(9)	−0.42(12)
1038.33(4)	1038.68(12)	−0.35(13)
1058.94(9)	1059.51(7)	−0.57(11)
1081.82(8)	1082.33(8)	−0.51(11)
1195.71(2)	1196.09(7)	−0.38(7)
1228.39(13)	1228.99(8)	−0.61(15)
1441.05(7)	1441.3(2)	−0.25(21)
1476.236(3)	1476.53(14)	−0.29(14)
1550.99(5)	1551.4(2)	−0.41(21)
1636.58(6)	1637.0(3)	−0.42(31)
1724.8(1)	1725.44(16)	−0.68(19)
1807.099(5)	1807.9(2)	−0.8(2)
1891.46(2)	1891.8(2)	−0.34(20)
2016.41(3)	2017.0(3)	−0.59(30)
2239.928(4)	2240.5(2)	−0.57(20)

The difference between the energies obtained using the initial calibration and the literature values for the transitions listed in Table 12.2 was investigated as a function of the γ-ray energy E_γ^{INI}, see Fig. 12.9. A systematic trend was observed, with the experimentally obtained energies of the γ-ray peaks, E_γ^{INI}, being consistently smaller than the literature values E_γ^{LIT}, and the difference between E_γ^{INI} and E_γ^{LIT} increasing with the γ-ray energy. The residuals were fitted with a linear function, yielding calibrated γ-ray energy $E_\gamma = E_\gamma^{INI} + \Delta E_\gamma$, where $\Delta E_\gamma = -0.000144399 * E_\gamma^{INI} - 0.249751$. To estimate the uncertainty of ΔE_γ, the covariance matrix C [173] resulting from the least square fit was used. The diagonal elements C_{11} and C_{22} of the covariance matrix correspond to the squared absolute uncertainties of the intercept and slope parameters, respectively. The ab-

solute uncertainty of ΔE_γ is then calculated via $\sqrt{C_{11} + 2C_{12}E_\gamma^{INI} + C_{22}E_\gamma^{INI\ 2}}$, where the elements of the covariance matrix were found to be $C_{11} = 8.12 \times 10^{-4}$, $C_{12} = -8.41 \times 10^{-7}$ and $C_{22} = 1.37 \times 10^{-9}$. Finally, the uncertainty of E_γ was calculated as a square root of the sum of the squared absolute uncertainty of the peak position originating from the fitting procedure, a systematic uncertainty estimated by performing the fit to different regions of the spectrum around the peak of interest, and the $\sigma(\Delta E_\gamma)$, calculated as explained above.

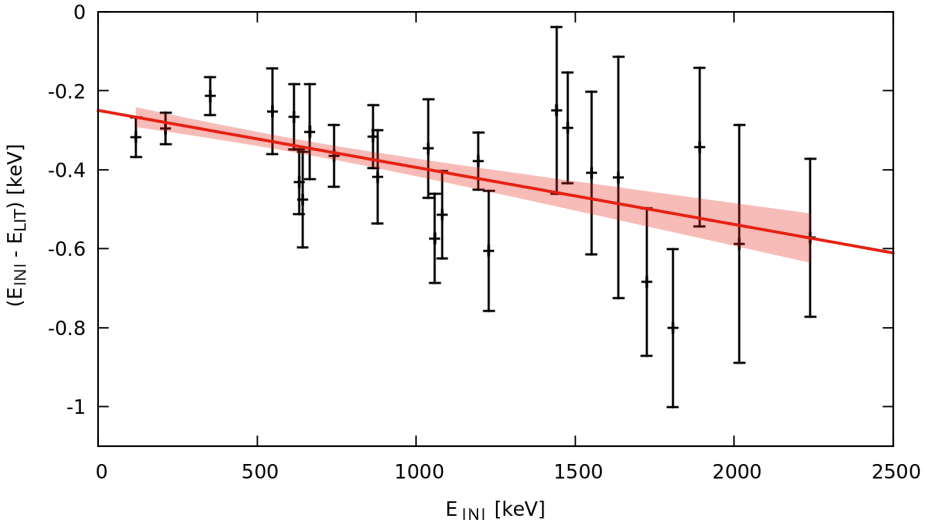

Figure 12.9 – A least-squares linear fit of the differences between the experimentally measured peak positions of the transitions in Table 12.2, $E_\gamma INI$, and the literature values [147], E_{LIT}, as a function of $E_\gamma INI$. The presented uncertainty corridor was calculated using the covariance matrix as explained in the text.

12.2.1 Measurement of branching ratios

In order to measure the relative transition intensities, a series of "gates from above" were applied on the total γ-γ matrix. The gates were set on the most intense transitions directly feeding each state of interest, summarized in Table 12.3. Some of these transitions (marked with daggers) were observed for the first time in the current study, while others were previously reported in Ref. [145]. They originate from the decay of the states listed in the second column of Table 12.3, including a new state at $4160.24(14)$ keV proposed in the current work.

The gating procedure was carried out using GRSISort [164]. A narrow gate region around the peak of interest was selected in order to avoid possible contaminants. In order to account for coincidences with nearby peaks or Compton-scattering background events, in addition to each gate on a transition of interest two background regions in its vicinity were selected. The spectra obtained by gating on those background regions were summed and scaled to the width of the gate.

Table 12.3 – Transitions directly feeding states, whose decay was investigated in the present work. E_x^f are the excitation energies of the investigated states, E_x^i those of the states feeding them, and E_γ are γ-ray energies of the feeding transitions. The values marked with asterisks are taken from Ref. [147]. The remaining values are extracted from the current work. The γ-ray energies E_γ marked with daggers correspond to transitions observed for the first time in the present study. The state marked with double daggers is also proposed in this work. The values marked with double asterisks were reported in Ref. [172].

E_x^f[keV]	E_x^i[keV]	E_γ[keV]
878.49(4)	1807.49(4)	929.00(6)†
	2770.76(8)*	1891.77(4)
	1937.97(6)	1059.44(5)
1196.08(5)	1937.97(6)	741.99(3)
	1970.75(7)	775.06(4)†
	2770.76(8)*	1574.5(1)†
1294.77(5)	2846.34(7)*	1551.39(4)
	1937.97(6)	643.4(1)
	2932.10(13)*	1637.07(4)
1441.36(4)	1937.97(6)	496.63(8)
	2770.76(8)*	1329.0(3)
1773.99(7)	2846.34(7)*	1072.0(2)†
1807.49(4)	2692.84(9)*	885.06(6)
	2846.34(7)*	1038.57(6)
	2932.10(13)*	1124.3(1)†
1883.16(6)	2846.34(7)*	962.9(1)†
1937.97(6)	2182.67(8)*	244.74(5)
	2770.76(8)*	832.3(3)
	2846.34(7)*	908.1(1)
	2692.84(9)*	754.7(1)
1970.75(7)	2770.76(8)*	799.6(3)†
2068.09(15)	2846.34(7)*	777.9(3)†
2143.70(4)	2846.34(7)*	702.55(3)†
2182.67(8)	4160.24(14)††	1977.6(1)†
	2932.10(13)*	749.26(6)†
2208.51(5)**	2846.34(7)*	637.6(1)**

The scaled background spectrum was then subtracted from the spectrum gated on the line of interest. Subsequently, in each gated spectrum, the area of each γ-ray peak corresponding to a transition depopulating the state of interest was extracted by fitting the peak with a combination of a Gaussian, a skewed Gaussian and a step function. For example, the 2_2^+ state at 878.5 keV is directly populated by three intense transitions with energies of 929, 1892 and 1059 keV, see Table 12.3, therefore

three gated spectra were obtained for each feeding transition. Subsequently, the γ-ray peaks corresponding to the decay of the 878-keV state (with energies of 314, 547, 878 and 666 keV, see Table 12.1), observed in each of the three gated spectra, were fitted. The extracted areas for each peak were summed together and efficiency corrected using the efficiency curve obtained in Section 11.2.4. A 3% systematic uncertainty was adopted in addition to the statistical errors resulting from the peak fitting procedure, as discussed in Section 11.2.4. The measured absolute intensities were normalized to those of the most intense branch, which in the current example is the $2_2^+ \rightarrow 2_1^+$ transition. The uncertainties of the relative intensities I_γ were calculated using standard error propagation. The obtained results can be found in Table 12.1. Note that to extract the branching ratios in the decay of the state at 1807 keV, the areas of the peaks at 366.2 keV and 611.5 keV were corrected for possible contamination from the 366.9-keV ($2_3^+ \rightarrow 0_3^+$) and 612.2-keV (depopulating the state at 1441 keV) lines (see level scheme in Fig. 12.5). This was done by subtracting the efficiency-corrected numbers of coincidence counts corresponding to the latter transitions, calculated using the measured relative intensities in the decay of the states at 1196.1 keV and 1441.4 keV. Similar procedure was adopted to evaluate the branching ratio for the 1109.2-keV transition, depopulating the state at 1938.0 keV, which was corrected for a possible contamination from the 1110.3-keV γ ray originating from the state at 1441.4 keV.

When two γ rays deposit their energy in the same crystal within a narrow time window, a sum peak at an energy $E_{\gamma 1} + E_{\gamma 2}$ appears in the singles spectra. If coincidence data are used, both the gating and the coincident γ rays will experience summing effects. An attempt was made to evaluate the influence of the "summing in" effects on the obtained relative I_γ by measuring the areas of sum peaks corresponding to forbidden $0^+ \rightarrow 0^+$ transitions. The obtained area was summed with the area of the $0^+ \rightarrow 2_1^+$ transition and the relative intensities I_γ were re-evaluated. It was found that the "summing in" effect for the states at 1295, 1774, 2068 and 2144 keV (assigned as 0^+ states in the present study, see Section 12.3), resulted in a reduction of the relative intensities of the remaining transitions by 1.9%, 2.0%, 2.7% and 2.8%, respectively, which is comparable with the relative uncertainties of the corresponding intensities, or smaller than them. Moreover, the competing process of "summing out" is often large enough to compensate the effects of the "summing in". As mentioned in Section 11.2.4, the magnitude of summing effects for each transition can be determined from the experimental data by using γ-γ coincidences between detectors separated by 180°. Such corrections have not been applied at this stage of the analysis and the obtained preliminary branching ratios will be refined in the future.

The branching ratios resulting from the present study are listed in Table 12.1. The obtained branching ratios can be compared to those measured in Ref. [145] and the evaluated data summarized in Ref. [147]. The relative intensities of the transitions depopulating the 2_2^+ state are in agreement within 1σ with the previous

measurement. Similarly, the $I_\gamma(2_3^+ \rightarrow 2_1^+)/I_\gamma(2_3^+ \rightarrow 0_1^+)$ branching ratio agrees within 1σ with the literature value. The current $I_\gamma(2_3^+ \rightarrow 2_2^+)/I_\gamma(2_3^+ \rightarrow 0_1^+)$ and $I_\gamma(2_3^+ \rightarrow 4_1^+)/I_\gamma(2_3^+ \rightarrow 0_1^+)$ values agree within 2σ with those reported in Ref. [147], while $I_\gamma(2_3^+ \rightarrow 0_2^+)/I_\gamma(2_3^+ \rightarrow 0_1^+)$ differs by 3σ. The relative intensity of the transitions depopulating the state at 1295 keV measured in the present study and in Ref. [145] are in agreement within 2σ, while those in the decay of the state at 1441 keV agree within 1σ. The relative intensities of transitions depopulating the state at 1807 keV differ from the literature values by 1 to 3σ, suggesting a stronger branch to the 0_2^+ state, as it is the case for the 1196-keV state.

The branching ratios of all transitions originating from the state at 1937 keV agree within a 1σ confidence interval with the literature values, with the only exception being the transition to the ground state. Also for the states at 1441, 1807 and 2183 keV excitation energy, ground-state decays were reported [145] to be considerably stronger than in the present work. A particularly large discrepancy is observed for the state at 2183 keV: the intensity of the transition to the ground state reported in Ref. [145] is seven times higher than the one obtained in the current work. The literature value, despite its large uncertainty, differs from the relative I_γ measured in the current study by more than 3σ. This may be related to the extraction of transition intensities by Wohn et al. [145] from singles γ-ray spectra.

12.3 Angular correlations with GRIFFIN

Angular-correlation data collected with large detector arrays such as GRIFFIN are affected by various experimental factors leading to attenuation of the observed distribution. These result from e.g. a finite detector size (i.e. the γ-ray angular distribution is integrated over the solid angle covered by the detector) or interactions with the electromagnetic field of cascading atomic electrons leading to depolarisation of nuclear states, which is known as the nuclear deorientation effect. Attenuation factors Q_{ii} can be defined to account for the effects of the finite crystal size. They depend on the γ-ray energies and on the solid angle covered by the detector, which is related to its size, shape and distance from the source. The attenuation factors can be calculated analytically for simple detector shapes, or obtained from a simulation. Similarly, attenuation factors for the deorientation effect can be introduced, as it is done e.g. in the Coulomb-excitation code GOSIA [88]. However, as the impact of the deorientation effect is strongly lifetime-dependent, for shortly-lived nuclear states, such as those considered in the present analysis, it can usually be neglected. Thus, the a_i parameters introduced in Section 10, describing the correlations between the emitted γ rays, can be expressed as $a_i = c_i/Q_{ii}$, where c_i are the coefficients extracted by fitting the data with the function given by Formula 10.3.

In the analysis of angular-correlation data it is also necessary to account for the fact that the numbers of detector pairs are not the same for each opening angle that can be investigated (see Appendix E for GRIFFIN), which is done by normalizing the measured intensities for each angle to the corresponding number of detector pairs. In order to take into account differences in the efficiency of individual crystals, one could a priori obtain efficiency curves for each detector separately, and fold the efficiency correction into the γ-γ coincidence matrix. Another possible solution, which is less time consuming, is to use the event-mixing technique described in the following section. The method used to handle the attenuation effects induced by the finite solid angle of the detectors is described in Section 12.3.4.

12.3.1 Event-mixing technique

Experimentally, the continuous physical angular correlation $W(\theta)$ is measured for discrete opening angles between two γ rays with energies of E_a and E_b. The discrete $\omega(\theta_i; E_a, E_b)$ values are related to $W(\theta)$ via:

$$\omega(\theta_i; E_a, E_b) = \sum_{j,k} \varepsilon_j(E_a)\varepsilon_k(E_b) \int_{\theta_i-\Delta\theta}^{\theta_i+\Delta\theta} N_{jk}(\theta; E_a, E_b) W(\theta) d\theta. \tag{12.1}$$

The angle θ_i is one of the considered angles between crystal pairs, the j and k indices denote crystals which satisfy the $\theta_i = |\theta_j - \theta_k|$ condition, $\varepsilon_{j,k}(E_{a,b})$ are the efficiencies of crystals j and k, and the $N_{jk}(\theta; E_a, E_b)$ weighting distributions, describing the crystal pair response, are related to the attenuation factors Q_{ii} introduced above. The integration is performed over the range of θ subtended by the detectors.

Let us now consider another experimental $y(\theta_i; E_a, E_b)$ and theoretical $Y(\theta)$ distributions related via:

$$y(\theta_i; E_a, E_b) = \sum_{j,k} \varepsilon_j(E_a)\varepsilon_k(E_b) \int_{\theta_i-\Delta\theta}^{\theta_i+\Delta\theta} N_{jk}(\theta; E_a, E_b) Y(\theta) d\theta. \tag{12.2}$$

If we divide Formula 12.1 by Formula 12.2 the dependence on the relative efficiencies of the individual crystals will cancel out:

$$\frac{\omega(\theta_i)}{y(\theta_i)} = \frac{\int_{\theta_i-\Delta\theta}^{\theta_i+\Delta\theta} N_i(\theta; E_a, E_b) W(\theta) d\theta}{\int_{\theta_i-\Delta\theta}^{\theta_i+\Delta\theta} N_i(\theta; E_a, E_b) Y(\theta) d\theta}. \tag{12.3}$$

If $Y(\theta) = 1$, i.e. the distribution is isotropic, and if the changes of $W(\theta)$ over the detector size $\Delta\theta$ can be neglected, Formula 12.3 reduces to $W(\theta_i) = \omega(\theta_i)/y(\theta_i)$.

It is possible to construct such an isotropic distribution $Y(\theta)$ using the experimental data collected at the same time as the coincidence data used to calculate $\omega(\theta_i; E_a, E_b)$. To construct $y(\theta_i; E_a, E_b)$, γ rays with the same energies E_a and E_b should be used, but originating from decays separated by a sufficiently long time to assure that they are not correlated. $y(\theta_i, E_a, E_b)$ obtained in this way will be uniform and affected by the same pair number and efficiency differences as $w(\theta_i, E_a, E_b)$.

12.3.2 Prompt and event-mixing γ-γ matrices

As mentioned in Section 11.1.3, the individual GRIFFIN crystals can be paired into 52 unique opening angles, corresponding to the angles between the two registered γ rays. The number of detector pairs for each unique opening angle θ_i in the current experiment (considering the exclusion of one GRIFFIN clover) are given in the last column of Table E.1 in Appendix E. Prompt coincidence γ-γ matrices ($\Delta t < 300$ ns) for each opening angle were created using the data collected in the "short cycle" mode. Additionally, a gate was set on the cycle time in order to exclude the data collected during the tape movement and the background period, corresponding to the first 1.0 s and 0.25 s of each cycle, respectively. This was necessary due to the impossibility to properly define the angle between the registered γ rays in these time periods, as the moving tape was not in the center of GRIFFIN.

Using add-back procedure resulted in a reduction of the number of opening angles. This is due to the similar time difference conditions of $\Delta t < 300$ ns for both prompt coincidences and add-back. Thus, if coincident γ rays were registered in different crystals of the same clover, their energies were added together. Therefore, coincidences in the same crystal ($\theta_i = 0^\circ$) or in two neighboring or diagonal crystals in the same clover (15.4° and 21.9°), were omitted, leaving 49 unique opening angles. Finally, a time random background subtraction was applied to the prompt matrix similarly to the procedure described in Section 11.2.5.

As explained in Section 12.3, it is possible to correct for differences in the efficiency of the individual crystals, as well as different numbers of detector pairs for each opening angle by constructing a uniform angular distribution from the same data set and using it for normalization. In practice, a histogram of uncorrelated events (separated by a large time difference eliminating any chance of correlation) has to be prepared for each opening angle. This is done by requiring coincidence between HPGe hits from different events, i.e. using event mixing (each event is $2\mu s$ long, while the prompt coincidence window is 300 ns). Since the angular-correlation distribution extracted from those event-mixing matrices will be used to divide the distribution extracted from the prompt matrices, the statistical error in the normalized distribution will increase. To reduce this effect, each individual detector hit can be paired with many other hits, creating a histogram much larger than the prompt matrix. Of course, a downside of this procedure is that it is time consuming, thus a compromise is necessary. In the present analysis, the level of statistics in the event-mixing matrices is about two orders of magnitude higher than in the prompt ones. One should note that a time-random subtraction is not needed, as essentially all "coincidences" resulting from event mixing are time random.

12.3.3 Extracting angular correlations

As a first step, for each selected cascade, gates were set on a transition either feeding or depopulating the intermediate state in the prompt and the event-mixing matrices sorted for each opening angle. A background-subtraction procedure was

also applied. Subsequently, the peak corresponding to the other transition in the investigated cascade was fitted using GRSISort in each gated spectrum. For all cases described in the following, cascades of the type $I_i \rightarrow 2^+ \rightarrow 0^+$ were studied.

As an example, for the $0_2^+ \rightarrow 2_1^+ \rightarrow 0_1^+$ cascade originating from the well-established 0_2^+ state, the gate was set on the 118.6-keV γ ray and the 212.6-keV peak was fitted in the gated spectra. The extracted absolute numbers of counts as a function of θ_i are presented in Fig. 12.10 (A) for both prompt (C_i^P) and event-mixing (C_i^M) coincidence conditions. These numbers are strongly affected by the different numbers of detector pairs for each opening angle θ_i. They were therefore divided, for each experimental point, by the corresponding number of detector pairs (taken from Table E.1) to obtain the normalized counts shown in Fig. 12.10 (B). Finally, the event-mixing technique was used to obtain the distribution in Fig. 12.10 (C), where each point is given by C_i^P/C_i^M multiplied by a global normalization constant of $\sum_i(C_i^M)/\sum_i(C_i^P)$. This way, the distribution in Fig. 12.10 (C) is corrected for the effect of different efficiencies of individual detectors and number of detector pairs, and is largely improved in comparison to that presented in Fig. 12.10 (B). However, small systematic deviations can still be observed with respect to the expected distribution calculated using Formula 10.4, presented with the red curve. They are related to finite sizes of the detectors and can be accounted for as explained in the following section.

12.3.4 Simulations accounting for the finite detector sizes

To calculate the impact of the finite size of the detectors a realistic Monte-Carlo simulation of the entire detector setup can be performed within the GEANT4 framework [174–176]. The approach adopted in the present work takes advantage of the fact that $W(\theta)$ is a linear combination of Legendre polynomials, see Formula 10.3. Therefore, it is sufficient to use the Legendre polynomials as a probability distribution in the simulation and then fit the experimental data with a linear combination of the simulated histograms to extract directly the corresponding $a_{2,4}$ coefficients. As the angular distributions always have positive values, the following distributions are used:

$$Z_0(\theta) = 1, \tag{12.4}$$

$$Z_2(\theta) = 1 + P_2(\cos(\theta)), \tag{12.5}$$

$$Z_4(\theta) = 1 + P_4(\cos(\theta)). \tag{12.6}$$

More details on the simulation procedure and validation of the method (referred to as "Method 1" in the following) can be found in Refs. [128, 152].

The simulated histograms can be used as a basis to construct histograms for any combination of level spins and mixing ratios δ, i.e. $a_{2,4}$ coefficients:

$$Z(\theta) = xZ_1(\theta) + yZ_2(\theta) + zZ_4(\theta) = A_{00}[(1 - a_2 - a_4)Z_0 + a_2Z_2 + a_4Z_4], \tag{12.7}$$

where $Z(\theta)$ is a linear combination of the $Z_{0,2,4}$ distributions given by Formulas 12.4-12.5 [128] and x, y, z are scaling factors.

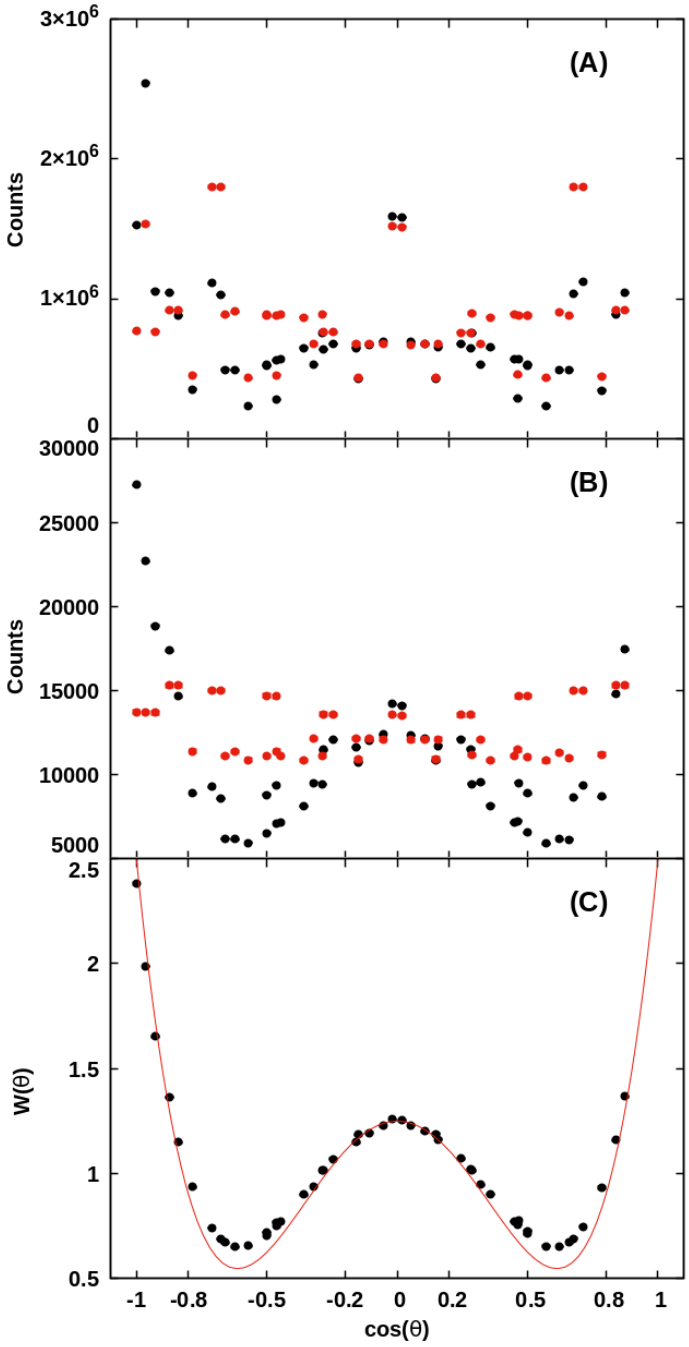

Figure 12.10 – Angular correlations for the $0_2^+ \rightarrow 2_1^+ \rightarrow 0_1^+$ cascade. (A) Raw coincidence counts obtained from the prompt (black) and event-mixing (red; scaled by a factor of $1/10$) γ-γ matrices. (B) Same as (A), but normalized to the number of detector pairs for each θ_i. (C) Angular correlation obtained from (A) using the event-mixing technique. The theoretically calculated curve for a $0^+ \rightarrow 2^+ \rightarrow 0^+$ cascade is presented in red. The observed discrepancies are due to the finite size of the detectors.

A large set of histograms for different spins and mixing ratios (if applicable) can then be easily constructed and fitted to the experimental data. The unknown transition mixing ratio and level spin can be determined by searching for the minimum of the obtained χ^2/NDF distribution as a function of these parameters. The number of degrees of freedom for a fit of the mixing ratio and the overall scaling factor are given by $N_{EXP}-2$, where N_{EXP} is the number of experimental points. The uncertainty of the mixing ratio can be extracted from the limits of the $\chi^2_{MIN}+1$ region [177]. This method is referred to as "Method 2" in the following.

12.4 Spin assignment and extraction of mixing ratios in ^{100}Zr

Properties of several excited states in ^{100}Zr, summarized in Table 12.4, were investigated via γ-γ angular correlations in the $I_i \rightarrow 2_1^+ \rightarrow 0_1^+$ cascades. The only exception is the state at 1937 keV, which was probed using the 1937 keV$\rightarrow 2_2^+ \rightarrow 0_1^+$ cascade. The spins I_i of the investigated states and/or the mixing ratios δ of the transitions depopulating these states were previously unknown.

Table 12.4 – Spins I_i of selected states with excitation energy E_i extracted via γ-γ angular correlations in the present study. Gates were applied on the transitions with E_γ given in the third column of the table. Cascades $I_i \rightarrow 2_1^+ \rightarrow 0_1^+$ were investigated for all states, except for the $1^{(-)}$ state at 1938 keV, which was probed using the $I_i \rightarrow 2_2^+ \rightarrow 0_1^+$ cascade. The experimental $a_{2,4}$ coefficients extracted from the fits using Method 1 are given in the fourth and fifth columns. The corresponding mixing ratio obtained with Method 2 is presented in the last column. The mixing ratios marked with daggers are extracted using the $Z(\theta)$ distributions simulated for the $0_4^+ \rightarrow 2_1^+ \rightarrow 0_1^+$ cascade.

I_i	E_i [keV]	E_γ [keV]	a_2	a_4	χ^2/NDF	δ
0_3^+	829.3	616.7	0.325(3)	1.052(4)	1.87	–
0_4^+	1294.8	1082.3	0.310(6)	1.061(8)	2.09	–
0_5^+	1774.0	1561.4	0.34(1)	1.15(2)	0.76	–
0_6^+	2068.1	1855.5	0.29(3)	0.89(4)	0.88	–
2_2^+	878.2	666.0	−0.226(3)	0.262(4)	1.54	4.2(1)†
2_3^+	1196.1	212.6	0.424(5)	0.120(7)	1.00	−1.01(3)
2	1441.4	1228.9	−0.153(6)	0.304(8)	0.62	9.4(9)†
1	1807.5	1595.0	−0.176(5)	−0.013(7)	0.96	−0.065(4)
$1^{(-)}$	1938.0	1059.4	−0.248(6)	−0.002(9)	2.16	−0.007(7)

The experimental angular correlations for all investigated states were extracted from the data organized into prompt and event-mixing γ-γ matrices. Gates were applied on the transitions given in the third column of Table 12.4 for every opening angle. The 212.6-keV γ-ray peak was fitted with a combination of a Gaussian and a skewed Gaussian function in all gated spectra except when the 1196-keV state

and the 1938-keV state were investigated, for which the 983.4-keV and 878.5-keV peaks were fitted, respectively. The areas extracted from the prompt coincidence spectra were normalized to those obtained from the event-mixed spectra. These results together with their uncertainties are presented in black in the left panels of Figs. 12.12-12.19.

The $Z(\theta)$ histograms were obtained from the simulations for the following cascades: 1295 keV$\rightarrow 2_1^+ \rightarrow 0_1^+$, $2_3^+ \rightarrow 2_1^+ \rightarrow 0_1^+$, 1807 keV$\rightarrow 2_1^+ \rightarrow 0_1^+$ and 1938 keV$\rightarrow 2_2^+ \rightarrow 0_1^+$. As an input for the simulation, energies of the γ rays and the levels in the investigated cascade, relative intensities, internal conversion coefficients, level half-lifes, etc., were provided. In the present study an intensity of 100% was adopted for both transitions in the cascade as each cascade was investigated separately. Additionally, information about the population mechanism had to be provided: the decay mode (β^- decay of ^{100}Y), half-life of the mother nucleus (732 ms), excitation energy of the β-decaying state in the mother nucleus (ground-state decay), decay Q value (9050 keV), etc. As a final result, γ-γ matrices for all opening angles corresponding to the Z_0, Z_2 and Z_4 distributions were obtained for each cascade. These individual γ-γ matrices were then gated on the transition given in the third column of Table 12.4. The other transition in the cascade was then fitted. The extracted areas were normalized to the number of detector pairs for each opening angle. The $Z_{0,2,4}$ distributions (defined by Formulas 12.4-12.6) extracted from the simulated data for the 1295 keV$\rightarrow 2_1^+ \rightarrow 0_1^+$ cascade are shown in Fig. 12.11. These distributions take into account the finite size of the detectors and were used as templates to fit the experimental data.

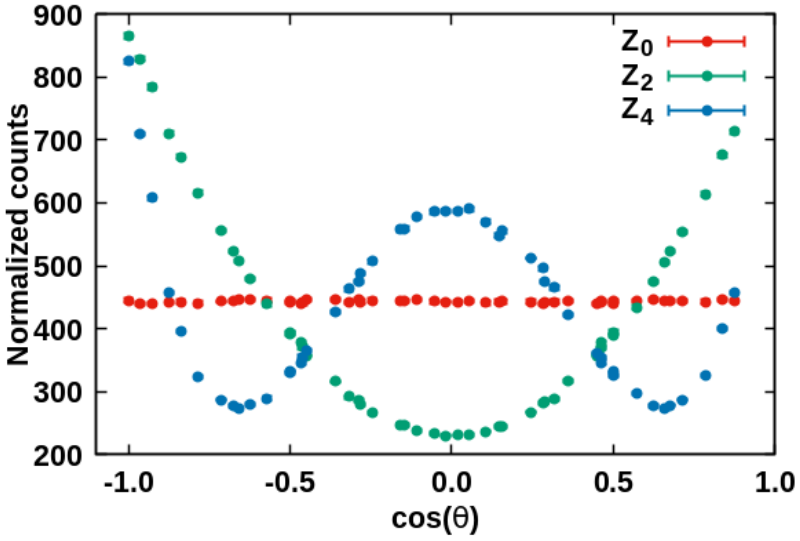

Figure 12.11 – Angular distributions Z_0, Z_2 and Z_4 defined by Formulas 12.4-12.6 extracted from the simulated data for the $0_4^+ \rightarrow 2_1^+ \rightarrow 0_1^+$ cascade. The number of coincidence counts normalized to the number of detector pairs for each opening angle is given on the Y axis.

The simulated basis distributions for the decay of the states at 1196, 1807 and 1938 keV were extracted with a similar procedure. Simulations could not be prepared for the remaining investigated states at 829, 878, 1441, 1774 and 2068 keV due to technical issues with the servers at the University of Guelph. However, although the attenuation factors depend on the energy of the investigated γ rays, this dependence is rather weak at energies above 100 keV as it can be concluded from Figs. 8 and 9 in Ref. [128]. Therefore the simulated distributions for the cascade with the initial state at 1295 keV were used instead. The mixing ratios δ obtained in this way are marked with daggers in Table 12.4. This approximation was validated by comparing the mixing ratios obtained for the 1807 keV$\rightarrow 2_1^+$ and $2_3^+ \rightarrow 2_1^+$ transitions using two sets of simulations. If the simulations performed for the 1807 keV$\rightarrow 2_1^+ \rightarrow 0_1^+$ cascade were used, a mixing ratio of $-0.065(4)$ was obtained for the 1595-keV transition. Analysing the same cascade but using the simulations performed for the 1295 keV$\rightarrow 2_1^+ \rightarrow 0_1^+$ cascade yielded an almost identical value of $-0.064(4)$. Similarly, the $\delta(2_3^+ \rightarrow 2_1^+)$ value obtained using the simulations for the 1295 keV$\rightarrow 2_1^+ \rightarrow 0_1^+$ cascade is $-1.00(3)$, consistent with the value reported in Table 12.4 within 1σ.

Following the Method 1 described in Section 12.3.4, the experimental angular correlations for all investigated cascades were fitted with the simulated data. The obtained $a_{2,4}$ coefficients are given in the fourth and fifth column of Table 12.4 together with the χ^2/NDF value corresponding to the fit. A fit of the simulated $Z(\theta)$ distributions to the experimental points as a function of θ is presented in the left panels of Figs. 12.12-12.19. These fits do not assume any particular spins in the cascade. The "residuals", i.e. differences between simulated and experimental points are given in the lower part of each plot. All fits corresponded to χ^2/NDF values smaller than 2.5. The mixing ratios and spins of the investigated transitions were obtained using the Method 2 described in Section 12.3.4, i.e. by comparing the experimental and simulated data for specific combinations of the spin of the initial state and δ of the first transition in the cascade. The obtained χ^2/NDF are larger than those obtained with Method 1 (left panel of Figs. 12.12-12.19) because assumptions concerning spins and delta values lead to additional constraints on the $a_{2,4}$ values. In some cases, the best fit does not correspond to a χ^2 value that is small enough to belong to the region encompassing 99% of the total probability distribution [128]. This limit, marked with a dashed horizontal line in Figs. 12.13-12.19 and referred to as the "99% limit" in the following, implies that there is less than a 1% chance of statistical fluctuations leading to a larger χ^2 value for the spin and mixing ratio solution and hence its rejection. If none of the spin and mixing ratio hypotheses result in a χ^2 value below the 99% limit, it likely indicates underestimated uncertainties, or the presence of a contaminating γ-ray influencing the distribution. Therefore the analysis of these cases will be refined in the future by refitting the corresponding γ-ray peaks and reevaluating the uncertainties of the extracted areas. For some of them, however, we may still confidently assign a spin value if the other spin hypotheses result in χ^2 values that are extremely large.

- **The mixing ratio of the $2_2^+ \rightarrow 2_1^+$ transition** was extracted using Method 2 to be $4.2(1)$. A spin of 2 was favoured, as previously reported in Ref. [147], see Fig. 12.12. However, the obtained mixing ratio is much larger than the previously reported value of $1.0(3)$ [145]. The value obtained by Wohn et al. was fitted to six experimental points, while in the present study a set of 49 opening angles were used. The new mixing ratio suggests that the transition has a strong $E2$ character. This solution corresponds to a χ^2/NDF value that is an order of magnitude lower than those obtained assuming other initial spins, even though it does not reach the 99% limit discussed above.

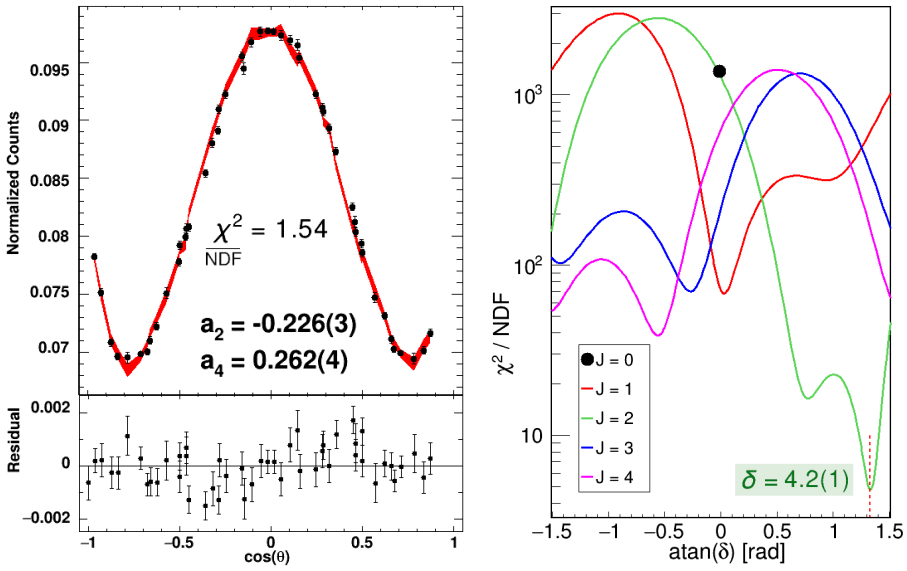

Figure 12.12 – Angular correlation for the $2_2^+ \rightarrow 2_1^+ \rightarrow 0_1^+$ cascade obtained via the two procedures described in Section 12.3.3. Left panel: The experimental distribution (black) compared with the simulated one (Method 1, red). The corresponding $a_{2,4}$ coefficients and the χ^2/NDF value are given in the plot. Right panel: Goodness of the fit (Method 2) for considered spins of the initial state ($J_i = 0,\ 1,\ 2,\ 3,\ 4$) as a function of the mixing ratio (δ). The best combination of initial level spin and transition mixing ratio for the $2_2^+ \rightarrow 2_1^+$ transition is determined from the minimum of the reduced χ^2 function.

- **The spin of the state at 1196 keV** was confirmed to be 2, as suggested by its decay pattern [147]. The $\delta(2_3^+ \rightarrow 2_1^+)$ value was measured for the first time in the present work. A value of $-1.01(3)$ was obtained, suggesting equal contributions of the $M1$ and $E2$ components to the intensity of the investigated transition. The 99% limit has not been reached in the present analysis.
- **The fourth 0^+ state in ^{100}Zr** was found to be the state at 1295 keV, which was previously assigned as $(2^-, 3)$ state by the ENSDF evalua-

tors [147]. The 99% level was not reached, but spin of 0 corresponds to χ^2/NDF orders of magnitude smaller than those for other spins as can be seen in the right panel of Fig. 12.14.

- For **the state at 1441 keV** Wohn et al. suggested a spin of $(1, 2^+)$ based on the its observed direct decay to the ground state. In the present work, the spin-1 solution is excluded by the least-square fit, as presented in the right panel of Fig. 12.15. The solution for spin 2 reaches the 99% limit discussed above. The transition to the 2_1^+ state was found to have a large positive mixing ratio (9.4(9)), i.e. a strong $E2$ character.

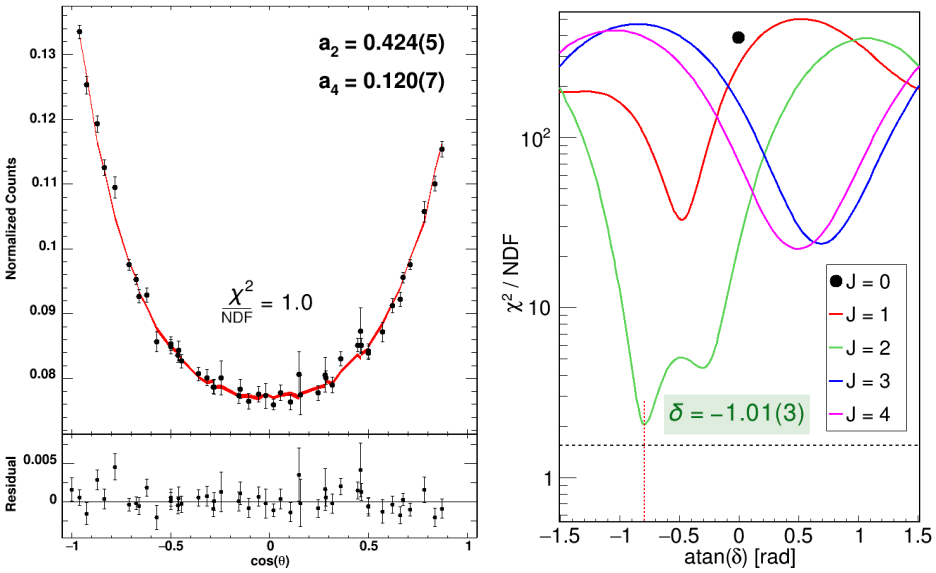

Figure 12.13 – Same as Fig. 12.12 but for the 1196 keV$\rightarrow 2_1^+ \rightarrow 0_1^+$ cascade.

- **The state at 1807 keV** was previously proposed to have a spin of $(1, 2^+)$. In the present study spin 2 was refuted by the χ^2 analysis as the green curve does not reach the 99% limit. The solutions with spin 1, 3 and 4 correspond to similar χ^2/NDF values. On the other hand, the decay pattern involving intense transitions to the ground and 0_2^+ states, and transitions to the $0_{3,4}^+$ states, hints that a spin-1 assignment is the most probable, as otherwise these transitions would correspond to higher-order multipolarities and their relative intensities with respect to the decay to 2^+ states would be hard to explain. The extracted mixing ratio for the transition to the 2_1^+ state has a negative value that is small, but not consistent with zero.
- **The state at 1938 keV** was also proposed to be a spin-1 or a 2^+ state by Wohn et al. The spin-2 solution is less probable than all other solutions. Similar arguments regarding the decay pattern of the 1938-keV state can be used as for the 1807-keV state, which also exclude spin 3 and 4 as possible

solutions - the 1938-keV state decays to all four $0^+_{1,2,3,4}$ states, although with much less intense transitions with respect to the decay to the 2^+_1 state than those from the 1807-keV state. The extracted mixing ratio for the 1938 keV$\rightarrow 2^+_2$ transition is very small and consistent with 0. Thus, the two possible scenarios for its parity, i.e. negative or positive, would result in a pure $E1$ or pure $M1$ transition to the 2^+_2 state, respectively. It seems more probable to observe a pure $E1$ than a pure $M1$ transition, which often have a significant $E2$ component. For this reason, a $1^{(-)}$ spin-parity was proposed for the 1938-keV state.

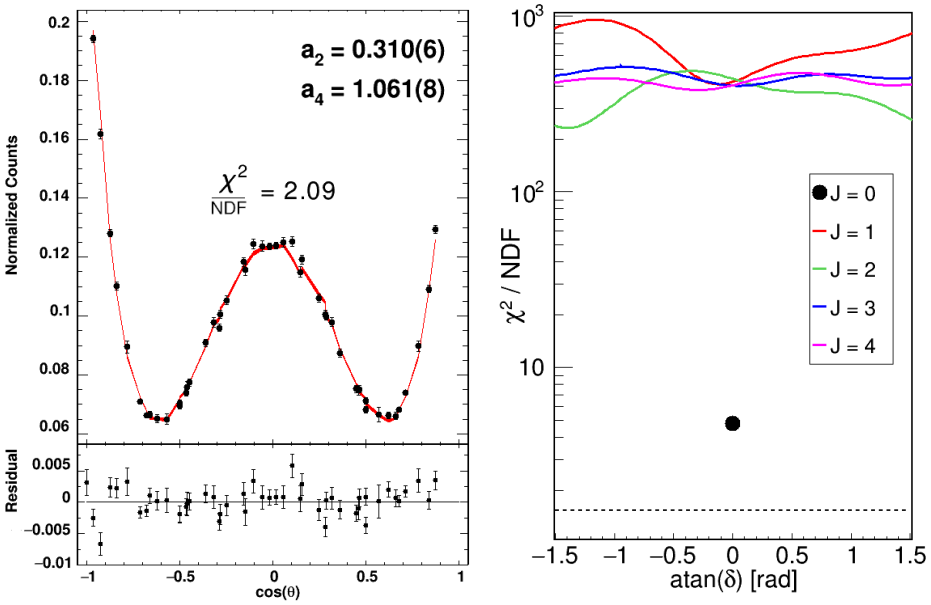

Figure 12.14 – Same as Fig. 12.12 but for the 1294 keV$\rightarrow 2^+_1 \rightarrow 0^+_1$ cascade.

- **The state at 1773-keV excitation energy**, proposed for the first time in the present study, was firmly assigned as a spin-0 state, making it the fifth excited 0 state in ^{100}Zr under 2 MeV excitation energy. This solution reached the 99% limit.
- **The proposed state at 2068 keV** was suggested to be the sixth spin-0 state in ^{100}Zr based on the results presented in Fig. 12.19.

In addition, the spin assignment of the 0^+_3 state was confirmed. The level at 1970 keV was investigated as well, although the obtained χ^2/NDF distributions as a function of the mixing ratio were inconclusive. Spins 1, 2, 3 and 4 (although it is unlikely to populate such high spin in a β-decay of the (1^-) ground state of ^{100}Y) were found equally probable, while 0 was excluded. No suggestions regarding the spin of the 1970-keV state were found in its decay pattern either, as it decays via roughly equally intense transitions to the 2^+_1, 2^+_2 and 2^+_3 states.

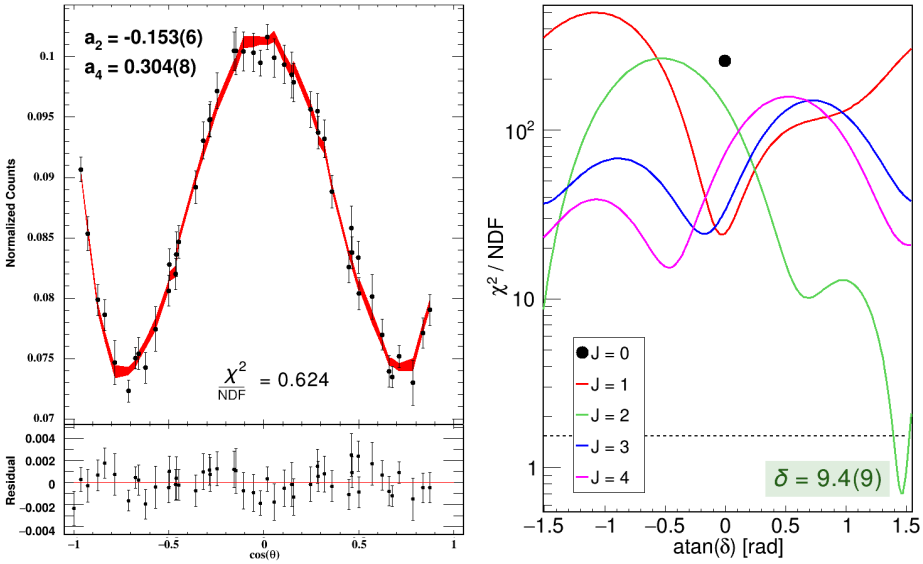

Figure 12.15 – Same as Fig. 12.12 but for the 1441 keV$\rightarrow 2_1^+ \rightarrow 0_1^+$ cascade.

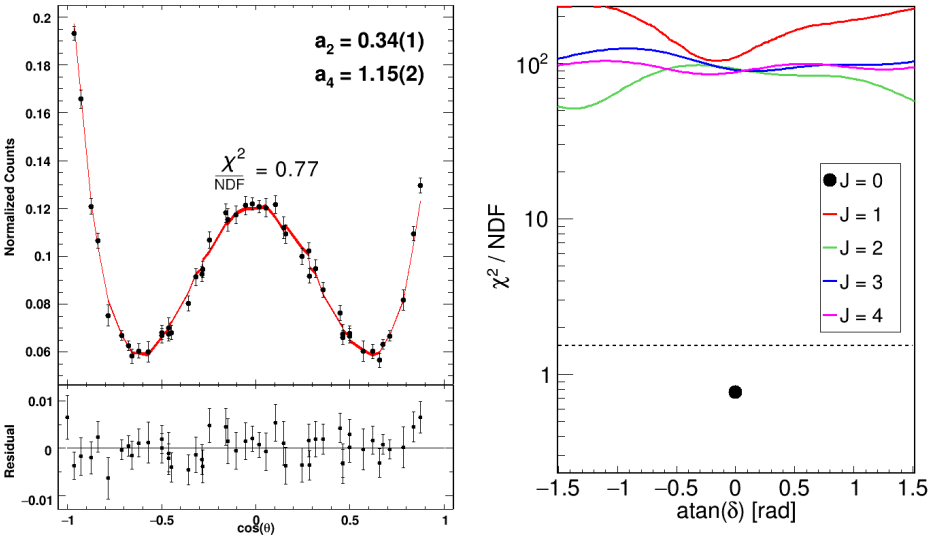

Figure 12.16 – Same as Fig. 12.12 but for the 1773 keV$\rightarrow 2_1^+ \rightarrow 0_1^+$ cascade.

The new level at 2143 keV was investigated as a possible candidate for a seventh 0 state in ^{100}Zr. The obtained correlations in the 2143 keV$\rightarrow 2_1^+ \rightarrow 0_1^+$ cascade suggested a preference for spins 2 and 0, however, the presence of a contamination in the γ-ray spectra prevented us from drawing unambiguous conclusions on the spin of the 2143-keV state. In the future, other cascades in the decay of the 1970-keV and 2143-keV states will be investigated.

Finally, the spins of the states at 1883.2 keV and 2182.7 keV have not been investigated via γ-γ angular correlations due to temporary unavailability of the data

following a server failure at the University of Guelph. However, based on the decay pattern of the former, spin of $(1, 2^+)$ was adopted. The strongest decay branch of the latter is observed to the state assigned as $1^{(-)}$, which suggests that it must be a partity-changing transition $(E1)$.

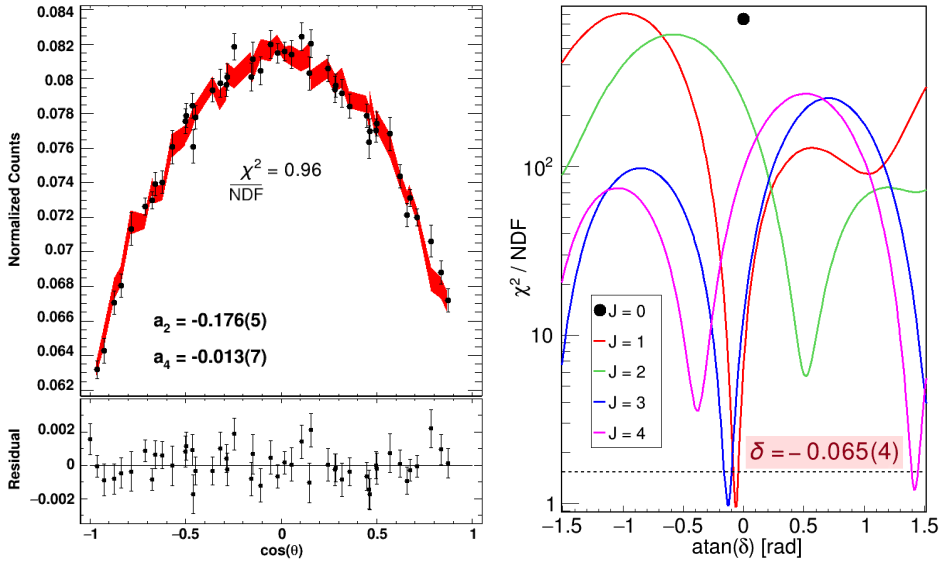

Figure 12.17 – Same as Fig. 12.12 but for the 1807 keV$\rightarrow 2_1^+ \rightarrow 0_1^+$ cascade.

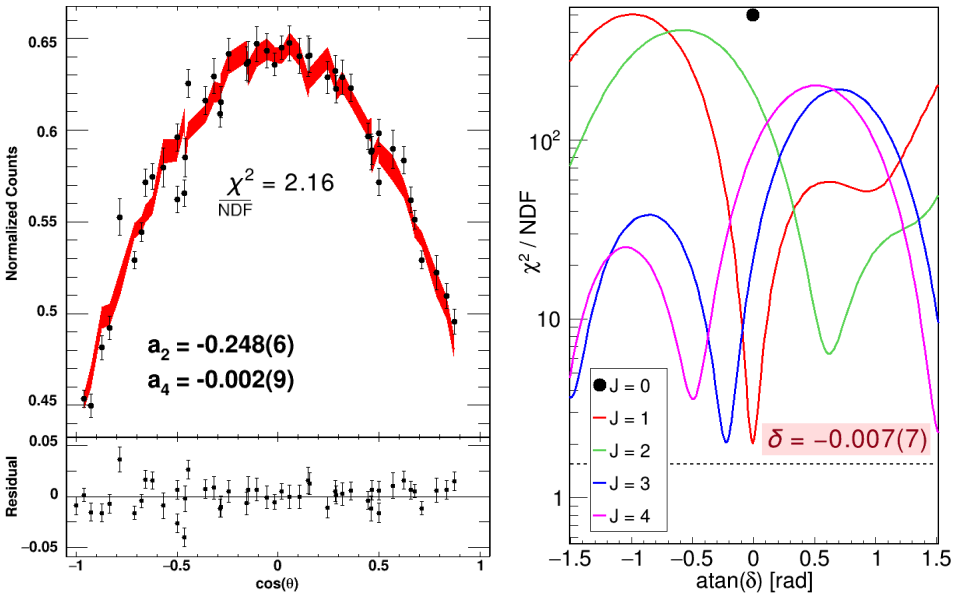

Figure 12.18 – Same as Fig. 12.12 but for the 1938 keV$\rightarrow 2_2^+ \rightarrow 0_1^+$ cascade.

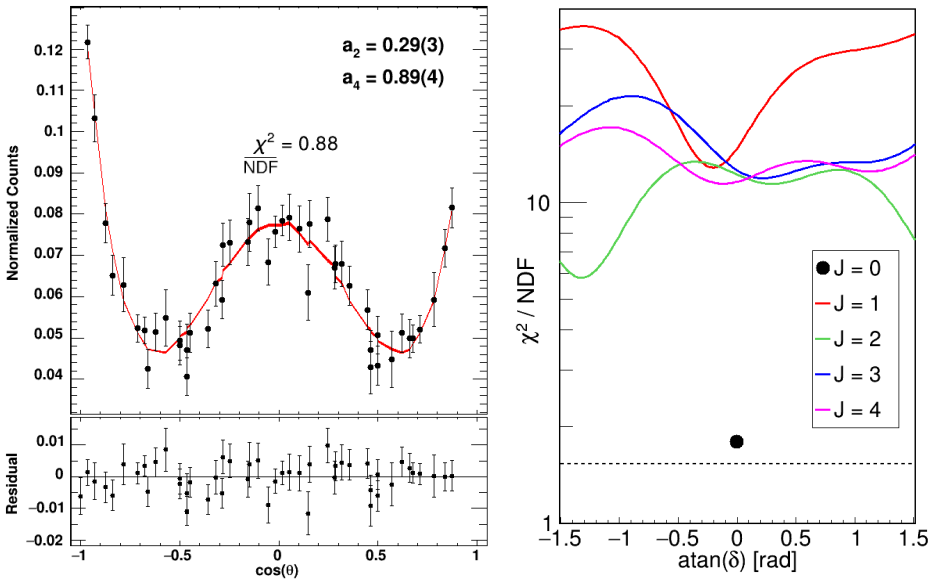

Figure 12.19 – Same as Fig. 12.12 but for the 2068 keV$\rightarrow 2_1^+ \rightarrow 0_1^+$ cascade.

13 - Discussion

As discussed in Section 8, the tremendous lowering of the excitation energy of the 2_1^+ state in ^{100}Zr with respect to ^{98}Zr could only be described in a satisfactory manner by the the Monte-Carlo Shell-Model (MCSM) calculations [134]. The results of these calculations are presented in more detail in Section 13.1. The experimental information about the collectivity of structures built on the ground state and on the first three excited 0^+ states in ^{100}Zr, obtained from the present data, is discussed in Section 13.2 in the context of multiple shape coexistence suggested by the MCSM calculation. Finally, the planned next steps in the analysis are presented in Section 13.3.

13.1 Monte-Carlo Shell-Model predictions

The rapid onset of deformation, occurring at $N = 60$ in the Zr isotopic chain, was investigated by Togashi et al. within the framework of the large-scale Monte Carlo shell model [134]. The model space used in the calculation included eight proton ($0g_{7/2}$, $1d_{5/2}$, $1d_{3/2}$, $2s_{1/2}$, $0g_{9/2}$, $0f_{5/2}$, $1p_{3/2}$, $1p_{1/2}$) and eight neutron ($1f_{7/2}$, $2p_{3/2}$, $0h_{11/2}$, $0g_{7/2}$, $1d_{5/2}$, $1d_{3/2}$, $2s_{1/2}$ and $0g_{9/2}$) orbitals with no truncation of the occupation numbers. Such a large model space is much beyond the current limits of conventional shell-model calculations. The effective interaction was constructed from the existing ones: JUN45 [178], SNBG3 [179] and V_{MU} [180] with small adjustments to better reproduce the experimental data as described in Ref. [134]. Effective charges $(e_\pi, e_\nu) = (1.3e, 0.6e)$ were used.

The calculated excitation energies of the $2_{1,2}^+$ states in Zr isotopes with $50 \leq N \leq 70$, presented in Fig. 13.1 (A), show a remarkably good agreement with the experimental values. Similarly, a reasonable reproduction of the experimental excitation energies of the 0_2^+ state is obtained, see Fig. 13.1 (B). Furthermore, the predicted reduced transition probabilities compare well with the experimental values, as illustrated by Fig. 13.1 (C). The sharp increase in collectivity appearing at $N = 60$ is reproduced for the first time.

A method, called a T-plot, was developed within the MCSM to obtain information on the intrinsic shape of individual MCSM eigenstates (see Refs. [181, 182] for details). Within the T-plot approach, a Potential Energy Surface (PES) is determined from a constrained Hartree-Fock calculation using the same effective interaction. Then each of the MCSM basis vectors is plotted as a circle on the PES, with an area corresponding to the overlap probability of a given vector with the investigated eigenstate. Thus, the location of each circle in the T-plot corresponds to the intrinsic shape of the basis vector, and its size reflects the importance of it in the considered eigenstate. The T-plot for the ground state of ^{100}Zr is presented in Fig. 13.2 (A). The basis vectors are concentrated in a rather small area and they

correspond to quadrupole moments $Q_0 \approx 380$ fm^2 and $Q_2 \approx 0$, which indicates a strongly deformed prolate shape. According to the T-plot presented in Fig. 13.2 (B), the first excited 0^+ state in ^{100}Zr is less deformed, but with an oblate shape.

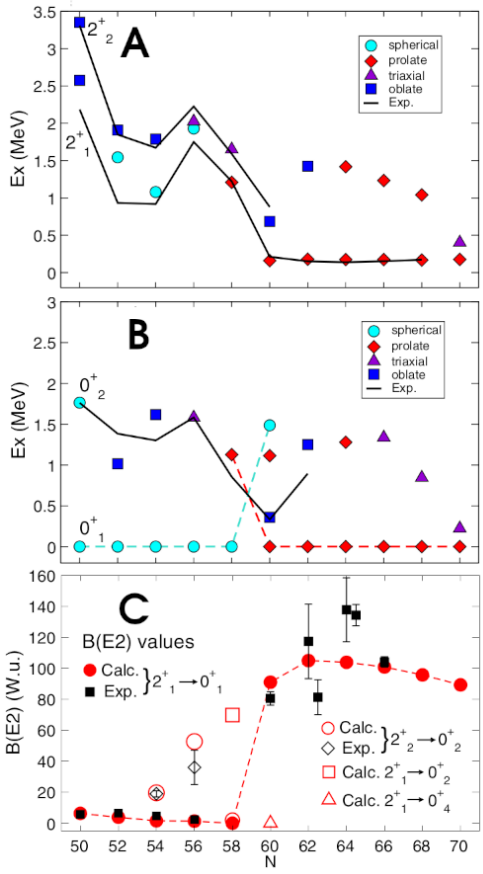

Figure 13.1 – Results of the MCSM calculations for Zr isotopes with $50 \leq N \leq 70$ [134]. (A) - excitation energy systematics of the $2^+_{1,2}$ states; (B) - excitation energy systematics of the $0^+_{1,2}$ states, with the first four 0^+ states shown for ^{100}Zr; (C) - reduced transition probables for selected $2^+ \rightarrow 0^+$ transitions. Figure adapted from Ref. [134].

Using this method, the shapes of 0^+ and 2^+ states in $^{90-110}$Zr were determined from the MCSM calculation. As presented in Figs. 13.1 (A) and (B), a variety of different intrinsic shapes (spherical, prolate, oblate, triaxial) is predicted at low excitation energy in the Zr isotopes. In particular, multiple shape coexistence appears for the ^{100}Zr ($N = 60$), with the ground state calculated to be prolate, followed by an oblate 0^+_2 state, a prolate 0^+_3 and a spherical 0^+_4 state. The proton occupation numbers [183] for these four states are presented in Fig. 13.3. A striking similarity is observed between those calculated for the 0^+_4 state in ^{100}Zr and the ground state of ^{98}Zr. This supports the scenario in which the spherical ground state of ^{98}Zr becomes the off-yrast fourth 0^+ state in ^{100}Zr. On the other

hand, the occupation numbers of the proton orbitals for the 0_2^+ state in ^{98}Zr are similar to those of the 0_1^+ state in ^{100}Zr. Compared to the spherical configuration, the average occupation of the proton $0g_{9/2}$ orbital strongly increases (from 0.4 to 3.5), while those of the pf-shell orbitals decrease.

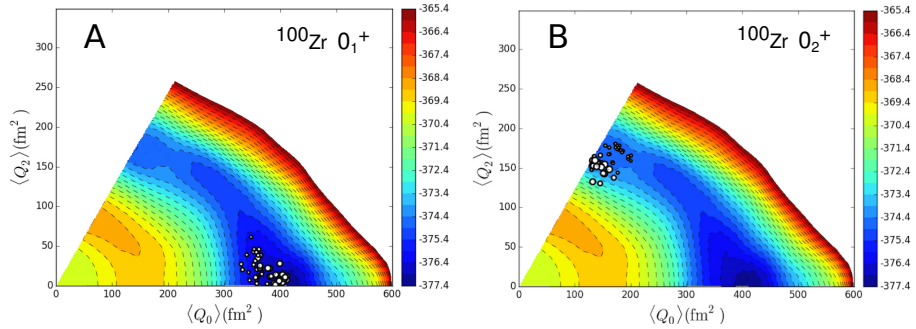

Figure 13.2 – T-plots for the 0_1^+ (A) and 0_2^+ (B) states of ^{100}Zr [183].

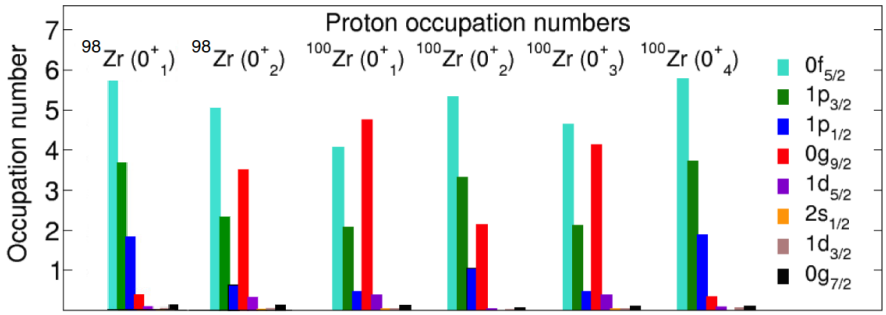

Figure 13.3 – Proton occupation numbers calculated within the MCSM framework for the $0_{1,2}^+$ states of ^{98}Zr and the first four 0^+ states in ^{100}Zr [183].

The corresponding neutron effective single-particle energies (ESPEs) for the $0_{1,2}^+$ states in ^{98}Zr and the ground state of ^{100}Zr are presented in Fig. 13.4. For the 0_1^+ state of ^{98}Zr the ESPEs of the neutron orbitals from $2s_{1/2}$ to $0g_{7/2}$ are distributed over a large energy range (4 MeV), while those for the excited prolate 0^+ state and for the ground state of ^{100}Zr span over only 2 MeV. The strong occupation of the $0g_{9/2}$ proton orbital is correlated with the neutron ESPEs reorganization. This effect is referred to as the type-II shell evolution, and it provides a microscopic explanation of the sudden shape transition observed in the Zr isotopes. It is related to the monopole part of the tensor force, which is attractive between proton and neutron orbitals with different spin-orbital coupling ($j_< - j'_>$ or $j_> - j'_<$, where "$j_<$" denotes $j = l - s$ (for example $g_{7/2}$) and "$j_>$" is $j = l + s$, e.g. $g_{9/2}$) and repulsive for orbitals with similar spin-orbit couplings ($j_> - j'_>$ or $j_< - j'_<$) [184]. Thus, a proton excitation from a $j_<$ to a $j_>$ orbital leads to a reduction of the spin-orbit splitting for certain neutron orbitals j', and vice versa. Consequently,

occupation of neutron $j'_<$ orbitals is enhanced, which further favours excitation of protons to $j_>$ orbitals. This self-reinforcing effect can stabilize low-lying deformed configurations.

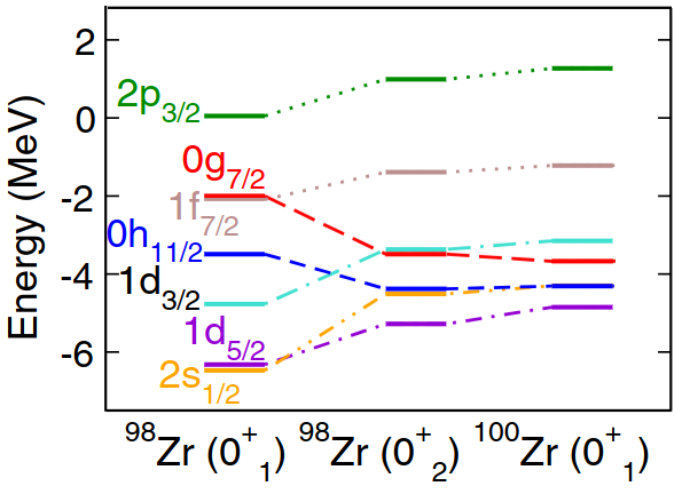

Figure 13.4 – Neutron effective single-particle energies for the $0^+_{1,2}$ states in ^{98}Zr and the ground state of ^{100}Zr. Figure adapted from Ref. [134].

In the Zr isotopes, the spherical configuration involves protons filling the $0f_{5/2}$ ($j_<$), $0p_{3/2}$ ($j_>$) and $0p_{1/2}$ ($j_<$) orbitals, as shown in Fig. 13.3 for e.g. the ground state of ^{98}Zr. Their promotion across the $Z = 40$ gap to the $0g_{9/2}$ ($j_>$) can thus predominantly be described as a $j_<$ to a $j_>$ excitation, leading to lowering of neutron $j'_<$ orbitals such as $0g_{7/2}$ (as shown in Fig. 13.4) and their enhanced occupation, which in turn reduces the $Z = 40$ gap and favours proton excitation across it.

The deformed configurations stabilized by the type-II shell evolution effect correspond to drastically different ESPEs, both for proton and neutrons, compared to the spherical configurations. Consequently, the mixing between deformed and spherical states is strongly suppressed in spite of their proximity in energy, which explains the rapidity of the ground-state shape transition at $N = 60$.

13.2 Multiple shape coexistence in ^{100}Zr

The results obtained in the present work support the multiple shape-coexistence scenario predicted by MCSM. Figure 13.5 presents excitation energies of low-lying levels in ^{100}Zr as well as in-band $B(E2)$ values resulting from the MCSM calculations. While an experimental verification of actual shapes predicted by the model would require a measurement of spectroscopic quadrupole moments of members of each band, certain conclusions can already be reached on the basis of level energies, as well as relative and absolute $E2$ transition strengths obtained in the present work, as discussed in the following.

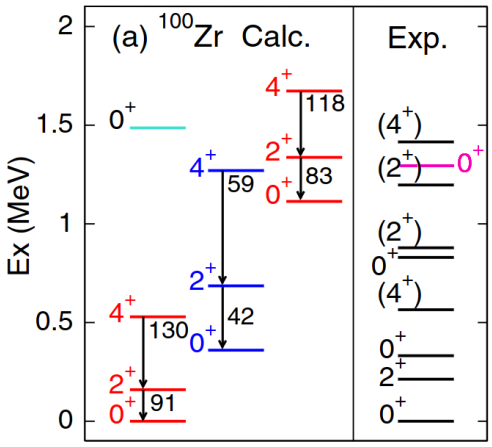

Figure 13.5 – Left: Low-lying levels of ^{100}Zr predicted by the MCSM calculation [134] organized into prolate (red) and oblate (dark blue) structures The 0_4^+ state (light blue) is predicted to be spherical. $B(E2)$ values are given in W.u. Right: Experimental low-energy level scheme of ^{100}Zr. The 0_4^+ state proposed in the present work is presented in magenta. Figure adapted from Ref. [134].

13.2.1 Properties of the band built on the 0_2^+ state

As discussed in Section 13.1, according to the MCSM calculation the 0_2^+ state is oblate deformed. Using Formulas 1.14 and 1.16, the $\langle Q^2 \rangle$ invariants and related deformation parameters $|\beta_2|$ can be calculated from the reduced transition probabilities obtained within the MCSM framework, summarized in Fig. 13.5. A rather large $|\beta_2|$ value of 0.38 is expected for the ground state. Only a lower limit of $|\beta_2(0_2^+)|$ can be extracted from the transition strengths reported in Fig. 13.5 as the $B(E2; 0_2^+ \rightarrow 2_1^+)$ value, likely to have a large contribution to the $\langle Q^2 \rangle$ invariant, has not been published. The obtained $|\beta_2(0_2^+)| > 0.26$ limit suggests that the 0_2^+ state is also strongly deformed. The calculation reproduces well the 0_2^+ excitation energy, as shown in Fig. 13.5, but not the level spacing in the corresponding band.

Using data obtained following spontaneous fission of ^{248}Cm and ^{252}Cf, Urban et al. [187] extended the level scheme of ^{100}Zr proposed in Ref. [145] towards higher spins. Several new levels were reported, forming the structures built on the ground state and on the 0_2^+ state, as well as related in- and inter-band transitions. Using γ-γ angular correlations, spins of several states were firmly assigned, including the ground-state band levels up to spin 10 and the 4^+ and 6^+ states built on the 0_2^+ state. These two bands are presented on the left side of Fig. 13.6.

Based on the energy systematics, notably the almost equidistant energy spacing in the corresponding band, the authors argued that the 0_2^+ state has a nearly spherical or weakly deformed shape. Within the Nilsson model framework, the 0_2^+ state was suggested to correspond to an oblate configuration, resulting from the promotion of a pair of neutrons from the $9/2^+[404]$ "extruder" to the $11/2^-[505]$ orbital, downsloping on the oblate side (see Fig. 7 in Ref. [187]). On the other

hand, the strongly deformed ground state of ^{100}Zr was described as resulting from a promotion of two neutrons from the $9/2^+[404]$ to the $3/2^-[541]$ orbital on the prolate side. The sharp shape transition of the ground state of Zr at $N = 60$ was suggested to occur [187] due to these local effects superimposed on the gradual evolution of the ground state towards prolate deformation in the $50 < N < 66$, $36 < Z < 50$ region caused by the interaction of the ground states with collective "intruder" 0^+ excited states [13].

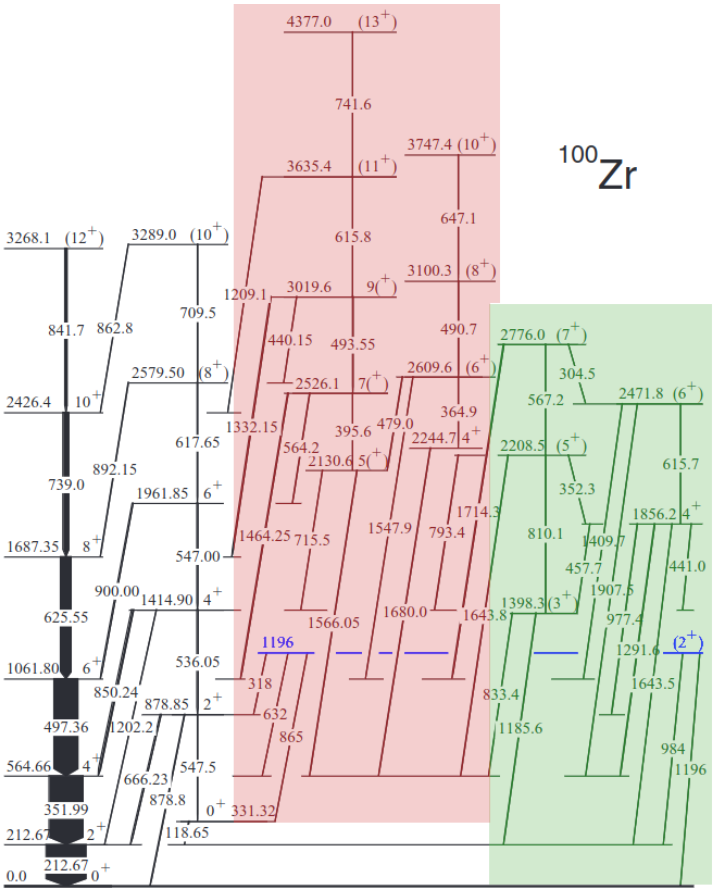

Figure 13.6 – Partial level scheme of ^{100}Zr including the ground-state band, the structure built on the 0_2^+ state, as well as the "proto-triaxial" (in red) and the "proto-γ" (in green) bands, reported in Ref. [146]. The presumed band head of the latter is indicated in blue. Figure adapted from Ref. [146].

From an experimental point of view, a firm statement whether the nucleus is prolate, oblate or triaxial can only be made on the basis of $\langle Q^3 \cos(3\delta) \rangle$ invariants, or, to some extent, the measured spectroscopic quadrupole moments. However, the magnitude of the deformation, given by the $\langle Q^2 \rangle$ invariant, can be deduced from the measured $B(E2)$ values and further related to the β_2 deformation parameter (Formulas 1.14 and 1.16). Using the γ-γ coincidence data collected in the present

study with the $LaBr_3$ detectors, the lifetimes of several key states were measured via the fast-timing technique as a part of the PhD thesis of H. Bidaman [163]. To extract the lifetime of the 2_2^+ state, which can be used to deduce the collectivity of the $2_2^+ \rightarrow 0_2^+$ transition, the γ rays directly feeding (1059.4 keV) and depopulating (666.0 keV) the state of interest were assigned as TAC START and STOP signals. Additionally, a gate on the 212.6-keV $2_1^+ \rightarrow 0_1^+$ transition observed in GRIFFIN HPGe detectors was applied in order to select the ^{100}Zr decay. Using the generalized centroid difference method [188] a lifetime of $13(5)$ ps was obtained. This value, combined with the branching ratios reported in Table 12.1 and the mixing ratio for the $2_2^+ \rightarrow 2_1^+$ transition taken from Table 12.4, yields the reduced transition probabilities summarized in Table 13.1. The experimental $B(E2; 2_2^+ \rightarrow 0_2^+)$ value of $7.7^{+5.4}_{-2.4}$ W.u. is significantly smaller than the value predicted by the MCSM calculations (42 W.u., as presented in Fig. 13.5).

Table 13.1 – Reduced transition probabilities of the transitions depopulating the 2_2^+ state obtained by combining the branching and mixing ratios obtained in the present study with the lifetime of the 2_2^+ state deduced from the same dataset in Ref. [163].

$2_2^+ \rightarrow I_f$	$B(E2)$ [W.u.]
$2_2^+ \rightarrow 0_1^+$	$1.3^{+0.9}_{-0.4}$
$2_2^+ \rightarrow 0_2^+$	$7.7^{+5.4}_{-2.4}$
$2_2^+ \rightarrow 2_1^+$	$8.8^{+5.8}_{-2.6}$
$2_2^+ \rightarrow 4_1^+$	$3.3^{+2.7}_{-1.2}$

Using the fast-timing technique, it was also possible to extract from the present dataset the lifetimes of the 2_1^+ ($852(32)$ ps) and 0_2^+ ($7.61(44)$ ns) states [163], which agree with the literature values within 1σ interval ($837(22)$ ps and $7.96(22)$ ns [147], respectively). The lifetimes obtained for other states, e.g. the 4_1^+ state, were subject to considerably larger uncertainties than those resulting from lifetime measurements using different experimental techniques [147]. The right panel of Fig. 13.7 presents the reduced $E2$ transition probabilities deduced from the lifetimes and branching ratios obtained from the present data set, with the exception of the $B(E2; 4_1^+ \rightarrow 2_1^+)$ value that was calculated from a more precise literature lifetime [147]. These values are in a good agreement with the MCSM calculation for the ground-state band (see Fig. 13.5 for comparison). Furthermore, on the basis of these experimental $B(E2)$ values, it is possible to extract deformation parameters $|\beta_2|$ as it was done earlier using $B(E2)$ values resulting from the MCSM calculation. The $|\beta_2| = 0.35(1)$ obtained for the ground state is in a rather good agreement with the predicted value of 0.38. However, a similar calculation for the 0_2^+ state using the obtained $B(E2; 0_2^+ \rightarrow 2_1^+)$ and $B(E2; 2_2^+ \rightarrow 0_2^+)$ values yields $|\beta_2| = 0.20(2)$, inconsistent with the lower limit given by the MCSM ($|\beta_2| > 0.26$). On the other hand, the $|\beta_2|$ values obtained from the experimental data are signi-

ficantly different for the 0^+_1 and 0^+_2 states, which puts on firm ground the shape coexistence scenario between a strongly deformed ground-state configuration and a less deformed one, related to the 0^+_2 state.

The shape-coexistence scenario was previously confirmed in the $N = 60$ isotone ^{98}Sr in an extensive Coulomb-excitation study [135, 136]. The deformation parameters obtained from the $\langle Q^2 \rangle$ invariants, $|\beta_2(0^+_1)| = 0.409(6)$ and especially $|\beta_2(0^+_2)| = 0.21(2)$, are similar to those obtained from the present study for ^{100}Zr. A comparison of level energies and reduced transition probabilities for transitions between key low-energy states in ^{98}Sr and ^{100}Zr, presented in Fig. 13.7, demonstrates a striking similarity in the structure of the two nuclei.

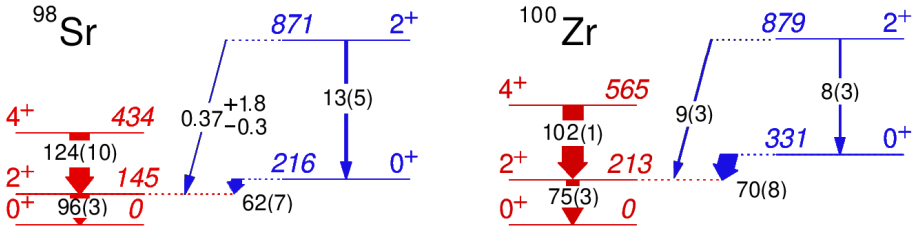

Figure 13.7 – Partial level schemes of ^{98}Sr (left) and ^{100}Zr (right) including the first few members of the structures built on the $0^+_{1,2}$ states. The arrow widths and labels represent reduced transition probabilities in W.u. obtained from the present study for ^{100}Zr [163] (with the only exception being the $B(E2; 4^+_1 \rightarrow 2^+_1)$ value, taken from Ref. [147]) and taken from Ref. [136] for ^{98}Sr.

One can test a hypothesis that the observed 0^+_1 and 0^+_2 states in ^{100}Zr, as well as their 2^+ band members, result from mixing of two "pure" configurations. In a simple two-state mixing model, commonly applied to shape-coexisting states [4], the experimentally observed $0^+_{1,2}$ and $2^+_{1,2}$ states are assumed to be linear combinations of two configurations $I^+_{A,B}$:

$$\begin{aligned} |\, I^\pi_1\rangle &= +\cos\theta_I \,|\, I^+_A\rangle + \sin\theta_I \,|\, I^+_B\rangle, \\ |\, I^+_2\rangle &= -\sin\theta_I \,|\, I^\pi_A\rangle + \cos\theta_I \,|\, I^+_B\rangle, \end{aligned} \tag{13.1}$$

where spin I takes values of 0 and 2, and θ_I is referred to as the mixing angle.

Under a simplifying assumption that no transitions between different pure configurations are allowed, e.i. $\langle 2^+_B \| E2 \| 0^+_A \rangle = \langle 2^+_A \| E2 \| 0^+_B \rangle = 0$, it is possible to extract the mixing amplitudes for the 0^+ and 2^+ states, as well as the $\langle 2^+_A \| E2 \| 0^+_A \rangle$, $\langle 2^+_B \| E2 \| 0^+_B \rangle$ matrix elements between the pure configurations, from four matrix elements coupling the $0^+_{1,2}$ and $2^+_{1,2}$ states. The relevant formulas can be found in Ref. [4].

Such a calculation based on the $E2$ matrix elements resulting from the current study of ^{100}Zr was carried out, using $\langle 2^+_1 || E2 || 0^+_1 \rangle = 1.01(2)$ eb, $\langle 2^+_1 || E2 || 0^+_2 \rangle = 0.54(2)$ eb, $\langle 2^+_2 || E2 || 0^+_1 \rangle = -0.13^{+0.04}_{-0.02}$ eb and $\langle 2^+_2 || E2 || 0^+_2 \rangle = 0.33^{+0.10}_{-0.06}$ eb. The

relative signs of matrix elements were adopted to be the same as those experimentally determined in ^{98}Sr [136] based on the observed similarities in the structure of the two nuclei. The obtained mixing amplitudes, $\cos^2(\theta_0) = 0.77^{+0.03}_{-0.05}$ and $\cos^2(\theta_2) = 0.999^{+0.001}_{-0.015}$, are consistent with a weak mixing between the strongly and weakly deformed configurations, predicted within the type-II shell-evolution scenario. This is the same conclusion as it was reached for ^{98}Sr from $E2$ matrix elements reported in Ref. [136] ($0.88(2)$ and $0.998(2)$, respectively). The intrinsic quadrupole moments for both the weakly deformed ($Q_0^A = +1.11^{+0.20}_{-0.12}$ eb) and strongly deformed configuration ($Q_0^B = +3.64^{+0.030}_{-0.003}$ eb) are smaller with respect to the ^{98}Sr case ($Q_0^A = 1.33(8)$ eb, $Q_0^B = +3.81(2)$ eb). Using these values, it is possible to calculate the $\langle 2_1^+||E2||2_2^+\rangle$ matrix element predicted by the two-level mixing model following formulas given in Ref. [185]. The resulting value, $-0.03^{+0.08}_{-0.05}$ eb, is much smaller than the experimental $\langle 2_1^+||E2||2_2^+\rangle$ matrix element of $|0.35^{+0.10}_{-0.06}|$ eb, see Fig. 13.7. This suggests that the two-level mixing model is not capable of a consistent reproduction of the measured transition strengths in ^{100}Zr and the mixing scenario involving the low-lying states is more complicated. This does not seem to be the case of ^{98}Sr, where the $\langle 2_1^+||E2||2_2^+\rangle = |0.07^{+0.10}_{-0.05}|$ eb obtained from the Coulomb-excitation analysis [136] agrees within 1σ with the value calculated assuming two-state mixing ($-0.04(2)$ eb).

13.2.2 Structure built on the 0_3^+ state and the question of triaxiality

The calculations of Togashi et al. [134] predict a rotational band built on a well-deformed prolate 0_3^+ state, with a level spacing within this structure resembling that observed in the ground-state band, as presented in Fig. 13.5. A good candidate for the 2^+ member of this band would be the 2_3^+ state at 1196 keV, however there was no direct transition observed between the two states. In the present study, the 366.9-keV γ ray corresponding to the $2_3^+ \rightarrow 0_3^+$ transition was observed for the first time, offering an argument in support of this interpretation.

Using Formula 5.4, the relative $B(E2; 2_3^+ \rightarrow I_f)$ values normalized to $B(E2; 2_3^+ \rightarrow 0_1^+)$ were calculated from γ-ray energies E_γ and relative γ-ray intensities I_γ taken from Table 12.1 via:

$$\frac{B(E2; 2_3^+ \rightarrow I_f)}{B(E2; 2_3^+ \rightarrow 0_1^+)} = \frac{\delta(2_3^+ \rightarrow I_f)^2}{\delta(2_3^+ \rightarrow I_f)^2 + 1} \frac{I_\gamma(2_3^+ \rightarrow 0_1^+)}{I_\gamma(2_3^+ \rightarrow I_f)} \frac{E_\gamma^5(2_3^+ \rightarrow 0_1^+)}{E_\gamma^5(2_3^+ \rightarrow I_i^+)}, \quad (13.2)$$

yielding the results summarized in Fig. 13.8. The mixing ratio $\delta(2_3^+ \rightarrow 2_1^+)$ was taken from Table 12.4. The $2_3^+ \rightarrow 2_2^+$ transition was not included in Fig. 13.8 as the corresponding mixing ratio has not yet been extracted from the current dataset. Based on the obtained relative $B(E2)$ values, the decay to the 0_3^+ state is preferred, in line with the interpretation of the 2_3^+ state as a member of the band built on the 0_3^+ state. The relatively large values for decay to the 0_2^+ and 4_1^+ states, however, are indicative of significant configuration mixing.

Using the $LaBr_3$ timing data collected in the present experiment a measurement of the lifetime of the 2_3^+ state was attempted [163]. Unfortunately, it seems that

$\tau(2_3^+)$ is outside of the sensitivity region of the fast-timing technique and only an upper limit of $\tau(2_3^+) < 23$ ps could be extracted. This value corresponds to a lower limit of the reduced transition probability of $B(E2; 2_3^+ \rightarrow 0_3^+) > 2.3$ W.u., which does not provide a meaningful constraint on the collectivity of the transition of interest. In a recent RDDS measurement performed at GANIL following a fusion-fission reaction [186] only yrast states in ^{100}Zr were populated. Hopefully, the future Coulomb-excitation study of ^{100}Zr will yield the $B(E2; 2_3^+ \rightarrow 0_3^+)$ value, or at least its upper limit.

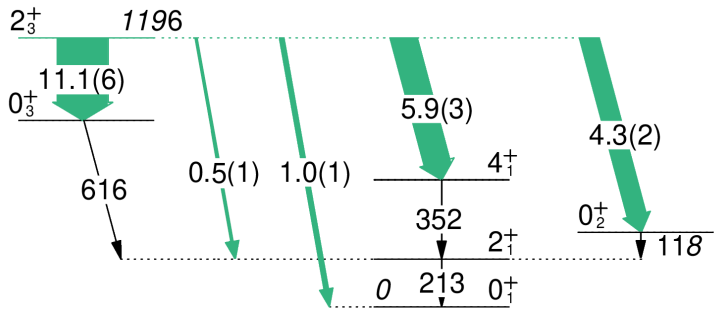

Figure 13.8 – Partial level scheme of ^{100}Zr for the decay of the 2_3^+ state. Arrow widths and labels represent $B(E2)$ values relative to the $B(E2; 2_3^+ \rightarrow 0_1^+)$ value. The decay to the 2_2^+ state is omitted due to the unknown mixing ratio. The remaining transitions, presented in black, are labeled with their energies in keV.

A rather different interpretation of the 2_3^+ state was offered in Ref. [146]. For the first time, $K = 2$ bands in ^{100,102}Zr were reported, suggesting the importance of triaxiality in structure of Zr isotopes. In the proposed structures indicated in green and red in Fig. 13.6, spins of the states at 1856.2 and 2244.7 keV were firmly identified to be 4 via γ-γ angular correlations. The spins of the remaining proposed states in ^{100}Zr were tentatively assigned on the basis of their decay pattern and the fact that the fission process populated predominately yrast states. Using the tentatively assigned spins and level energies, the energy staggering $S(I)$ in each band was calculated and investigated as a function of the spin I. Based on the observed patterns, the two proposed bands were identified as "proto-triaxial" (γ-rigid, marked in red) and "proto-γ" (γ-soft, marked in green) structures. Guided by the energy systematics, Urban et al. suggested the state at 1196 keV (indicated in blue in Fig. 13.6) as a possible candidate for the band head of the proto-γ band, although no transitions connecting higher-spin members of the proto-γ band to the 1196-keV state are known. No candidate was proposed for the band head of the proto-triaxial band, expected at about 1.9 MeV excitation energy [146].

However, as discussed above, based on the data obtained in the current study, the presumed band head of the γ-soft structure at 1196 keV appeared more likely to be the 2^+ band member of a rotational band built on the 0_3^+ state due to its preferred decay to the 0_3^+ state and only a weak decay branch to the 2_1^+ state,

which would be an expected decay pattern of a $K = 2$ bandhead. No other possible candidate, i.e. a 2^+ state with excitation energy lower than that of the proposed (3^+) γ-band member (1398.3 keV) was identified in the present data, and thus the question of triaxiality in ^{100}Zr remains open.

The state at 1970 keV identified in the present study could potentially be a candidate for the band head of the γ-rigid (aka proto-triaxial) structure. However, there is currently not enough information to confirm such claim. While in the further analysis it may be possible to firmly assign the spin of this level, one would also expect to observe a strong decay from higher-spin members of the proto-triaxial band to the band head. Due to the low spin of the parent nucleus ^{100}Y, it is not likely that those states were populated in the present experiment.

13.2.3 Possible band built on the 0_4^+ state

According to the MCSM calculations reported in Ref. [134], the spherical ground state of ^{98}Zr becomes the off-yrast fourth 0^+ state in ^{100}Zr. As shown in the left panel of Fig. 13.5, the predicted 0_4^+ state has an excitation energy of ≈ 1.5 MeV. The 0_4^+ state assigned in the current work, presented in magenta in the right panel of Fig. 13.5, has an excitation energy of ≈ 1.3 MeV. Although at a first glance the theoretical and experimental excitation energy are similar, in order to obtain more information on the collectivity of this state, an attempt has been made to identify the 2^+ member of a rotational-like structure built upon it.

To this aim, all states with excitation energies lower than 4 MeV that were observed in the present dataset to decay to the 0_4^+ state were investigated, as presented in Fig. 13.9. Several of the transitions feeding the 0_4^+ state - represented in Fig. 13.9 with blue arrows - were already reported in Ref. [145] and confirmed in the present study. These are summarized in Table 13.2. The transitions reported for the first time in the present study are indicated in Fig. 13.9 with green arrows. Four among them originated from $(1^\pm, 2^+)$ states proposed in Ref. [145], however, those transitions have not been observed previously. These are listed in Table 13.3. Finally, a number of new states were proposed (indicated in green in Fig. 13.9) decaying via transitions observed for the first time in the present work, summarized in Table 13.4. The spin-parities of those states have not been assigned, with the only exception being the 2^+ state at 2208.5 keV [172]. The γ-ray energies reported in Tables 13.2-13.4 were extracted by fitting the corresponding peaks in the spectrum obtained by gating on the 1082.3-keV γ ray depopulating the 0_4^+ state.

As reported in Table 12.1, the states at 1807.5 keV and 1938.0 keV decay via 16% and 7% branches, respectively, to the 0_4^+ state. Although they are lowest in energy among those that directly feed the state of interest, both the 1807.5-keV and 1938.0-keV states were assigned to have spin 1 in the present work (see Section 12.4). The next possible candidate for a 2^+ state built on the 0_4^+ state is the newly proposed state at 2208.5 keV [172]. To further test this hypothesis the relative reduced transition probabilities (normalized to $B(E2; 2^+ \rightarrow 0_1^+)$) were calculated for the pure $E2$ transitions, i.e. those between the state at 2208 keV

and the $0^+_{2,3,4}$ and 4^+_1 states. The remaining decays (to the $2^+_{1,2}$ states and the state at 1441 keV, assigned as spin 2) may have a mixed $E2/M1$ character. As the corresponding mixing ratios have not been determined yet, these transitions were not considered in the comparison.

Table 13.2 – Excitation energies E_i of states that decay directly to the 0^+_4 state, and energies E_γ of the corresponding γ-ray transitions. These transitions were reported in Ref. [145]. The values marked with asterisks are taken from Ref. [147].

E_i [keV]	E_γ [keV]
1807.49(4)	512.73(5)
1937.97(6)	643.40(13)
2846.34(7)*	1551.39(4)
2932.10(13)*	1637.07(4)

Table 13.3 – Same as Table 13.2, but for transitions that have been observed for the first time in the present work originating from states reported in Ref. [145].

E_i [keV]	E_γ [keV]
2692.84(9)*	1398.0(5)
2770.76(8)*	1475.4(3)
3069.82(20)*	1774.9(5)
3956.64(24)*	2656(2)

Table 13.4 – Same as Table 13.2, but for new transitions originating from states proposed in the present study.

E_i [keV]	E_γ [keV]
2208.51(5)	913.78(7)
2287.9(2)	992.4(2)
3271.3(3)	1975.9(3)
3477.5(5)	2182.1(5)
3590.3(3)	2294.8(3)
3915.9(4)	2620.5(4)

The obtained normalized $B(E2)$ values are summarized in Fig. 13.10. The 2^+ state at 2208.5 keV has a clear preference to decay to the 0^+_4 state with respect to all other possible stretched $E2$ branches. This observation supports the possible interpretation of the state at 2208.5 keV as a member of a rotational-like band built on the 0^+_4 state. In order to firmly evaluate the collectivity of the $2^+ \rightarrow 0^+_4$ transition, the lifetime of the 2^+ state at 2208.5 keV is needed. However, a first

estimate can be made based on the level spacing within the band. The $2_1^+ \rightarrow 0_1^+$ transition energy is 212.6 keV, while the $2_2^+ \rightarrow 0_2^+$ transition has an energy of 547.5 keV. The state at 1196 keV, proposed to be built on the 0_3^+ state, decays to it via a 366.9-keV transition. If the state at 2208.5 keV is built on the 0_4^+ state, this would correspond to 913.8-keV spacing between the two lowest band members, much larger than those observed for other rotational bands in ^{100}Zr, which suggests a lower collectivity of the structure built on the 0_4^+ state. For comparison, the 2_3^+ state in ^{98}Zr, interpreted as built on the quasi-spherical ground state, is observed at 1745-keV excitation energy.

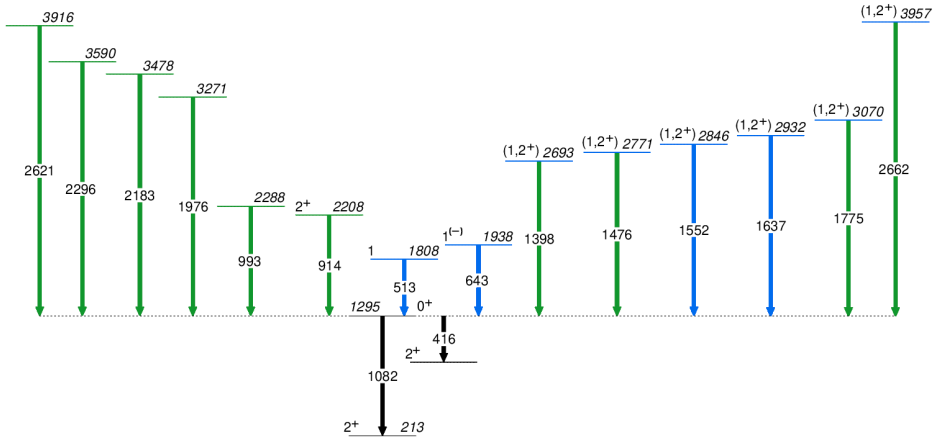

Figure 13.9 – Partial level scheme of ^{100}Zr presenting all decays to the 0_4^+ state originating from states below 4 MeV excitation energy, which were observed in the present work, as well as decay branches of the 0_4^+ state. States and transitions plotted in green were identified in the present study. Level and transition energies are given in keV.

The remaining candidates for the spin-2 0_4^+ band member have even higher excitation energies, and thus would indicate an even lower collectivity. In the future, an attempt will be made to determine spins at least of some of these states from the analysis of γ-γ correlations in their decay.

13.3 Summary and outlook

In the present work, the level scheme of ^{100}Zr was investigated up to ≈ 2.2 MeV excitation energy and six new levels were proposed within this energy range. However, numerous observed γ rays with higher energies, including some intense ones, remain to be placed. Therefore, in the future, it will be possible to largely extend the existing level scheme of ^{100}Zr. Multiple new levels have already been identified, e.g. during the investigation of possible candidates for the 2^+ member of a structure built on the 0_4^+ state presented in Section 13.2.3.

The branching ratios within the investigated level scheme were extracted using gates from above. For the moment, no summing corrections were applied due to

the temporary unavailability of the data stored on the servers of the University of Guelph. Although it was shown in Section 12.2.1 that the summing-in effect influences the extracted branching ratios by only a few percent (i.e. within their relative uncertainties), in the near future corrections for both summing-in and summing-out effects will be determined from the experimental data by using γ-γ coincidences between detectors separated by 180°, as described in Section 11.2.4. The branching ratios in the decay of higher-lying states will also be extracted. Once the complete level scheme is established, limits of the $\log(ft)$ values will be determined.

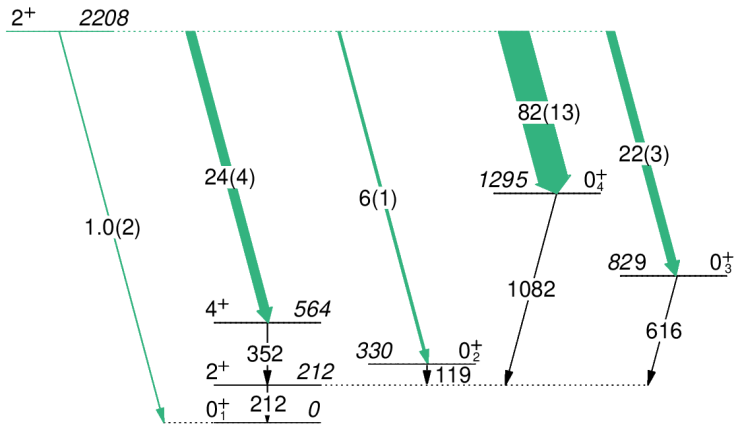

Figure 13.10 – Relative transition probabilities for the $E2$ transitions depopulating the proposed 2^+ state at 2208.5 keV, normalized to the $B(E2, 2^+ \rightarrow 0^+_1)$ value. The relevant transitions are indicated with green arrows and the arrow widths reflect the relative $B(E2)$ values. The remaining transitions (in black) are labeled with their energies in keV.

Using γ-γ angular correlations, three new 0^+ states were identified at relatively low excitation energies. A possible member of a presumed rotational band built on the 0^+_4 state was proposed. However, there exist other candidates for the 2^+ member of this band, and their spins and decay patterns will be analysed in the future. Possible candidates for rotational states built on the excited $0^+_{5,6}$ states proposed in the present study will also be investigated. Furthermore, a search for the "proto-triaxial" and "proto-γ" band heads will be carried out.

Some of the angular correlations presented in Section 12.4 need further refinement to reach the 99% limit, including those for key states, e.g. $2^+_{2,3}$ and 0^+_4. The spin assignments for several of the reported states were not conclusive, e.g. for the levels at 1971 keV and 2144 keV, which will be investigated using different cascades (with the 2^+_3 and 2^+_2 intermediate state, respectively). In addition, the mixing ratios of several transitions remain to be extracted from the current data set. Apart from nuclear-structure interest, their determination is important for the analysis of the future Coulomb-excitation experiment on ^{100}Zr. Furthermore, it

will be attempted to provide spin assignments for other states that are observed to decay via intense γ ray transitions.

The full simulations accounting for the attenuation of the correlations due to the finite detector size of GRIFFIN crystals were performed only for the $2_3^+ \rightarrow 2_1^+ \rightarrow 0_1^+$, $0_4^+ \rightarrow 2_1^+ \rightarrow 0_1^+$, 1807 keV$\rightarrow 2_1^+ \rightarrow 0_1^+$ and 1938 keV$\rightarrow 2_2^+ \rightarrow 0_1^+$ cascades. Although it was shown in Section 12.4 that the attenuation effects only marginally influence the extracted results, the simulations for at least some of the remaining cascades will be performed.

Furthermore, using γ-γ angular correlations, it is not possible to directly obtain the parity of the investigated states. The parities of certain states could be deduced using arguments regarding their decay pattern, however, the high coincidence efficiency and granularity of GRIFFIN would make it possible to perform a Compton polarimetry analysis [189] in the future and firmly establish the parities of other states. This method makes use of the fact that the linear polarization of γ rays emitted in a cascade differs for electric and magnetic types of radiation [190].

Finally, the conversion-electron data collected with PACES has not yet been analysed in detail. While all of the conversion-electron transitions reported in Ref. [145] were observed on-line, most of the collected data was affected by a low-frequency noise appearing at random moments during the experiment. Thus, as a first step, the usable data has to be identified.

In parallel to the work presented in this manuscript, a β-decay measurement into ^{98}Zr and ^{98}Sr performed using the 8π spectrometer [191] is being analysed at the University of Guelph. The new structural information obtained from these studies can be used for systematic comparisons with the ^{100}Zr case, improving our understanding of the shape-coexisting structures observed in this region of the nuclear chart. Moreover, the MCSM calculations for the Zr isotopes are currently being refined by the group of T. Otsuka, Center for Nuclear Study, University of Tokyo.

A - FRESCO input file

```
   106Cd + 92Mo at 757-MeV
NAMELIST
&FRESCO hcm=0.005, rmatch=400.0 jtmin=0.0 jtmax=5500.0 absend=-1
thmin=5.0 thmax=-100.0 thinc=1.0 iblock=7 smats=2 xstabl=1 elab=756.7 /
&PARTITION namep='106Cd' massp=106.0 zp=48
           namet='92Mo' masst=92 zt=42 qval=0.0000 nex=7 /
&STATES jp=0.0 bandp=1 ep=0.0 cpot=1 jt=0.0 bandt=1 et=0.0 /
&STATES jp=2.0 bandp=1 ep=0.63264 cpot=1 copyt=1 /
&STATES jp=4.0 bandp=1 ep=1.49378 cpot=1 copyt=1 /
&STATES jp=2.0 bandp=1 ep=1.71653 cpot=1 copyt=1 /
&STATES jp=0.0 bandp=1 ep=1.79525 cpot=1 copyt=1 /
&STATES jp=4.0 bandp=1 ep=2.30492 cpot=1 copyt=1 /
&STATES jp=3.0 bandp=-1 ep=2.3785 cpot=1 copyt=1 /
&partition /
&POT kp=1 ap=106.0 at=92.0 rc=1.200 /
&POT kp=1 type=12 shape=10 p1=0.064 p2=63.3 p3=280.0 /
     &STEP ib=1 ia=2 k=2 str=62.216 /
     &STEP ib=2 ia=1 k=2 str=62.216 /
     &STEP ib=2 ia=2 k=2 str=-28.0 /
     &STEP ib=2 ia=3 k=2 str=105.190 /
     &STEP ib=3 ia=2 k=2 str=105.190 /
     &STEP ib=3 ia=3 k=2 str=-28.0 /
     &STEP ib=1 ia=4 k=2 str=16.798 /
     &STEP ib=4 ia=1 k=2 str=16.798 /
     &STEP ib=2 ia=4 k=2 str=42.25 /
     &STEP ib=4 ia=2 k=2 str=42.25 /
     &STEP ib=4 ia=4 k=2 str=132 /
     &STEP ib=2 ia=5 k=2 str=17.255 /
     &STEP ib=5 ia=2 k=2 str=17.255 /
     &STEP ib=2 ia=6 k=2 str=7.075 /
     &STEP ib=6 ia=2 k=2 str=7.075 /
     &STEP ib=3 ia=6 k=2 str=21.98 /
     &STEP ib=6 ia=3 k=2 str=21.98 /
     &STEP ib=2 ia=7 k=1 str=0.064 /
     &STEP ib=7 ia=2 k=1 str=0.064 /
     &STEP ib=1 ia=7 k=3 str=280 /
     &STEP ib=7 ia=1 k=3 str=280 /
&step /
&POT kp=1 type=1 p1=89.23 p2=1.18074 p3=0.69523 p4=22.3075
```

```
p5=1.18074  p6=0.69523  /
&POT  kp=1  type=12  shape=10  p2=0.95614  /
      &STEP  ib=1  ia=2  k=2  str=0.95614    /
      &STEP  ib=2  ia=1  k=2  str=0.95614    /
      &STEP  ib=2  ia=2  k=2  str=−0.43      /
&step  /
&POT  kp=1  type=12  shape=10  p2=1.6166  /
      &STEP  ib=2  ia=3  k=2  str=1.6166    /
      &STEP  ib=3  ia=2  k=2  str=1.6166    /
      &STEP  ib=3  ia=3  k=2  str=−0.43     /
&step  /
&POT  kp=1  type=12  shape=10  p2=0.258  /
      &STEP  ib=1  ia=4  k=2  str=0.25815  /
      &STEP  ib=4  ia=1  k=2  str=0.25815  /
      &STEP  ib=4  ia=4  k=2  str=2.0283   /
&step  /
&POT  kp=1  type=12  shape=10  p2=0.6493  /
      &STEP  ib=2  ia=4  k=2  str=0.6493    /
      &STEP  ib=4  ia=2  k=2  str=0.6493    /
&step  /
&POT  kp=1  type=12  shape=10  p2=0.265  /
      &STEP  ib=2  ia=5  k=2  str=0.26517  /
      &STEP  ib=5  ia=2  k=2  str=0.26517  /
&step  /
&POT  kp=1  type=12  shape=10  p2=0.1087  /
      &STEP  ib=2  ia=6  k=2  str=0.10873  /
      &STEP  ib=6  ia=2  k=2  str=0.10873  /
&step  /
&POT  kp=1  type=12  shape=10  p2=0.3378  /
      &STEP  ib=3  ia=6  k=2  str=0.3378    /
      &STEP  ib=6  a=3  k=2  str=0.3378     /
&step  /
&POT  kp=1  type=12  shape=10  p1=0.005585  /
      &STEP  ib=2  ia=7  k=1  str=0.005585    /
      &STEP  ib=7  ia=2  k=1  str=0.005585    /
&step  /
&POT  kp=1  type=12  shape=10  p3=0.7576  /
      &STEP  ib=1  ia=7  k=3  str=0.7576     /
      &STEP  ib=7  ia=1  k=3  str=0.7576     /
&step  /
&pot  /
&overlap  /
&coupling  /
```

B - Structure of the GOSIA input files

The main GOSIA input file consists of a sequence of option commands. The option names start by "OP," followed by four characters which indicate the specific command.

- **OP,FILE** - with this command the user defines the additional files to be used in the calculation. Each file corresponds to a unit number, which is called and then the file name is given [88]. The units used in the present work are: 22 - an output file (106Cd.out), 3 - a file with experimentally obtained γ-ray yields (106Cd.yld), 4 - a file with these γ-ray yields modified to resemble point-like yields corresponding to a specific beam energy and scattering angle, as explained in Section 5.7.2 (106Cd.f4), 8 and 9 - files containing information on the solid angle covered by the γ-ray detectors, and the related γ-ray attenuation factors (agata.f8, agata.f9), 7 - a file containing information used in the fast approximation of the Coulomb-excitation process [88] (106Cd.f7) and 12 - a file listing the values of the matrix elements (106Cd.me).

- **OP,TITL** - a user-given title to be displayed as a header of the output.

- **OP,GOSI** - option that sets the mode in which GOSIA will be used, namely fitting a set of MEs to experimental data. Within GOSI, the user defines the investigated nucleus and the experiments to be used in the fitting procedure. This is done in four sub-options - LEVE, ME, EXPT and CONT:
  1. **LEVE** - LEVEls is used to declare the level scheme of the nucleus of interest. Each state is defined with a single record: n, P_n, S_n, E_n, which correspond to a user-given state index (from 1 to the total number of states N), parity ($\pm$ 1), spin and excitation energy in MeV, respectively.
  2. **ME** - the reduced Matrix Elements used in the fitting procedure are defined here. They are separated according to the type (electric, magnetic) and multipolarity (λ) of the electromagnetic operator. One has to first provide the $E1$ matrix elements ("1 0 0 0 0" marks the beginning of $E1$ MEs definition), followed by the $E2$ (2 0 0 0 0) and $E3$ (3 0 0 0 0), with the highest possible multipolarity for electric transitions being $E6$. The definitions continue with the magnetic matrix elements - $M1$ (7 0 0 0 0), or at most $M2$ (8 0 0 0 0).

     Each matrix element is defined by a single line providing n_I, n_F, ME, R_L and R_U, which correspond to the index of the initial and final states (according to the indexation in LEVE), the matrix element given in $e\mathrm{b}^{\lambda/2}$ for electric and $\mu_N \mathrm{b}^{(\lambda-1)/2}$ for magnetic MEs, and the lower and upper limits in which the matrix element can be varied during

the fitting procedure, respectively. The matrix elements provided in this sub-option can be understood as the initial set of MEs for the minimization procedure. They will be varied within their limits in order to obtain the best fit of the data.

3. **EXPT** - within the EXPEriment sub-option, the user defines the experiments to be considered. Each experiment corresponds to a particular combination of bombarding energy, scattering angle and geometry of the particle and γ-ray detectors. First, one declares N_{ex}, Z_I, A_I, which refer to the total number of experiments to be analysed, atomic number and mass number of the investigated nucleus. Then, Z_U, A_U, E_{LAB}, θ_{LAB}, M_c, M_a, IAX, ϕ_L, ϕ_U, $IKIN$, LN are provided for each experiment separately. Z_U and A_U are the atomic and mass numbers of the collision partner. A negative sign in front of Z_U signifies that excitations of the projectile are analysed. E_{LAB} is the mean projectile energy in the laboratory coordinate system. The mean scattering angle θ_{LAB} is usually taken to be the middle of each $\Delta\theta_{LAB}$ region covered by the particle detector. M_c and M_a are the numbers of magnetic substates to be included in the full and in the approximate Coulomb-excitation calculation, respectively [88]. The IAX flag is used to declare if the particle detector is axially symmetric, which is not the case for the present experiment. Thus, IAX=1 and a more detailed description of the detector geometry is given later in another option. The coverage in ϕ of the particle detector is given via ϕ_L and ϕ_U, which in the present analysis are taken to be the azimuthal angular limits of the particle detector at the middle of each $\Delta\theta_{LAB}$ slice. The IKIN flag is used to select which of the two possible kinematic solutions should be used (relevant when $A_{projectile} > A_{target}$). Finally, LN can be used to tie together the normalisation constants C_m (see Formula 5.28) for a pair of experiments. In the present case each experiment has an independent normalization and $LN = N_{ex}$.

4. **CONT** - this sub-option is used to control the execution and output. Without going into details (which can be found in Ref. [88]), a few control sequences were called in the input file used for the present analysis: LCK, WRN, INR, SPL, INT and PRT. LCK can be used for fixing values of specific matrix elements in the fit. The remaining parameters control various aspects of the calculation, e.g. accuracy and printout, including warning statements, etc. The option definition is terminated by END, and a blank line.

- **OP,YIEL** - option which is used for calculating de-excitation γ-ray yields following Coulomb excitation. First, the internal conversion coefficients are provided at specific energies (mesh points) for each of the multipolarites

listed in the definition of the MEs in OP,GOSI. Subsequently, the geometry of the γ-ray detection system is described. The number of detectors used in each experiment is declared first (21 in this work). A sequence of 21 numbers follows, each corresponding to a particular detector type, then the θ and ϕ angle coordinates of the center of each defined detector. This procedure is repeated for each experiment. Seven types of detectors were defined in the current work, depending on their distance from the target, ranging from 18.9 to 20.8 cm. The size and shape of each detector was also provided - 4 cm radius of the crystal, 9 cm height of the detector cylinder, 0.1 cm inner electrode (to be excluded from the active volume of the detector) and 0.1 cm Al absorber covering every crystal [52]. This information was provided in option OP,GDET in order to calculate the solid angle covered by each type of detector and the related γ-ray attenuation factors, stored in files "agata.f8" and "agata.f9".

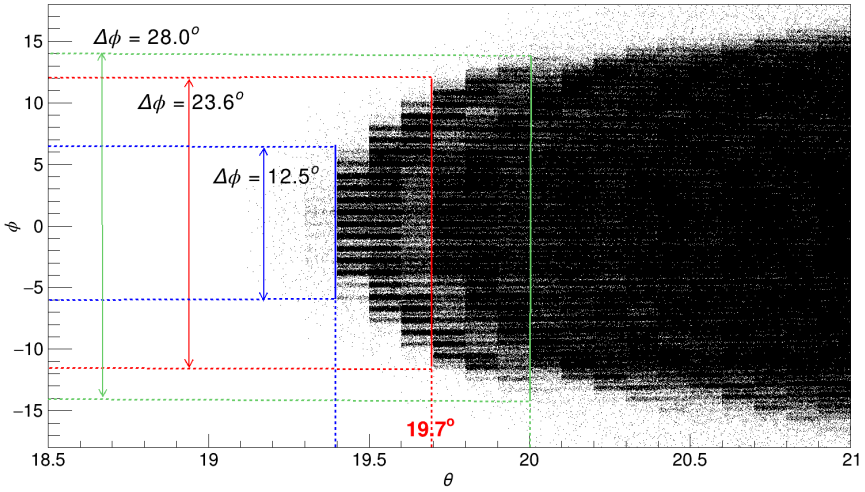

Figure B.1 – Part of the hit pattern of ^{106}Cd ions identified in VAMOS, corresponding to the first (θ_{LAB} between $19.4°$ and $20.0°$) and second (θ_{LAB} between $20.0°$ and $21.0°$) experiments defined in GOSIA. The description of the particle detector shape for the first region is illustrated. The $\Delta\phi$ coverage is given for three distinct θ_{LAB} angles - beginning of the region (blue), middle (red) and end (green).

The information needed for the fitting procedure is provided next. First, a transition to be used for normalization is defined. In the current work, the intensity of the $2_1^+ \rightarrow 0_1^+$ transition, denoted by "$2\ \ 1$", is used to normalize all calculated intensities in each experiment. Then $NDST$, UPL and $YNRM$ are provided for each experiment, corresponding to the number of data sets per experiment (1), upper limit (assumed to be 0.1% of the normalizing transition, see Section 5.7.1) and relative normalization factors of the γ-ray detectors (1), respectively. Finally, one has to select the file

from which the intensities to be fitted will be imported: either 106Cd.yld (3), 106Cd.f4 (4) or none (0), if the intensities will be simulated instead.

Additional spectroscopic information needed for the least-square fit is provided in OP,YIEL starting with the declaration of the number of known branching ratios and the weight with which they are considered in the fit (1.0). They are defined by a sequence n_1, n_2, n_1, n_3, $BR((n_1 \rightarrow n_2)/(n_1 \rightarrow n_3))$, $\sigma(BR)$. The second transition $(n_1 \rightarrow n_3)$ is typically the most intense transition, which is used for normalization of the other branches.

As a next step, the number and weight (1.0) of lifetimes to be considered in the least-square search are declared. The lifetimes are introduced as: n, τ, $\sigma(\tau)$, where n is the index of the state, τ the mean lifetime (not the half-life) expressed in picoseconds, and $\sigma(\tau)$ is its absolute uncertainty. Subsequently, $\delta(E2/M1)$ mixing ratios to be used in the analysis are provided. The used syntax is as follows: n_1, n_2, δ, $\sigma(\delta)$, where n_1 and n_2 are the indices of the states involved in the mixed transition.

Finally, the previously measured matrix elements may also be defined to be included in the least-square fit. They are introduced by a record: λ, n_1, n_2, ME, $\sigma(ME)$, where λ is defined as in the ME section of OP,GOSI, i.e. 2 denotes an $E2$ matrix element and 3 an $E3$ one, and ME is $\langle n_1||^E_M\lambda||n_2\rangle$. The matrix elements are expressed in $e\mathrm{b}^{\lambda/2}$ for electric and $\mu_N \mathrm{b}^{(\lambda-1)/2}$ for magnetic transitions.

- **OP,RAW** - this option is used if the measured γ-ray intensities are not corrected for detection efficiency and/or if spectra from individual detectors are summed together in the analysis. Separately for each experiment, the efficiency curve parameters for every γ-ray detector are provided (in the present case they are equal to $0, 0, 0, 0, 0, 0, 0, 0$, as the data are efficiency corrected), the number of detector clusters, i.e. groups of detectors that have their energy spectra summed together (1) and which detectors are included in each cluster, following their definitions in OP,YIEL $(1, 2, .., 21)$.

- **OP,POIN** - within this option one can calculate the so called "point-like" γ-ray yields (Formula 5.23). Those are the yields calculated at the mean beam energy E_{LAB} and mean scattering angle θ_{LAB} characterizing each experiment in the EXPT sub-option.

- **OP,INTI** - this option can be used to perform integration over the finite scattering angle range covered by the particle detector $d\Omega_P$ and over the bombarding energies resulting from the projectile energy loss over the target thickness (Formula 5.24). In the first stage of the calculation, γ-ray yields, integrated over the azimuthal angle phi, are calculated at specific

energy and scattering angle θ_{LAB} mesh points (similar to OP,POIN). This is followed by integration over the relevant ranges of bombarding energy and scattering angle, relying on interpolation between the calculated γ-ray yields at the energy and scattering angle mesh points specified by the user. The user provides first N_E and $\pm N_\theta$, which are the number of energy and θ_{LAB} mesh points at which the full Coulomb-excitation calculation will be performed. If the sign in front of N_θ is negative, the particle detector is declared to be non-axial and additional information needs to be provided at a later stage. The following records: E_{MIN}, E_{MAX}, θ_{MIN}, θ_{MAX} are the limits of the incident energy in MeV and the limits of the scattering angle of the detected particles in the laboratory frame between which the integration is carried out (Formula 5.24).

Three beam energy mesh points were declared in the current work - before ($E_{MAX} = 770$) MeV, at the middle (756.7 MeV) and after the target ($E_{MIN} = 743.4$ MeV). The θ_{MIN} and θ_{MAX} values for each experiment followed Fig. 4.9. The scattering angle mesh points were taken to be the largest, the smallest and the mean scattering angle of each $\Delta\theta_{LAB}$ region, i.e. the "experiment" defined in tge EXPT section. For example, in the first experiment, the scattering angle mesh points were 19.4°, 19.7°, 20.0° (see Fig. B.1). For each θ mesh point, it was also necessary to provide the lower and upper limit of the ϕ coordinate of the particle detector. The selected regions for the first experiment are illustrated in Fig. B.1 with the dashed lines. The information discussed above was provided for each experiment defined in the sub-option EXPT.

Furthermore, the energy loss in the target material has to be considered during the evaluation of the γ-ray yields. Therefore, at the specified energy mesh points the stopping powers dE/dx were calculated with the program elo [58] and provided in units of MeV/(mg/cm^2) in the input file. Finally, the numbers of equal subdivisions of the ranges of energy and scattering angle (E_{MIN} to E_{MAX}, θ_{MIN} to θ_{MAX}) are provided. These are used for interpolation of the Coulomb-excitation yields between the mesh points in the integration procedure. In total ten energy subdivisions were requested, while for the θ only two were considered necessary. If the detector has no axial symmetry, for each subdivision one has to provide the $\Delta\phi$ covered by the particle detector, as illustrated in Fig. B.1 for the first experimental region.

The input to OP,INTI, summarized in Appendix D, can be directly attached to the main input file in Appendix C to perform intensity calculations using the matrix elements defined in the ME sub-option. A set of matrix elements given in an external file (106Cd.me) can also be included in the calculation if OP,REST is called before OP,INTI.

- **OP,MINI** - this option is used to perform a χ^2 fit of a set of matrix elements to the experimental data. Additional information for the minimization routine has to be provided: number of steps, minimum χ^2 value at which the procedure is terminated, convergence criterion (maximum difference between the sets of MEs in two subsequent minimization steps, before the procedure is terminated), etc. [88]. If OP,REST is also called, the initial set of MEs will be read before OP,MINI is executed, otherwise the matrix elements defined in OP,GOSI will be used.

C - Main part of the GOSIA input file

```
OP,FILE
22 3 1
106Cd.out
3 3 1
106Cd.yld
4 3 1
106Cd.f4
8 3 1
agata.f8
9 3 1
agata.f9
7 3 1
106Cd.f7
12 3 1
106Cd.me
0 0 0
OP,TITL
Exp. 106Cd+92Mo
OP,GOSI
LEVE
1,1     0   0.0
2,1     2   0.63264
3,1     4   1.49378
4,1     2   1.71653
5,1     0   1.79525
6,1     4   2.10453
7,1     4   2.30492
8,1     5   2.33056
9,-1    3   2.37850
10,1    4   2.48572
11,1    6   2.49166
12,1    6   2.50308
13,1    2   2.56626
14,-1   5   2.6292
15,-1   5   2.92014
16,1    8   3.04413
17,1    0   2.14406
18,1    2   2.2541
19,1    2   2.63008
```

```
20,1    2   2.71786
21,-1   1   2.82458
22,1    2   2.7108
0 0 0 0
ME
1 0 0 0 0
  1   21        0.00517         0.0000001       0.021
  2   9         0.0064          0.0000001       0.03
  2   21        0.00128         0.0000001       0.021
  3   14        0.00103         0.0000001       0.04
  3   15        0.0102          0.0000001       0.04
  5   21        0.00535         0.0000001       0.021
  6   14        0.0067          0.0000001       0.04
  8   14        0.00380         0.0000001       0.04
  9   20        0.0096          0.0000001       0.03
2 0 0 0 0
  1   2         0.62272         0.0000001       2.114
  1   4         0.168           0.0000001       2.114
  1   19        0.032           0.0000001       2.114
  2   2         -0.28           -3.0            -0.0000001
  2   3         1.08326         0.0000001       2.837
  2   4         0.422           0.0000001       2.114
  2   5         0.17255         0.0000001       0.945
  2   6         0.09263         0.0000001       2.837
  2   7         0.07075         0.0000001       2.837
  2   10        0.0953          0.0000001       2.837
  2   13        0.1151          0.0000001       2.114
  2   17        0.0689          0.0000001       0.945
  2   18        0.253           0.0000001       2.837
  2   19        0.0263          0.0000001       2.114
  2   20        0.1487          0.0000001       2.114
  3   3         -0.28           -3.0            -0.0000001
  3   6         0.3497          0.0000001       2.837
  3   7         0.2193          0.0000001       2.837
  3   8         0.00456         0.0000001       3.136
  3   10        0.2845          0.0000001       2.837
  3   11        0.732           0.0000001       3.409
  3   12        0.91094         0.0000001       3.409
  3   22        0.97702         0.0000001       2.114
  4   4         1.32            0.0000001       4.000
  4   6         0.64181         0.0000001       2.837
  4   10        0.3270          0.0000001       2.837
```

```
  4   13        0.2685          0.0000001       2.114
  4   17        0.35            0.0000001       0.945
  4   19        0.5079          0.0000001       2.114
  4   20        0.3929          0.0000001       2.114
  5   13        0.1886          0.0000001       2.114
  5   19        0.1562          0.0000001       2.114
  6   8         0.5467          0.0000001       3.136
  6   10        1.0201          0.0000001       2.837
  11  16        0.17094         0.0000001       3.899
  12  12        -1.3            -4.0            -0.0000001
  12  16        0.14302         0.0000001       3.899
  17  19        0.5573          0.0000001       2.114
3 0 0 0 0
  1   9         0.28            0.0000001       0.684
  2   14        0.2             0.0000001       0.857
  2   15        0.3             0.0000001       0.857
  2   22        0.3             0.0000001       0.447
7 0 0 0 0
  2   4         -0.265          -2.99           -0.0000001
  2   13         0.596          0.0000001        2.99
  2   19        -0.3983         -2.99           -0.0000001
  3   6         -0.5676         -4.01           -0.0000001
  3   7         -0.8734         -4.01           -0.0000001
  3   8         -0.0177         -4.44           -0.0000001
  6   8         -0.1807         -4.44           -0.0000001
EXPT
3 48 106
-42 92 756.7 19.7 3,1,1 -11.6 12.0 1 1
-42 92 756.7 20.5 3,1,1 -16.0 16.0 1 2
-42 92 756.7 21.5 3,1,1 -19.0 19.0 1 3
CONT
LCK,
0,0
WRN,3.
INR,
SPL,1.
INT,1.
1,1000
PRT,
4,0
5,1
10,0
```

```
11,0
12,0
13,0
14,0
17,0
18,1
0,0
END,

OP,YIEL
0
23 4
0.1 0.2 0.4 0.6 0.8 1.0 1.2 1.4 1.6 1.7 1.8 1.9
2.0 2.1 2.2 2.3 2.4 2.5 2.6 2.8 3.0 3.1 3.2
1
1.669E-01 2.34E-02 3.67E-03 1.400E-03 7.55E-04 4.86E-04
3.83E-04 4.24E-04 5.21E-04 5.78E-04 6.36E-04 6.96E-04
7.56E-04 0.000815 0.000874 0.000931 0.000987 0.001041
0.001096 0.001203 0.001294 0.001339 0.001386
2
1.495E+00 1.287E-01 1.295E-02 4.00E-03 1.92E-03 1.1140E-03
7.75E-04 6.08E-04 5.50E-04 5.45E-04 5.51E-04 5.64E-04 5.84E-04
0.000608 0.000635 0.000666 0.000698 0.000732 0.000766 0.000836
0.000906 0.000942 0.000977
3
15.08 0.667 0.0417 0.01036 0.00436 0.0023 0.001513 0.001068 0.000832
0.000759 0.000708 0.000673 0.000652 0.00064 0.000635 0.000637
0.000645 0.000656 0.000671 0.000708 0.000751 0.000775 0.000799
7
4.63E-01 6.88E-02 1.152E-02 4.30E-03 2.20E-03 1.329E-03 8.97E-04
6.83E-04 5.93E-04 5.76E-04 5.72E-04 5.78E-04 5.91E-04 0.00061
0.000635 0.000662 0.000692 0.000723 0.000756 0.000826 0.000896
0.000932 0.000968
21 21 21
1 2 1 3 1 3 2 1 3 2 4 5 6 5 6 4 5 6 5 6 7
162.3 145.2 162.5 149.6 162.7 149.7 144.6 162.4 150.0 144.9 119.3
115.8 132.7 117.2 133.2 119.2 115.7 132.5 117.1 133.1 126.4 268.9
267.5 53.6 85.4 123.1 157.7 123.0 196.5 229.9 194.9 85.6 67.1 73.0
106.1 100.4 157.7 139.2 144.9 177.9 172.3 194.1
1 2 1 3 1 3 2 1 3 2 4 5 6 5 6 4 5 6 5 6 7
162.3 145.2 162.5 149.6 162.7 149.7 144.6 162.4 150.0 144.9 119.3
115.8 132.7 117.2 133.2 119.2 115.7 132.5 117.1 133.1 126.4 268.9
```

```
267.5 53.6 85.4 123.1 157.7 123.0 196.5 229.9 194.9 85.6 67.1 73.0
106.1 100.4 157.7 139.2 144.9 177.9 172.3 194.1
1 2 1 3 1 3 2 1 3 2 4 5 6 5 6 4 5 6 5 6 7
162.3 145.2 162.5 149.6 162.7 149.7 144.6 162.4 150.0 144.9 119.3
115.8 132.7 117.2 133.2 119.2 115.7 132.5 117.1 133.1 126.4 268.9
267.5 53.6 85.4 123.1 157.7 123.0 196.5 229.9 194.9 85.6 67.1 73.0
106.1 100.4 157.7 139.2 144.9 177.9 172.3 194.1
2 1
1
0.001
1
1
0.001
1
1
0.001
1
4
22,1.0
  4   2   4   1         0.94    0.14
  6   2   6   3         0.512   1.0
  6   4   6   3         0.0312  0.0024
  7   2   7   3         0.109   0.007
  8   3   8   6         0.379   0.026
  10  3   10  2         0.392   0.025
  10  4   10  2         0.1452  0.010
  10  6   10  2         0.0423  0.004
  13  4   13  2         0.0079  0.0008
  13  5   13  2         0.0024  0.0007
  14  3   14  6         0.238   0.016
  14  8   14  6         0.0591  0.008
  16 12   16 11         0.630   0.053
  17  4   17  2         0.376   0.022
  19  1   19  2         0.0701  0.0044
  19  4   19  2         0.0894  0.0058
  19  5   19  2         0.0054  0.0008
  19  17  19  2         0.0046  0.0008
  20  4   20  2         0.178   0.089
  20  9   20  2         0.054   0.027
  21  2   21  1         0.0287  0.003
  21  5   21  1         0.0519  0.004
```

```
6,1.0
  2                10.35      0.08
  8                870        290
  9                0.204      0.030
  14               8.2        0.4
  15               0.20       0.05
  21               0.029      0.001
7,1.0
  4     2          -1.44      0.11
  6     3          -0.314     0.022
  7     3          -0.17      0.04
  8     3          -0.18      0.05
  8     6          -0.58      0.12
  13    2           0.312     0.033
  19    2          -0.11      0.04
4,1.0
  2   2   2        -0.28      0.04
  2   3   3        -0.28      0.18
  2   4   4         1.32      0.08
  2   12  12       -1.30      0.80
OP,RAW
1
0,0,0,0,0,0,0,0
0,0,0,0,0,0,0,0
0,0,0,0,0,0,0,0
0,0,0,0,0,0,0,0
0,0,0,0,0,0,0,0
0,0,0,0,0,0,0,0
0,0,0,0,0,0,0,0
0,0,0,0,0,0,0,0
0,0,0,0,0,0,0,0
0,0,0,0,0,0,0,0
0,0,0,0,0,0,0,0
0,0,0,0,0,0,0,0
0,0,0,0,0,0,0,0
0,0,0,0,0,0,0,0
0,0,0,0,0,0,0,0
0,0,0,0,0,0,0,0
0,0,0,0,0,0,0,0
0,0,0,0,0,0,0,0
```

```
0,0,0,0,0,0,0,0
1
21
1 2 3 4 5 6 7 8 9 10 11 12 13 14 15 16 17 18 19 20 21
2
0,0,0,0,0,0,0,0
...............
0,0,0,0,0,0,0,0
1
21
1 2 3 4 5 6 7 8 9 10 11 12 13 14 15 16 17 18 19 20 21
3
0,0,0,0,0,0,0,0
...............
0,0,0,0,0,0,0,0
1
21
1 2 3 4 5 6 7 8 9 10 11 12 13 14 15 16 17 18 19 20 21
0
```

D - Second part of the GOSIA input file

The following options can be directly attached to the file in Appendix C in order to perform minimization, error estimation or integration:

- **OP,MINI**

  OP,MAP has to be executed before OP,MINI is called for the first time. The first run of OP,MINI does not require OP,REST. The following section is attached to the main part of the input file to fit a set of matrix elements to to the experimental data:

```
OP,REST
0,0
OP,MINI
2100,30,0.001,0.001,0.1,1,2,1,1,0.001
OP,MINI
2100,30,0.001,0.001,0.1,1,2,1,1,0.001
OP,MINI
2100,30,0.001,0.001,0.1,1,2,1,1,0.001
OP,EXIT
```

- **OP,ERRO**

  The following section is attached to the main part of the input file to perform error estimation (to account for correlations between the matrix elements, the option parameters have to be changed to 1,0,0,1,1,1E+36):

```
OP,REST
0,0
OP,ERRO
0,0,0,0,0,1E+36
OP,EXIT
```

- **OP,INTI**

  To perform a simulation of γ-ray intensities considering the particle detector geometry and target thickness, the following section can be attached to the main part of the input file:

```
OP,REST
0,0
OP,INTI
3 -3 743.4 770 19.4 20
743.4 756.7 770
19.4 19.7 20.0
1
-6.0 6.5
1
-11.6 12.0
1
-14.0 14.0
3 -3 743.4 770 20 21
743.4 756.7 770
20 20.5 21
1
-14.0 14.0
1
-16.0 16.0
1
-17.0 17.0
3 -3 743.4 770 21 22
743.4 756.7 770
21 21.5 22
1
-17.0 17.0
1
-19.0 19.0
1
-20.4 20.0
4
743.4 750 760 770
37.26 37.21 37.13 37.05
10 -2
12.5 23.6 28.0
4
743.4 750 760 770
37.26 37.21 37.13 37.05
10 -2
28.0 32.0 34.0
4
743.4 750 760 770
```

```
37.26 37.21 37.13 37.05
10 -2
34.0 38.0 40.4
OP,EXIT
```

Only the first three θ_{LAB} ranges declared in the analysis are described here. The description of the remaining eight angular ranges was provided when simulating the γ-ray intensities at the full coverage of VAMOS++.

The same input file can be used to transform the experimental intensities to point like yields, by calling OP,CORR before OP,EXIT. In addition the number of the file containing γ-ray intensities to be read has to be changed to 3 in OP,YIEL (which corresponds to the 106Cd.f3 file).

E - GRIFFIN crystal coordinates

Table E.1 – Coordinates (polar ϑ_i and azimuthal φ_i angles) of the centre of each HPGe crystal with respect to the beam direction ($\vartheta = 0°$) in the "optimized peak-to-total" GRIFFIN configuration used in the S1790 experiment (with Clover 13 removed). Possible opening angles (θ) between the centers of a detector pair, including cases where a crystal pairs with itself ($\theta = 0°$), and the corresponding number of pairs are given in the two last columns [127, 162].

Crystal	Clover	ϑ_i	φ_i	θ	N_{PAIRS}
1	1	37.9	80.1	0	60
2	1	53.2	77.2	15.442	120
3	1	53.2	57.8	21.905	60
4	1	37.9	54.9	29.143	60
5	2	37.9	170.1	33.143	60
6	2	53.2	167.2	38.382	40
7	2	53.2	147.8	44.57	120
8	2	37.9	144.9	47.445	120
9	3	37.9	260.1	48.741	80
10	3	53.2	257.2	51.473	80
11	3	53.2	237.8	55.17	40
12	3	37.9	234.9	59.978	60
13	4	37.9	350.1	60.102	80
14	4	53.2	347.2	62.34	60
15	4	53.2	327.8	62.492	40
16	4	37.9	324.9	63.423	80
17	5	82.3	30.3	68.957	80
18	5	97.7	30.3	71.431	56
19	5	97.7	14.7	73.358	80
20	5	82.3	14.7	73.629	56
21	6	82.3	75.3	75.774	56
22	6	97.7	75.3	80.942	56
23	6	97.7	59.7	81.546	40
24	6	82.3	59.7	83.894	56
25	7	82.3	120.3	86.868	56
26	7	97.7	120.3	88.966	112
27	7	97.7	104.7	91.034	112
28	7	82.3	104.7	93.132	56
29	8	82.3	165.3	96.106	56

Table E.1 – continued

Crystal	Clover	ϑ_i	φ_i	θ	N_{PAIRS}
30	8	97.7	165.3	98.454	40
31	8	97.7	149.7	99.058	56
32	8	82.3	149.7	104.226	56
33	9	82.3	210.3	106.371	56
34	9	97.7	210.3	106.642	80
35	9	97.7	194.7	108.569	56
36	9	82.3	194.7	111.043	80
37	10	82.3	255.3	116.577	80
38	10	97.7	255.3	117.508	40
39	10	97.7	239.7	117.66	60
40	10	82.3	239.7	119.898	80
41	11	82.3	300.3	120.022	60
42	11	97.7	300.3	124.83	40
43	11	97.7	284.7	128.527	80
44	11	82.3	284.7	131.259	80
45	12	82.3	345.3	132.555	120
46	12	97.7	345.3	135.43	120
47	12	97.7	329.7	141.618	40
48	12	82.3	329.7	146.857	60
49	13	–	–	150.857	60
50	13	–	–	158.095	56
51	13	–	–	164.558	112
52	13	–	–	180.000	56
53	14	126.8	167.2		
54	14	142.1	170.1		
55	14	142.1	144.9		
56	14	126.8	147.8		
57	15	126.8	257.2		
58	15	142.1	260.1		
59	15	142.1	234.9		
60	15	126.8	237.8		
61	16	126.8	347.2		
62	16	142.1	350.1		
63	16	142.1	324.9		
64	16	126.8	327.8		

Bibliography

[1] K.S. Krane, "Introductory Nuclear Physics", Wiley, 1988.

[2] A. Bohr, B. Mottelson, "Nuclear Structure", New York, W. A. Benjamin edition, 1969.

[3] L. Wilets and M. Jean, Phys. Rev. **102**, 788 (1956).

[4] P.E. Garrett, M. Zielińska and E. Clément, Prog. Part. Nucl. Phys. **124**, 103931 (2022).

[5] D. Cline, Annu. Rev. Nucl. Part. Sci. **36**, 683 (1986).

[6] K. Kumar, Phys. Rev. Lett. **28**, 249 (1972).

[7] H. Morinaga, Phys. Rev. **101**, 254 (1956).

[8] A.N. Andreyev *et al.*, Nature **405**, 430 (2000).

[9] J. Ojala *et al.*, Nature Commun. Phys. **5**, 213 (2022).

[10] P.E. Garrett et al. Phys. Rev. Lett. **123**, 142502 (2019).

[11] P.E. Garrett et al. Phys. Rev. C **101**, 044302 (2020).

[12] S. Leoni *et al.*, Phys. Rev. Lett. **118**, 162502 (2017).

[13] K. Heyde and J.L. Wood, Rev. Mod. Phys. **83**, 1467 (2011).

[14] A. Görgen, J. Phys. G: Nucl. Part. Phys. **37**, 103101 (2010).

[15] A. Görgen and W. Korten, J. Phys. G: Nucl. Part. Phys. **43**, 024002 (2016).

[16] M. Rocchini and M. Zielińska, Physics **3**, 1237 (2021).

[17] T. Huus, C. Zupancic, Dan. Mat. Fys. Medd. **28**, 1 (1953).

[18] B. Elbek and C.K. Bockelman, Phys. Rev. **105**, 657 (1957).

[19] M.P. Fewell, D.C. Kean, R.H. Spear, and A.M. Baxter, J. Phys. G: Nucl. Phys. **3**, L27 (1977).

[20] M.T. Esat, D.C. Kean, R.H. Spear, M.P. Fewell, and A.M. Baxter, Phys. Lett. **72B**, 49 (1977).

[21] M.T. Esat, M.P. Fewell, R.H. Spear, T.H. Zabel, A.M. Baxter, and S. Hinds, Nucl. Phys. **A362**, 227 (1981).

[22] R.H. Spear, T.H. Zabel, M.T. Esat, A.M. Baxter, and S. Hinds, Nucl. Phys. **A378**, 559 (1982).

[23] W.J. Vermeer, M.T. Esat, and R.H. Spear, Nucl. Phys. **A389**, 185 (1982).

[24] W.J. Vermeer, M.T. Esat, J.A. Kuehner, R.H. Spear, A.M. Baster, and S. Hinds, Phys. Lett. **122B**, 23 (1983).

[25] D. Ward *et al.*, Nucl. Phys. A **600**, 88 (1996).

[26] I. Wiedenhöver *et al.*, Phys. Rev. Lett. **83**, 2143 (1999).

[27] S. Zhu *et al.*, Phys. Rev. C **81**, 041306(R) (2010).

[28] K. Abu Saleem *et al.*, Phys. Rev. C **70**, 024310 (2004).

[29] X. Wang *et al.*, Phys. Rev. Lett. **102**, 122501 (2009).

[30] P.E. Garrett *et al.*, Phys. Rev. C **106**, 064307 (2022).

[31] J. Henderson *et al.*, Phys. Rev. C **97**, 044311 (2018).

[32] N. Benczer-Koller *et al.*, Phys. Rev. C **94**, 034303 (2016).

[33] O. Kenn *et al.*, Phys. Rev. C **65**, 034308 (2002).

[34] A. Chester *et al.* Phys. Rev. C **96**, 011302(R) (2017).

[35] P.A. Butler *et al.*, Nature Commun. **10**, 2473 (2019).

[36] I.J. Thompson, Comput. Phys. Rep. **7**, 167 (1988); FRESCO web page: http://www.fresco.org.uk

[37] D.H. Gloeckner, M.H. Macfarlane, S.C. Pieper, Techn. Report (1976), OSTI: 7363080.

[38] M. Rhoades-Brown, M.H. Macfarlane and S.C. Pieper, Phys. Rev. C **21**, 2417 (1980).

[39] M.W. Guidry *et al.*, Phys. Rev. Lett. **40**, 1016 (1978).

[40] W.J. Kernan *et al.*, Nucl. Phys. A **524**, 344 (1991).

[41] G. Eckert *et al.*, Z. Phys. A **343**, 267 (1992).

[42] K. Alder and A. Winther, "Electromagnetic Excitation", North-Holland: Amsterdam, Netherlands, 1975.

[43] Fayyazudin and Riazuddin, "Quantum Mechanics", World Scientific, Singapore, 1990.

[44] O. Häusser, "Coulomb reorientation", in: "Nuclear spectroscopy and reactions", ed. J. Cerny, part C (Academic Press, New York, 1974) p. 55.

[45] A.M. Moro, Lecture notes on "Quantum scattering theory and direct nuclear reactions", ISOLDE, April 2014.

[46] GANIL website: https://www.ganil-spiral2.eu

[47] P. Sortais *et al.*, Nuclear Physics News, **6**, 6 (1996).

[48] M. Siciliano, PhD thesis, University of Padova, 2017.

[49] M. Siciliano *et al.*, Phys. Lett. B **806**, 135474 (2020).

[50] M. Siciliano *et al.*, Phys. Rev. C **104**, 034320 (2021).

[51] H. Savajols, Nucl. Instrum. Methods Phys. Res. B **204**, 146 (2003).

[52] S. Akkoyun *et al.*, Nucl. Instrum. Methods Phys. Res. A **668**, 26 (2012), and references therein.

[53] A. Dewald, S. Harissopulos, P. Von Brentano, Z. Phys. A **334**, 163 (1989).

[54] A. Dewald, O. Möller, P. Petkov, Prog. Part. Nucl. Phys. **67**, 786 (2012).

[55] G.F. Knoll, "Radiation detection and measurement", John Wiley & Sons, 1979.

[56] A. Lopez-Martens *et al.* Nucl. Instrum. Methods Phys. Res. A **533**, 454 (2004).

[57] Rosa María Pérez Vidal, PhD thesis, University of Valencia, 2019.

[58] elo.f, available from https://www.pas.rochester.edu/~cline/Gosia/

[59] D. De Frenne and A. Negret, Nucl. Data Sheets **109**, 943 (2008).

[60] A. Linnemann *et al.* Phys. Rev. C **75**, 024310 (2007).

[61] A. Linnemann, PhD thesis, University of Cologne, 2005.

[62] T. Schmidt, PhD thesis, University of Cologne, 2019.

[63] S.A. Berendakov, L.I. Govor, A.M. Demidov, I.V. Mikhailov, Proc. 38th Ann. Conf. Nucl. Spectrosc. Struct. At. Nuclei, Baku, p.82 (1988); INDC(CCP)299/G, p.26 (1988).

[64] Rene Brun and Fons Rademakers, ROOT - An Object Oriented Data Analysis Framework, Proceedings AIHENP'96 Workshop, Lausanne, Sep. 1996, Nucl. Instrum. Methods Phys. Res. A **389** 81 (1997).

[65] M. Siciliano, Nuovo Cimento C **40**, 84 (2017).

[66] G.J. Kumbartzki *et al.*, Phys. Rev. C **93** 044316 (2016).

[67] M.C. Mermaz *et al.* Phys. Rev. C **15**, 307 (1977).

[68] T. Czosnyka *et al.*, Bull. Am. Phys. Soc. **28**, 745 (1983).

[69] M. Zielińska *et al.* Eur. Phys. J. A **52**, 99 (2016).

[70] I.N. Wischnewski *et al.* Z. Phys. A **298**, 21 (1980).

[71] T.J. Gray *et al.*, Phys. Lett. B **834**, 137446 (2021).

[72] W.T. Milner *et al.*, Nucl. Phys. A **129**, 687 (1969).

[73] M.T. Esat *et al.* Nucl. Phys. A **274**, 237 (1976).

[74] A. Kleinfeld *et al.* Nucl. Phys. A **158**, 81 (1970).

[75] D. Rhodes *et al.* Phys. Rev. C **103**, L051301 (2021).

[76] G. Gusinsky and V. Zvonov, Izv. Akad. Nauk SSSR, Ser. Fiz. **47**, 862 (1983).

[77] D. Kalaydjieva *et al.*, to be submitted to Eur. Phys. J. A.

[78] W. D. Hamilton, "The electromagnetic interaction in nuclear spectroscopy", North-Nolland/American ELSEVIER, 1975.

[79] L.E. Samuelson, J.A. Grau, S.I. Popik, F.A. Rickey, and P.C. Simms, Phys. Rev. C **19**, 73 (1979).

[80] W. Andrejtscheff, *et al.*, Nucl. Phys. A **437**, 167 (1985).

[81] T.K. Alexander, J.S. Forster, Adv. Nucl. Phys. **10**, 197 (1978).

[82] "Nuclear Data Sheets, General Policies – Presentation of Data", available at https://www.nndc.bnl.gov/nds/docs/NDSPolicies.pdf

[83] M.P. Fewell *et al.* Aust. J. Phys. **38**, 555 (1985).

[84] P. Ring, P. Schuck, "The nuclear many-body problem", New York, Springer-Verlag, 1985.

[85] I. Thompson, F. Nunes, "Nuclear Reactions for Astrophysics" (Cambridge University Press, Cambridge, 2009). Appendix - User Guide of FRESCO.

[86] R.O. Akyuz and A. Winther, Proc. Enrico Fermi Int. School of Physics, 1979, "Nuclear structure and heavy-ion reactions", ed. R.A. Broglia, C.H. Dasso and R. Ricci (North-Holland, Amsterdam, 1981) p. 491.

[87] Dr. Nicholas Keeley, Nuclear Physics Division, National Centre for Nuclear Research, Warsaw, Poland, private communication.

[88] D. Cline, T. Czosnyka *et al.*, "GOSIA user manual for simulation and analysis of Coulomb excitation experiments", 2012, available from https://www.pas.rochester.edu/~cline/Gosia/

[89] P.M. Endt, At. Data Nucl. Data Tables, **26**, 47 (1981).

[90] N. Amzal *et al.*, Nucl. Phys. A **34**, 4654 (2004).

[91] T. Kibédi *et al.* Nucl. Instrum. Methods Phys. Res. A **589**, 202 (2008).

[92] O.B. Tarasov and D. Bazin, "LISE++": Radioactive beam production with in-flight separators. Nucl. Instrum. Methods Phys. Res. B, 266(19):4657–4664, 2008.

[93] S.Kasemann - The Virtual Targetlab, Institute for nuclear physics, University of Cologne, Germany, 1996.

[94] James F. Ziegler, M.D. Ziegler, J.P. Biersack, SRIM – The stopping and range of ions in matter, Nucl. Instrum. Methods Phys. Res. B, Volume 268, 2010.

[95] S.A. Berendakov, L.I. Govor, A.M. Demidov, I.V. Mikhailov, INDC(CCP)299/G, p.26 (1988).

[96] M. Pignanelli *et al.*, Nucl. Phys. A **540**, 27 (1992).

[97] M. Pignanelli *et al.*, Nucl. Phys. A **519**, 567 (1990).

[98] A. Gade *et al.* Phys. Rev. **65**, 041305(R) (2002).

[99] P.E. Garrett *et al.*, Phys. Rev. C **59**, 2455 (1999).

[100] D. Bandyopadhyay, C.C. Reynolds, S.R. Lesher *et al.*, Phys. Rev. C **68**, 014324 (2003).

[101] W. Donner and W. Greiner, Z. Phys. **197**, 440 (1966).

[102] D.S. Jamieson *et al.*, Phys. Rev. C **90**, 054312 (2014).

[103] P.E. Garrett *et al.* Phys. Rev. C **75**, 054310 (2007).

[104] D.J. Rowe, "Nuclear Collective Motion: Models and Theory", London: Methuen, 1970.

[105] P.E. Garrett and J.L. Wood J. Phys. G: Nucl. Part. Phys. **37** 064028 (2010).

[106] J. Kumpulainen *et al.*, Phys. Rev. C **45**, 640 (1992).

[107] C. Fahlander *et al.* Nucl. Phys. A **485** 318 (1988).

[108] A. Leviatan *et al.* Phys. Rev. C **98**, 031302(R) (2018).

[109] P.E. Garrett *et al.* Phys. Rev. C **64**, 024316 (2001).

[110] T.R. Rodríguez and J.L. Egido, Phys. Rev. C **81**, 064323 (2010).

[111] M. Borrajo, T. R. Rodríguez, and J. L. Egido, Phys. Lett. B **746**, 341 (2015).

[112] J.L. Egido, M. Borrajo, T.R. Rodríguez, Phys. Rev. Lett. **116**, 052502 (2016).

[113] T. Schmidt *et al.* Phys. Rev. C **96**, 014302 (2017).

[114] R. Machleidt, Phys. Rev. C **63**, 024001 (2001).

[115] N. Boelaert *et al.* Phys. Rev. C **75**, 014316 (2007).

[116] A. Blazhev *et al.* Phys. Rev. C **69**, 064304 (2004).

[117] N. Boelaert *et al.*, Phys. Rev. C **75**, 054311 (2007).

[118] K. Wrzosek-Lipska *et al.*, Acta Phys. Pol. B **51**, 789 (2020).

[119] K. Wrzosek-Lipska *et al.*, LNL Annual Report 2022, INFN-LNL Report **273**, p.24 (2023).

[120] I. Thorslund *et al.* Nucl. Phys. A **568**, 306 (1994).

[121] T.R. Rodriguez, private communication.

[122] K. Wrzosek-Lipska, private communication.

[123] C.Y. Wu, D. Cline, T. Czosnyka *et al.*, Nucl. Phys. A **607**, 178 (1996).

[124] J.L. Wood, EPJ Web of Conferences **93**, 01006 (2015).

[125] J. Blachot, Nucl. Data Sheets **91**, 135 (2000).

[126] S. Drissi *et al.*, Nucl. Phys. A **614**, 137 (1997).

[127] A.B. Garnsworthy *et al.*, Nucl. Instrum. Methods Phys. Res. A **918**, 9 (2019).

[128] J.K. Smith *et al.*, Nuclear Instrum. Methods Phys. Res. A **922**, 47 (2019).

[129] G. Audi *et al.*, Chin. Phys. C **36**, 1287 (2012).

[130] H. Mei *et al.*, Phys. Rev. C **85**, 034321 (2012).

[131] P. Singh *et al.*, Phys. Rev. Lett. **121**, 192501 (2018).

[132] K. Nomura, R. Rodriguez-Guzmán, and L.M. Robledo, Phys. Rev. C **94**, 044314 (2016).

[133] K. Sieja, F. Nowacki, K. Langanke, and G. Martinez-Pinedo, Phys. Rev. C **79**, 064310 (2009).

[134] T. Togashi, Y. Tsunoda, T. Otsuka, and N. Shimizu, Phys. Rev. Lett. **117**, 172502 (2016).

[135] E. Clément *et al.*, Phys. Rev. Lett. **116**, 022701 (2016).

[136] E. Clément *et al.*, Phys. Rev. C **94**, 054326 (2016).

[137] G. Jung *et al.*, Phys. Rev. C **22**, 252 (1980).

[138] K. Kawade *et al.*, Z. Phys. A **304**, 293 (1982).

[139] V. Karayonchev *et al.* Phys. Rev. C **102**, 064314 (2020).

[140] T. Kibédi and R.H. Spear, At. Data Nucl. Data Tables **89**, 77 (2005).

[141] K. Becker *et al.*, Z. Phys. A **319**, 193 (1984).

[142] J. McLain *et al.*, J. Phys.: Conf. Ser. **2244**, 012062 (2022).

[143] T.A. Khan *et al.*, Z. Phys. A **283**, 105 (1977).

[144] P.E. Garrett *et al.*, Acta Phys. Pol. B **38**, 1169 (2007).

[145] F.K. Wohn *et al.*, Phys. Rev. C **33**, 677 (1986).

[146] W. Urban *et al.*, Phys. Rev. C **3100**, 014319 (2019).

[147] B. Singh and J. Chen, Nucl. Data Sheets **172**, 1 (2021).

[148] H.J. Rose and D.M. Brink, Rev. Mod. Phys. **39**, 306 (1967).

[149] R.G. Arns and M.L. Wiedenbeck, Phys. Rev. **111**, 1631 (1958).

[150] K. Krane, R. Steffen, R. Wheeler, At. Data Nucl. Data Tables **11**, 351 (1973).

[151] E. der Mateosian and A. Sunyar, At. Data Nucl. Data Tables **13**, 407 (1974).

[152] A.D. MacLean, PhD thesis, University of Guelph, 2019.
https://hdl.handle.net/10214/26382

[153] TRIUMF website: https://www.triumf.ca

[154] "ISAC and ARIEL: The TRIUMF Radioactive Beam Facilities and the Scientific Program"; dedicated volume of Hyperfine Interactions (Hyperfine Interact. 225 (2014)).

[155] P. Van Duppen, "Isotope Separation On Line and Post Acceleration", in: "The Euroschool Lectures on Physics with Exotic Beams, Vol. II" Lecture Notes in Physics **700**, Springer, Berlin, Heidelberg, 2006.

[156] G.C. Ball, G. Hackman and R. Krücken, Phys. Scr. **91**, 093002 (2016).

[157] I. Bylinskii, M.K. Craddock, Hyperfine Interact. **225**, 9 (2014).

[158] P.G. Bricault, F. Ames, M. Dombsky, P. Kunz and J. Lassen, Hyperfine Interact. **225**, 25 (2014).

[159] Data extracted from ENDSF database, https://www.nndc.bnl.gov/ensdf/

[160] E. Browne, J.K. Tuli, Nucl. Data Sheets **145**, 25 (2017).

[161] M. Rocchini, private communication.

[162] GRIFFIN Array angles for gamma-gamma angular correlations:
https://adamgarnsworthy.github.io/griffin-angle-mapper/griffin-angle-mapper.html

[163] H. Bidaman, PhD thesis, University of Guelph, 2023.
https://hdl.handle.net/10214/27505

[164] https://github.com/GRIFFINCollaboration/GRSISort/wiki

[165] S. Ritt *et al.*, https://daq00.triumf.ca/MidasWiki/index.php/Main_Page

[166] A. Garnsworthy *et al.*, Nucl. Instrum. Methods Phys. Res. A **853**, 85 (2017).

[167] GRIFFIN efficiency calculator:
https://griffincollaboration.github.io/efficiencyCalculator/

[168] R. Dunlop, PhD thesis, University of Guelph (2019).
http://hdl.handle.net/10214/16278

[169] T. Zidar, MSc thesis, University of Guelph (2019).
http://hdl.handle.net/10214/14706

[170] D.C. Radford, https://radware.phy.ornl.gov/

[171] J. Münzel *et al.*, Z. Phys. A **321**, 515 (1985).

[172] D. Kalaydjieva *et al.*, Acta Phys. Pol. B Proc. Suppl. **316**, 4-A15 (2023).

[173] P.H. Richter, "Estimating Errors in Least-Squares Fitting",
TDA Progress Report 42-122 (1995).

[174] C.E. Svensson and A.B. Garnsworthy, Hyperfine Interact. **225**, 127 (2013).

[175] J. Allison *et al.*, Nucl. Instrum. Methods Phys. Res. A **835**, 186 (2016).

[176] S. Agostinelli *et al.*, Nucl. Instrum. Methods Phys. Res. A **506**, 250 (2003).

[177] S. Robinson, Nucl. Instrum. Methods Phys. Res. A **292**, 386 (1990).

[178] M. Honma, T. Otsuka, T. Mizusaki, and M. Hjorth-Jensen,
Phys. Rev. C **80**, 064323 (2009).

[179] M. Honma *et al.*, RIKEN Accel. Prog. Rep. **45**, 35 (2012).

[180] T. Otsuka *et al.*, Phys. Rev. Lett. **104**, 012501 (2010).

[181] Y. Tsunoda *et al.*, Phys. Rev. C **89**, 031301 (2014).

[182] T. Otsuka and Y. Tsunoda, J. Phys. G **43**, 024009 (2016).

[183] T. Togashi, private communication.

[184] C. Kremer *et al.*, Phys. Rev. Lett. **117**, 172503 (2016).

[185] E. Clément *et al.*, Phys. Rev. C **75**, 054313 (2007).

[186] G. Pasqualato *et al.*, Eur. Phys. J. A **59**, 276 (2023).

[187] W. Urban *et al.* Phys. Rev. C **99**, 064325 (2019).

[188] J.-M. Régis *et al.*, Nucl. Instrum. Methods Phys. Res. A **726**, 191 (2013).

[189] B. Alikhani *et al.*, Nucl. Instrum. Methods Phys. Res. A **675**, 144 (2012).

[190] L. W. Fagg and S.S. Hanna, Rev. Mod. Phys. **31**, 711 (1959).

[191] A. B. Garnsworthy and P.E. Garrett, Hyperfine Interact. **225**, 121 (2014).